# MINERALOGY AND GEOCHEMISTRY OF ALKALI FELDSPARS FROM THE TANCO PEGMATITE, SOUTHEASTERN MANITOBA

by

JARROD A. BROWN

A Thesis
Submitted to the Faculty of Graduate Studies
In Partial Fulfillment of the Requirements
For the Degree of

MASTER OF SCIENCE

Department of Geological Sciences
University of Manitoba
Winnipeg, Manitoba, Canada

THE UNIVERSITY OF MANITOBA

FACULTY OF GRADUATE STUDIES

*****

COPYRIGHT PERMISSION

# MINERALOGY AND GEOCHEMISTRY OF ALKALI FELDSPARS FROM THE TANCO PEGMATITE, SOUTHEASTERN MANITOBA

BY

JARROD A. BROWN

A Thesis/Practicum submitted to the Faculty of Graduate Studies of The University of Manitoba in partial fulfillment of the requirement of the degree

of

MASTER OF SCIENCE

## ABSTRACT

The alkali feldspar paragenetic sequence in the Tanco pegmatite at Bernic Lake, Manitoba, spans the entire crystallization and cooling history of the pegmatite, and includes six different K(Rb)-feldspar and six different albite varieties. Total feldspar modal abundances approach 50% for the entire pegmatite volume. Blocky K-feldspar, aplitic albite and cleavelandite together account for more than 95% of total feldspar volumes. The other, late, low-temperature feldspars include (Rb,K) or (K) adularia and albite in veins and cavities, mostly contained in inner zones associated with pollucite and petalite. Feldspars collected from each of the nine major zones of the pegmatite have been assessed in terms of composition and structural state, along one east-west transect and two north-south transects.

In an inward progression through the concentrically zoned pegmatite, average bulk-compositional data for blocky K-feldspar reveal steady increases in $Rb_2O$ (1.45 - 3.08 wt.%), and $Cs_2O$ (0.11 - 0.29), increasing followed by decreasing contents of $P_2O_5$ (0.34 - 0.47 - 0.38 wt.%), $Li_2O$ (0.014 - 0.095 - 0.048) and Tl (105 - 239 - 118 ppm), decreasing $Na_2O$ (2.5 - 1.1 wt.%) and CaO (0.13 - 0.08), and variable BaO (0.004 - 0.17 wt.%) and $Ga_2O_3$ (0.006 - 0.010). Rare-alkali contents in albite determined by EMPA are consistently at, or below, limits of detection and exhibited poor to random geochemical trends. CaO in aplitic albite and cleavelandite decreases (0.08 - 0.03 wt.%), $P_2O_5$ in both types increases then decreases (0.15 - 0.20 - 0.11 wt.%). Overall $K_2O$ content is variable (0.03 - 0.09 wt.%) but is slightly enriched in aplitic albite relative to cleavelandite. Individual late (K-Rb) adularian feldspars from veins and clusters in pollucite exhibit extreme ranges in $Rb_2O$ (1.80 - 24.84 wt.%) and $Cs_2O$ (0.10 - 1.43), and significant $P_2O_5$ (b.l.d. - 0.51 wt.%). X-ray powder-diffraction data indicate near

maximum structural order of the early feldspar varieties as maximum microcline and high albite. Hydrothermal adularia crystals are essentially end-member ($Or_{100}$) high sanidine.

The large and economically significant Tanco pegmatite represents an extreme in terms of petrologic processes involving fractional and disequilibrium crystallization from granitic melts enriched in volatiles and fluxing components ($H_2O$, B, F, P), rare-alkalis (Li, Rb, Cs) and HFSE (Ta, Nb, Zr, Hf). The omnipresent alkali feldspars are the most significant carriers of P, Li, Rb, Tl, and Cs prior to the stabilization of large volumes of amblygonite-montebrasite, petalite, lepidolite and pollucite. The rise and fall of trace-element content in feldspars, in relation to the spatial distribution of different zones and mineral assemblages, has implications in terms of the internal evolution of complex granitic pegmatites, as well as on the types and extents of subsolidus readjustments. Large-scale textures of the blocky K-feldspars in relation to matrix-forming albites are representative of primary magmatic crystallization, but the phase constitution of the K-feldspar – maximum microcline and low albite in perthitic intergrowth, was produced by subsolidus readjustment. This is also responsible for the origin of late K-Rb-feldspars and associated albites.

## ACKNOWLEDGMENTS

The making of this thesis would not have been possible without the generous support of colleagues, friends and family.

I would foremost like to thank P. Černý for his thoughtful and patient guidance during these 3 years in Winnipeg, as guide and mentor through the wonderful world of 'pegmatology'. Petr's warm-hearted humour, and passion for pegmatites inspires open dialogue, and an infective enthusiasm for pegmatites and the sciences in general.
Na vas'e zdraví.

Invaluable analytical and technical support was provided by Ron Chapman, Neil Ball, Greg Morden, and Sergio Mejia at the University of Manitoba, and administrative support by Elizabeth Ross, Margo MacBride and Sharon Kirsch.

Special thanks goes out to Tanco staff – Peter Vanstone for access to information and technical support, and also to Jamie Law and Shane Moran for their assistance in the core-shack and in underground sampling.

And finally to Amy, who has shared all manners of life with me in Winnipeg, and who lovingly offered to drive me back to BC at the earliest possible date.

I dedicate this work to my parents, Sharon and Ted Brown, whose love and support have made it possible for me to rise to the greatest challenge – life itself.

## TABLE OF CONTENTS

## LIST OF FIGURES

## LIST OF TABLES

## CHAPTER 1: INTRODUCTION

The Tanco pegmatite located at Bernic Lake, Manitoba is one of the largest and most fractionated granitic pegmatites in the world. On the basis of texture and mineralogy, 9 different zones are defined which collectively contain more than 100 different mineral species, including economic quantities of Li, Cs and Ta bearing minerals. Tanco is essentially an undeformed, blind pegmatite that crystallized rapidly from high T, low P conditions, under relatively closed conditions. Consequently, primary textures and bulk composition of the pegmatite are well preserved, making this site ideal for detailed work on the mineralogy, geochemistry and petrology of primary processes in highly evolved granitic pegmatites.

Feldspars in Tanco are eminently useful in the study of granitic pegmatites for several reasons. The modal abundance of all feldspars in the Tanco pegmatite approaches 50% by volume, and controls a significant portion of the bulk geochemical budget for major and trace-elements. There are at least 6 different varieties of K-feldspar, and 6 different varieties of albite, with at least 3 varieties of each species found in most zones of the pegmatite. Each feldspar type has unique properties in terms of texture, composition, and crystal structure, some of which are broadly variable. Trace-element substitutions, particularly in blocky K-feldspars, are sensitive to the time-temperature dependent geochemical evolution during primary crystallization. The crystal structure of individual feldspars depends largely upon cooling rate, subsolidus fluid interactions, and to a lesser degree, trace-element substitutions. Thus the purpose of this thesis is:

i) to review the distribution and textural features of different feldspar types in the zoned pegmatite;

ii) to establish the range of variations in chemical compositions, crystal-chemistry and structural state for each feldspar type;

iii) to establish spatial variations in chemical composition and structural state of feldspars across the pegmatite;

The data and interpretations presented in this thesis will be beneficial in terms of petrologic considerations and comparisons between other pegmatites in granitic systems. This applies particularly to highly fractionated granitic pegmatites, the feldspars of which have never been subject to a detailed scrutiny.

# CHAPTER 2: INTRODUCTION TO FELDSPAR NOMENCLATURE, CRYSTAL STRUCTURE, AND CHEMICAL COMPOSITION

Feldspars constitute a substantial percentage of the Earth's crust, are found in almost every geological environment, and exhibit a wide range of physical and chemical properties which are diagnostic of the physico-chemical conditions under which they formed. The available literature on general aspects of feldspar crystal structure, mineralogy, geochemistry, thermodynamics and petrologic implications is exhaustive; however, specific information on feldspars in highly evolved pegmatitic systems is rather limited. This is in part due to the complexities of the pegmatitic environment: processes involved during primary crystallization of granitic melts may reach extreme limits in terms of disequilibrium or fractional crystallization. Such processes ultimately lead to exceptional petrological textures, and accumulations of rare elements including Li, Be, Rb, Cs, Tl, Mn, Ta, Nb, Sn, Ga, U, REEs, and volatile fluxing components such as B, F, P, Cl, and $H_2O$. The transition from magmatic to subsolidus conditions is often difficult to characterize, as the specific mechanisms leading to the diverse textural and compositional features of pegmatites are not yet fully understood.

Pegmatite systems are difficult to model in comparison to less evolved systems that crystallized at, or near, equilibrium; nevertheless, an understanding of the general physical and chemical properties of feldspars is required in order to facilitate further discussion. The following sections on nomenclature, crystal structure and chemistry borrow heavily from general feldspar texts written by Ribbe (1983), and Smith and Brown (1988).

## 2.1 Nomenclature

The general chemical formula of feldspars is $MT_4O_8$: *T*, in most natural feldspars is primarily (Al,Si); divalent, group-II *M*-cations form alkali-earth feldspars [(Ca,Ba) $Al_2Si_2O_8$], monovalent, group-I *M*-cations form alkali feldspars [(Na, K) $AlSi_3O_8$]. Mineral stabilities and solid-solution series are commonly discussed with reference to the feldspar An-Ab-Or ternary diagram (Figure 2.1) which encompasses the three most widespread components – anorthite, albite, and K-feldspar. Complete solid solution is characteristic of the plagioclase series $Na_yCa_{1-y}\ Al_{2-y}\ Si_{2+y}\ O_8$ ($0 \geq y \geq 1$), corresponding to the coupled substitution $Na^{1+}\ Si^{4+} = Ca^{2+}\ Al^{3+}$. There is a complete to incomplete solid solution series in the alkali-feldspar system; the extent of solid solution is mostly dependent on T and P. At low temperature (*i.e.*: below 750 °C at constant $P_{H2O}$; Figure 2.1), the large ionic size difference between K and Na promotes immiscibility in the alkali feldspar series, which is, in part, largely responsible for the development of perthite texture.

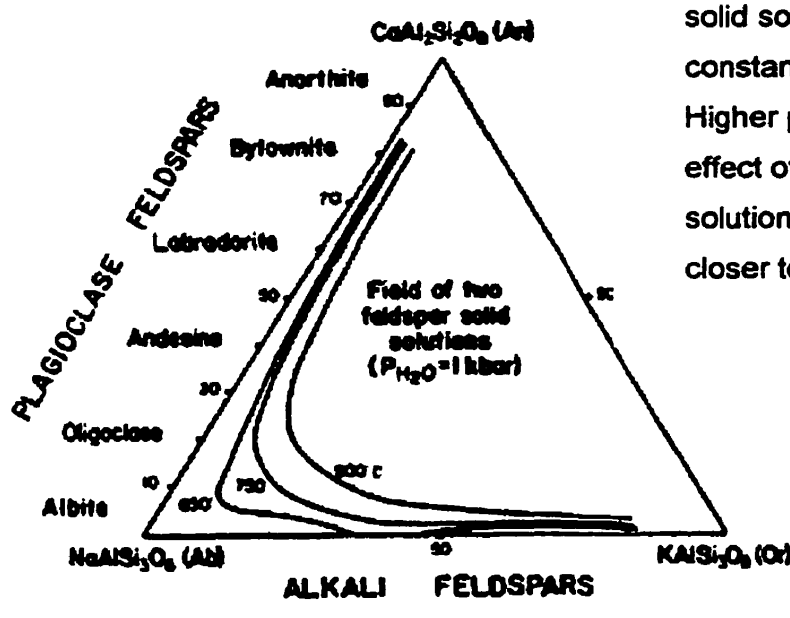


**Figure 2.1** The ternary feldspar system (An-Ab-Or) highlighting the two major solid solution series at constant $P_{H2O}$ (Ribbe, 1983). Higher pressures have the effect of moving the solid-solution field boundaries closer to the binary joins.

Different structural states, characterized by different degrees of ordering of the tetrahedral (Al,Si) cations, are also considered in the naming of feldspar species. K-feldspar structural varieties include: 1) high sanidine (HS) for highly disordered monoclinic feldspar; 2) orthoclase for ordered monoclinic feldspar; 3) intermediate microcline (IM) for disordered triclinic feldspar; and 4) low or maximum microcline (MM) for highly ordered triclinic feldspar. The structural varieties of albite include: 1) monalbite (MA) – highly disordered and monoclinic, 2) high albite (HA) – disordered and triclinic, and 3) low albite (LA) – ordered and triclinic. Smith and Brown (1988) adopted the use of 'high' and 'low' as modifiers in front of the compositional names of Figure 2.1, for high temperature (Figure 2.2) and low-temperature (Figure 2.3) feldspars.

## 2.2 Crystal structure

Feldspars are framework silicates characterized by corner-sharing $AlO_4$ and $SiO_4$ tetrahedra linked in an infinite 3-dimensional array. The basic structural unit consists of four-membered rings of these $TO_4$ tetrahedra (Figure 2.4) which, when corner-shared with other such rings, form double crankshaft-like chains parallel to (100) (Figure 2.5). The simplest and highest symmetry feldspar structure is that of C2/m sanidine. The four-membered ring of this feldspar as envisioned down the a-axis, consists of two pairs of non-identical tetrahedral sites ($T_1, T_2$); one $T_1$-$T_2$ pair has apices pointing up (U), the other has apices pointing down (D). $T_1$ and $T_2$ are related by a mirror plane parallel to (010). At lower symmetry, the (010) mirror plane is absent and the $T_1$ and $T_2$ sites expand into four non-identical tetrahedral sites, arbitrarily defined: $T_1o$, $T_1m$, $T_2o$, and $T_2m$. This loss of symmetry corresponds to the shift from monoclinic to triclinic symmetry. Fully ordered K-feldspar and albite belong to the metrically triclinic space group C $\bar{1}$. The topology of the four $T$-sites is conveniently described with reference to the 'dog-face' or c*-axis projection (Figure 2.6).

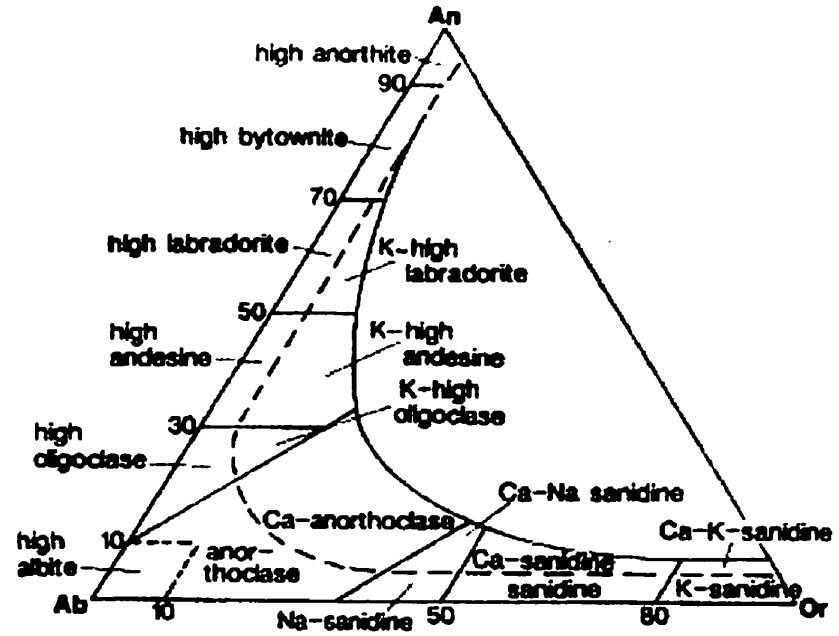


**Figure 2.2** Nomenclature for high temperature, disordered ternary feldspars (Smith and Brown 1988).

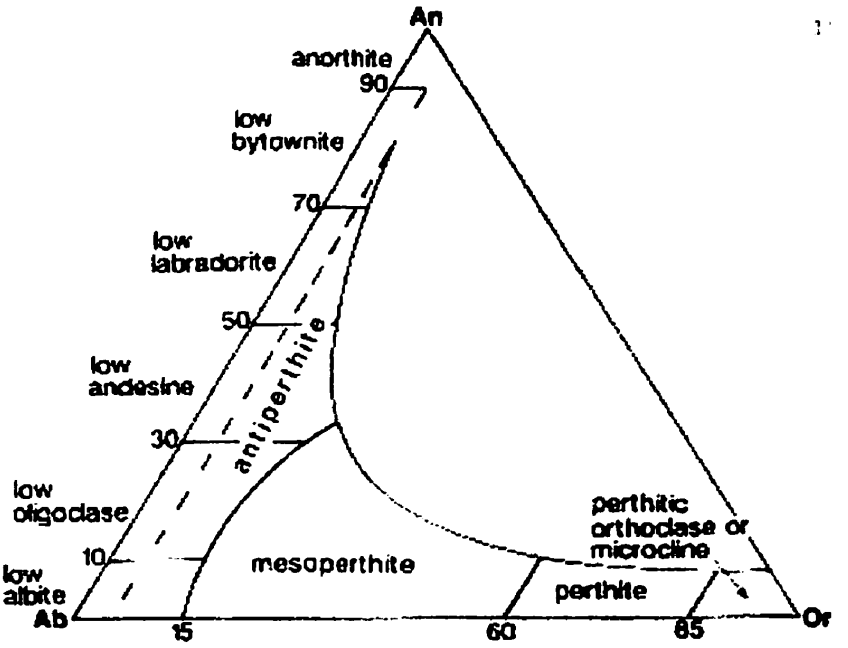


**Figure 2.3** Nomenclature for low temperature, ordered ternary feldspars (Smith and Brown 1988).

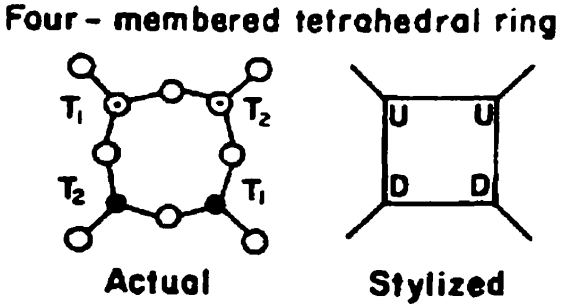


**Figure 2.4** Projection of the four-fold tetrahedral ring on (20 $\bar{1}$) (left) and a stylized representation (right): U=upward pointing tetrahedron; D=downward pointing tetrahedron. (Ribbe, 1983).

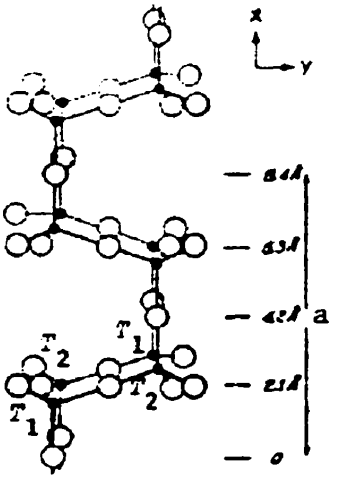


**Figure 2.5** The double-crankshaft chain of four-membered tetrahedral rings that run parallel to *a* in all feldspars (Ribbe, 1983).

The 'dog-face' projection illustrates how the double-crankshaft units are connected through adjacent $T_2$ vertices in the b-direction, thereby generating sheets of crankshaft chains. There is one such sheet per c-repeat. $T_2$ tetrahedra only have bonds within the double crankshaft sheets, whereas the $T_1$ tetrahedra link adjacent sheets.

## 2.3 Order-disorder reactions

At high temperature, *i.e.* in a more energized state, a random distribution of Si and Al ensures similar $T_1$-*O* and $T_2$-*O* bond lengths. At lower temperature however, the differences in valency and size of Si and Al are more influential, and result in the preferential movement of Al into the *T1* site (Ribbe, 1983). The resulting local structural distortion favours the migration of Al into adjacent $T_1o$ sites, and propagates longer-range ordering (Smith and Brown, 1988).

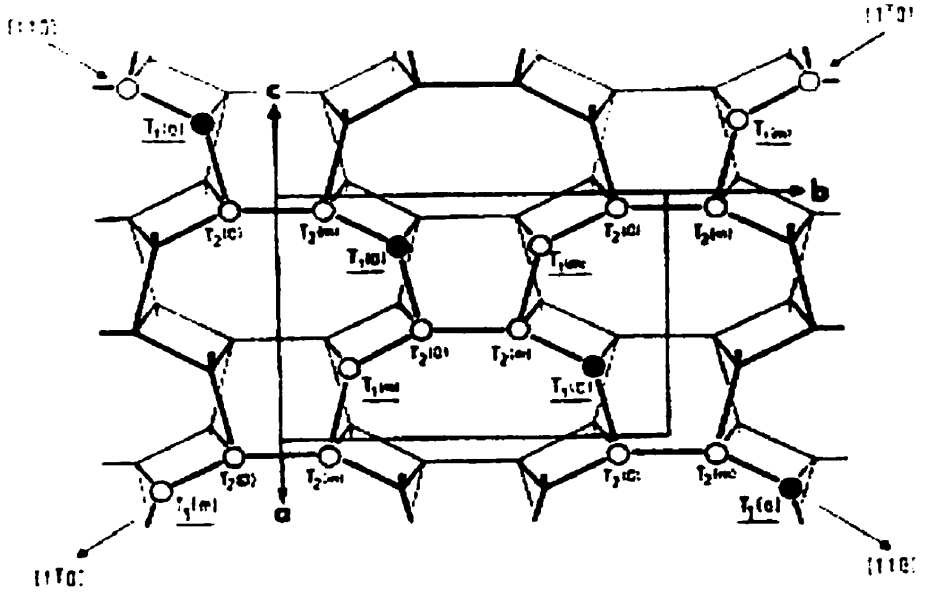


**Figure 2.6** Idealized 'dog-face' projection of the feldspar structure onto the plane (001) along $c^*$, featuring the tetrahedral sequence within chains along the [110] and [1 $\bar{1}$0] directions, respectively. In a completely ordered alkali feldspar structure $T^{3+}$ is found only in the [110] chains (solid circles), whereas the [1 $\bar{1}$0] chains are free from $T^{3+}$. (Ribbe, 1983).

Variable cooling rates, pressure, deformation, surface area, feldspar compositions, and presence and composition of fluids, all influence the ordering of primary, homogeneous and disordered feldspars (Cerný, 1994). Martin (1974) examined hundreds of natural and synthetic feldspars and performed a series of P,T, and time variable experiments to better understand the ordering processes of alkali feldspars. He determined that the rate of cooling is one of the most important variables controlling subsolidus ordering of feldspars. Ordering rates are also strongly influenced by the presence of aqueous fluids. $H_2O$ is an important catalytic agent; hydrolysis of alkali feldspars proceeds by the following reaction:

$$Na(\text{or } K)\,AlSi_3O_8 + 2H_2O \leftrightarrow (H_3O)AlSi_3O_8 + OH^- + Na^+ (\text{or } K^+)$$

This is the first step in Al-Si ordering leading to a series of solution and redeposition reactions involving the breaking of Si-O and Al-O bonds by $H^+$:

$$Si\text{-}O\text{-}Si + H^+ \leftrightarrow Si\text{-}OH + \text{-}Si$$

$$Al\text{-}O\text{-}Al + H^+ \leftrightarrow Al\text{-}OH + \text{-}Al$$

Local redistribution of tetrahedral cations to satisfy minimum chrystallographic energies results in increasing order with decreasing temperature. The ordering process is reversible – annealed feldspars tend to revert to disordered states. Regardless of the direction of order-disorder process, $H_2O$ is an essential catalytic agent; without it, the strong *T-O* bonds of the tetrahedral framework cannot be broken (Martin, 1974).

Although albite and K-feldspar both share the same tendency toward Al accumulation in the $T_1o$ site with decreasing temperature, the specifics of the ordering process differ. Two first-order breaks define the thermodynamic stability fields of albite (Figure 2.7): the first, at ~ 980°C ($Ab_{100}$), marks the displasive transition between monalbite and triclinic high albite, the second boundary at ~680 °C marks the transition between high and low albite.

Two first-order breaks also define stability fields for K-feldspars (Figure 2.7): the first at ~800°C ($Or_{100}$) delineates the stability fields of high sanidine and orthoclase, both are monoclinic feldspars; the second break at ~575 °C, marks the displacive transition from monoclinic orthoclase to triclinic microcline. Ordering of K-feldspar is more complex and initially much slower than that of albite. The large $K^+$ ions, in the 8-coordinated M-sites of K-feldspar, have a stabilizing effect on the larger-volume monoclinic structure (Smith and Brown, 1988). Also, at elevated temperature, the development of coherent

cryptoperthite in orthoclase inhibits further ordering. However, at low temperatures and in the presence of an aqueous fluid, orthoclase becomes very reactive because of the large elastic-strain energy associated with cryptoperthite (Waldron *et al.*, 1993). From an optical standpoint, orthoclase is readily identifiable by the presence of strain-controlled tweed microtexture. Microcline can be characterized optically by the irregular tartan microtexture of intersecting albite and pericline twins. The transformation from monoclinic orthoclase to triclinic microcline, as discussed above, typically results in recrystallization to a coarse mosaic of subgrains, and an increase in turbidity and microporosity (Teertstra, 1997). A detailed analysis of the orthoclase to microcline transformation, the generation of turbidity, microporosity and permeability, and the role of $H_2O$ is discussed by Waldron *et al.* (1993) and Walker *et al.* (1995).

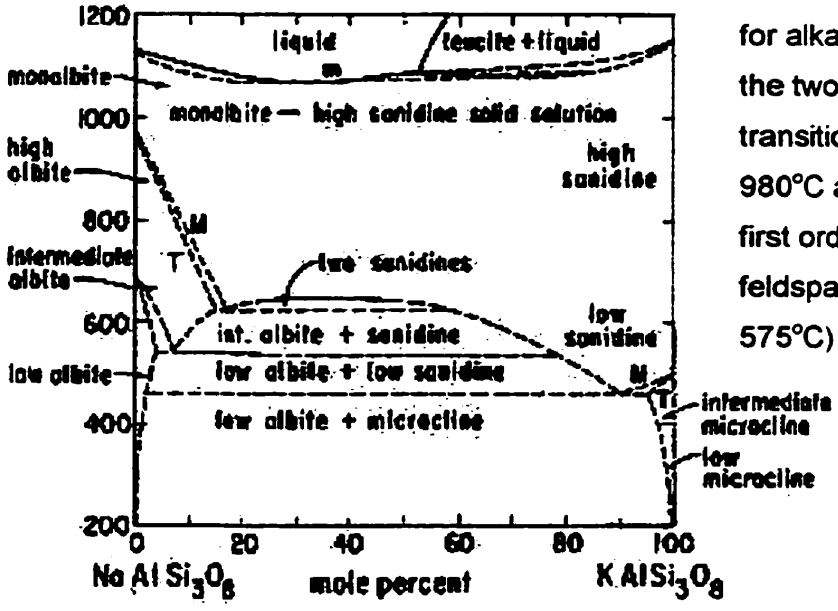


**Figure 2.7** Schematic subsolvus phase diagram for alkali feldspars showing the two first order structural transitions for albite ($Ab_{100}$: 980°C and 680°C), and two first order transitions for K-feldspar ($Or_{100}$: 800°C and 575°C) (Martin, 1974).

## 2.4 Physical properties: cleavage, parting, intergrowths, colour

Physical properties such as cleavage and parting are an expression of heterogeneous bond strengths between structural units of the tetrahedral framework. Most feldspars

have at least two well-developed cleavage planes: 1-perfect along (001), the other less than perfect, along (010). A third imperfect cleavage may be observed along (1 $\bar{1}$0). An examination of crystal structure and topology reveals that the (001) and (010) cleavages break along planes with the smallest number of tetrahedral bonds per unit area (Barth, 1969). Parting is sometimes observed parallel to (100) and less commonly, in K-feldspars, parallel to ( $\bar{8}$01). The ( $\bar{8}$01) parting is explained by being nearly perpendicular to the axis of maximum thermal expansion (Barth, 1969).

Two categories of intergrowths are present in feldspar types: homogeneous and heterogeneous. Homogeneous intergrowths are comprised of a single phase with differential growth orientations; twinning is the most common, and is found in all types of feldspar. Twins are the expressions crystallographic imperfections formed at the time of crystal growth or after crystal growth in response to deviatory stress. More than 20 different feldspar twin laws are known, but only 5 are important: Albite, Pericline, Carlsbad, Baveno, and Manebach. Twins can be very informative in the understanding of phase transformations and exsolution (Smith and Brown,1988; Ribbe 1983; Barth (1969).

Heterogeneous intergrowths of feldspars include antiperthite (K-feldspar lamellae in plagioclase host), and perthite (albite lamellae in a K-feldspar host). These intergrowths are developed during subsolidus readjustment of originally homogeneous feldspars, which became unstable at low temperature. The driving force for exsolution is the reduction in the chemical or bulk free energy due to segregation. If the collective free energies of the separate phases and the interface, are lower than the free energy of the original single phase, then exsolution can proceed spontaneously. The temperature at

which exsolution can proceed in the Ab-Or system is defined by the order-independent, but strain-dependant solvus (Figure 2.8).

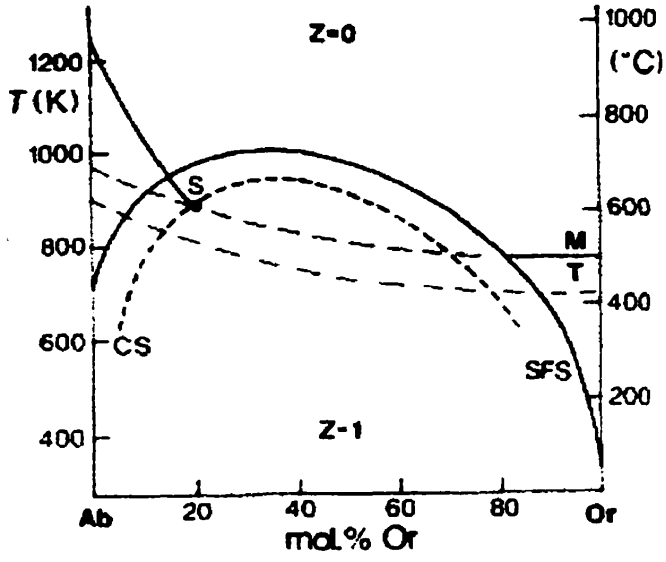


**Figure 2.8** Relations between strain-free solvus (SFS), coherent solvus (CS) and the monoclinic (M) – triclinic (T) phase transformation, for supposed equilibrium cooling. The dashed band shows the zone of rapid ordering (Smith and Brown 1988).

The overall texture of perthites and antiperthites as well as the morphology and relative volume of the individual phases are largely dependent on the bulk composition of the original feldspar, and the extent of hydrous-fluid interactions. Brown and Parsons (1994) produced a schematic diagram based on microtextures in a series of ternary feldspars from the Klokken intrusion (Figure 2.9). The texture, composition and distribution of natural feldspars in igneous deposits are a combined product of 3 processes (Brown and Parsons, 1994): i) magmatic crystallization, ii) subsolidus transformation and iii) deuteric alteration. The first stage involves the processes of nucleation and crystal growth of highly disordered feldspars. Bulk composition, rate of cooling and $P_{H_2O}$ are the main considerations. At the subsolidus transformation stage, phase-transformation leads to the development of exsolution microtextures, such as coherent crytoperthite in alkali feldspars. The scale and extent to which these textures form is inversely proportional to the rate of cooling, and leads to substantial elastic strain within the crystal lattice. Stored

elastic energy within the microtextures facilitates formation of secondary porosity, which promotes rapid and efficient dissolution-reprecipitation reactions during the deuteric alteration stage. Deuteric alteration involves dissolution-reprecipitation reactions under the influence of a locally derived hydrous phase. Results vary depending on the relative volumes of fluid *vs.* mineral, and the rate of infusion of $H_2O$, which in turn is controlled by the availability of primary and secondary porosity and permeability within the feldspar. Fluid interactions with metastable feldspars, under conditions of decreasing temperature, generally leads to increasing structural order, in conjunction with the development of turbidity in K-feldspars, and coarsening of albite lamellae from film perthite (at low to moderate levels of fluid interaction), to coarse vein perthite at moderate to high levels. Patch perthite develops at even higher degrees of fluid interaction, and may be indicative of dissolution and replacement by more distal hydrothermal alkali-rich fluids.

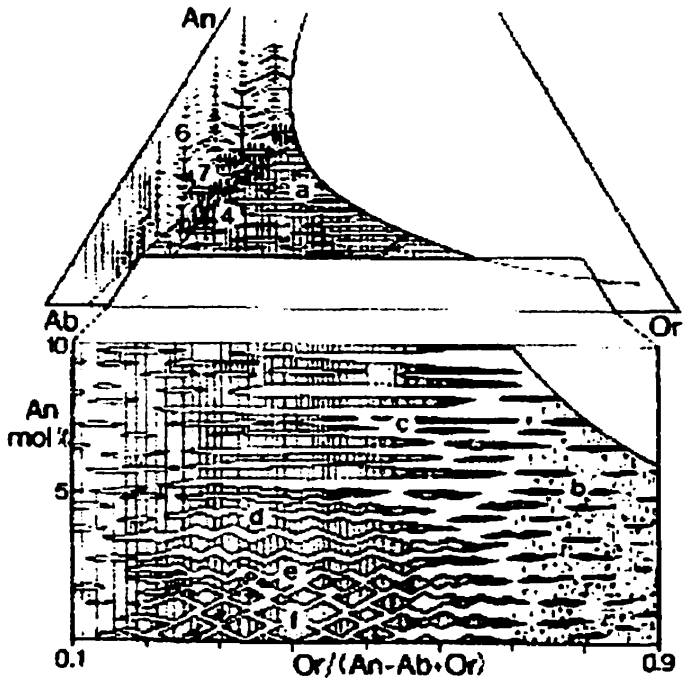


**Figure 2.9** Schematic diagram of microtextures in a series of spatially related feldspar compositions from the Klokken intrusion (Brown and Parsons 1994). Vertical hatching: albite twins in plagioclase. Cross hatching: tweed orthoclase. Unornamented: other Or-rich feldspar: low sanidine in straight lamellar intergrowths, high microcline in wavy intergrowths, and low microcline in zig-zag lozenge intergrowths.

The variety of feldspar colours could be informative with respect to differences in compositional or structural characteristics; however, a large number of intrinsic and extrinsic factors may be involved, making straightforward interpretations of colour with respect to these characteristics difficult. Cerný and Macek (1972) studied 9 hand-picked K-feldspars from the upper intermediate zone (50) of the Tanco pegmatite. Pink-white-grey feldspars roughly correlated to an increase in $Na_2O$ (average wt% 1.2-1.4), decreases in $K_2O$ (13.0-12.5%) and $Rb_2O$ (2.5-2.3%), and a range in $Cs_2O$ from ~0.20-0.25 wt% which culminated in the white phase. X-ray powder-diffraction data for the same feldspar series yielded a systematic decrease in triclinicity ($\Delta$) from a maximum of ~1 (pink) to a minimum of ~0.85 (grey). Pink feldspar tends to have greater microporosity, and the pink to red colouration is attributed to the presence of dusty inclusions, some of which resemble hematite and/or iron hydroxides (Cerný and Macek, 1972).

### 2.5 Chemical composition

The recorded number of trace-element substitutions in natural feldspars is extensive. Well-established *T*-site substitutions include: B, Ga, Fe, Mg, Ge, Ti, Be, P, Sn. Several other transition elements are thought to fit into *T*-sites, but with less certainty: Sc, V, Cr, Mn, Co, Ni, and Cu. Well-established *M*-site substitutions include: Li, Rb, Cs, Tl, NH4, Sr, Ba, Pb. Additionally, the following elements have been detected but structural positions are uncertain: H, F, Cl, Br, Zr, Hf, Th, U, Nb, Ta, W, PGEs, REEs, Au, Cd, Hg, In, Sb, and Bi (Smith and Brown, 1988).

A few elements traditionally considered trace-elements may be encountered at minor or even major concentrations. A good example is Ba in celsian ($BaAl_2Si_2O_8$); found only in Mn-rich deposits, it has a structure similar to K-feldspar, and forms the Ba end-member

of an isomorphous series from orthoclase to celsian (Deer *et al.*, 1992). Teertstra (1998) reported the occurrence of Rb-dominant feldspar (up to 91 mol % $RbAlSi_3O_8$) from the interior zones of highly evolved granitic pegmatites. He has proposed two new species to be added to the feldspar group, namely rubicline and rubidine as Rb-end-member equivalents to microcline and sanidine, respectively; rubicline has IMA approval as a mineral (Teertstra *et al.*, 1999), but the proposal for rubidine is still under consideration. In addition to the natural feldspar variants mentioned above, a wide variety of end-member feldspar species have been produced synthetically (Table 2.1). There is presently no definitive theory available to predict which compositions will generate a feldspar structure; however, it appears that only M-cations with radii between 0.09 and 0.14 nm form end-member compositions (Bruno and Pentinghause, 1974). Elements such as Li, Tl, and Cs are outside this range, however significant K-site substitutions of Tl (up to 60%; Smith and Brown, 1988), and Li (>91 mol%; Deubener *et al.*, 1991) have been attained in synthetic alkali feldspars.

## 2.6 Element partitioning

A number of factors may influence the partitioning of trace-elements between melt and crystal. Factors to be considered include P-T conditions during crystallization, crystal growth rate, and fugacities of volatile components such as F, B, P, Cl, and $H_2O$ (Long, 1978). Additionally, the bulk composition of the liquid and crystalline phases is of paramount importance, along with the concentration of the trace-element in question. Various authors, who have derived partition coefficients [$D(M)^{Fsp/gl}$] for Ba, Sr, Rb, and Cs between alkali feldspar and siliceous melts of varying compositions, have found limited consensus with regards to the true values of these coefficients (Icenhower and London, 1996; Mahood and Hildreth, 1983; Long, 1978). It is not surprising that some researchers have suggested distribution coefficients are not universal among differing

rock types (Mahood and Hildreth, 1983). However, most authors tend to agree that composition, particularly the Or content of the crystallizing feldspar, and the concentration of the trace-element in question, are the most significant factors to be considered. Heier (1959a, 1959b) noted that K-feldspar tends to control the distribution of Rb, Ba, and Cs, whereas Sr has an affinity for albite. Icenhower and London (1996), found that $D(Ba)^{Fsp/gl}$ and $D(Rb)^{Fsp/gl}$ were strongly dependent on the Or content of feldspar, but that $D(Sr)^{Fsp/gl}$ was independent of albite or orthoclase content. Interestingly, the above study also indicated that [$D(M)^{Fsp/gl}$, for M= Ba, Sr, Rb, Cs] did not depend on either temperature or bulk composition of the peraluminous melt. This last statement is in contrast to the behavior of P in peraluminous granitic melts, as described by London *et al.* (1999). Phosphorus substitutes into the feldspar structure via the berlinite substitution ($AlPSi_{-2}$). This substitution is strongly affected by the Al-content of the melt, such that P becomes a compatible element in K-feldspar above an ASI (aluminum saturation index) value of ~1.3.

**Table 2.1**: Selected synthetic feldspars: formulae, notes and references (from Teertstra,1997).

---

$RbAlSi_3O_8$: monoclinic, from hydrothermal synthesis (Voncken *et al.* 1993b, Borutskaya 1975, Bruno & Pentinghaus 1974, Ghelis & Gasperin 1970, Barrer & McCallum 1953). Structure refined by Gasperin (1971).

$RbAlSi_3O_8$: triclinic, prepared by cation exchange (McMillan *et al.* 1980, Pentinghaus & Henderson 1979, Weitze & Viswanathan 1971). Thermal expansion was studied (Henderson 1978).

$KFeSi_3O_8$: may be monoclinic and triclinic (Wones & Appleman 1963, Faust 1936, Hautefeuille & Perry 1888). Solid solution with $KAlSi_3O_8$ prepared by Lindqvist (1966).

$KBSi_3O_8$: forms a series with $KAlSi_3O_8$ (Martin 1971).

$HAlSi_3O_8$: prepared by cation exchange of Na-exchanged sanidine in $H_2SO_4$ (Müller 1988). Structure refined by Paulus & Müller (1988).

$LiAlSi_3O_8$: prepared by cation exchange (Müller 1988), Deubener *et al.* 1991).

$NH_4AlSi_3O_8$: prepared under anhydrous conditions(Voncken *et al.* 1993a), earlier work by Barker (1964) and Hallum & Eugster (1976).

$NaBSi_3O_8$: hydrothermal synthesis using $H_3BO_3$ (structure refined, Fleet 1992), earlier work was by Kimata (1977), Bruno & Pentinghaus (1974), Eugster & McIver (1959). Morphology was studied by Mason (1980a, 1980b).

$LaAl_3SiO_8$: containing trivalent non-tetrahedral cations (Kneip & Liebau 1994)

---

## 2.7 Substitution mechanisms

A number of different crystal-chemical substitution mechanisms in feldspars from various granitic pegmatites and granites were considered by Teertstra (1997). This included the berlinite substitution (P + Al = 2Si), also documented by London *et al.* (1990) and London (1992a), plagioclase substitution [Ca (Sr, Ba) + Al = Na (K) + Si], vacancy

substitution [(Na, K) Al = □ Si)], and light-element substitutions (*e.g. T*- sites: Be, B; *M*-sites: H, Li, $NH_4$).

Ideal feldspar stoichiometry stipulates that the sum of tetrahedral cations ($\Sigma T$) should be equal to 4 (Figures 6.12a,b). It is evident from Figure 6.12a that Si and Al alone do not account for full tetrahedral occupancy. With the berlinite substitution accounted for in Figure 6.12b, the tetrahedral stoichiometry closely approaches the ideal (*i.e.* Si+Al+P =4).

Ideal stoichiometry for alkali feldspars is represented by the apices of the dashed lines in Figure 6.13a [*Si+2P* =3.00, and sum of *monovalent M-cations* ($\Sigma M$) =1.000] and Figure 6.13b [*Al-P* ($TO^{2-}$) = 1.000, *M-cation charge* (*M+*) = 1.000]. Deviations beyond the experimental error of approximately +/- 0.01 apfu, can be considered real systematic shifts. If one can rule out systematic analytical bias, then the shifts can be interpreted as the result of one, or the combination of several substitution mechanisms, indicated by the vectors labeled 1,2, 3 in Figures 6.13a,b. The plagioclase-type, vector [1], is indicated by an increase in divalent cations (at the expense of monovalent M-cations), with a concurrent increase in Al (at the expense of Si). The vacancy substitution, vector [2], is indicated by increasing Si with decreasing Al, M-cation charge, and monovalent M-cations. Light element substitution, vector [3], is indicated by decreasing M-cation charge and monovalent M-cations, at constant Si and Al.

# CHAPTER 3: INTRODUCTION TO THE TANCO PEGMATITE

The Tanco pegmatite is a member of the *rare-element class* of granitic pegmatites as defined by Černý (1991). In more detail, the internal structure and mineralogy indicates that Tanco belongs to the *petalite subtype*, of the *complex type*, of *rare-element class* granitic pegmatites (Černý *et al.*, 1998). The pegmatite is also designated a member of the **LCT** *family* of granitic pegmatites, alluding to the petrochemical character of enrichment in Li, Cs and Ta (Černý, 1991). Tanco is host to dozens of rare mineral species, including the Cs-bearing aluminosilicate pollucite. To the best of our knowledge, pollucite is only found in granitic pegmatites and is, in part, an indication that Tanco is a product of very advanced fractional crystallization (Teertstra, 1997)

## 3.1 Location and Economic significance

The Tanco pegmatite is located under Bernic Lake, 180 km ENE of Winnipeg, Manitoba within the Bird River Greenstone Belt of the Superior Province (Figure 3.1). Year round access can be gained by paved and all-weather gravel roads eastward from Lac du Bonnet, Manitoba. The orebody is accessed from the surface via a 5m x 4m 20%-grade inclined ramp, and much of the ore is removed by hoist. Since commercial-scale mining was initiated in the mid-1950's, significant quantities of ore-grade material containing Li, Cs, Ta, and Rb mineralization have been recovered. Up to 1961, production from the Tanco pegmatite had been sporadic and of very limited tonnage; there was essentially no upgrading of the material mined. Preparations for tantalum production (drilling, underground development, and mill construction, etc.) began in 1967 with commercial production commencing in 1969. Table 3.1 highlights reserves and economic mineralization.

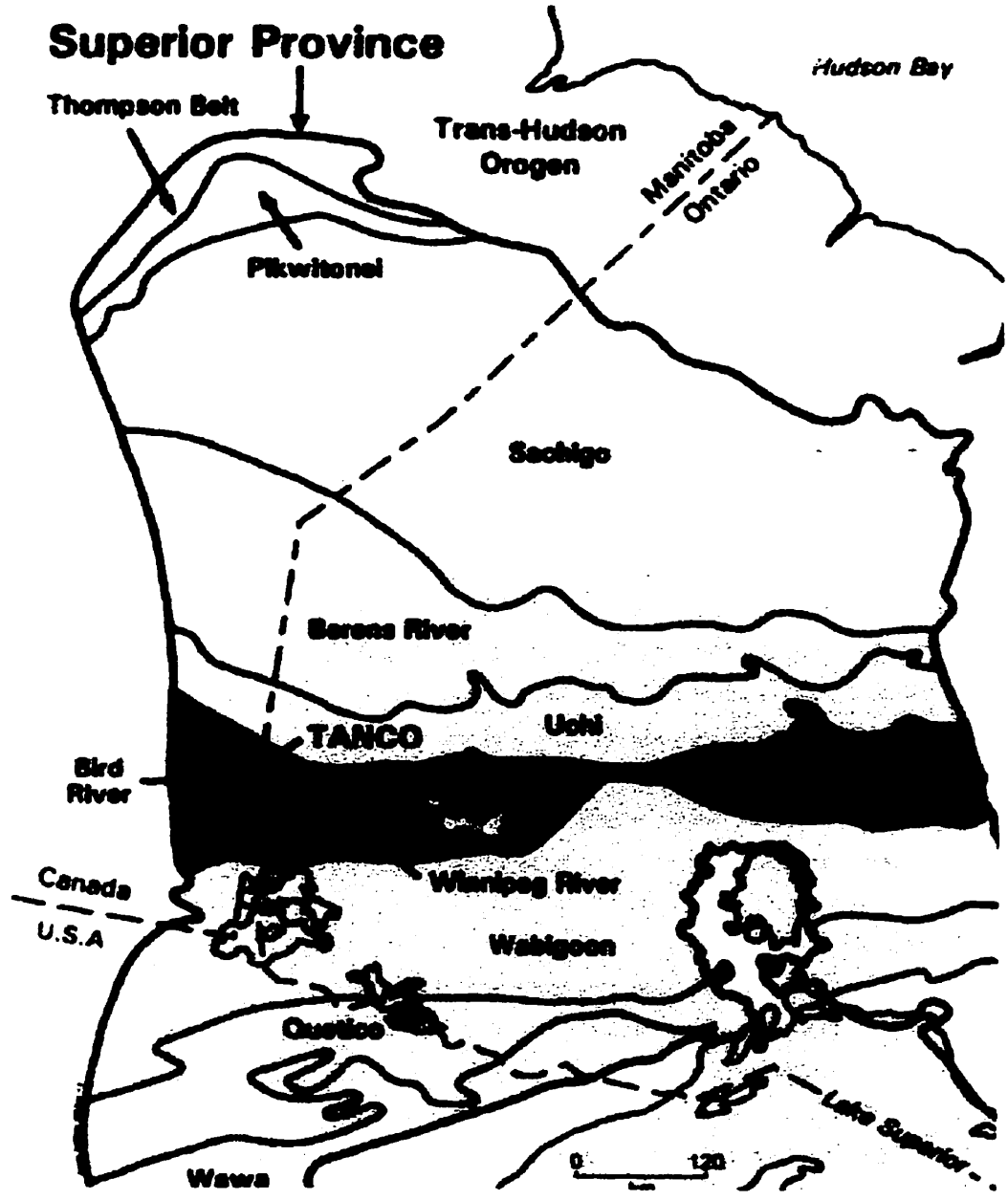


**Figure 3.1** Tanco location within the Bird River Greenstone Belt of the Superior province, SE Manitoba (modified from Stilling, 1998).

**Table 3.1** Preproduction ore and mineral reserves.
(Černý *et al.*, 1998)

| Commodity | Primary mineral sources | Tons | Average Grade |
|---|---|---|---|
| Lithium | spodumene, petalite, lepidolite | > 7.3 million | 2.76 % $Li_2O$ |
| Cesium | pollucite | 350 000 | 23.3 % $Cs_2O$ |
| Tantalum | tantalite, wodginite, microlite | > 2.0 million | 0.216 % $Ta_2O_5$ |
| Rubidium | lepidolite | 107 700 | 3% $Rb_2O$ |
| Beryllium | Beryl | 920 000 | 0.20 % BeO |
| Quartz | Quartz | 780 800 | - |

Among pegmatites of the same petrological and geochemical type, only three other known localities are comparable in terms of size: i) the Bikita deposit in southern Rhodesia (Cooper 1964), ii) the Greenbushes pegmatite in southwest Australia (Partington, 1995), and iii) the Big Whopper pegmatite, located 50 km east of Tanco, in NW Ontario (Breaks and Tindle, 1997). Another comparable pegmatite of the same type but smaller in size occurs at Varuträsk in Sweden (Quensel, 1956). More information on the history and economic aspects of Tanco can be found in Crouse *et al.* (1984) and Černý *et al.* (1998).

### 3.2 Regional Geology

The Bird River Greenstone belt is part of the Bird River Subprovince (Figure 3.1), bordering the batholithic belt of the Winnipeg River Subprovince to the south, and the Manigotogan gneiss belt of the English River Subprovince to the north (Figure 3.2; Trueman, 1980). Tanco is just one of several pegmatite bodies within the Bernic Lake pegmatite group: an east-west trending suite of pegmatites comprising some of the most highly fractionated pegmatites in the region (Černý *et al.*, 1998). This group is thought to represent the westernmost extension of a series of pegmatites belonging to the larger Cat-Lake-Winnipeg River pegmatite field (Figure 3.2; Černý *et al.*, 1981), possibly also

connected to the rare-element pegmatites at Separation Lake in northwestern Ontario (Breaks and Tindle, 1997).

Emplacement of many pegmatite suites in the region appears to be controlled by both regional-scale, E-W trending, antiformal-synformal packages of Archean crust (Figures 3.2, 3.3), and more localized crosscutting joint-sets, fractures and faults related to major and minor diapiric intrusions. Most rock assemblages of the Bird River Subprovince, visible in Figure 3.2, range in age from 2780-2640 Ma, but several remnant lithologies are as old as ~3 Ga (Černý *et al.*, 1998).

*Bird River Greenstone Belt*

Lithologic assemblages of the Bird River Greenstone Belt, include metavolcanic, related and derived metasedimentary rocks with synvolcanic to late-tectonic intrusive rocks (Černý *et al.*, 1981). Six lithologic/metamorphic assemblages are identified (Figure 3.2); from oldest to youngest they include: **1)** the Eaglenest Lake Formation, **2)** the Lamprey Falls Formation, **3)** the Peterson Creek Formation, **4)** the Bernic Lake Formation, **5)** the Flanders Lake Formation, and **6)** the Booster Lake Formation. (Trueman, 1980; Crouse *et al.*, 1984; Černý *et al.*, 1981, 1998; Stilling, 1998). Figure 3.3 focuses on the general geology proximal to the Tanco pegmatite, and draws attention to the major E-W trending structures, which help delimit assemblages 1-6.

*Lithology*

Assemblages 2 and 3 contain mostly metavolcanic rocks of basaltic and rhyolitic compositions, respectively. Subordinate metasedimentary rocks include intercalated tuffs, hyaloclastites and banded iron formations in (2), and local volcaniclastic and epiclastic derivatives in (3). Assemblages 1 and 4 are dominated by the presence of fine to coarse volcaniclastic metasedimentary rocks, and lesser banded iron

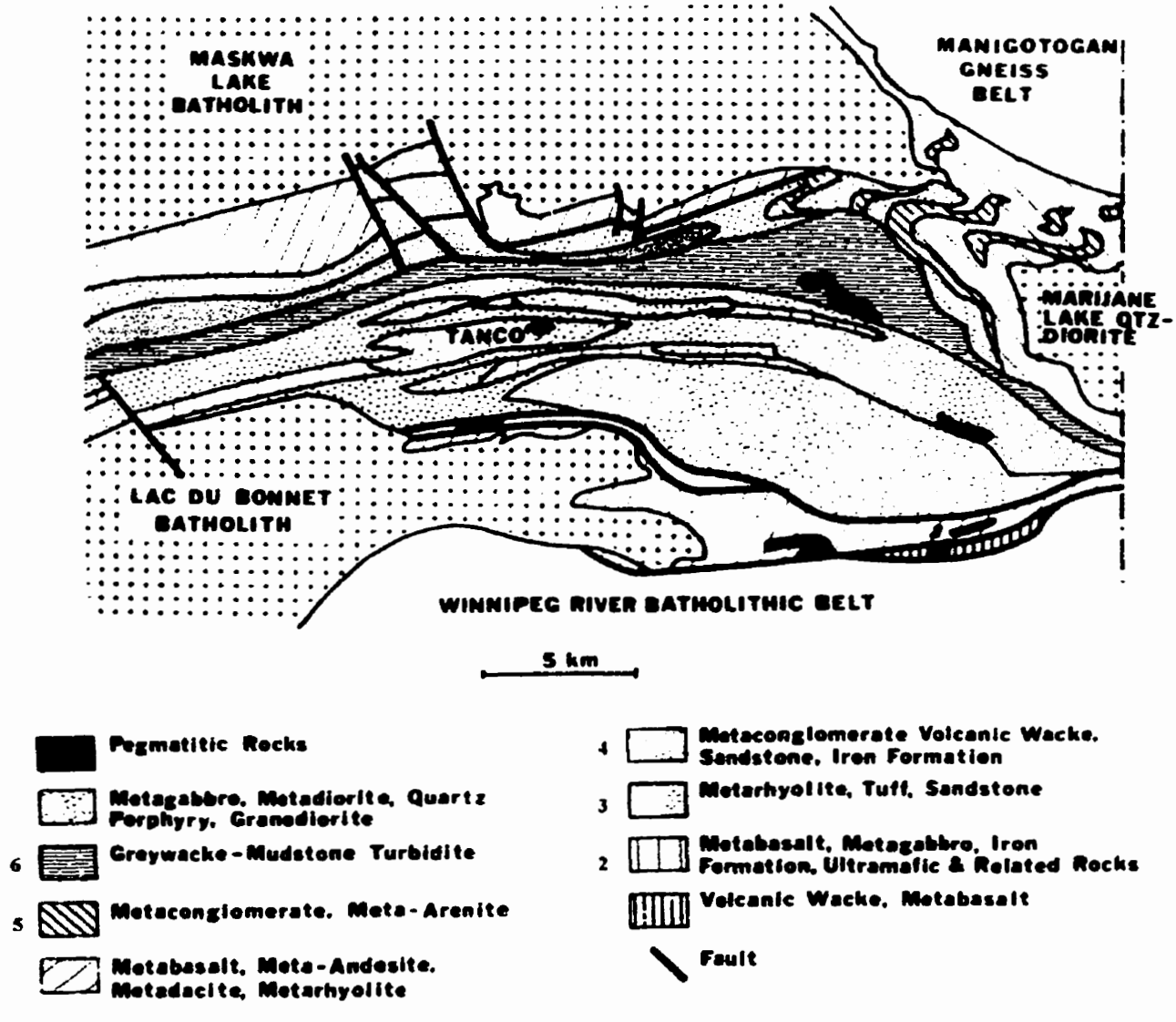


**Figure 3.2** Geology of the Bird River Greenstone Belt. Numbers correspond to lithotectonic units described in the text: 2 Lamprey Falls, 3 Peterson Creek, 4 Bernic Lake, 5 Flanders Lake, and 6 Booster Lake. Unit #1does not outcrop within the map area. Modified from Crouse et al. (1979).

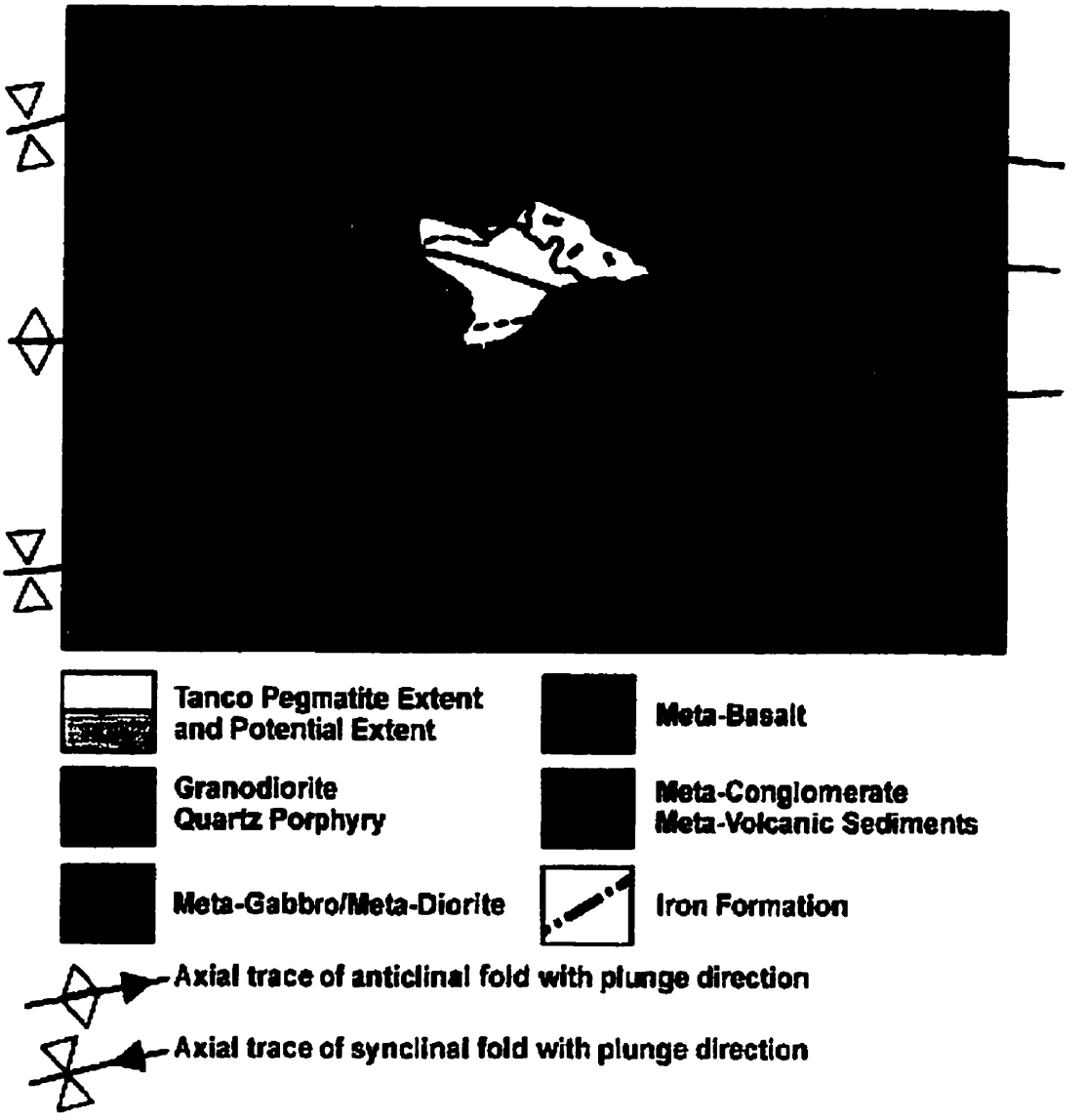


**Figure 3.3** Structural and geological setting of the Tanco Pegmatite at Bernic Lake, Manitoba (modified from Crouse et al., 1979).

formations. Minor lithologies include biotite schist and amphibolite in (1), and a spectrum of metavolcanics in (4), ranging in composition from basalt to rhyolite. Assemblages 5 and 6 consist mainly of metasediments including pebbly meta-arenite interbedded with metaconglomerate in (5), and finer-grained meta-greywacke-mudstone turbidites and interbedded iron formations in (6).

*Metamorphism and structure*

Essentially all assemblages of the Bird River Greenstone Belt attain at least greenschist-facies metamorphism, with most units exhibiting at least one generation of penetrative tectonic foliation. Unit 2 also contains mineral assemblages of the hornfels facies, and is intruded by several metagabbro-ultramafic sills and stocks, quartz (feldspar) porphyry dykes, and in the south and eastern parts of Figure 3.3 by pegmatitic granite and pegmatite stocks and dykes. The structural geology of unit 2 is quite simple; the rocks of this unit form the basal sequence of a major east-west trending synclinorium that is unmodified by minor folding (Černý *et al.*, 1998). Only the latest pegmatite bodies intruding this unit escape the regional metamorphism to greenschist facies. Most of unit 5 and parts of units 3 and 4 also approach amphibolite-facies grade. These units exhibit a complex structural history involving two major periods of folding which yielded Ramsay's Type III interference fold patterns (Černý, 1998). The degree of folding culminates in unit 4 as tight, near horizontally-plunging folds. Local intrusions of gabbro, diorite and quartz-feldspar granodiorite stocks and sills are also reported in unit 4. The Tanco pegmatite is largely in contact with metagabbro/diorite and granodiorite (Figure 3.3), hosted in the Bernic Lake Formation. Unit 6 unconformably overlies units 1-5 and has also been intruded by pegmatitic sills and stocks. The structural geology of unit 6 is simple and consists of a monoclinic sequence marked by open flexures of bedding and

schistosity. Metamorphic assemblages reach lower amphibolite facies and were subsequently retrogressed (Černý, 1998). As is the case for units 2 and 4, pegmatites of unit 6 are relatively undeformed.

*Intrusions and Regional evolution*

Granitoid rocks in the region (Figure 3.2) include the Maskwa Lake, Marijane Lake, and Lac du Bonnet Batholiths, respectively located north, east and southwest of the Bird River Greenstone Belt. These diapiric intrusions consist of tonalite and granodiorite cores, which appear to have been emplaced synchronously to the formation of tectonic foliations in assemblages of the Bird River Greenstone Belt (Černý *et al.*, 1998). Each of these intrusions is mantled and dissected by late tectonic biotite granites. In the case of the Lac du Bonnet batholith, the late biotite granites predominate over other rock types, and appear to have been emplaced synchronously to the initiation of east-west faulting within the greenstone belt. This faulting probably controlled subsequent intrusions of pegmatitic granites and pegmatites of the Winnipeg River pegmatite district (Černý *et al.*, 1981, 1998).

The Winnipeg River pegmatite district includes the Bernic Lake pegmatite group. The Tanco pegmatite is the largest and most fractionated pegmatite of this group and exhibits the subhorizonatal joint-controlled morphology typical of other pegmatites in the group. For many other pegmatite groups of the Winnipeg River pegmatite district, direct links can be made to late- to post- tectonic leucogranites (*e.g.* Greer Lake, Eaglenest Lake, Axial, Rush Lake and Tin Lake groups). The Shatford Lake group, which is dominated by pegmatites of the NYF family, is associated with the easternmost termination of the Lac du Bonnet batholith (Černý *et al.*, 1981). However, attempts at finding a parental granitic source for the Bernic Lake group (and Tanco) have so far

failed. Geophysical and regional geochemical evidence suggest a blind parental granitoid source may exist towards the NE (Černý, personal comm., 1999).

### 3.3 Tanco morphology and internal zonation

The following section includes a brief summary of morphology and zonation based on Crouse *et al.* (1984), Černý *et al.* (1998), and Stilling (1998). Bulk composition and specific mineral abundances by zone are from Stilling (1998). The shape, size and orientation of the pegmatite and interior zones have been completely bracketed by diamond drilling. The main body is best described as a doubly-plunging, saddle-shaped bi-lobate ellipsoid, approximately 1990 by 1060 m (Figure 3.4) by 100 m thick (Figures 3.5, 3.6). Observations of the pegmatite, based largely on differences in texture and mineralogy, have led to the discrimination of 9 different zones (Table 3.2, Figures 3.5, 3.6). Table 3.2 compares general textural and compositional characteristics of the different zones.

As a historical footnote, zonal designations prior to 1998 were based on a single digit numbering system (*i.e.* 1,2,3,...); however, in order to adequately categorize the wide variety of apparent transitional assemblages in a computer-friendly manner, a two digit number system has been adopted. The full range of zonal designations now in use includes: (10) (12) (20) (30) (36) (40) (45) (46) (47) (50) (58) (60) (63) (67) (69) (70) (80) (90) (P. Vanstone, personal comm., 1999). Transitional assemblages are invariably very minor in volume relative to the major (X0) zones. General mineralogical and compositional characteristics of the major zones are described below:

**Table 3.2:** General compositional and textural characteristics of the nine major zones of the Tanco pegmatite.

| Zones | | Main Constituents | Characteristic Subordinate (Accessory) & ((Rare)) Minerals | Textural & Structural Characteristics | Geochemically Important Major & (Minor) Elements |
|---|---|---|---|---|---|
| | Exomorphic Zone | biotite, tourmaline, holmquistite | (arsenopyrite) | fine-grained reaction rims and diffuse veins | K, Li, B, (P, Rb, Cs, F) |
| (10) | Border Zone | albite, quartz | tourmaline, apatite, (biotite), ((beryl, triphylite)) | fine-grained layers | Na, (B, P, Be, Li) |
| (20) | Wall Zone | albite, quartz, muscovite, lithian muscovite, microcline-perthite | beryl, (tourmaline) | medium-grained with giant K-feldspar crystals | K, Na, (Li, Be, F) |
| (30) | Aplitic Albite Zone | albite, quartz, (muscovite) | muscovite, Ta-oxide minerals, beryl, (apatite, tourmaline, cassiterite), ((ilmenite, zircon, sulphides)) | fine-grained undulating layers, fracture fillings, rounded blebs, diffuse veins | Na, (Be, Ta, Sn, Zr, Hf, Tl) |
| (40) | Lower Intermediate Zone | microcline-perthite, albite, quartz, spodumene, amblygonite | lithian-muscovite, lithiophilite, ((lepidolite, petalite, Ta-oxide minerals)) | medium- to coarse-grained heterogeneous | K, Na, Li, P, F, ((Ta)) |
| (50) | Upper Intermediate Zone | spodumene, quartz, amblygonite | microcline-perthite, pollucite, lithiophilite, (albite, lithian-muscovite), ((petalite, eucryptite, Ta-oxide minerals)) | giant crystals of most major and subordinate minerals | Li, P, F, (K, Na, Cs, Ta) |
| (60) | Central Intermediate Zone | microcline-perthite, quartz, albite, muscovite | beryl, (Ta-oxide minerals), ((zircon, ilmenite, spodumene, sulphides, lithiophilite, apatite, cassiterite)) | medium- to coarse-grained | K, (Na, Be, Ta, Sn, Zr, Hf, Tl) |
| (70) | Quartz Zone | quartz | ((spodumene, amblygonite)) | massive, monomineralic | Si, (Li) |
| (80) | Pollucite Zone | pollucite | quartz, spodumene, ((petalite, muscovite, lepidolite, albite, microcline, apatite)) | essentially monomineralic | Cs, (Li) |
| (90) | Lepidolite Zone | lithian muscovite, lepidolite, microcline-perthite | albite, quartz, beryl, (Ta-oxide minerals), ((zircon)) | fine-grained | Li, K, Rb, F, (Na, Be, Ta, Sn, Zr, Hf, Ga) |

* Underlined minerals occur in economic quantities in the indicated zones.

(Source: after Černý *et al.*, 1998, p.9).

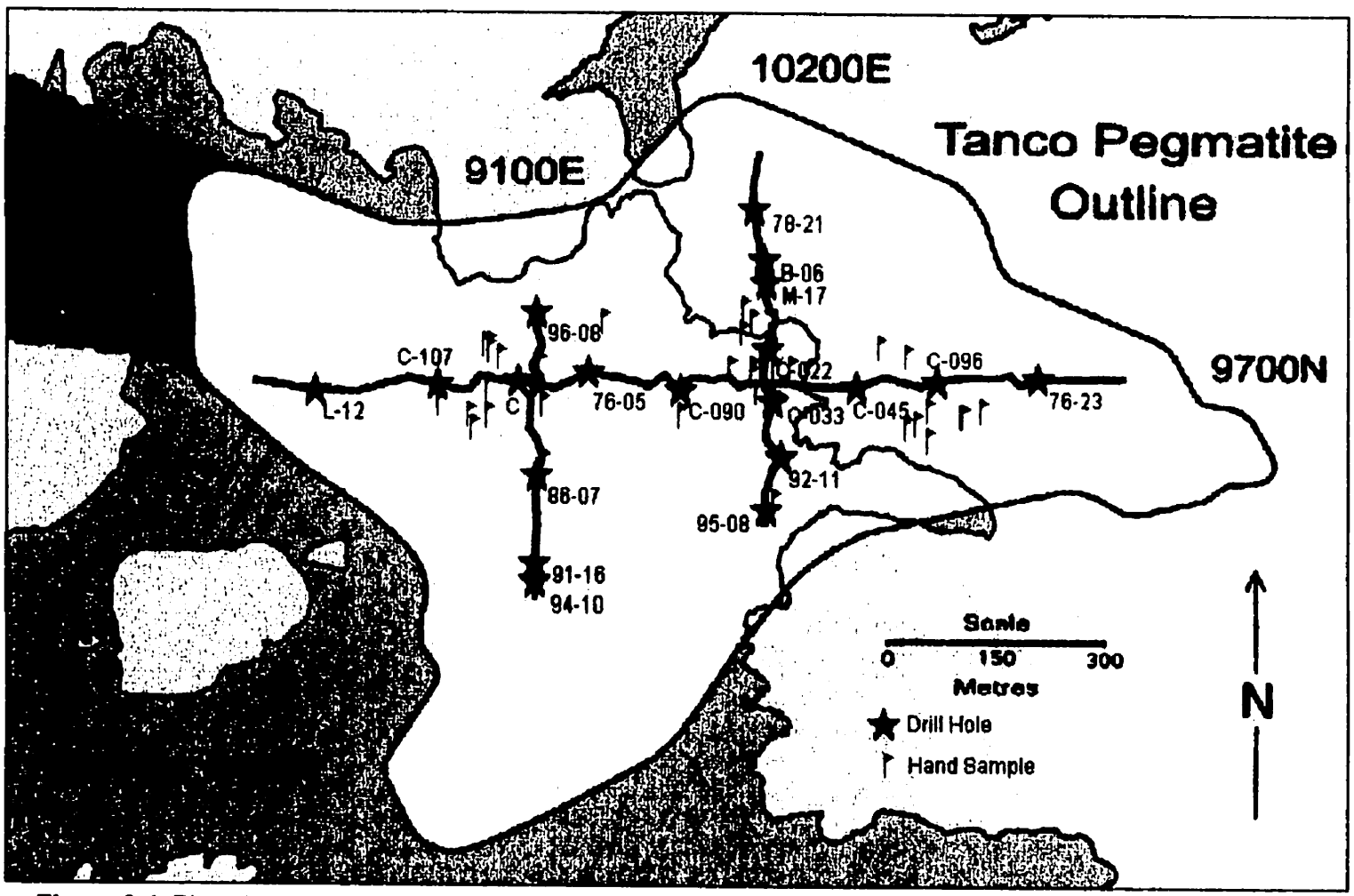


**Figure 3.4** Plan view of sample locations in relation to traces of the three vertical transects: 9700N, 10200E, and 9100E. The three fences are defined by the labelled drill holes. Red flags represent single underground hand samples mostly collected from zones (10) (30) (50) (80) and (90). (Map modified from Stilling, 1998)

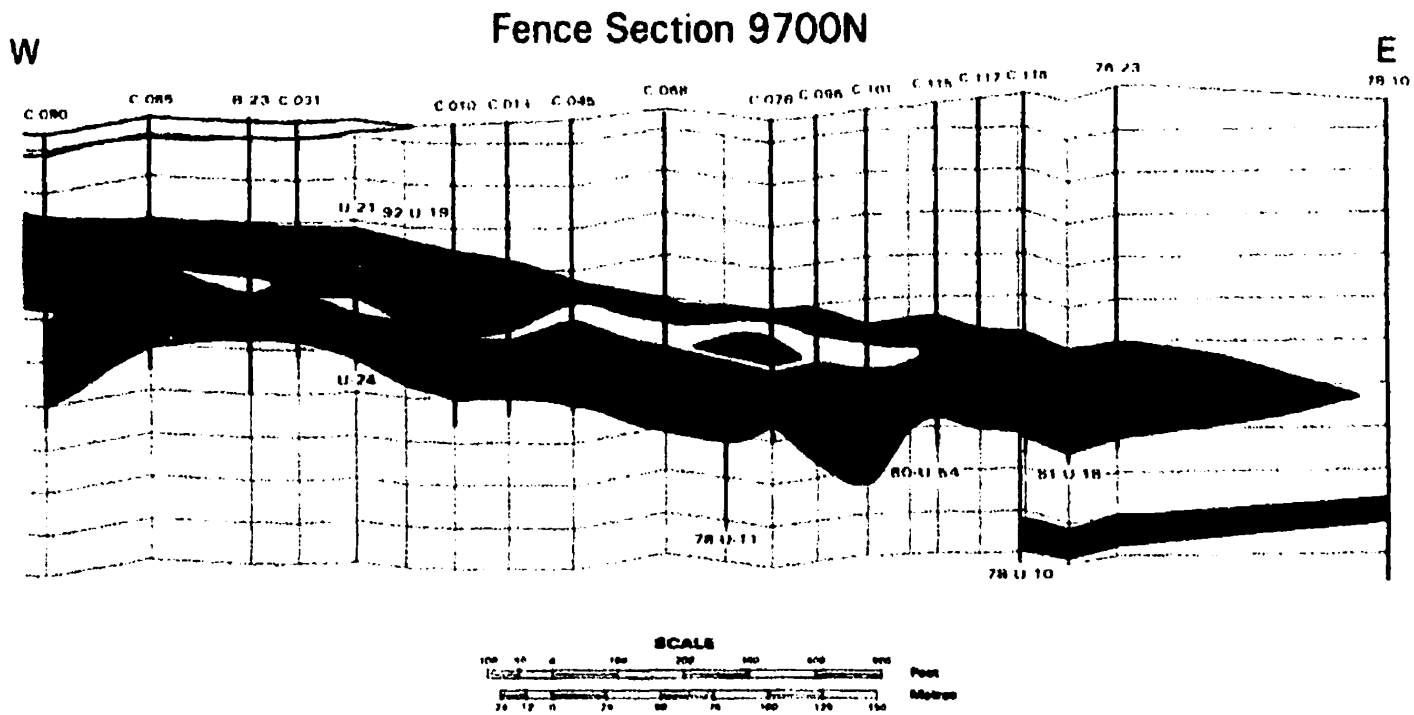


**Figure 3.5a** Eastern half of E-W fence through the Tanco pegmatite looking north. The 10200E transect extends into the page through the main pollucite body in red (at hole C-031). Modified from Stilling (1998)

- Zone 20 Wall Zone
- Zone 30 Aplitic Albite Zone
- Zone 40 Lower Intermediate Zone
- Zone 50 Upper Intermediate Zone
- Zone 60 Central Intermediate Zone
- Zone 70 Quartz Zone
- Zone 80 Pollucite Zone
- Zone 90 Lepidolite Zone
- Amphibolite Xenoliths/Country Rock

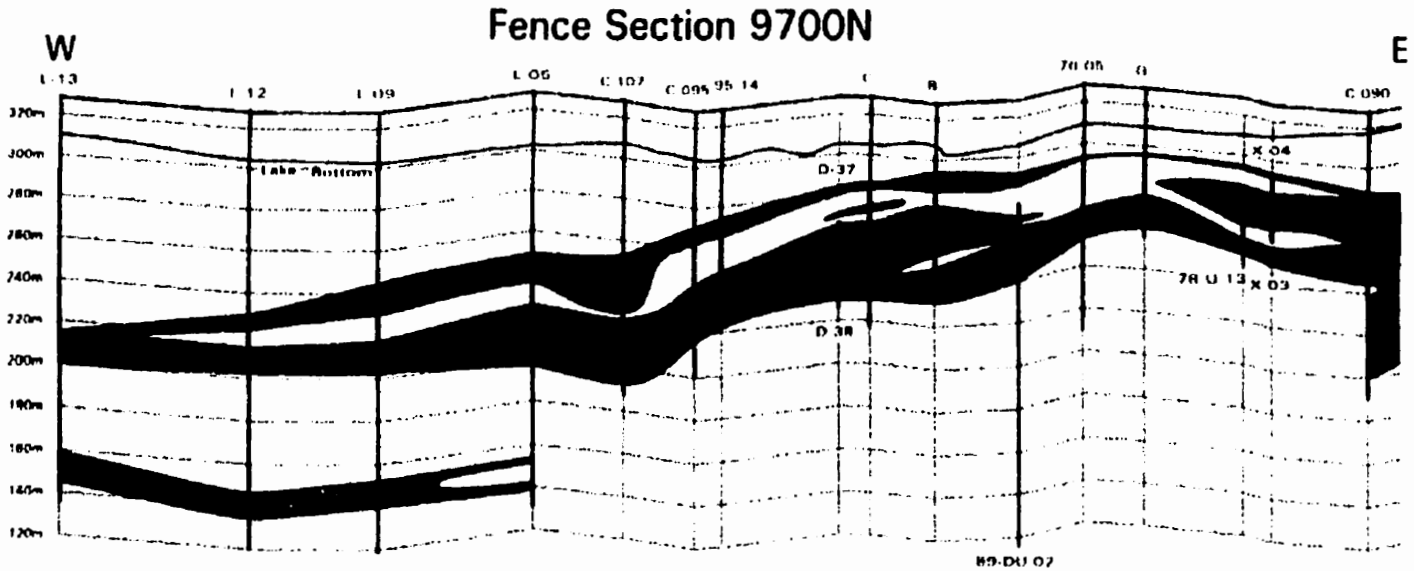


**Figure 3.5b** Western half of E-W fence through the Tanco pegmatite looking north. The 9100E transect extends into the page through the main lepidolite body in pink (at hole B). Modified from Stilling (1998)

| | | |
|---|---|---|
| ● | Zone 20 | Wall Zone |
| ■ | Zone 30 | Aplitic Albite Zone |
| ■ | Zone 40 | Lower Intermediate Zone |
| □ | Zone 50 | Upper Intermediate Zone |
| ■ | Zone 60 | Central Intermediate Zone |
| ■ | Zone 70 | Quartz Zone |
| ■ | Zone 80 | Pollucite Zone |
| ■ | Zone 90 | Lepidolite Zone |
| ● | Amphibolite | Xenoliths/Country Rock |

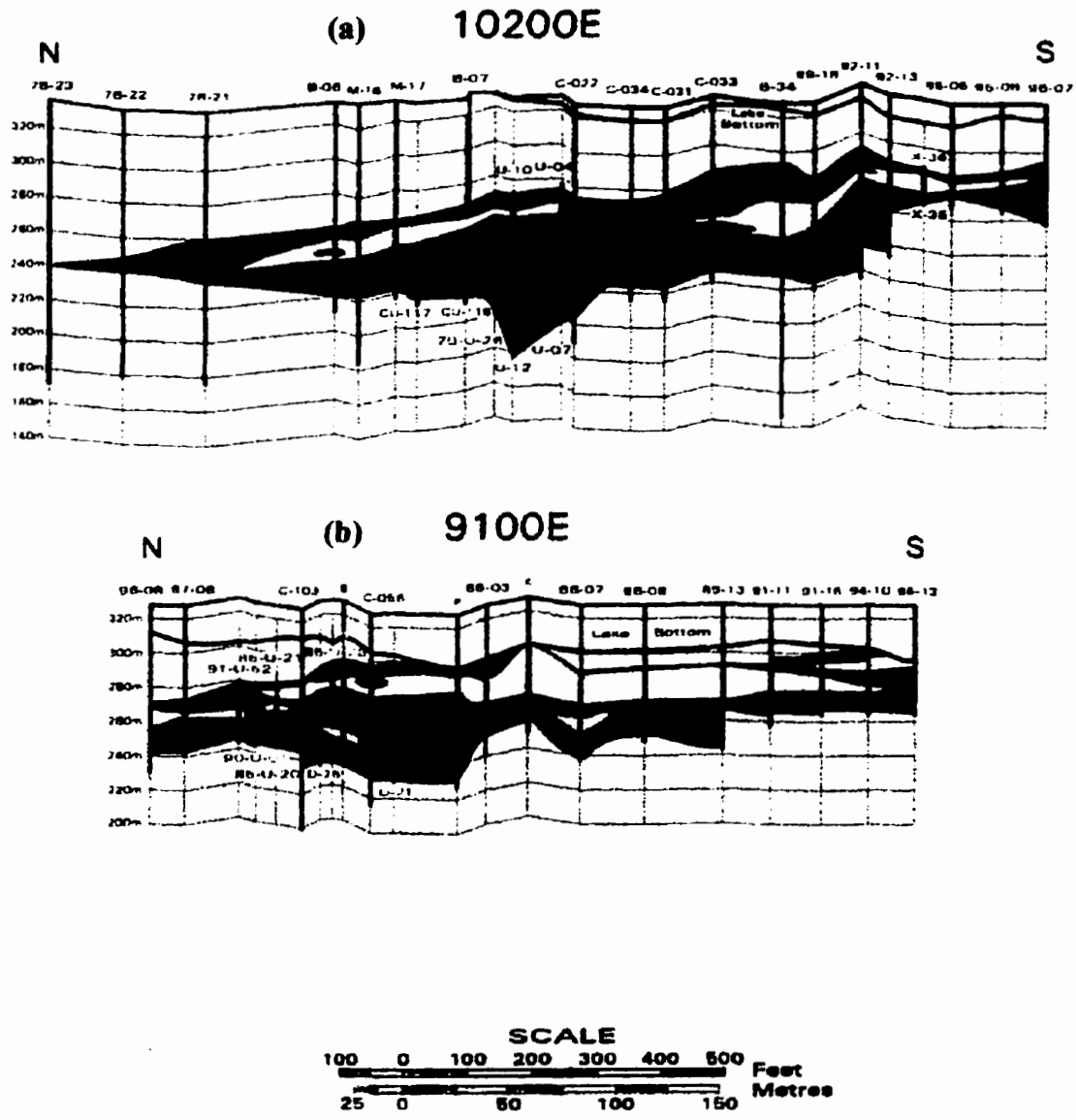


**Figure 3.6** Eastern (a) and Western (b) N-S fences through the Tanco pegmatite looking east. The 9700N transect extends into the page through the main pollucite pody in (a) (at hole C-031), and through the lepidolite body in (b) (at hole B). Modified from Stilling (1998).

**Zone (10)**, *the border zone*, is a thin <30 cm intermittent concentric shell formed between the main body of the pegmatite and host rocks. It is made up mostly of fine-grained albite and quartz, with biotite, muscovite, apatite, beryl, and tourmaline as common accessory minerals. Tourmaline and beryl crystals up to 20 cm in length sometimes form comb-like structures normal to the contact. Reaction rims of similar texture and composition are reported to form around amphibolite xenoliths in the pegmatite. This zone is too thin to be shown in Figures 3.5, 3.6.

**Zone (20)**, *the wall zone*, is the most voluminous zone (31% by volume) attaining a thickness of up to 38 m along the footwall contact. The main constituents include abundant medium-grained albite (40 %; up to 30 cm) and very coarse microcline-perthite (15%; up to 3 m) in a quartz-albite matrix, and tabular greenish muscovite (up to 10 cm). Common accessory minerals include lithian muscovite with apatite, beryl, and tourmaline (up to 20 cm in length). Albite is more dominant in the footwall portion, and commonly occurs as footwall aplitic albite; K-feldspar is more dominant in the hangingwall portion (P. Vanstone, personal comm., 2001). Localized mineral assemblages containing albite, columnar lithian muscovite, and tourmaline display metasomatic features.

**Zone (30)**, *the albitic aplite zone* forms sheet-like discontinuous layers up to 16 m thick, which are concentrated in the central to eastern parts of the pegmatite. Bluish, greenish to purplish, relatively homogeneous aplitic albite is widespread (in other zones, other mineral phases intimately associated with aplitc albite are considerably more abundant). Modal abundances of albite and quartz make up 67% and 25% of the zone, respectively. The remaining constituents include significant amounts of muscovite, and beryl along contacts with zones (60) and (40), and traces of

tourmaline, apatite, lithian muscovite +/- lepidolite. Zone (30) also contains economically significant quantities of Ta, and Sn oxide mineralization, along with minor amounts of Be, Zr, and Hf. Based on texture, morphology and timing of crystallization zone (30) is generally considered a core zone of the pegmatite. This zone constitutes approximately 2.6% of the pegmatite.

**Zone (40)**, *the lower intermediate zone*, occurs mainly in the lower half of the pegmatite and is second overall in terms of volume (29%). In contrast to zone (20), albite and K-feldspar occur at near equal modal abundances, 25% and 24% respectively. Notable mineralogical features of this zone are the appearance of significant quantities of amblygonite-montebrasite and spodumene, and the conspicuous absence of tourmaline. Overall, compositional and textural heterogeneity appears to be a diagnostic characteristic of the zone. Two mineral assemblages are noteworthy: 1) large crystals of microcline-perthite and spodumene plus quartz pseudomorphs after petalite (up to 2 m), embedded in a matrix of medium-grained quartz, albite and mica; and 2) 0.5-2 m quartz pods with amblygonite-montebrasite and spodumene plus quartz aggregates. Radial rims of cleavelandite and micas around the feldspar-rich assemblages usually separate them from the quartz-rich accumulations.

**Zone (50)**, *the upper intermediate zone* is somewhat restricted to the upper regions of the pegmatite and is frequently in contact with the hanging wall of zone (20). This zone attains thicknesses up to 24 m, and accounts for 13% of the bulk volume of Tanco. Zone (50) evolves in an upwards direction from zone (40) with a gradual decrease in albite and mica, and greatly increasing proportions of Li-(P) aluminosilicates. Petalite (recrystallized to secondary intergrowth of spodumene and

quartz) accounts for 46% of the modal abundance of the zone; K-feldspar and albite comprise 25% and 7% respectively. Giant crystal sizes are characteristic of this zone with amblygonite to 2 m, microcline-perthite to 10 m, and petalite to 13 m in length. Miarolitic cavities are rare, but leaching cavities with low-temperature mineral assemblages are locally abundant. This zone is the main source for ceramic-grade spodumene, and amblygonite.

**Zone (60)**, *the central intermediate zone*, also known as the *MQM* zone (microcline, quartz, and mica assemblage), occupies a large portion of the central, eastern and western flanks of the pegmatite, inside concentric shells of comprising zones (40) and (50). It is particularly enriched in K-feldspar (50%) followed by albite (20%) and fine-grained greenish muscovite (12%). Minor constituents include beryl, spodumene, wodginite, cassiterite, microlite, tantalite, apatite, lithiophilite, and tapiolite. This zone is one of the primary producers of tantalum and tin oxide minerals. In contrast to transitions between other zones, contacts with zone (60) tend to be quite sharp; exceptions are noted with more gradual transitions into zones (30) and (90). This zone constitutes 13.5% of the pegmatite.

**Zone (70)**, *the quartz zone* occurs as a series of widely-dispersed discontinuous pods of essentially pure massive white to faintly rose-coloured quartz. The types of other trace constituents vary in relation to the identity of the neighboring zone; the most common are amblygonite-montebrasite, microcline-perthite, apatite, lithiophilite, spodumene, and pollucite. Miarolitic cavities, although not common at Tanco, are quite common within zone (70). These cavities vary in size from a few centimtres (common) to >1 metre (rare), and are commonly occupied by quartz crystals

(sometimes smokey) with occasional dustings of sulphides (predominantly pyrite), or mica. This zone constitutes 7.5% of the pegmatite.

**Zone (80)**, *the pollucite zone* actually includes two main bodies and a series of smaller blebs, largely in contact with zones (50) and (60). Petrologically, this zone is related to zone (50), but is designated as a separate zone because of the exceptional sizes of almost mono-mineralogical bodies of pollucite. The Main Pollucite zone, located in the upper, central-eastern half of the pegmatite (at 10200E and 9700N; Figures 3.5a, 3.6a) has dimensions of 180 x 75 x 12 m. This represents a rather unique economic concentration of pollucite with a purity of about 75%. Other significant minerals include lepidolite (7%), quartz (5%), K(Rb) - feldspar (2.5%), albite (5%), petalite (1.2%) and spodumene (1.0%). Assemblages of these minor minerals generally occur as coarse veins within the pollucite bodies. Occasional spodumene blades (up to a few cm in size) are scattered throughout the pollucite. This zone constitutes 1.3% of the pegmatite.

**Zone (90)**, *the lepidolite zone* includes two flat lying, E-W elongated sheets up to 18 m thick, and several smaller bodies within zone (60), or along contacts with spodumene-rich parts of zones (40) and (50). Fine-grained lithian muscovite predominates over true lepidolite; together they constitute 70% of the zone, and are generally found as intergrowths with microcline-perthite and quartz. Quartz and microcline each constitute 10% of the zone, albite content is about 8%. Other notable mineral occurrences include amblygonite (0.5 %), beryl (0.5%), lithiophilite (0.2%) and apatite (0.1%). This zone constitutes 2.1% of the pegmatite.

A close inspection of the spatial distribution of zones (Figures 3.5, 3.6) reveals the following: Zones (10) and (20) form concentric shells around the entire pegmatite. Zone (40) forms a discontinuous shell, which is disproportionately thicker along the footwall, and is transitional with zone (50) mostly along the hangingwall part; these two zones compose a continuous shell, much more coherent than zone (40) alone. Zone (50) is the largest inner-intermediate zone, and forms almost a continuous lozenge shaped zone along the E-W transect through 8400E-11000E. In general, the zone is thicker and more continuous within the western half of the deposit; this is in contrast to zone (60), which attains greater continuity and volume towards the east. Zone (60) is the most centrally located in vertical sections, and almost always lies beneath zone (50). Zone (30) occurs as discontinuous pods in two distinct zonal associations: i) as lenses between zones (50) and (40), and (40) and (20) in the eastern quarter-section along fence 9700N, and as a lens between zones (20) and (70) along the north quarter-section of fence 10200E; and ii) as two distinct lensoid pods interfingering with zone (60) near the main pollucite zone at the intersection of 9700N and 10200E. Despite the lack of zone (30) designations in the western half of the pegmatite, significant volumes of aplitic albite are present as non-mappable but widespread units permeating zone (60) (P. Černý, personal comm., 2001).

Zone (70) occurs as discontinuous lenses between zones (40) and (50), (50) and (60), and as distinct pods within zone (50) and occasionally (60). Zone (70) overlies zones (60) and (30) in the eastern portion and the Farwest Zone area of the mine, and adjoins the west margin of zone (60) in the west portion. The main pollucite body, zone (80), is a large continuous pod which lies above zone (60) along 9700E, and above zones (50) and (60) along 10200N. Small pods also occur within zone (60) along (10200E), occasionally with a thin shell of zone (70). The western pollucite body (centered on

9700N and 9100E) occurs as a thin lens separating zone (50) above, from zone (60) below. There are two main lepidolite bodies[zone (90)]. The main body (in the central portion of the mine) adjoins zone (50) and protrudes into zone (60). In places it may be overlain by zone (20). The second body occurs as a southward extension of the West Orebody, zone (60). This lepidolite body is in contact with zone (50) to the south, east and west, and zone (60) to the north. It partially encases a pod of pollucite near the conatact with zone (50), and in general, overlies zone (40) (P. Vanstone, personal comm., 2001). Small discontinuous lenses of a lepidolite-dominated assemblage are also found within zones (60) (50) (40) and (30). Compositions within the latter three zones are primarily Li-muscovite.

The above observations, based principally on the three cross-sections in Figures 3.5 and 3.6, indicate the complexity of the internal structure of the Tanco pegmatite, in contrast to earlier interpretations made by Norton (1983).

### 3.4 Internal morphology and evolution

Over the last fifty years, several attempts have been made at establishing a universal systematic method for describing the morphology, composition, and crystallization sequence of internal zones of granitic pegmatites (*e.g.* Cameron *et al.*, 1949; Norton 1983). However, with the steadily increasing number of new and more detailed descriptions of pegmatites it becomes readily apparent that the number of omissions and/or anomalous zones at any given locale defies any universal systematic method of comparison.

The internal evolution of granitic pegmatites has long been a topic of considerable debate. Theories applied to the internal evolution of granitic pegmatites have evolved rapidly over the last 2 decades with experimental studies of Li-aluminosilicates in the systems albite-quartz-eucryptite (Stewart, 1978) and $LiAlSiO_4$-$SiO_2$-$H_2O$ (London,1984); fluid inclusions (London 1986a), crystal-melt and fluid-melt distribution coefficients (Icenhower and London, 1996), and the effects of lithophile and volatile enrichments in evolving melt compositions (London, 1986b, 1987; London *et al.*, 1988, 1989).

According to the Jahns and Burnham model (1969), the initiation of pegmatite textures marks the transition from vapour undersaturated to vapour saturated conditions during near-equilibrium primary magmatic crystallization at eutectic composition. According to London (1990, 1992b), the internal evolution of granitic pegmatites involves largely disequilibrium crystallization from melt with increasing concentrations of $H_2O$, Li, B, F and P, but consistently at vapour-undersaturated conditions. Volatile components in the evolving melt effectively reduce the thermal minimum in the haplogranitic system from >800 °C to below 640 °C (Černý, 1998), by inhibiting polymerization of the silicate framework. This promotes low melt viscosity, and high alkali-diffusion rates throughout the primary sequence of crystallization, while simultaneously inhibiting the formation of nucleation sites. As a result, volatile enriched zones typically exhibit substrate-controlled crystal growth leading to the formation of very large crystals with directional fabrics including comb-structures, or dendritic or graphic features. Fine-grained units, consisting predominantly of aplitic albite and quartz, are explained by the periodic removal of fluxing components, primarily B and F, by the stabilization of tourmaline and lepidolite (London, 1992b). This leads to a rapid release of supercritical fluid and consequently rapid nucleation and crystallization of albite and silica from supersaturated residual melt.

Rapid solidification by 'chemical quench' generally signifies a transition from a primary magmatic regime to one dominated by processes involving supercritical-to-hydrothermal fluids (Černý *et al.*, 1998). London's experimental determination of the $LiAlSiO_4$-$SiO_2$-$H_2O$ phase diagram (London,1984), in combination with Tanco fluid-inclusion data (London, 1986a) allows for a reliable determination of the cooling path and fluid evolution across the magmatic-hydrothermal transition at Tanco (Figure 3.7).

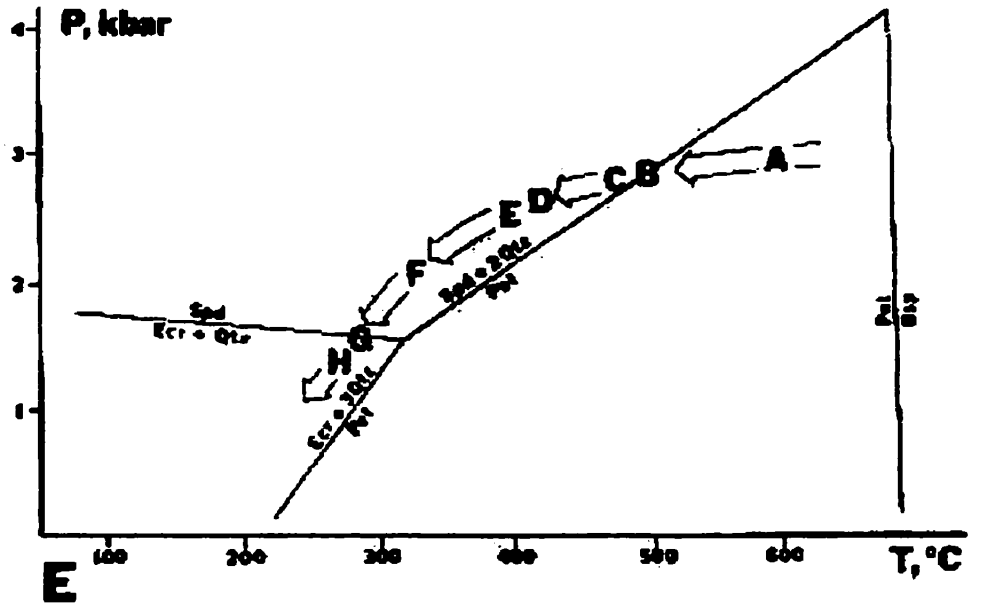


**Figure 3.7** Internal evolution of the Tanco Pegmatite in relation to P-T stability fields of petalite, spodumene, and eucryptite. Points along the cooling curve (A-H) are discussed in text.

Primary crystallization of petalite occurred below 680°C and 4100 bars (A), and proceeded until ~500 °C and 2900 bars [intersection of univarient at (B): petalite = spodumene + 2 quartz; Figure 3.7], at which point primary spodumene became the stable Li-Al silicate. Crystallization of primary spodumene continued to at least 470°C and 2700 bars (C) (Figure 3.7), with preceding spodumene crystallization occurring in

the presence of a dense, hydrous alkali borosilicate fluid. Fluid inclusions within spodumene showed increasing $CO_2$ content with decreasing temperature, and verged on $H_2O$-$CO_2$ immiscibility at about 390°C and 2500 bars (E) through to a complete $CO_2$-liquid separation from a saline-rich hydrous phase at point (F) (300°C and 1800 bars). The Tanco pegmatite entered the stability field of eucryptite and quartz at approximately 280°C and 1600 bars. Eucryptite is not particularly abundant at Tanco despite the large volumes of petalite and spodumene. Evidently the breakdown of these phases was largely inhibited in the presence of the exsolved $CO_2$ liquid, virtually free of the otherwise catalyzing hydrous fluid (Černý and London, 1983), thus limiting the extent of retrograde reequilibrium.

The studies on experimental petrology completed over the last 2 decades, provide a sound scientific footing from which to attempt reasonable interpretations of zonal differentiation, as well as the observed zonal distributions and paragenetic sequences within rare-element granitic pegmatites. However, a full understanding of pegmatite evolution is far from being achieved. In light of the current knowledge, many textural features at Tanco still have questionable origins: "Textural and paragenetic features strongly suggest that the bulk of all nine zones was produced by primary crystallization from a liquid/fluid phase. However, zones 10, 30 and in part also 90 show metasomatic relations with adjacent zones, and small-scale plus very low-volume replacements can be seen within each of the zones 40-90 (Černý *et al.*, 1998, p. 12)."

## CHAPTER 4: PREVIOUS WORK

A broad overview of Tanco, in terms of regional setting and composition can be found in Nickel (1961), with more comprehensive data found in Černý *et al.* (1981) and in IMA guidebooks Černý *et al.* (1996, 1998). An updated analysis of Tanco zonal distributions and bulk composition was completed by Stilling (1998). More detailed information on Tanco feldspar mineralogy and geochemistry, can be found in Černý (1982), Gaupp *et al.* (1984), and Morteani and Gaupp (1989); as well as Ga geochemistry (Černý and Hawthorne, 1989), trace-element partitioning between reportedly coexisting feldspar and mica (Marshall, 1972), and feldspar colour in relation to composition and structural order-disorder (Černý and Macek, 1972).

General fractionation trends in pegmatitic feldspars (and other minerals) from a variety of locations, including Tanco, are discussed by Černý (1994), and Černý *et al.* (1985). Various theses and papers have been written on late-secondary feldspars from Tanco, including albite (Teertstra, 1991), adularia (Černý and Chapman, 1984; Teertstra *et al.*, 1998a), and Rb-rich to Rb-dominant feldspars plus adularia (Teertstra, 1997; Teertstra *et al.*, 1998b). A number of papers have also been written on isotopic systems involving feldspars from Tanco: oxygen isotope systematics (Taylor and Friedrichsen, 1983), and Rb-Sr isotopic data (Penner and Clark, 1971; Clark, 1982; and Clark and Černý, 1987).

Aside from the detailed studies of late-secondary Rb-bearing feldspar and adularia, previous work on the mineralogy and geochemistry of Tanco feldspars has been rather spotty, and has not provided a comprehensive, statistically significant, all-encompassing story of feldspars in Tanco.

# CHAPTER 5: ANALYTICAL TECHNIQUES

## 5.1 Sampling strategy

Samples were collected during four visits to the Tanco mine site. During the first two visits in the spring of 1998 and 1999, the majority of 'primary' blocky K-feldspar, aplitic albite, and cleavelandite samples were selected from drill core. This was followed by two more visits in the fall of 1999 to supplement samples from zones that were under-represented in the drill cores; in particular, from the spatially restricted zones (10) (30) (80) and (90). A limited number of hand specimens representing late-stage K-(Rb) feldspar species were provided by P. Černý, and A. Stilling. In all, a total of 461 samples was collected, consisting of 230 K-feldspar and 231 albite specimens. Zonal designations of drill-core samples were derived from drill logs provided by Tanco staff. Each individual sample was chosen for a specific mineral variety (*i.e.* aplitic albite, cleavelandite, K (Rb)-feldspar, adularia), from a specific zone, and then briefly described in terms of colour, grain-size, and texture. A brief description of associated minerals in the sample was also included in the sampling notes.

The first priority at the sampling stage was to collect representative samples of blocky K-feldspar, aplitic albite, and cleavelandite from each zone. The second objective was to select samples of each type, within individual zones along east-west and north-south transects, in order to adequately represent compositional variations in 3-dimensions. Both objectives were achieved by selecting samples from drill cores previously utilized by Stilling (1998) for Tanco bulk composition calculations (Figure 3.4), along the east-west transect (9700N: Figures 3.5a,b), and along the two north-south transects (10200E: Figure 3.6a and 9100E: Figure 3.6b); due attention was paid to obtaining samples from both hangingwall and footwall portions of individual zones.

## 5.2 Sampling statistics

The analytic flow chart in Figure 5.1 displays the number of samples obtained and analysed, as well as the number of analytical results used in subsequent chapters on mineralogy (Chapters 6,7) and geochemistry (Chapter 8). Several dozen additional compositions of various late-stage and secondary K-feldspars were supplied by D. Teertstra; most of these were unpublished data, but several adularia compositions were taken directly from Teertstra (1997). Compositional data from outside sources are not included in Figure 5.1.

Four different analytical techniques are shown in Figure 5.1a,b: 1) bulk wet chemistry by inductively coupled plasma (ICP) and atomic absorption (AA) spectrometry, 2) phase chemistry by electron-microprobe analysis (EMPA), 3) degree of order-disorder by powder X-ray diffraction (XRD), and 4) light- and volatile-element chemistry by secondary ion mass spectrometry (SIMS).

The final number of results used for plotting and interpretation in subsequent chapters (bottom of Figure 5.1a,b), are presented in histogram form (Figure 5.2), emphasizing the number of available compositions for each feldspar type, and for each individual zone. This sample distribution can be compared to the modal distribution of albite and K-feldspar (Figure 5.3), highlighting the availability and relative abundances of the two major feldspar subdivisions in individual zones.

**(a) K-feldspar**

| | | | | |
|---|---|---|---|---|
| Initial pool of samples | **230** | 122 primary + 15 secondary | 82 | 82 |
| Select samples | 176 | 100 | 31 | 11 |
| Analysis | ICP/AA | EMP | XRD | SIMS |
| Good totals | 150 | 90 | | |
| **Final filtered data points** | **128** | **82** | 31 | 11 |
| = "Primary" | 122 | 68 | 31 | 7 |
| + "Secondary" | 6 | 14 | 0 | 4 |

**(b) Albite**

| | | | |
|---|---|---|---|
| Initial pool of samples | **231** | 118 | 118 |
| Select samples | 210 | 31 | 12 |
| Analysis | EMP | XRD | SIMS |
| Good totals | 168 | | |
| **Final filtered data points** | **118** | 28 | 11 |
| = aplites | 61 | 13 | 5 |
| + cleavelandites | 57 | 15 | 7 |

**Figure 5.1** K-feldspar (a) and albite (b) flowcharts listing numbers of samples obtained and analysed, followed by number of final compositions (in bold) presented in subsequent chapters. Does not include the small number of compositions obtained from literature (e.g. Teertstra, 1997).

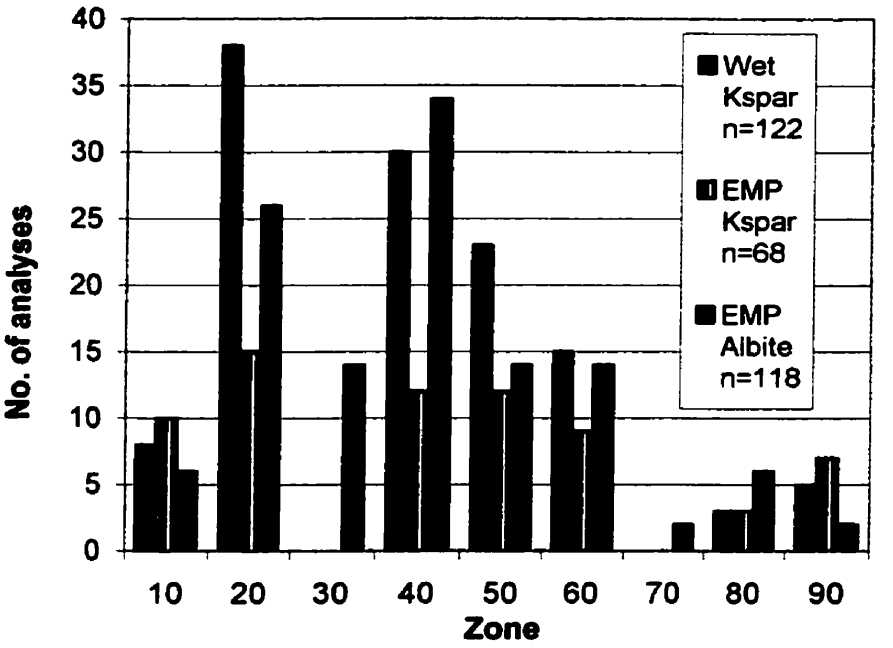


**Figure 5.2** Number of results used in subsequent charts and interpretations for K-feldspar (Type 1), and albite (Types A+B).

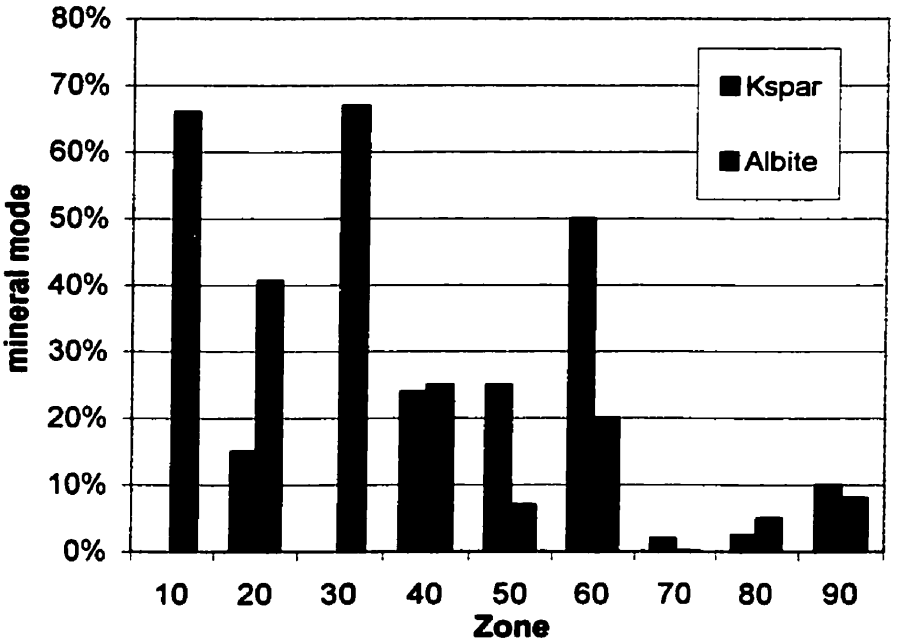


**Figure 5.3** Modal abundances of K-feldspar (Type-1) and albite (Types A+B) in each major zone (data from Stilling, 1998).

Sample-set reduction and data filtering occurred for a variety of reasons. Visual inspection of the original 230 K-feldspar and 231 albite samples in the lab revealed a number of samples that were either misidentified or contained insufficient quantity or quality of the required mineral. The remaining 176 K-feldspar and 210 albite samples, which passed visual scrutiny, then underwent ICP/AA and EMP analysis, respectively. Results from these analyses were filtered for gross error or non-feldspar compositions, and yielded compositions of 150 K-feldspar and 168 albite samples. This was followed by statistical filtering, based on expected compositional limits for pure feldspars, at which point subtly contaminated samples were removed from the data set. This procedure yielded a final dataset of 128 K-feldspar, and 118 albite compositions.

Mineralogical heterogeneity within several of the late K-feldspar samples counterindicated bulk analysis during the initial sampling run. These samples were subsequently added to the 128 wet K-feldspar results, to form a pool of 143 samples. From this pool, 100 K-feldspar samples were selected for EMPA. The same set of filters mentioned above was applied, and resulted in a final data set of 82 EMPA K-feldspar compositions (Figure 5.1).

From the final pool of filtered EMPA compositions of K-feldspar and albite, samples were selected for further XRD and SIMS work. In addition to a sample selection based on zonal designation, compositional data was also considered. High and low contents of P, Rb and Cs were considered during K-feldspar selection, whereas high and low P and Ca contents were considered during albite selection.

### 5.3 Sample preparation

The drill-core library at the Tanco mine site includes more than 1000 drill holes, representing more than 50 years of drilling for the purposes of assessment and exploration. The cores were found to be in varying states of preservation, with, as expected, older boxes in poorer condition. Older cores are visibly bleached and oxidized. Many older boxes have also been exposed to fall-out from the local milling of Li and Cs rich ore. The first core storage facility was constructed in 1980 over the pre-existing core racks. Today, all pegmatite intersections are stored indoors, and host-rock lithologies stored outside.

Samples were initially cleaned of gross debris in water and alcohol, and coarse separates selected from the interior of feldspar crystals to avoid the contaminated exterior. This was followed by visual separation under 4x magnification to yield visibly pure 2-5 mm chips. The most common mineral contaminants seen in the K-feldspar separates were fine-grained albite and/or muscovite, visible on cleavage faces or in small veinlets, with or without quartz. Other less common, but readily visible contaminants included small (<1mm), equidimensional grains of apatite or lithiophilite, and/or various Ta, Nb, Ti, Fe, oxides and Fe, Zn, or Bi sulfides. In contrast, aplitic albite separates were invariably contaminated with microscopic quartz +/- muscovite, tourmaline, apatite, and/or Ta-Nb oxides. 2-5 mm chips were archived for all feldspar types, and later used for EMP mounts and XRD work. The remaining K-feldspar separates (5-10 chips per sample) were crushed to a uniform fine powder in a mechanical mortar and pestle for wet-chemical analysis.

### 5.4 Wet chemistry – ICP/AA emission spectrometry

K-feldspar was the only mineral to undergo bulk wet-chemical analysis. The main reason is that K-feldspar from Tanco is almost invariably perthitic, and bulk analysis provides the most realistic and complete estimate of primary compositions before subsolidus transformations occurred. The technique is advantageous because multi-element analysis is relatively inexpensive, and limits of detection (LOD) are considerably lower (5-10 x lower) than electron-microprobe limits (Appendix I). EMPA is also limited to elements above Z=6.

On the down side, wet-chemical results are generally less precise than EMPA. Precision for most elements is +/- 5% relative (+/- 15% relative for Na); in contrast, EMPA analytical precision is about +/- 1% relative (Appendix I). Contaminants also are an important consideration. Albite 'contaminant' grains in K-feldspar are particularly noteworthy; most samples examined contain 2-10% fine-grained platy albite laths (0.5-3mm) visible along cleavage planes, irregularly disseminated within the perthitic K-feldspar individuals. The pervasive nature of these albite grains made complete removal from the K-feldspar host impossible.

Acid digestion and ICP/AA analyses were done by Gregg Morden (Geochemistry Laboratory Manager) at the Department of Geological Sciences, University of Manitoba. Procedures for sample preparation, digestion and analysis followed: *EPA Method 3052 - - Microwave Assisted Acid Digestion of Siliceous and Organically Based Matrices, Revision 0, Dec. 1996,* outlined by the US Environmental Protection Agency (EPA) at: http://www.epa.gov/oerrpage/superfund/programs/clp/download/ilm/ilm40D.pdf.

Al, Ca, Ba, Sr, Li, Na, K, Rb, P, Ga were analysed on the Varian "Liberty 200" sequential Inductively Coupled Plasma Optical Emission Spectrometer (ICP-OES). Cesium, with its relatively low ionization potential, was analysed on the Varian "Spectra 300" AA (atomic absorption) spectrometer, in emission mode.

All results of wet-chemical analysis were found satisfactory relative to earlier data collected in different laboratories by the same or different methods, except Al and Ga for K-feldspars (albite was not analyzed). Aluminum determined in this study turned out to be erratically excessive from the crystal-chemical viewpoint, and could not be used for calculation of Al/Ga. Gallium values proved to be generally similar to, but somewhat lower than, the data determined for the Tanco K-feldspars and albite at the geochemical laboratory, Ecole Polytechnique, Montreal (analyst: P. Hébert) for P. Černý in 1978 (see Figure 6.7f). As shown in Figures 8.1q,r and Figures 8.2a,b, the Ecole Polytechnique data are used here for the geochemistry of Ga of both feldspar categories. The present Ga data for K-feldspar will be cautiously applied [to zones (80) and (90)] on the assumption that relative differences among the present data are correct, despite the absolute shift of approximately -20 ppm from the Ecole Polytechnique values (see Figure 6.7f).

### 5.5 Electron-microprobe analysis (EMPA)

Albite and K-feldspar samples were analysed using EMPA, mainly to assess the crystal-chemistry of albite samples, and of the potassic phase of perthitic K-feldspar samples. Trace-element contents of perthitic albite lamellae were also determined in a limited number of cases. In general, trace-element contents (particularly in albite) proved to be of limited use because many were present at concentrations near their limits of detection (Appendix I).

EMP analyses of albite and K-feldspar were collected at identical conditions, except for the use of analytical standards for Si and Al (Table 5.1). The analytical procedure follows Teertstra (1997), using wavelength dispersion (WDS) on a CAMECA SX-50 electron-microprobe operating at 15 kV and 20 nA, with a beam diameter of 5 μm. Data reduction was achieved by the PAP procedure of Pouchou & Pichoir (1985). At the prescribed conditions, Teertstra *et al.* (1998b) determined the precision of elemental weight percent measurements at a 4σ confidence level to be about 1% relative. By using a beam diameter of 5 μm, and analyzing first for Na, Si, and K, alkali-loss from the analysed volume was insignificant.

*Statistical treatment of EMPA data*

All EMPA compositions in this thesis represent averages of a minimum of 2, to a maximum of 8 individual point compositions: albite compositions average 5 points, K-feldspar compositions average 3 points. Non-zero contents recorded below limits of detection were used in the averaging on the premise they do represent, at least, a semiquantitative estimate of real values (Černý, personal comm., 2001). Earlier comparisons of K-feldspar compositions analyzed by both SIMS and EMPA (Černý *et al.*, 1984; and unpublished data) justify this assumption.

**Table 5.1:** EMPA analytical conditions, standards, and detection limits for K-feldspar.

| Standard | Element | Line | Time (s) | Detection | limit (wt%) |
|---|---|---|---|---|---|
| Eifel sanidine | K | $K\alpha$ | 20 | $K_2O$ | 0.036 |
| | Al | $K\alpha$ | 20 | $Al_2O_3$ | 0.045 |
| | Si | $K\alpha$ | 20 | $SiO_2$ | 0.060 |
| anorthite | Ca | $K\alpha$ | 20 | CaO | 0.025 |
| Amelia albite | Na | $K\alpha$ | 20 | $Na_2O$ | 0.049 |
| 1RbLeucite | Rb | $L\alpha$ | 60 | $Rb_2O$ | 0.057 |
| 1fayalite | Fe | $K\alpha$ | 60 | $Fe_2O_3$ | 0.086 |
| 2olivine | Mg | $K\alpha$ | 30 | MgO | 0.010 |
| pollucite | Cs | $L\alpha$ | 60 | $Cs_2O$ | 0.032 |
| $SrTiO_3$ | Sr | $L\alpha$ | 60 | SrO | 0.059 |
| | Ti | $K\alpha$ | 80 | $TiO_2$ | 0.057 |
| riebickite | F | $K\alpha$ | 120 | F | 0.069 |
| $VP_2O_7$ | P | $K\alpha$ | 60 | $P_2O_5$ | 0.073 |
| barite | Ba | $L\beta$ | 60 | BaO | 0.087 |
| spessartine | Mn | $K\alpha$ | 60 | MnO | 0.025 |
| $GdGaO_3$ | Ga | $K\alpha$ | 60 | $Ga_2O_3$ | 0.031 |
| PbTe | Pb | $M\alpha$ | 60 | PbO | 0.041 |

Albite analyses were collected under identical conditions, but with Amelia albite as the standard for Al and Si, instead of Eifel sanidine.

Limits of detection were calculated using
L.D. = [3 (wt.% oxide) $(R_b/t_b)^{1/2}$] / $(R_p-R_b)$ where $R_p$ = background count rate (counts/s), $t_b$ = background count time (s), $R_p$ = peak count rate.

## 5.6 Comparison of wet-chemical and EMPA data for K-feldspar

Comparisons of same-sample wet-chemical and EMPA K-feldspar compositions indicate that results obtained by the two techniques are not identical. There are a number of

reasons for discrepancies, but the most obvious is the invariable presence of perthitic lamellae in bulk samples. For this reason, major element data show little or no correlation. On the other hand, minor- and trace-element contents, which are above EMP detection limits (Appendix I) in more than 90% of compositions, do correlate well; Rb, Cs, and P meet these criteria and are shown in Figures 5.4a,b,c.

The correlation for rubidium is very good (Figure 5.4a; $R^2 = 0.87$), and approaches an ideal 1:1 correlation with a slope of m=1.1. Average $Rb_2O$ contents by wet-chemical analysis from zones (10) (20) (40) and (50) (Figure 5.5a) are slightly lower than average EMPA-determined contents; however the situation is reversed for $Rb_2O$ contents in zones (60) (80) and (90). The $Cs_2O$ correlation is also very good (Figure 5.4b; $R^2 = 0.88$), but the low slope (m=0.70) and the significant positive y-intercept (+ 0.07) suggest a less than ideal relation between results from the two techniques. In contrast to $Rb_2O$, average $Cs_2O$ contents by wet-chemical analysis from zones (10) (20) (40) and (50) (Figure 5.5a) are slightly higher than average EMPA-determined contents. In contrast, average $Cs_2O$ contents are comparable in zones (60) (80) and (90), between the two techniques. The phosphorus correlation is close to ideal (Figure 5.4c; $R^2 = 0.85$, m=1.00, b=0.05), however average wet-chemical data appear to be systematically higher than EMPA data (Figure 5.5c).

Other reasons for the analytical discrepancies noted above include: i) the use of different standards for the different techniques, and ii) hydrothermal remobilization, leaching, and/or alteration leading to localized preferential element redistributions.

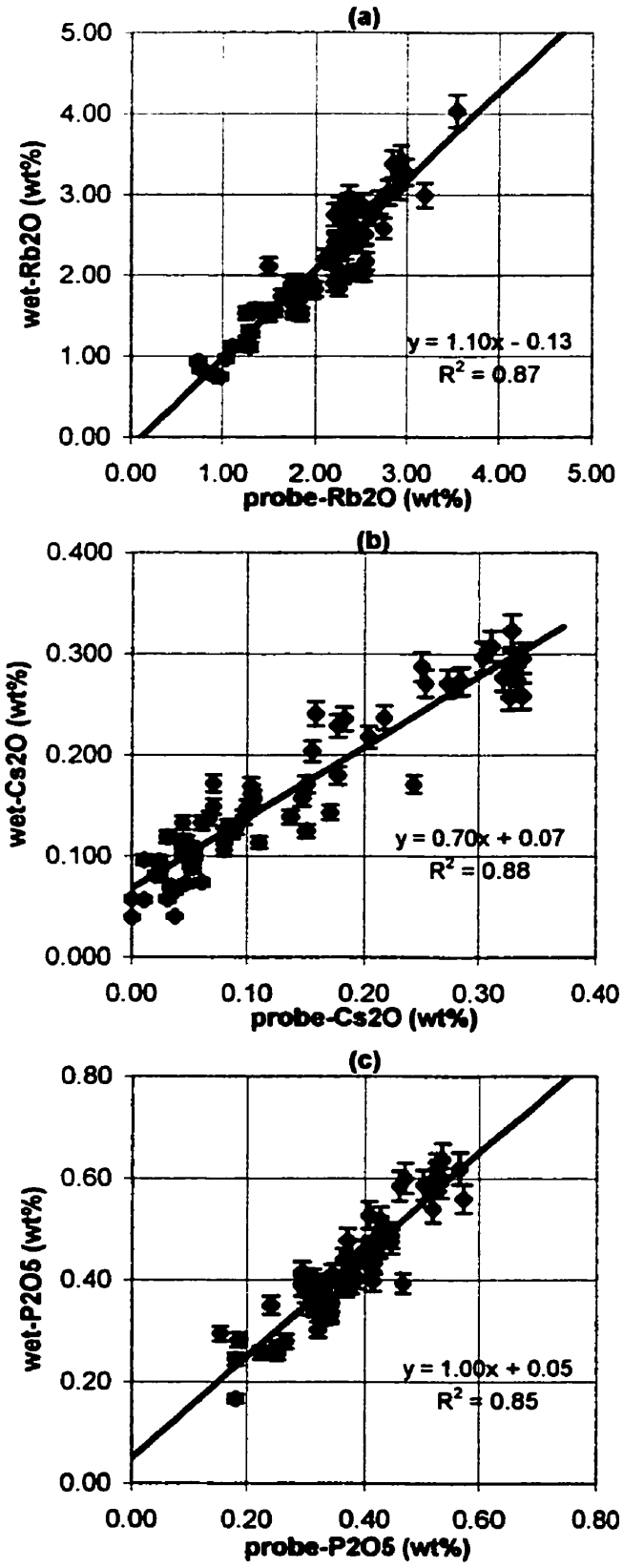


**Figure 5.4** Wet chemistry - EMPA correlation diagrams

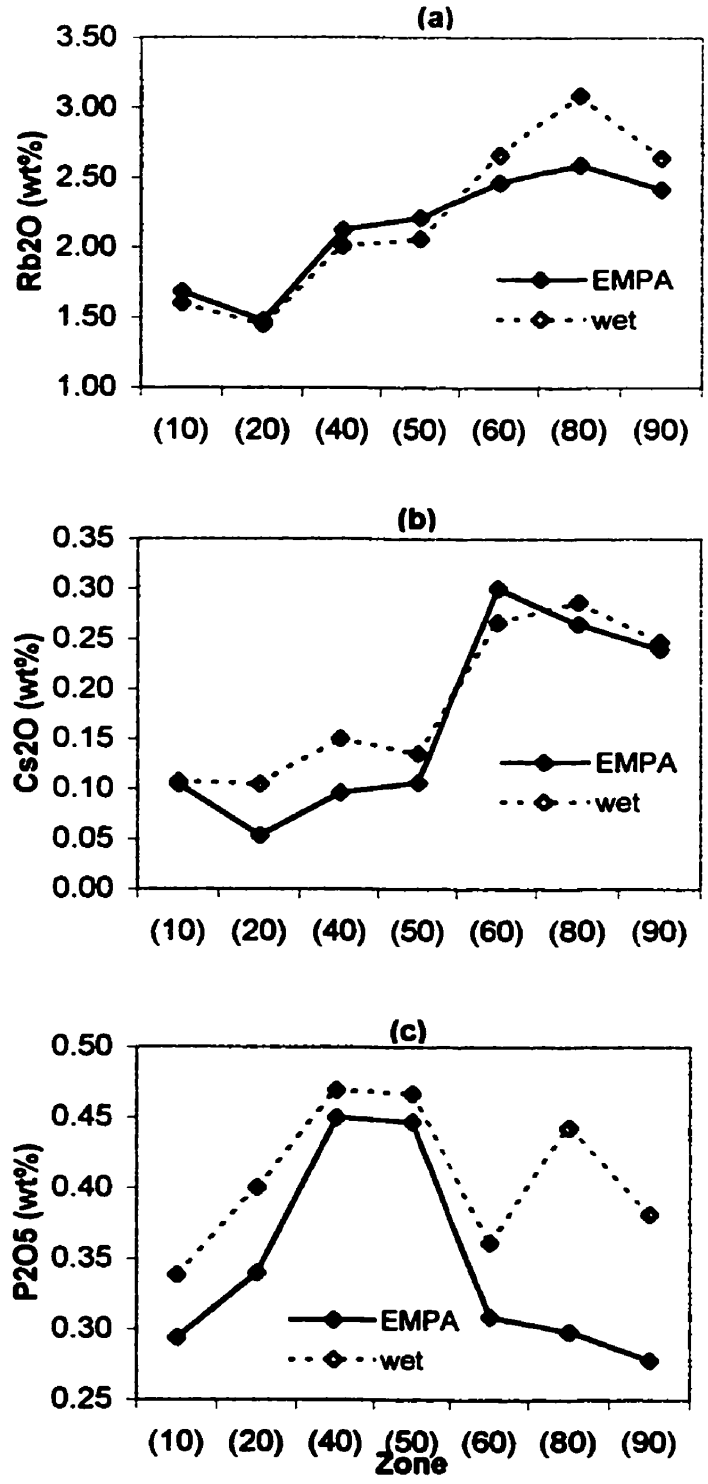


**Figure 5.5** Average oxide contents per zone -- a comparison between wet-chemical results and EMPA results.

In studies on alkali feldspars from variably altered monzogranitic host rocks, Kontak and Martin (1997) found Rb to be relatively immobile compared to Li, Sr, Ba and Cs. However, even Rb is to a certain degree subject to open-system behavior at a localized scale. Teertstra (1997) found variations in Rb content typically between 0.3 to 0.5 wt% oxide, on microscopic scale, and up to 1% variations in Tanco microcline veins in pollucite. Heterogeneous blotchy textures in BSE images, at a scale of several tens of microns, commonly comprise coexisting Rb-rich and Rb-poor microcline. Microprobed homogeneous areas may be somewhat depleted in Rb, as it has a tendency to move toward cracks and grain margins (Teertstra, 1997, P. Černý, personal comm., 2001). Mason (1982) reported a tendency for higher than average Rb contents proximal to albite lamellae in perthite.

During microprobe analysis, I specifically and consistently selected areas (points) that were homogeneous under BSE, and were approximately midway between albite lamellae. This point-selection-bias could account for the relatively low EMPA Rb contents relative to wet-chemical results.

Phosphorus (Figure 5.4c, 5.5c) correlates well and the subtle positive y-intercept can easily be justified by the prevalence of minute secondary phosphate contaminants. Five outliers centered around x= 0.10, y= 0.45 (Figure 5.4c), were removed from the data set, as they were suspect contaminated by adjacent lithiophilite and secondary phosphates. Microscopic phosphate contaminants may explain the spike in average wet-chemistry $P_2O_5$ contents for zones (80) and (90) (Figure 5.5c). Interestingly, samples containing lithiophilite as an accessory mineral, either contained excessive P (in comparison to

EMPA results) or contained abnormally low P concentrations suggesting that lithiophilite consumes most of the available P.

### 5.7 X-ray powder-diffraction (XRD)

X-ray diffraction work was done on a Philips PW1729 X-ray powder diffractometer at the University of Manitoba under conditions outlined in Table 5.2. Powder samples were prepared in the same manner as for the wet-chemical samples (sections 5.3, 5.4). Annealed $BaF_2$ was added to samples as an internal standard at approximately 5% of the total sample volume. Standard sets of *hkl* diffractions were selected for unit-cell refinements of both K-feldspar (Figure 5.6) and albite (Figure 5.7) samples. Unit-cell refinements were determined using the least-squares refinement program included with the JADE™ 5.0.32 XRD pattern processing program.

**Table 5.2:** XRD acquisition parameters.

| | **K-feldspar** | **Albite** |
|---|---|---|
| Voltage (KV) | 40 | 40 |
| Amperage (mA) | 40 | 40 |
| Cu K $\alpha$1 (Å) | $\lambda$ = 1.54056 | $\lambda$ = 1.54056 |
| 2$\theta$ range (°) | 19 - 51 | 20.5 - 51.3 |
| Step width (°) | 0.02 | 0.02 |
| Step time (s) | 4 | 3 |

### 5.8 Secondary Ion Mass Spectrometry (SIMS)

Eleven K-feldspar and twelve albite samples were analysed for Li, B and Be using a Cameca IMS 4f ion microprobe installed at CNR-CSCC in Pavia, Italy. Luisa Ottolini oversaw the analyses and provided the following description of the analytical conditions and procedures used.

Oxygen gas with a purity of more than 99.99% was supplied to the duoplasmatron to generate a negatively charged primary ion beam which was subsequently filtered by a magnetic prism to provide 16O- ions. The primary accelerating voltage was -12.5 kV. The beam was focused onto the sample surface with a diameter of < 10 microns at a primary current intensity of about 5 nA. Counting times were 20 seconds for Li and 30 seconds, each, for Be, B and Si over 10 analytical cycles. Steady state-sputtering conditions were achieved after 450 sec waiting time.

Positive secondary ions were nominally accelerated through 4.5 kV. Secondary ions at masses 7, 9, 11 and 30 were collected under an ion imaged-field of 25-micron diameter. The selected contrast diaphragm and field aperture were the 400 and 1800 micron inner-diameter, respectively). Medium-to-high energy ions were selected by offsetting the sample accelerating voltage while keeping constant the settings of the electrostatic analyzer (ESA) voltages and the width and position of the energy slit. The energy-slit width was 50 eV (i.e., +- 25 eV relative to the axis). For Li, Be and B measurements, a voltage offset of -100 V was applied to the accelerating voltage of + 4500 V at the maximum of the energy distribution (or equivalently, a voltage offset by -125 V was chosen relative to the voltage at which this latter distribution drops to 10% of the maximum). This implies analyzing secondary ions with emission energies of about 100 +- 25 eV (i.e., in the range: 75-125 eV).

Matrix effects affecting Li/Si, Be/Si and B/Si ionization were minimized using the "energy filtering technique," (Ottolini et al., 1993). A set of well characterized samples (standards) was used for quantifying secondary ion signals as light-element concentrations (wt% oxides). Si was used as the inner reference element for the matrix and was monitored as $_{30}Si^{+}$ signal. The energy filtered analyses were done at a mass

resolving power of about 600 (M/delta M) to discriminate the contribution of $_{9}Be^{+}$ (analytical ions) from $_{27}Al^{3+}$ interfering signal.

Ceran glass was used as a calibration standard for Li, danalite for Be, and the synthetic glass Pyrex™ for B. Accuracy is estimated in the range 5-10% for all the light elements and detection limits are on the order of 10 ppb for Li and Be and about 15 ppb for B.

**PDF#00-0006: QM=Star/Calculated; d=Other/Unknown; I=(Unknown)** | **PDF Card**

C-096-I: 13-52; 3sec @.02

Radiation=CuKa1 | Lambda=1.5406 | Filter=
Calibration= | d-Cutoff= | I/Ic(RIR)=0.64
Ref= JADE's Userfile

Triclinic, C-1(2) | Z=4 | mp=
Cell=8.607x12.968x7.224<90.61x116x87.83> | Pearson=
Density(c)=2.617 | Density(m)= | Mwt= | Vol=
Ref= Ibid.

Strong Line: 3.49/X 2.95/8 3.71/6 3.03/6 3.83/6 3.30/6 1.81/5 4.24/5

18 Lines, Wavelength to Compute Theta = 1.54056A(Cu), I%-Type = (Unknown)

| # | d(A) | I(f) | h | k | l | 2-Theta | Theta | 1/(2d) | # | d(A) | I(f) | h | k | l | 2-Theta | Theta | 1/(2d) |
|---|---|---|---|---|---|---|---|---|---|---|---|---|---|---|---|---|---|
| 1 | | | | | | | | - | 10 | 2.9550 | 75.0 | 1 | -3 | 1 | 30.220 | 15.110 | 0.1692 |
| 2 | 4.2351 | 51.0 | -2 | 0 | 1 | 20.959 | 10.479 | 0.1181 | 11 | 2.9078 | 46.0 | 0 | 4 | 1 | 30.722 | 15.361 | 0.1720 |
| 3 | 3.9841 | 41.0 | 1 | 1 | 1 | 22.296 | 11.148 | 0.1255 | 12 | 2.7565 | 24.0 | -1 | 3 | 2 | 32.453 | 16.227 | 0.1814 |
| 4 | 3.9307 | 13.0 | 1 | -1 | 1 | 22.602 | 11.301 | 0.1272 | 13 | 2.5960 | 14.0 | -3 | 1 | 2 | 34.522 | 17.261 | 0.1926 |
| 5 | 3.8312 | 55.0 | 1 | 3 | 0 | 23.197 | 11.599 | 0.1305 | 14 | 2.5701 | 28.0 | 1 | 1 | 2 | 34.880 | 17.440 | 0.1945 |
| 6 | 3.7111 | 59.0 | -1 | 3 | 0 | 23.959 | 11.979 | 0.1347 | 15 | 2.1603 | 51.0 | 0 | 6 | 0 | 41.778 | 20.889 | 0.2314 |
| 7 | 3.4853 | 100.0 | -1 | -1 | 2 | 25.537 | 12.768 | 0.1435 | 16 | 2.0448 | 11.0 | 0 | -6 | 1 | 44.258 | 22.129 | 0.2445 |
| 8 | 3.2971 | 55.0 | -2 | 0 | 2 | 27.021 | 13.510 | 0.1516 | 17 | 1.9928 | 40.0 | 2 | 2 | 2 | 45.478 | 22.739 | 0.2509 |
| 9 | 3.0317 | 59.0 | 1 | 3 | 1 | 29.438 | 14.719 | 0.1649 | 18 | 1.8057 | 52.0 | -2 | 0 | 4 | 50.502 | 25.251 | 0.2769 |

**Figure 5.6** Example of a K-feldspar unit-cell refinement. The set of *hkl* reflections and other conditions were consistently applied to all other K-feldspar refinements. Occasional peak omissions were made for poorly resolved or overlapping peaks. Unit-cell dimensions and d-spacings are in Ångstroms. Angular values are in degrees of angle.

**PDF#00-0007: QM=Star/Calculated; d=Other/Unknown; I=(Unknown)** | **PDF Card**

C-F 20.5-51.3; 3sec/.02step

Radiation=CuKa1 | Lambda=1.5406 | Filter=
Calibration= | d-Cutoff= | I/Ic(RIR)=2.1
Ref= JADE's Userfile

Triclinic, C-1(2) | Z=4 | mp=
Cell=8.136x12.785x7.159<94.25x116.6x87.76> | Pearson=
Density(c)=2.62 | Density(m)= | Mwt= | Vol=
Ref= Ibid.

Strong Line: 3.78/X 4.03/9 3.67/6 2.97/5 1.80/4 3.86/3 3.15/3 2.86/3

19 Lines, Wavelength to Compute Theta = 1.54056A(Cu), I%-Type = (Unknown)

| # | d(A) | I(f) | h | k | l | 2-Theta | Theta | 1/(2d) | # | d(A) | I(f) | h | k | l | 2-Theta | Theta | 1/(2d) |
|---|---|---|---|---|---|---|---|---|---|---|---|---|---|---|---|---|---|
| 1 | 4.0334 | 88.0 | -2 | 0 | 1 | 22.019 | 11.010 | 0.1240 | 11 | 2.5603 | 24.0 | -2 | -4 | 1 | 35.018 | 17.509 | 0.1953 |
| 2 | 3.8569 | 34.0 | 1 | -1 | 1 | 23.040 | 11.520 | 0.1296 | 12 | 2.4444 | 12.0 | -2 | 4 | 1 | 36.737 | 18.368 | 0.2046 |
| 3 | 3.7793 | 100.0 | 1 | 1 | 1 | 23.520 | 11.760 | 0.1323 | 13 | 2.4300 | 10.0 | -1 | -5 | 1 | 36.961 | 18.481 | 0.2058 |
| 4 | 3.6651 | 60.0 | -1 | 3 | 0 | 24.264 | 12.132 | 0.1364 | 14 | 2.3178 | 20.0 | -3 | -3 | 1 | 38.821 | 19.410 | 0.2157 |
| 5 | 3.5068 | 23.0 | -1 | -1 | 2 | 25.377 | 12.689 | 0.1426 | 15 | 2.1261 | 16.0 | 0 | 6 | 0 | 42.483 | 21.241 | 0.2352 |
| 6 | 3.1533 | 34.0 | -2 | 2 | 0 | 28.278 | 14.139 | 0.1586 | 16 | 2.0777 | 12.0 | 2 | -4 | 1 | 43.522 | 21.761 | 0.2407 |
| 7 | 2.9662 | 52.0 | 1 | -3 | 1 | 30.103 | 15.051 | 0.1686 | 17 | 2.0340 | 5.0 | 2 | 4 | 1 | 44.507 | 22.254 | 0.2458 |
| 8 | 2.8627 | 28.0 | 1 | 3 | 1 | 31.219 | 15.609 | 0.1747 | 18 | 1.8192 | 10.0 | 4 | 0 | 0 | 50.100 | 25.050 | 0.2748 |
| 9 | 2.8417 | 6.0 | -1 | -3 | 2 | 31.456 | 15.728 | 0.1760 | 19 | 1.8024 | 40.0 | 1 | 1 | 3 | 50.600 | 25.300 | 0.2774 |
| 10 | 2.6405 | 20.0 | -1 | 3 | 2 | 33.921 | 16.961 | 0.1894 | | | | | | | | | |

**Figure 5.7** Example of an albite unit-cell refinement. The set of *hkl* reflections and other conditions were consistently applied to all other albite refinements. Occasional peak omissions were made for poorly resolved or overlapping peaks. Unit-cell dimensions and d-spacings are in Ångstroms. Angular values are in degrees of angle.

# CHAPTER 6: MINERALOGY OF TANCO K(RB)-FELDSPARS

Based on crystal morphology, texture, and mineral associations, six different (K-Rb)-feldspar and six albite varieties are identifiable in the Tanco pegmatite (Table 6.1). The sequence of mineral types listed in Table 6.1 generally corresponds to a progression from high-temperature 'primary' to lower-temperature 'late', or 'vein', and 'cavity' mineral assemblages. The side-by-side arrangement of K-feldspar and albite varieties in Table 6.1 is meant to convey temporal association; this does not, however, guarantee spatial association, except where specifically stated.

General descriptions and distribution of 'primary' feldspar assemblages, as well as variations in crystal shape and size by zone, have been briefly covered in section 3.3. Volumetric compositions and common contaminants were discussed in chapter 5. This chapter [6: K-(Rb)-feldspars] and the following chapter [7: albite] are largely descriptive, and elaborate on the physical attributes and compositional ranges of the different feldspar types listed in Table 6.1.

## 6.1 Type 1: *blocky microcline-perthite* (10) (20) (40) (50) (60) (70) (80) (90)

Blocky microcline-perthite can be found in essentially every zone of the Tanco pegmatite. However, only samples collected from zones (10) (20) (40) (50) (60) (80) and (90) have yielded statistically meaningful analytical data. Type-1 feldspar is by far the most volumetrically significant K-feldspar type, comprising 22% of the pegmatite. Textural and chemical attributes do vary by zone; some of these are discussed below.

**Table 6.1:** Tanco feldspar types.

| K(Rb)-feldspar | Albite |
|---|---|
| **Type 1:** blocky microcline-perthite<br>(10) (20) (40) (50) (60) (70) (80) (90)<br><br>Blocky, grey-white-pink K-feldspar; dimensions up to 10 m x 1.5 m, locally club-shaped. | **Type A:** aplitic albite<br>(10) (20) (30) (40) (50) (60) (70) (80)<br><br>Very fine-grained, white-blue-purple; texture is variable from homogeneous to banded ('line rock') depending on abundance of accessory minerals.<br><br>**Type B:** cleavelandite<br>(10) (20) (40) (50) (60) (70) (80) (90)<br><br>White-grey, aggregates of parallel to radiating lamellae up to 10 cm long. |
| **Type 2:** granular non-perthitic microcline veins in (60)<br><br>Medium-grained, beige to pale-grey, non-perthitic microcline in veins 10 to 30 cm across. | |
| | **Type C:** saccharoidal albite (40) (50)<br><br>Very fine-grained aplitic albite, which displays metasomatized margins against neighboring lithologies. Locally replaces squi, K-feldspar. |
| **Type 3:** metasomatic microcline replacement veins in pollucite (80)<br><br>Beige to rusty, anastomosing veins of non-perthitic microcline (+/- lepidolite) in pollucite of zone (80); a few mm to 4 cm across. | **Type D:** metasomatic albite veins in pollucite (80)<br><br>white to dark-grey veins of albite in pollucite (80), X mm to 2 cm across |
| **Type 4:** adularian (K-Rb) feldspar metasomatic along vein-type-3 in pollucite (80)<br><br>Pure K-feldspar transitional to Rb-rich compositions and Rb-feldspar along margins of metasomatic microcline (type 3) replacing pollucite (80) and microcline; generally microscopic. | **Type E:** anhedral albite metasomatic along vein-type-3 in pollucite (80)<br><br>Associated with type-4 adularian (K-Rb) feldspar; generally microscopic. |
| **Type 5:** adularian (K>Rb) feldspar metasomatic clusters in pollucite (80)<br><br>Occurs as crystal aggregates comprised of anhedral to subhedral individuals (<1mm), within spherical clusters (1-3 mm in diameter). Clusters occur along contacts of sericitic veinlets in pollucite, and as apparently isolated spherical clusters within pollucite. | |
| **Type 6:** adularia crystals in leaching cavities (40),(50)<br><br>Euhedral (K>Rb)-adularia crystals in leaching cavities, locally with darker outer zone in BSE. Individual crystals are generally less than 1 mm across. | **Type F:** albite crystals in leaching cavities (40) (50)<br><br>Associated with type-6 adularia (40, 60). Individual crystals are significantly less than 1 mm across. |

**Note:** Order implies paragenetic sequence – see text for details. Types 1, A, and B are occasionally referred to as 'primary' in text, all other types fall under the general category, 'late'.

*Colour*

The majority of primary K-feldspar samples range in colour from pink, beige, or white to various shades of grey. Most samples from zone (10) and (20) are pink to light-grey. Zone (40) contains mostly white K-feldspar with subordinate pinks and greys. Zones (50), and (80) contain mostly white to grey feldspars with localized pink areas. Černý and Macek (1972) noted that many of the large K-feldspar crystals of zone (50) contained striped grey and white cores, grading into light-pink to beige rims. K-feldspar colours in zone (60) are more variable than in other zones: light-greys to beige is dominant, with lesser pinks; green altered-looking assemblages are also locally present. K-feldspar from zone (90) is grey-white, and locally lavender due to fine inclusions of lepidolite. Diffuse to brick red staining by Fe-hydroxides is locally extensive, particularly near wall-rock contacts with amphibolite.

*Crystal morphologies and structure*

Individual crystals are blocky in character, with two excellent planes of cleavage. There is an exceptional range of crystal sizes, from subhedral, mm-sized grains or aggregates found in matrix assemblages throughout the pegmatite, to giant crystals with dimensions in excess of 10 m x 1.5 m found mainly in zones (20) (40) and (50). In many cases, larger crystals form aggregate comb-like structures with orientations normal to major or local zone boundaries. Many of the large K-feldspar individuals form club-shaped crystals (Figure 6.1), with crystal-growth directions indicated by changes in girth from narrow to wide (Černý *et al.*, 1998).

**Figure 6.1** Club shaped crystal of blocky K-feldspar (left), and aplitic albite 'line-rock' (upper right) [zone (24)], both in matrix of albite, quartz and white-micas.

*Perthitic lamellae*

Most Type-1 K-feldspars at Tanco are perthitic, except for a small number of samples from zones (60) (80) and (90). Non-perthitic samples from zone (60) appear to be associated with alteration assemblages containing quartz, mica, feldspar and Ta/Nb mineralization. Most but not all non-perthitic samples from zone (90) contain lepidolite inclusions. Some non-perthitic to perthite-poor samples showed evidence of alteration, in the form of micropore development and fine micas or clays, +/- iron sulfide (Figure 6.2).

Vein (Figure 6.3) and patch (Figure 6.4) perthite were the most common intergrowths observed; film (string) perthite was observed occasionally (Figure 6.5). Two morphological varieties of 'patch' albite are observed: i) large subrounded blebs overprinted on poorly defined irregular vein perthite, and ii) discreet rounded to angular grains dispersed randomly throughout the K-feldspar phase. Although patch perthite is observed in all zones, it is more commonly observed in samples collected from inner zones, and in samples with obvious signs of alteration.

The average size of perthitic lamellae is variable by zone, with a notable decrease in the volume of albite from outer to inner zones (Table 6.2). The best-formed vein perthite occurs in zones (10) and (20) with average albite lamellae widths of approximately 100 μm and a relative albite/K-feldspar width ratio of 0.17. This ratio steadily decreases from outer to inner zones; zone (60) has a ratio of only 0.04. Perthitic samples from zones (80) and (90) appear to contain only irregular, patchy, fine- to micro-vein perthite.


**Figure 6.2** Alteration of microcline from zone (80). Note distinct boundary between unaltered K-feldspar (top-left) and altered perthite (bottom-right). Irregular black albite lamellae persists in both volumes. Visible features in altered volume include micropores (small circular specks), pyrite, and Cl, F, Na, K-rich micas or clays (sub-rounded bright specks).

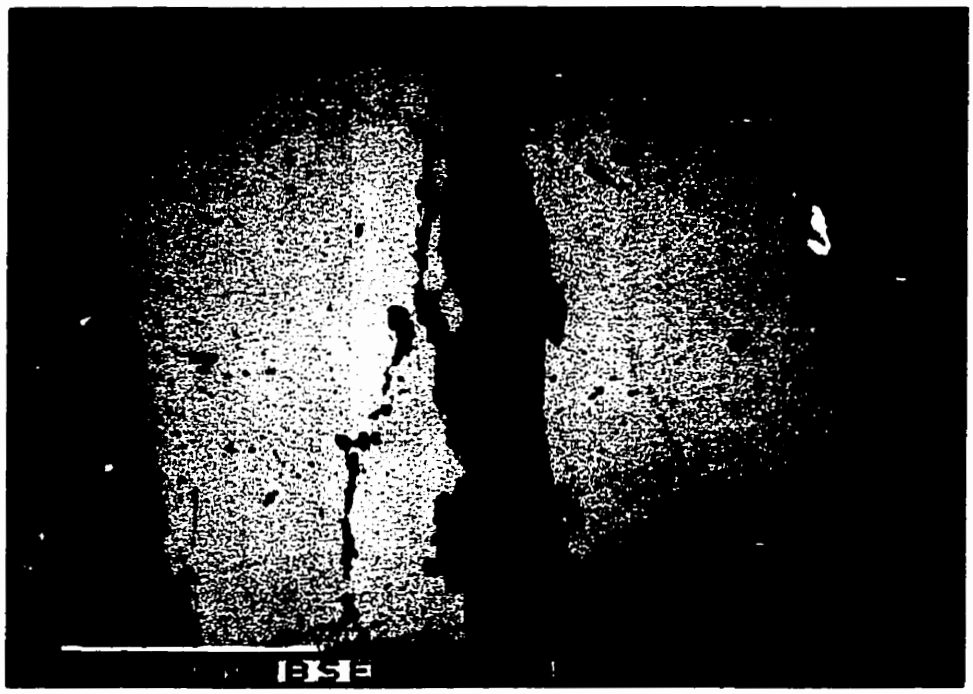


**Figure 6.3** Coarse vein albite in microcline-perthite from zone (20).

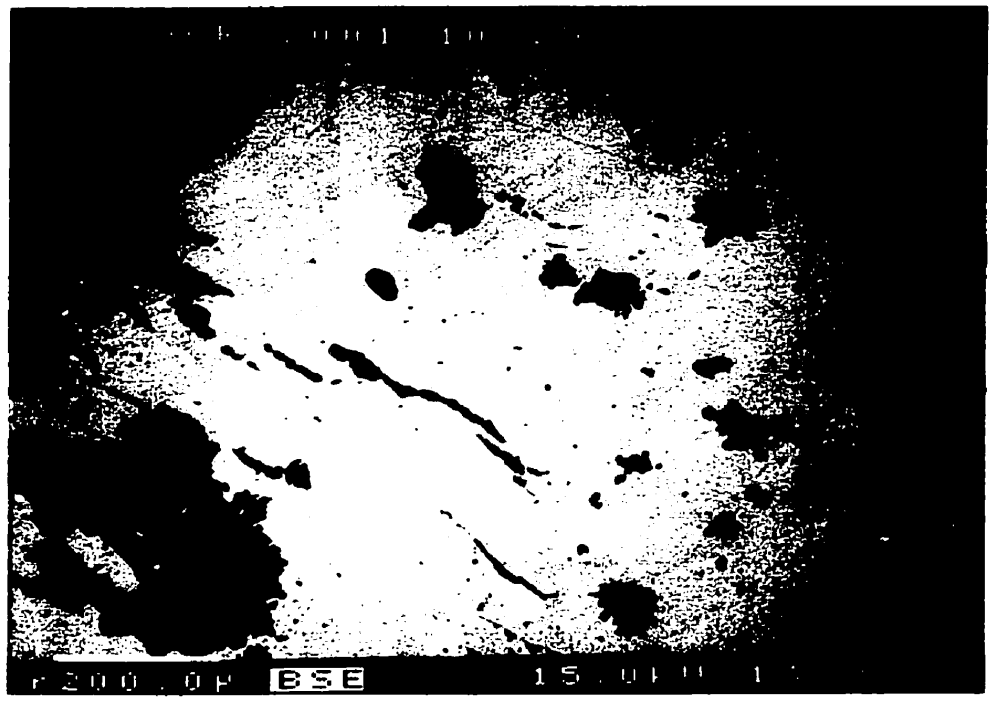


**Figure 6.4** Fine and coarse albite patches in microcline from zone (80). Heterogeneous BSE intensity in K-feldspar reflects variable Rb content.

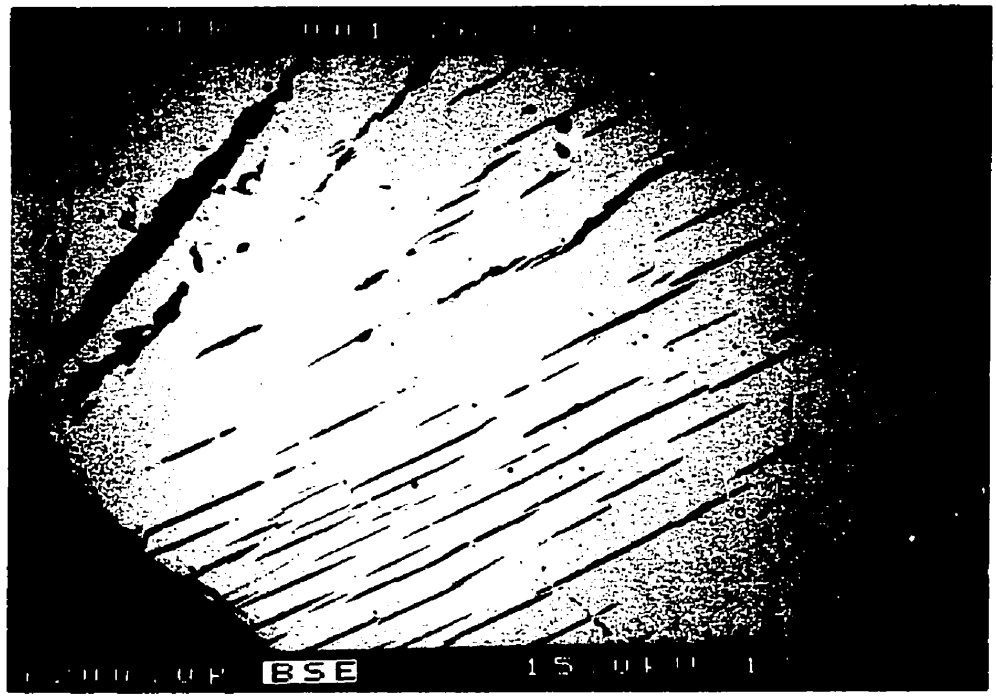


**Figure 6.5** Different orientations of string albite (fine black streaks) and vein albite (coarse black veinlets) in microcline-perthite from zone (40).

**Table 6.2:** Average size and relative volume of albite lamellae in type-1 perthite

| Zone | albite lamellae average width (μm) | Kspar host average width (μm) | relative width albite/Kspar |
|---|---|---|---|
| 20 | 100 | 600 | 0.17 |
| 50 | 3 | 30 | 0.10 |
| 60 | 5 | 120 | 0.04 |
| 80 | patch | | - |

*Graphic K-feldspar and quartz*

Reported occurrences of graphic intergrowths of K-feldspar and quartz are extremely rare at Tanco. Only one graphic sample (94-10-B) is noted from the present data set (see Appendix III). The sample was collected from drill core which intersected the hangingwall part of zone (20) in the far SW corner of the pegmatite (Figure 3.4). Other rare examples have been reported from eastern (southeastern?) regions of the pegmatite (P. Černý, personal comm., 2001).

*Chemical composition*

Representative compositions of blocky K-feldspar of individual zones, including atomic contents and crystal-chemical data, are summarized in Table 6.3. A complete listing of EMPA-determined compositions is given in Appendix III, and of the results of wet-chemical analyses in Appendix V. As noted in chapter 5 and Appendix I, EMPA-determined contents for Fe, Pb, Mg, Ca, and F were consistently below detection. Subsequent analytical data listings and discussions of all K-feldspar types will be limited to the following suite of elements: Li, Na, K, Rb, Cs, Tl, Be, Sr, Ba, Al, Ga, B, Si and P. Histograms of select oxide contents are presented in Figures 6.6a-e. Average compositions by zone are presented for wet-analyzed data in Figures 6.7a-e, and for EMPA-determined data in Figures 6.8a-c. Corresponding statistics for $P_2O_5$, $Li_2O$, $Rb_2O$,

$Cs_2O$, and $Tl_2O$, including maxima, minima, averages and 1-sigma variations by zone, are listed in Tables 6.4 and 6.5.

Lithium contents range from a minimum of 25 ppm to a maximum of 1600 ppm (0.005 - 0.191 wt% $Li_2O$). The frequency distribution (Figure 6.6b) is skewed heavily towards low Li contents with a maximum frequency peak between 0.02 and 0.04 wt% $Li_2O$. In terms of average compositions by zone (Figure 6.7b), Li attains a distinct maximum in zone (50) with an average value of 0.095 wt% $Li_2O$. The large associated standard error for this average results from a bimodal distribution of Li contents of samples from zone (50). The group of above average Li values consists of 5 data points, all greater than 0.16 wt% $Li_2O$, with one composition as high as 0.191 wt%. Note, however, that the SIMS data for Li (Table 6.6) are on average lower than those determined by ICP.

Rubidium contents (EMPA) range from 0.73 to 3.19 wt% $Rb_2O$. The $Rb_2O$ histogram (Figure 6.6c) indicates a bimodal distribution with maximum frequencies between 1.00 and 1.50, and 2.25 and 2.50 wt% $Rb_2O$.

**Table 6.3:** Representative compositions (wt%) and formula (apfu) of blocky K-feldspar (Type 1) (EMPA data)

| Sample | SLE-18 | 94-10-B | C-045-Q | 10-25-3a | C-S | 10-25-2 | 12-15-21 |
|---|---|---|---|---|---|---|---|
| Zone | (12) | (20) | (40) | (50) | (60) | (80) | (90) |
| P2O5 | 0.22 | 0.36 | 0.45 | 0.46 | 0.34 | 0.43 | 0.30 |
| SIO2 | 64.02 | 63.65 | 63.66 | 62.71 | 63.20 | 62.40 | 62.95 |
| AL2O3 | 18.37 | 18.44 | 18.55 | 18.81 | 18.38 | 18.36 | 18.57 |
| MGO | 0.00 | 0.00 | 0.00 | 0.00 | 0.00 | 0.00 | 0.00 |
| CAO | 0.00 | 0.00 | 0.00 | 0.00 | 0.00 | 0.00 | 0.00 |
| MNO | 0.00 | 0.00 | 0.01 | 0.00 | 0.01 | 0.01 | 0.01 |
| FE2O3 | 0.00 | 0.00 | 0.02 | 0.01 | 0.00 | 0.00 | 0.02 |
| SRO | 0.02 | 0.03 | 0.03 | 0.02 | 0.02 | 0.04 | 0.04 |
| BAO | 0.03 | 0.03 | 0.01 | 0.01 | 0.01 | 0.03 | 0.01 |
| PBO | 0.02 | 0.00 | 0.01 | 0.01 | 0.00 | 0.00 | 0.00 |
| NA2O | 0.19 | 0.37 | 0.32 | 0.25 | 0.28 | 0.25 | 0.25 |
| K2O | 15.87 | 15.57 | 15.34 | 15.27 | 14.96 | 14.87 | 15.23 |
| RB2O | 1.56 | 1.49 | 2.24 | 2.23 | 2.51 | 2.50 | 2.51 |
| CS2O | 0.06 | 0.04 | 0.11 | 0.09 | 0.33 | 0.33 | 0.33 |
| TOTAL | 100.37 | 99.99 | 100.74 | 99.87 | 100.05 | 99.19 | 100.24 |
| P5+ | 0.009 | 0.014 | 0.018 | 0.018 | 0.014 | 0.017 | 0.012 |
| SI4+ | 2.980 | 2.969 | 2.962 | 2.944 | 2.969 | 2.958 | 2.958 |
| AL3+ | 1.008 | 1.014 | 1.017 | 1.041 | 1.017 | 1.026 | 1.028 |
| MG2+ | 0.000 | 0.000 | 0.000 | 0.000 | 0.000 | 0.000 | 0.000 |
| CA2+ | 0.000 | 0.000 | 0.000 | 0.000 | 0.000 | 0.000 | 0.000 |
| MN2+ | 0.000 | 0.000 | 0.000 | 0.000 | 0.000 | 0.000 | 0.000 |
| FE3+ | 0.000 | 0.000 | 0.001 | 0.000 | 0.000 | 0.000 | 0.001 |
| SR2+ | 0.001 | 0.001 | 0.001 | 0.001 | 0.000 | 0.001 | 0.001 |
| BA2+ | 0.000 | 0.000 | 0.000 | 0.000 | 0.000 | 0.001 | 0.000 |
| PB2+ | 0.000 | 0.000 | 0.000 | 0.000 | 0.000 | 0.000 | 0.000 |
| NA+ | 0.017 | 0.033 | 0.029 | 0.023 | 0.026 | 0.023 | 0.023 |
| K+ | 0.943 | 0.927 | 0.911 | 0.915 | 0.897 | 0.900 | 0.913 |
| RB+ | 0.047 | 0.045 | 0.067 | 0.067 | 0.076 | 0.076 | 0.076 |
| CS+ | 0.001 | 0.001 | 0.002 | 0.002 | 0.007 | 0.007 | 0.006 |
| $\Sigma T$ | 3.997 | 3.997 | 3.997 | 4.003 | 3.999 | 4.000 | 3.998 |
| $TO_2$ | 0.999 | 1.000 | 1.000 | 1.023 | 1.003 | 1.009 | 1.017 |
| Si+2P/Al-P | 3.001 | 2.997 | 2.996 | 2.913 | 2.986 | 2.966 | 2.932 |
| $\Sigma M$ | 1.008 | 1.005 | 1.008 | 1.007 | 1.005 | 1.005 | 1.018 |
| $M+$ | 1.011 | 1.008 | 1.010 | 1.009 | 1.006 | 1.008 | 1.021 |
| $M^*$ | 0.012 | 0.008 | 0.010 | -0.014 | 0.003 | -0.001 | 0.004 |

-values listed represent averages of 3-6 data points each
-atomic contents normalized to 8 oxygens

**Table 6.4:** Blocky K-feldspar (Type 1) statistics for selected elements by zone
(wet chemistry data in wt%)

**P2O5**

| Zone | (10) | (20) | (40) | (50) | (60) | (80) | (90) |
|---|---|---|---|---|---|---|---|
| n | 8 | 38 | 29 | 17 | 14 | 3 | 5 |
| max | 0.39 | 0.64 | 0.76 | 0.62 | 0.51 | 0.49 | 0.43 |
| min | 0.24 | 0.14 | 0.19 | 0.18 | 0.08 | 0.47 | 0.29 |
| average | 0.34 | 0.40 | 0.47 | 0.47 | 0.36 | 0.48 | 0.38 |
| 1σ | 0.06 | 0.08 | 0.12 | 0.12 | 0.12 | 0.01 | 0.05 |

**Li2O**

| Zone | (10) | (20) | (40) | (50) | (60) | (80) | (90) |
|---|---|---|---|---|---|---|---|
| n | 8 | 38 | 29 | 17 | 14 | 3 | 5 |
| max | 0.022 | 0.067 | 0.101 | 0.191 | 0.076 | 0.068 | 0.094 |
| min | 0.009 | 0.005 | 0.024 | 0.019 | 0.023 | 0.028 | 0.028 |
| average | 0.014 | 0.032 | 0.048 | 0.095 | 0.050 | 0.048 | 0.059 |
| 1σ | 0.005 | 0.013 | 0.020 | 0.056 | 0.016 | 0.028 | 0.032 |

**Rb2O**

| Zone | (10) | (20) | (40) | (50) | (60) | (80) | (90) |
|---|---|---|---|---|---|---|---|
| n | 8 | 38 | 29 | 17 | 14 | 3 | 5 |
| max | 2.11 | 2.19 | 3.10 | 3.28 | 3.79 | 3.43 | 3.37 |
| min | 1.12 | 0.75 | 0.94 | 1.30 | 1.89 | 2.87 | 1.51 |
| average | 1.60 | 1.45 | 2.01 | 2.06 | 2.66 | 3.15 | 2.64 |
| 1σ | 0.31 | 0.41 | 0.64 | 0.47 | 0.47 | 0.40 | 0.69 |

**Cs2O**

| Zone | (10) | (20) | (40) | (50) | (60) | (80) | (90) |
|---|---|---|---|---|---|---|---|
| n | 8 | 38 | 29 | 17 | 14 | 3 | 5 |
| max | 0.17 | 0.20 | 0.30 | 0.24 | 0.38 | 0.30 | 0.44 |
| min | 0.07 | 0.04 | 0.06 | 0.09 | 0.17 | 0.26 | 0.07 |
| average | 0.11 | 0.11 | 0.15 | 0.14 | 0.27 | 0.28 | 0.25 |
| 1σ | 0.04 | 0.04 | 0.07 | 0.03 | 0.06 | 0.03 | 0.13 |

**Tl2O**

| Zone | (10) | (20) | (40) | (50) | (60) | (80) |
|---|---|---|---|---|---|---|
| n | 1 | 20 | 7 | 14 | 9 | 3 |
| max | | 0.017 | 0.016 | 0.033 | 0.031 | 0.014 |
| min | | 0.006 | 0.009 | 0.016 | 0.015 | 0.011 |
| average | 0.011 | 0.012 | 0.012 | 0.025 | 0.020 | 0.012 |
| 1σ | | 0.003 | 0.003 | 0.006 | 0.005 | 0.002 |

**Table 6.5:** Blocky K-feldspar (Type 1) statistics for selected elements by zone
(EMPA data in wt%)

**P2O5**

| Zone | (10) | (20) | (40) | (50) | (60) | (80) | (90) |
|---|---|---|---|---|---|---|---|
| n | 10 | 15 | 12 | 12 | 9 | 3 | 7 |
| max | 0.47 | 0.54 | 0.57 | 0.53 | 0.43 | 0.45 | 0.38 |
| min | 0.18 | 0.08 | 0.33 | 0.29 | 0.19 | 0.03 | 0.10 |
| average | 0.29 | 0.34 | 0.45 | 0.45 | 0.31 | 0.30 | 0.28 |
| 1σ | 0.10 | 0.10 | 0.09 | 0.09 | 0.07 | 0.24 | 0.11 |

**Rb2O**

| Zone | (10) | (20) | (40) | (50) | (60) | (80) | (90) |
|---|---|---|---|---|---|---|---|
| n | 10 | 15 | 12 | 12 | 9 | 3 | 7 |
| max | 2.65 | 2.54 | 2.90 | 3.19 | 2.73 | 2.92 | 2.83 |
| min | 1.25 | 0.73 | 1.04 | 1.64 | 2.21 | 2.36 | 1.46 |
| average | 1.69 | 1.48 | 2.13 | 2.22 | 2.47 | 2.59 | 2.42 |
| 1σ | 0.47 | 0.59 | 0.61 | 0.48 | 0.16 | 0.29 | 0.45 |

**Cs2O**

| Zone | (10) | (20) | (40) | (50) | (60) | (80) | (90) |
|---|---|---|---|---|---|---|---|
| n | 10 | 15 | 12 | 12 | 9 | 3 | 7 |
| max | 0.33 | 0.16 | 0.30 | 0.22 | 0.37 | 0.34 | 0.35 |
| min | 0.02 | 0.00 | 0.01 | 0.05 | 0.24 | 0.14 | 0.04 |
| average | 0.10 | 0.05 | 0.10 | 0.11 | 0.30 | 0.27 | 0.24 |
| 1σ | 0.09 | 0.05 | 0.08 | 0.05 | 0.04 | 0.11 | 0.12 |

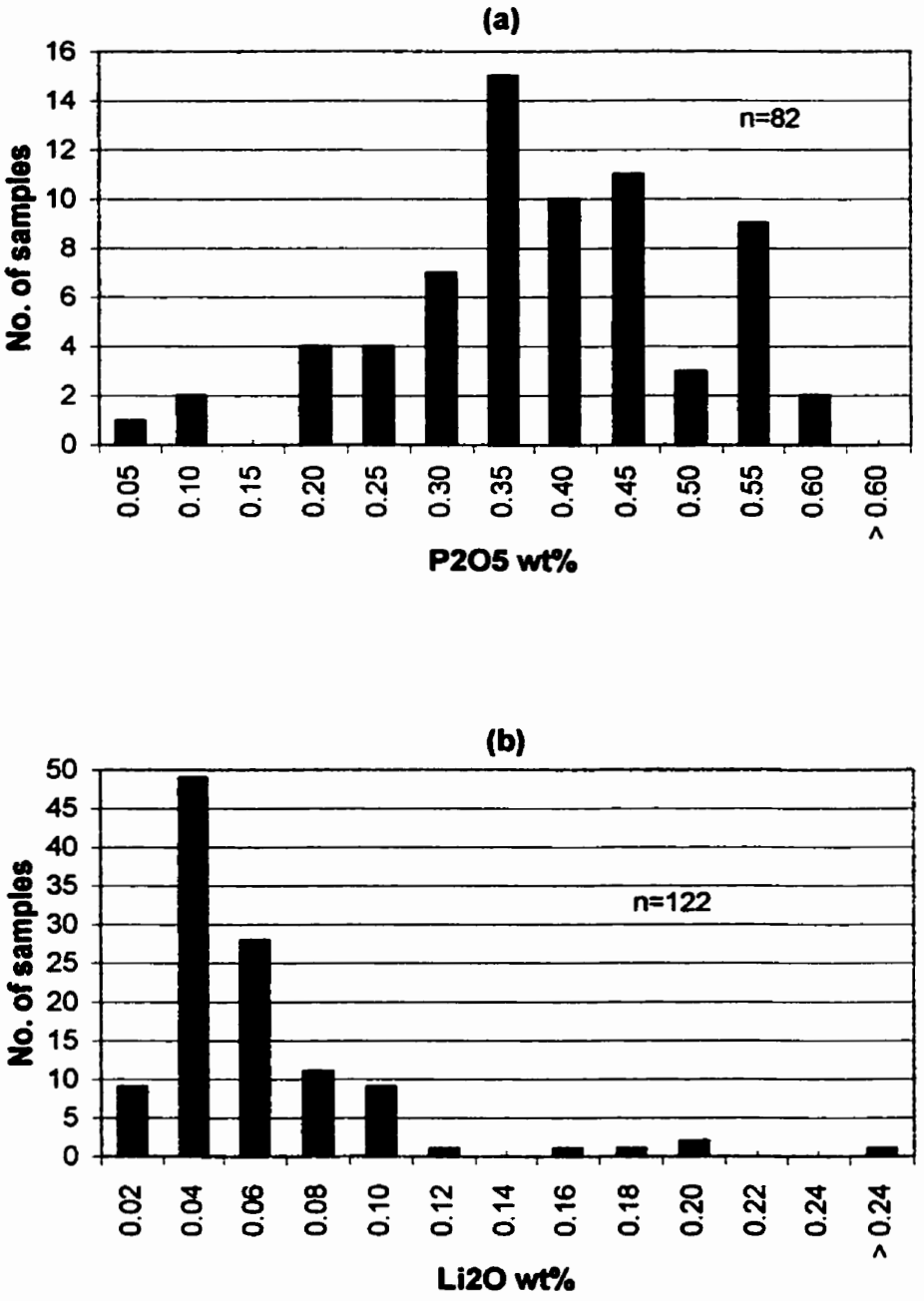


**Figure 6.6** Blocky K-feldspar (Type 1) histograms for selected elements. (a) EMPA data; (b) wet chemistry data

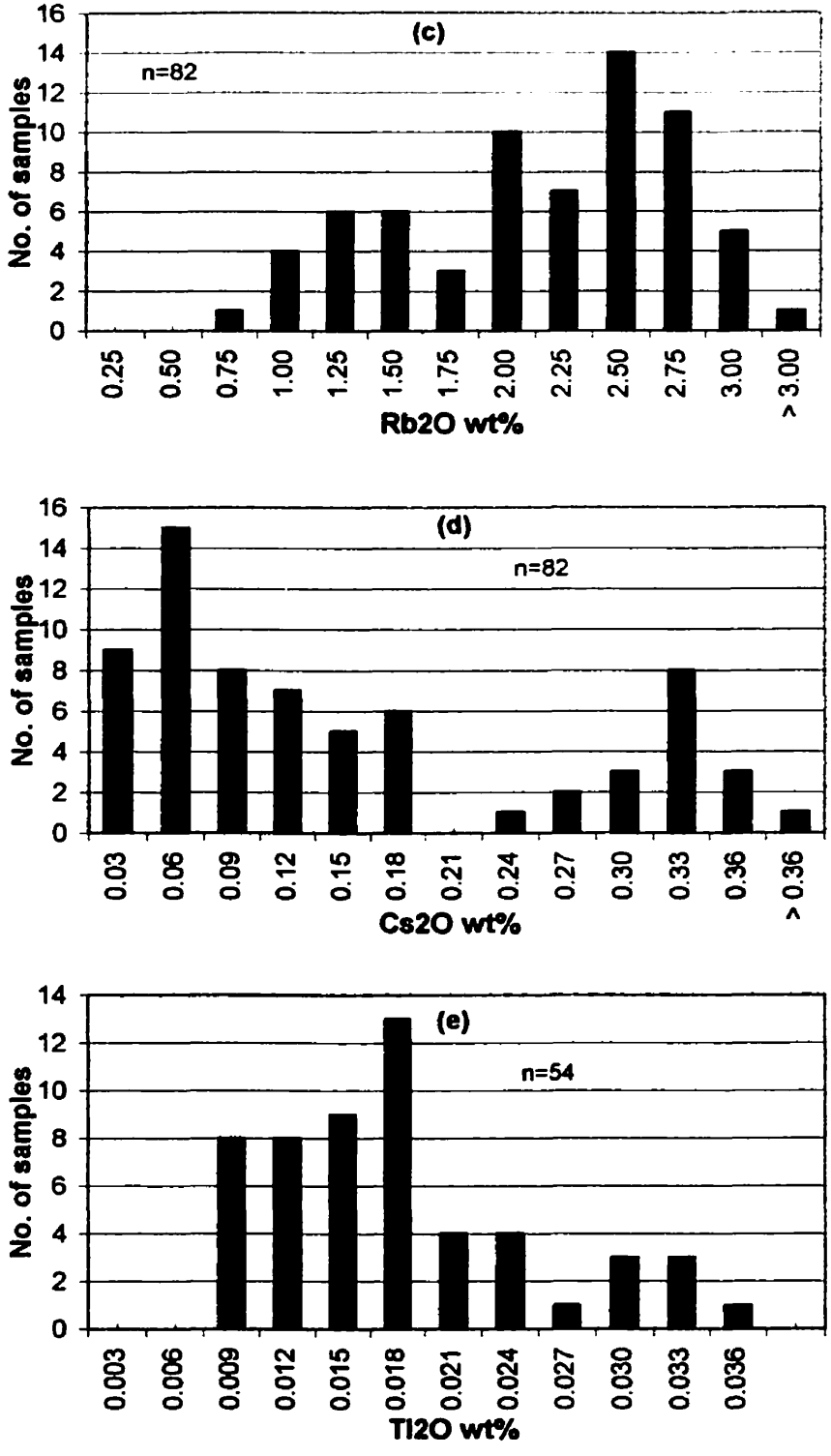


**Figure 6.6** Blocky K-feldspar (Type 1) histograms for selected elements. (c) & (d) EMPA data; (e) wet chemistry data

Cesium also has a distinct bimodal distribution (Figure 6.6d). The full range of data includes a minimum of 0.04 wt% up to a maximum of 0.38% $Cs_2O$, with a low-value maximum frequency between 0.03 and 0.06 wt% and a high-value maximum frequency between 0.30 and 0.33 wt%. There is a distinct paucity of $Cs_2O$ compositions between 0.18 and 0.21 wt%.

As expected, Rb and Cs (Figures 6.7c,d; Figures 6.8b,c) exhibit analogous average trends by zone, with generally increasing compositions from outer to inner zones. On average, $Rb_2O$ is approximately 10x more abundant than $Cs_2O$. Despite the general upward trends in Figures 6.7c,d and Figures 6.8b,c, a few notable irregularities are apparent in the results of both wet-chemical and EMP analyses. For both elements, zone (10) has a higher average composition than zone (20). The same trend reversal is apparent between zones (80) and (90). Between zones (20) and (80), $Rb_2O$ increases at a relatively constant rate, whereas the rate increase for $Cs_2O$ is more irregular, especially considering the steep increase between zones (50) and (60).

A plot of $K_2O$ *vs.* $Rb_2O$ (Figure 6.9a) indicates a relatively tight inverse correlation ($R^2$= -0.88), with $K_2O$ varying from 14.50 to 16.04 wt% and a concomitant variation in $Rb_2O$ from 3.19 to 0.73 wt%. Despite the broad spread of data points from individual zones along the trend in Figure 6.9a, sample points from outer zones tend to group towards the upper left of the diagram (low Rb), whereas sample points from inner zones tend to cluster towards the bottom right (high Rb). The relation between $K_2O$ and $Cs_2O$ (Figure 6.9b) is more complex. There are two distinct fields of data points; the first consists of a linear trend of samples mainly from zones (10) (20) (40) and (50), with $Cs_2O$ contents varying between 0.00 to 0.22 wt%. The second field, which is non-linear, is shifted significantly to the right of the first field, and includes samples with elevated $Cs_2O$

contents between 0.25 to 0.38 wt%. These samples are mostly from zones (60) (80) and (90). In general, there is a positive correlation between $Rb_2O$ and $Cs_2O$ (Figure 6.9c) and a similar bimodal distribution of sample points as in Figure 6.9b. For whatever reason, the uptake of Rb into the K-feldspar structure, appears to taper off above 2.5 wt% $Rb_2O$, whereas the relative rate of Cs uptake seems to increase.

Thallium values range from 0.006 to 0.033 wt% $Tl_2O$ (Table 6.4), with a more-or-less uni-modal distribution containing a maximum frequency between 0.015 and 0.018 (Figure 6.6e). Average contents per zone (Figure 6.7e) rise and then fall in zonal succession, with a distinct maximum average of 0.025 wt% $Tl_2O$ attained in zone (50).

The contents of Be are very low, and range from 0.1 to 5.8 ppm (Table 6.6)

Strontium shows a good positive correlation with Rb (Figure 6.10), which contradicts the normal fractionation process in granitic rocks. Calculation of radiogenic $^{87}Sr$ generated by $^{87}Rb$ in the Tanco K-feldspar since the consolidation of the pegmatite 2.64 Ga ago (Baadsgaard and Černý, 1993) yields a reference line which indicates that all present-day Sr in the Tanco feldspars in radiogenic, and in most cases some of it was lost (Figure 6.10). This is in agreement with the results of isotopic analysis of a few selected samples by Clarke and Černý (1987).

Barium contents are relatively low with only 11% of individual point analyses exceeding the EMPA limit of detection of 0.087 wt% BaO. Sample values range between 0.00 and 0.09 wt%. Averages by zone are consistently close to 0.006 wt% BaO.

Gallium shows a slight increase from 31 to 116 ppm with Al, with an apparently random scatter and overlap of data from original zones (see Figure 8.1q). However, zonal averages show a modest increase in Ga from zone (10) to zone (60) (0.009 to 0.012 wt% $Ga_2O_3$) in the Ecole Polytechnique data set (Figure 6.7f), relatively closely paralleled, and extended to zones (80) and (90) by the present data (Figure 6.7f).

Boron is present in very low concentrations varying from 1.0 to 10.2 ppm (Table 6.6). This is in remarkable contrast to the B content of Tanco micas (Margison, 2001).

The distribution of $P_2O_5$ contents (Figure 6.6a) is Gaussian, with a frequency peak between 0.30 and 0.35 wt% $P_2O_5$. Individual P contents (EMPA) attain values up to 0.57 wt% $P_2O_5$, with 99% of EMP analyses above the detection limit of 0.073 wt%, and 76% of analyses with more than 0.30 wt% $P_2O_5$. Average phosphorus contents by zone (Figures 6.7a, 6.8a) attain a maximum of about 0.45 wt% $P_2O_5$ in zones (40) and (50) and minimum EMPA-determined average values of 0.29 and 0.28 wt% in zones (10) and (90) respectively.

*$Na_2O$ and trace-element distributions in perthite*

Average bulk $Na_2O$ content (Figure 6.11a) decreases steadily from 2.5 to 1.0 wt% from zone (10) to (80). This is in agreement with the observed decrease in volume of albite lamellae from outer to inner zones (Table 6.2). Average $Na_2O$ contents determined by EMPA are significantly lower than wet-chemical values (Figure 6.11b,c). They also are more uniform, but still vary systematically from a high of 0.36 wt% in zone (20) to a low of 0.21 wt% in zone (80).

**Table 6.6:** Individual K(Rb)-feldspar (Type 1,2,4,6) SIMS analyses.

| Sample | grain | Zone | Type | Li (ppm wt) | B (ppm wt) | Be (ppm wt) |
|---|---|---|---|---|---|---|
| 94-10-R | R2 | 10 | 1 | 52 | 6.0 | 5.4 |
| 94-10-R | R1 | 10 | 1 | 47 | | 5.6 |
| 78-21-H | H-2 | 20 | 1 | 70 | 5.0 | 4.9 |
| 78-21-H | H-1 | 20 | 1 | 104 | 3.7 | 5.8 |
| C-045-Q | Q2 | 40 | 1 | 73 | 8.0 | 2.8 |
| C-045-Q | Q1 | 40 | 1 | 102 | 6.0 | 3.9 |
| 94-10-G | G2 | 50 | 1 | 116 | 5.2 | 3.7 |
| 94-10-G | G1 | 50 | 1 | 94 | 5.0 | 3.5 |
| C-090-J | J-2 | 60 | 1 | 101 | 10.2 | 2.3 |
| C-090-J | J-1 | 60 | 1 | 144 | 4.4 | 1.9 |
| 10-25-1 | 1-2 | 80 | 1 | 203 | 7.6 | 3.2 |
| 10-25-1 | 1.1 | 80 | 1 | 214 | 7.3 | 3.0 |
| 12-15-10 | 10-2 | 90 | 1 | 46 | 0.98 | 0.07 |
| 12-15-10 | 10-1 | 90 | 1 | 37 | 1.3 | 0.06 |
| | | max | | 214 | 10.2 | 5.8 |
| | | min | | 37 | 1.0 | 0.1 |
| | | **average** | | **100** | **5.4** | **3.3** |
| | | 1σ | | 55 | 2.6 | 1.8 |
| L-M-1 | 1-2 | 60 | 2 | 53 | 1.65 | 0.46 |
| L-M-1 | 1-1 | 60 | 2 | 49 | 3.7 | 0.19 |
| Poll-6A | 1 | 80 | 4 | 56 | 3.34 | 0.37 |
| Poll-6-A | 2 | 80 | 4 | 50 | 1.8 | 0.18 |
| A-10 | A-10-2 | 80 | 4 | 175 | 8.0 | 0.26 |
| A-10 | A-10-1 | 80 | 4 | 160 | 5.73 | 0.06 |
| ADPV-1 | 1-2 | 50 | 6 | 1.9 | 2.52 | 0.21 |
| ADPV-1 | 1-1 | 50 | 6 | 7.2 | 2.44 | 0.04 |

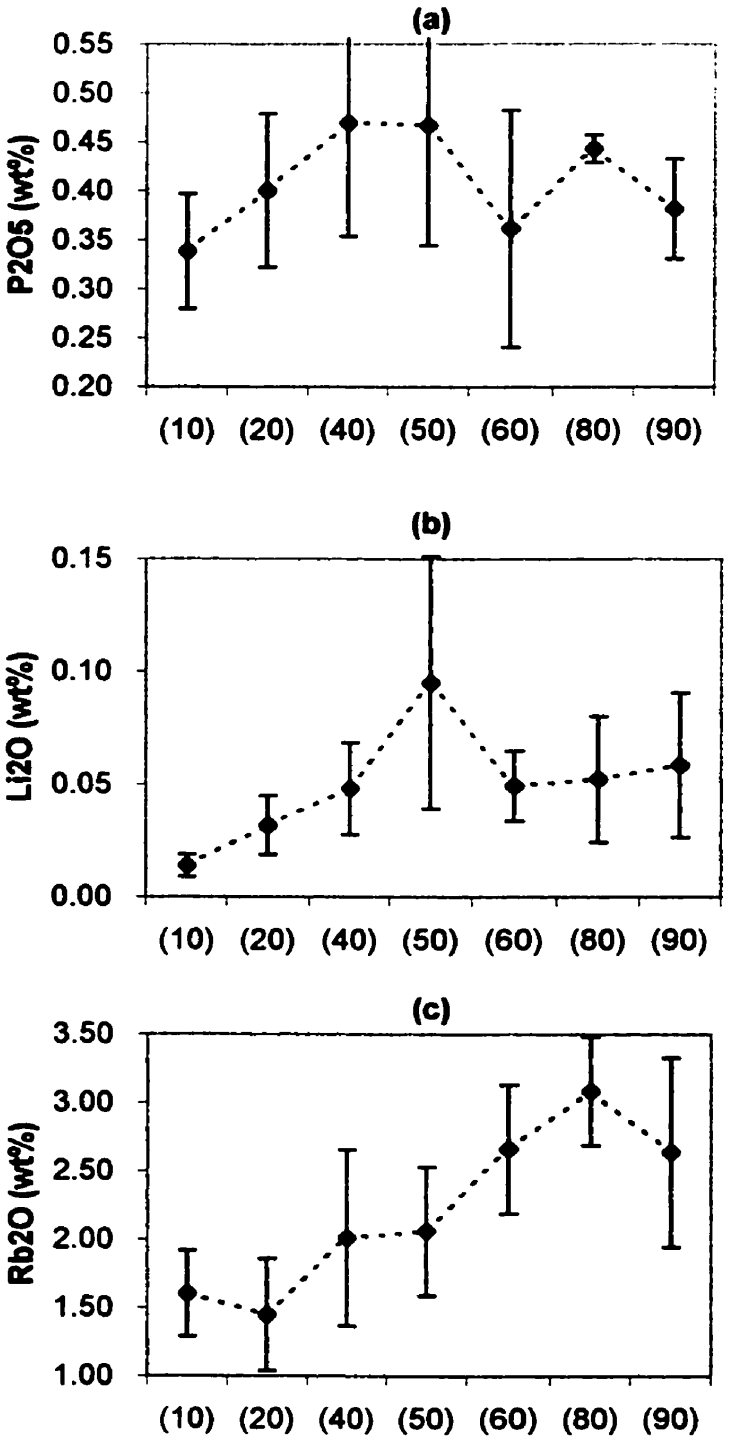


**Figure 6.7** Average oxide contents per zone (wet-chemistry data) Bars represent 1σ deviations.

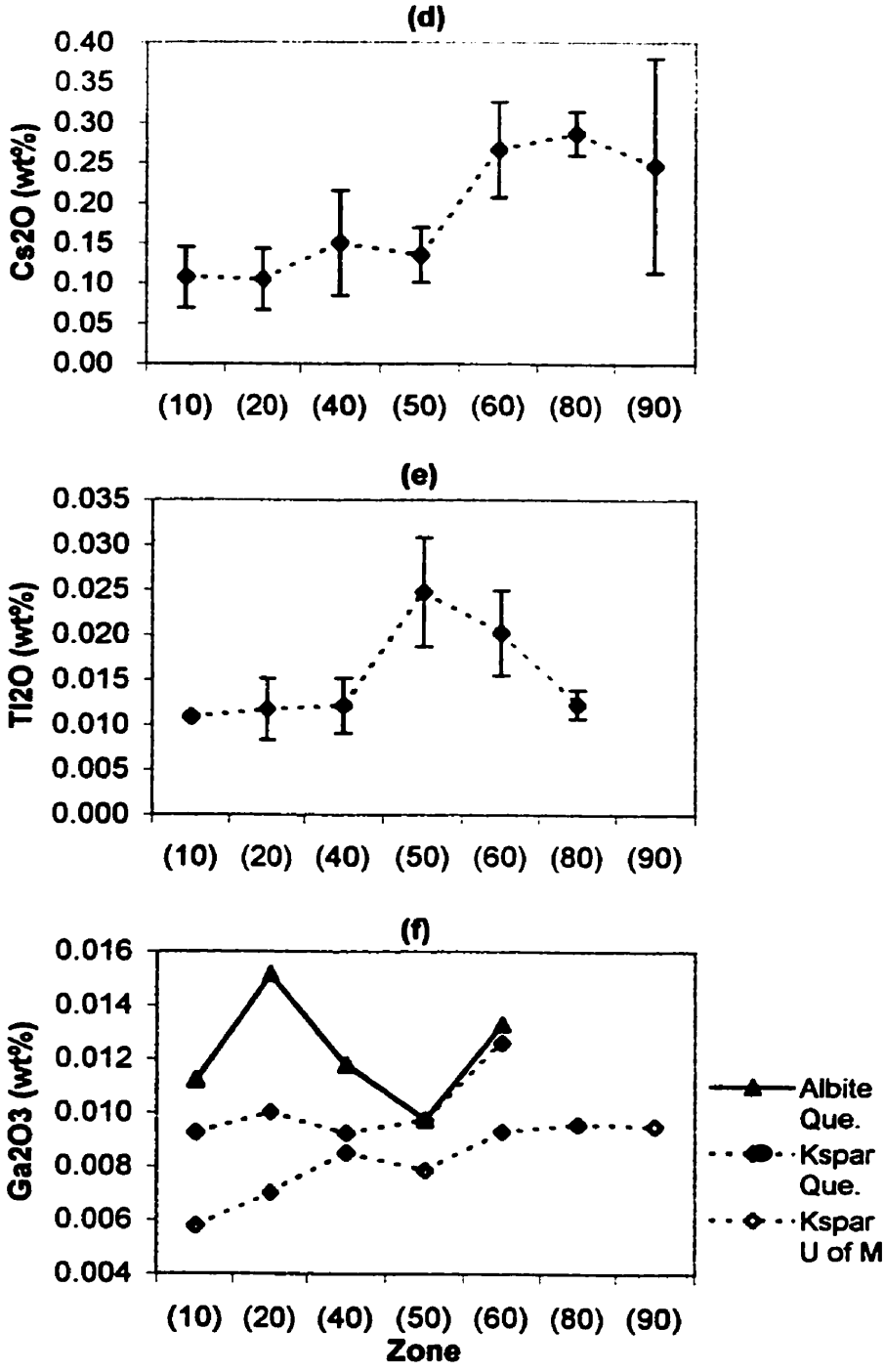


**Figure 6.7** Average oxide contents per zone (wet-chemistry data). Bars represent 1σ deviations. (f) Comparison of albite and K-feldspar Ga2O3 contents analyzed at Ecole Polytechnique, Montreal, Que. to Keldspar contents determined at the University of Manitoba (this study).

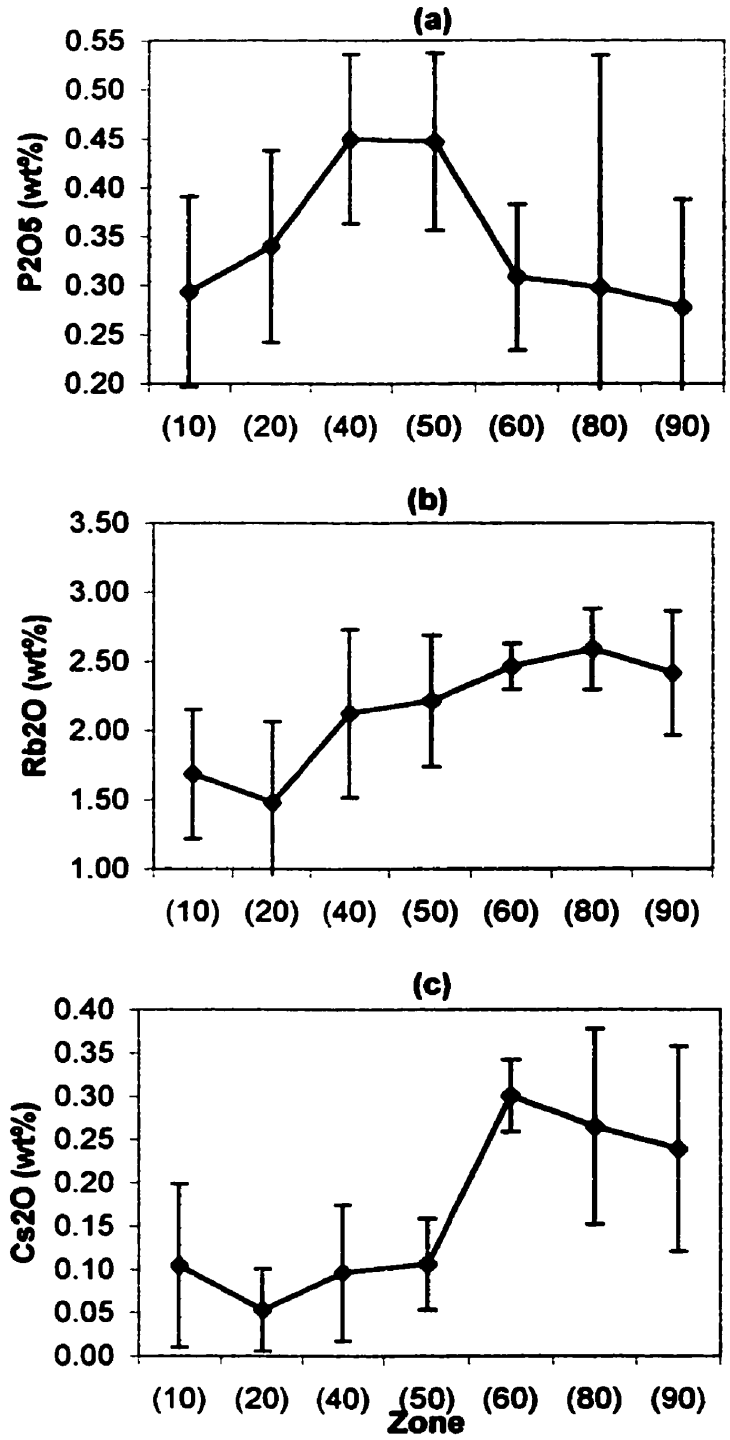


**Figure 6.8** Average oxide contents per zone (EMPA data) Bars represent 1σ deviations.

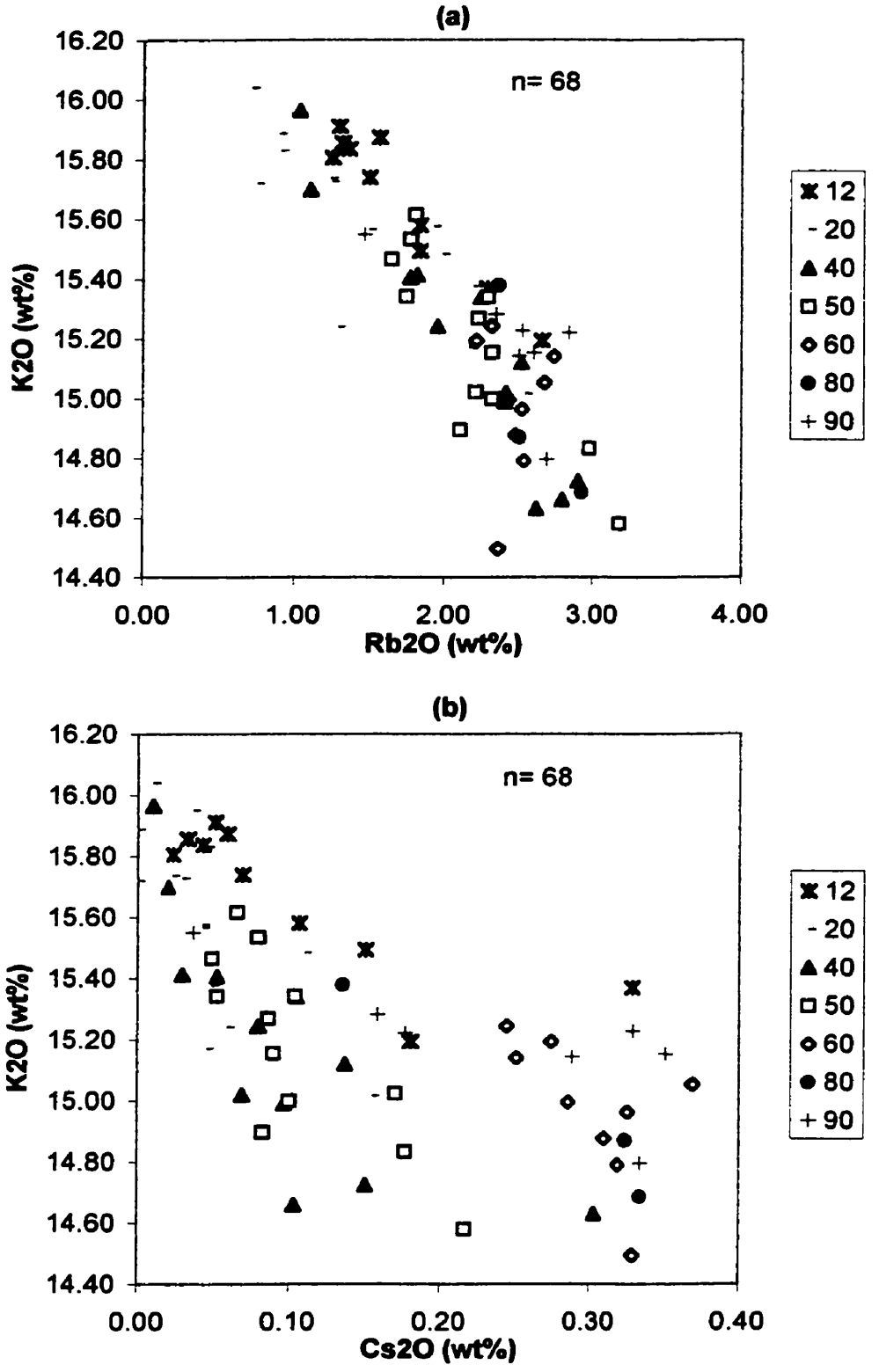


**Figure 6.9** K-feldspar (Type 1): EMPA-determined oxide contents per zone

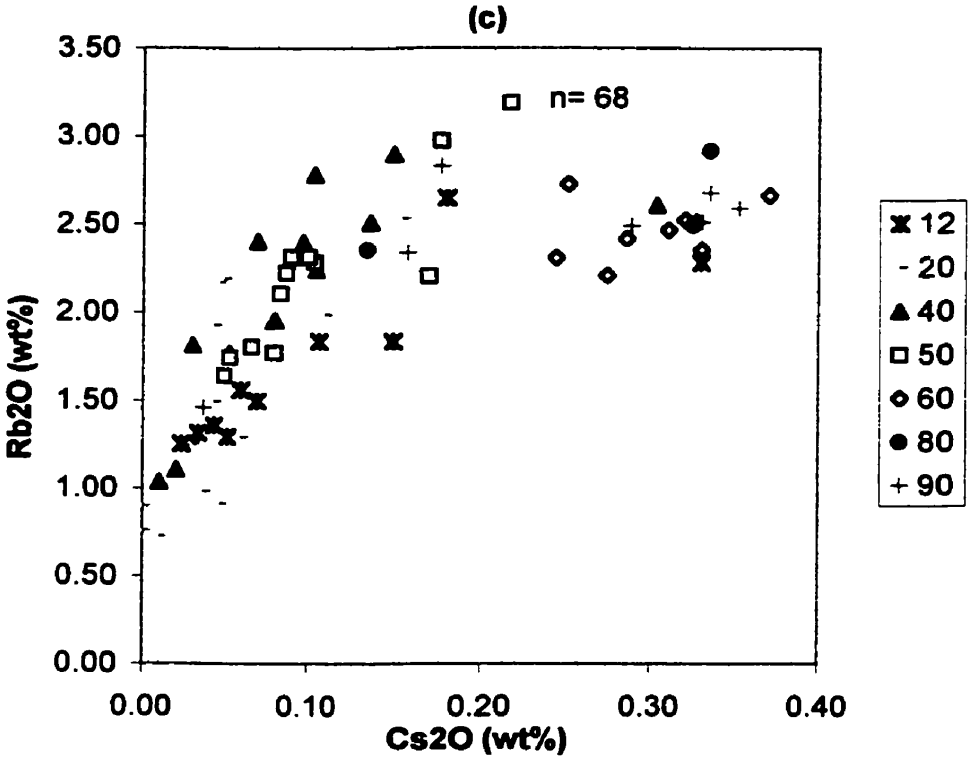


**Figure 6.9** K-feldspar (Type 1): EMPA-determined oxide contents per zone

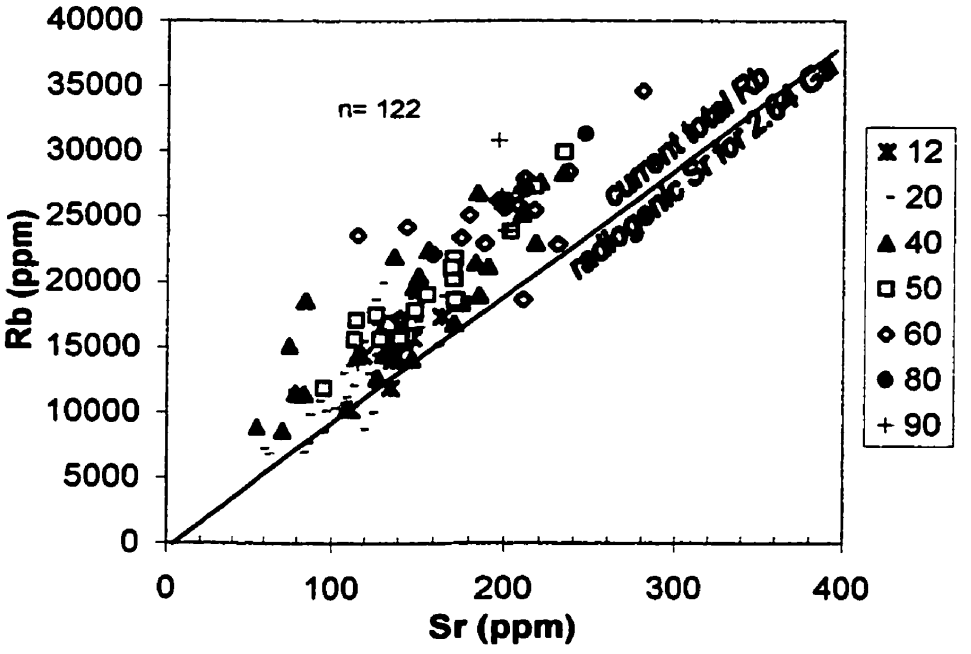


**Figure 6.10** K-feldspar (Type 1 - wet-chemistry). Rb-Sr plot indicating the radiogenic origin of Sr.

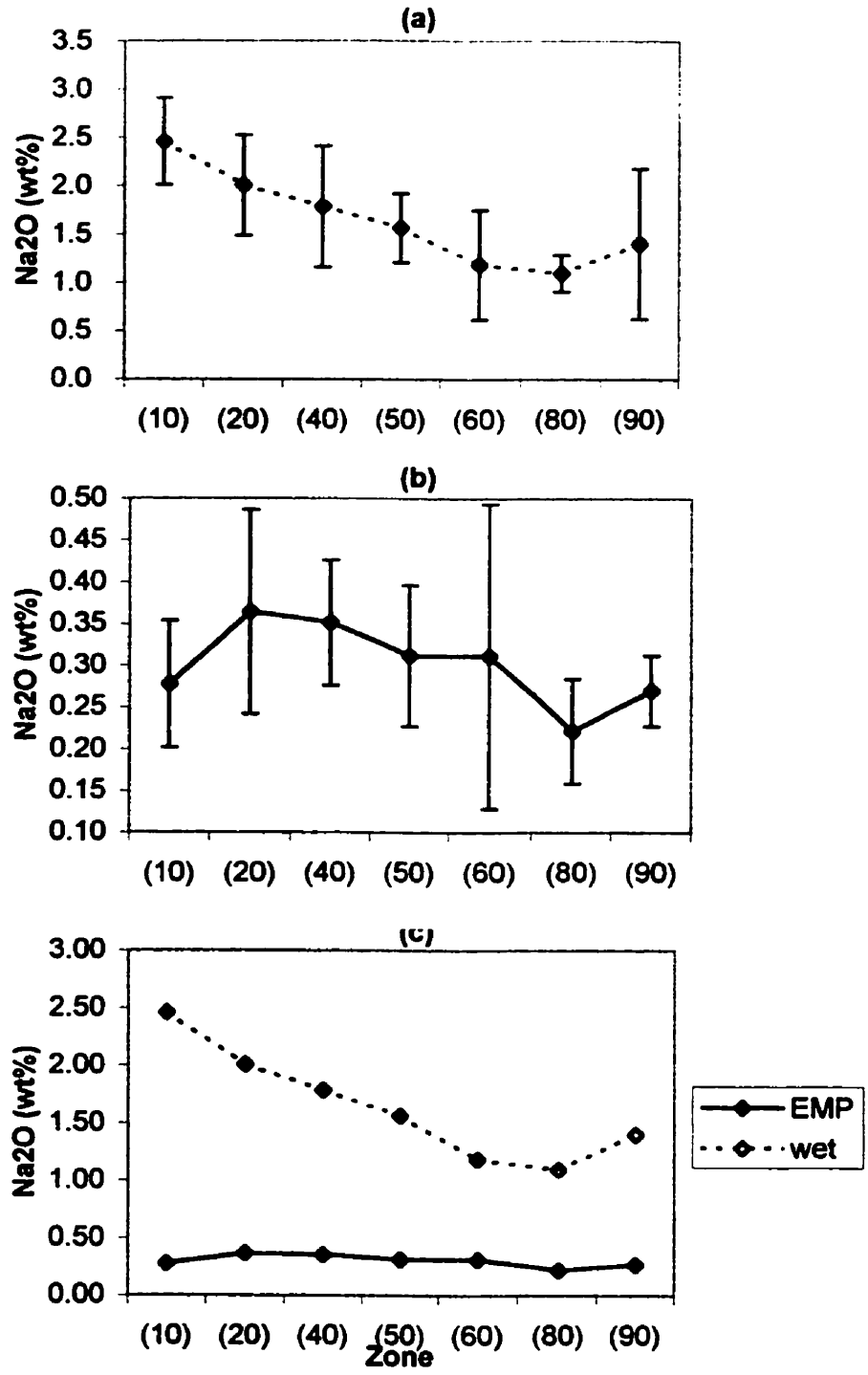


**Figure 6.11** Average Na oxide content per zone, (a) wet-chemistry data, (b) EMPA data. Discrepency between the two analytical techniques in (c) is a consequence of perthite lamellae.
Bars represent 1σ deviations.

Of all the trace-elements analysed by EMPA, only Rb, P, Sr and Ba occur in both co-existing K-feldspar and albite phases of the perthitic intergrowths, in a sufficient number of samples at above-detection levels, to warrant statistically meaningful comparison. From Figures 6.12a,b it is evident that Rb and P are strongly preferred by the K-feldspar phase. The Rb distribution coefficient ($Rb_{Ksp/Palb}$) varies from 10.1 to 99.6 with 95% of values greater than 14. $P_{Ksp/Palb}$ varies from 0.3 to 46.7 with 95% of values greater than 1. Both Sr and Ba (Figures 6.12b,c) have distribution coefficients greater than unity in 69% and 62% of cases respectively, suggesting they are only slightly preferred by K-feldspar over albite. However, their contents are very low in both feldspars, and the apparent differences may be strongly affected by the large analytical errors involved.

*Radiogenic Strontium*

The distribution of Sr between albite and K-feldspar is complex, mainly because of differences in ionic potentials of Sr, Na, and K, but the coefficient is close to 1 in most environments (Černý *et al.*, 1985; Heier *et al.*, 1959a; Smith and Brown, 1988). The behavior of Sr is made even more complex because of its radiogenic relation with Rb. Clark and Černý (1987) demonstrated how the decay of $^{87}Rb$ to $^{87}Sr$ significantly boosts Sr contents above those normally attributed to petrological processes alone, especially in geologically old, Rb-enriched pegmatites. In some samples of K-feldspar from Cross Lake, Tanco and Huron claim pegmatites in Manitoba, 35% to 96% of the analysed Sr was found to be radiogenic. Baadsgaard and Černý (1993) confirmed this, and also found anomalous high contents of radiogenic Sr in albite. Consequently, all Sr contents of the Tanco feldspars are considered suspect and will not be considered further.

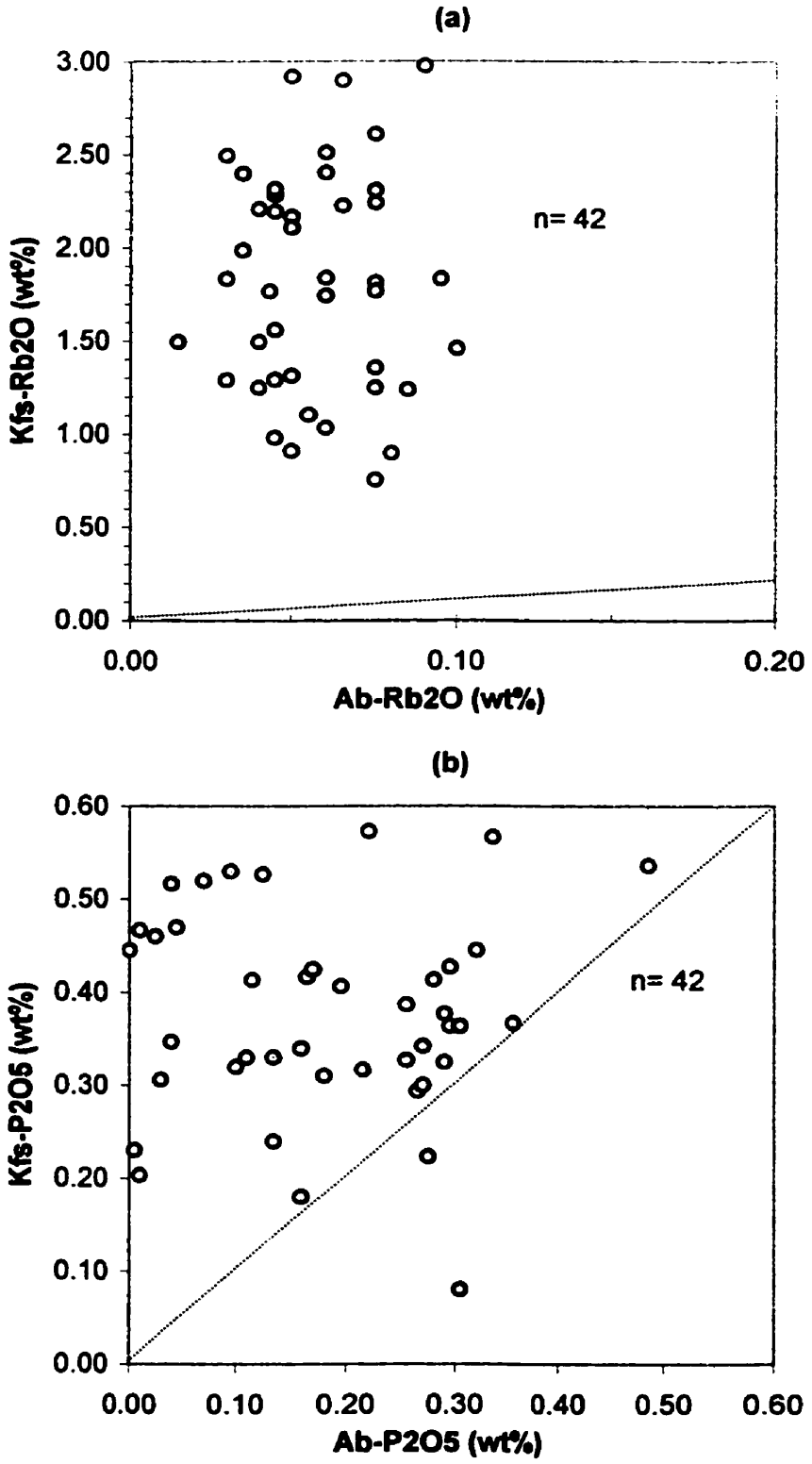


**Figure 6.12** Oxide contents in K-feldspar and coexisting albite lamellae. Dashed lines represent 1:1 ratio.

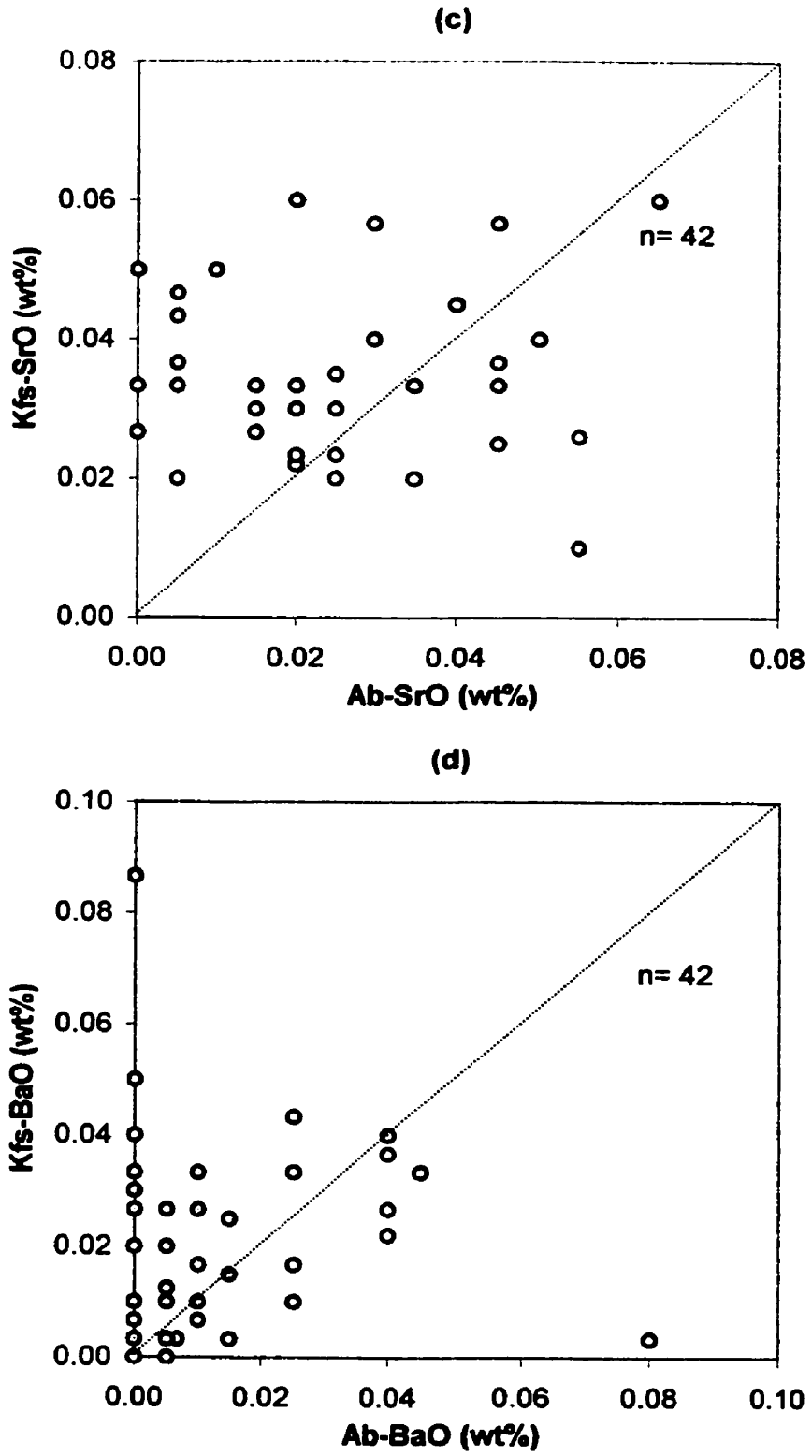


**Figure 6.12** Oxide contents in K-feldspar and coexisting albite lamellae. Dashed lines represent 1:1 ratio.

*Crystal-chemistry*

Figure 6.13a shows that the sum of Si+Al alone does not fill the 4 tetrahedral sites per formula unit. Adding P *via* the berlinite substitution $AlPSi_{-2}$ alleviates most of the problem, although most of the data still show a slight deficit (Figure 6.13b). The main cluster of data is centered on the ideal values of Si+2P = 3.000 and Al-P = 1.000. Most deviations show higher Al-P and lower Si+2P values; a distinctly smaller number of compositions have a reversed relation.

In the diagrams showing Si+2P *vs.* sum of monovalent cations (Figure 6.14a) and Al-P *vs.* total *M*-cation charge (Figure 6.14b), the data cluster close to ideal values of 3.000 and 1.000, and 1.000 and 1.000, respectively. However, both diagrams show systematic trends away from the ideal values, which goes beyond the analytical error of +/- 0.01 atoms. In Figure 6.14a, the trend forms a largely negative extension of the $\square Si_4O_8$ vector, suggesting excess monovalent cations over 1.000 and deficit of Si+2P below 3.000. In Figure 6.14b, the trend suggests excess *M*-cation charge and excess of Al-P over 1.000. The excesses of monovalent *M*-cations and of the *M*-cation charge are, for most of the data, distinctly greater than the excess of Al-P: the main cluster of data extend to ~0.025 over ideal *M*-cation occupancy of 1.000, but only to ~ 0.013 over the same ideal value of Al-P.

In both Figures 6.14a and 6.14b, a small number of data plot at low values of the $\square Si_4O_8$, along the light-element vectors 2 and 3, respectively. However, these data are well within the limit of analytical error, and their significance seems to be doubtful. Also, a very slight spread along the plagioclase-type vector [1] is observed in both figures.

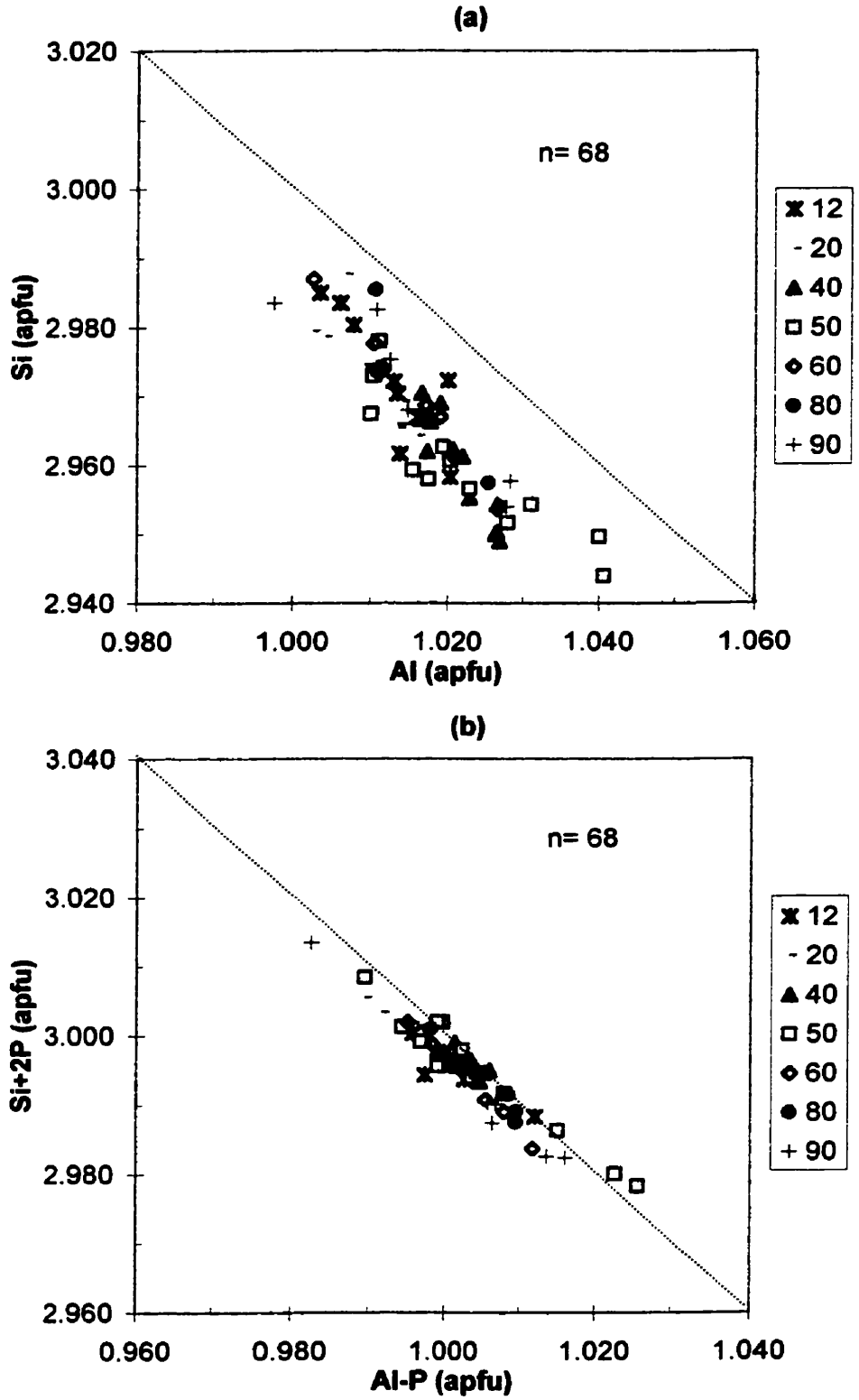


**Figure 6.13** **(a)** Si and Al atomic contents in blocky K-feldspar (Type-1). **(b)** correction for berlinite substitution. In both diagrams, dashed diagonal represents sum of tetrahedral cations *($\Sigma T = 4.000$)*.

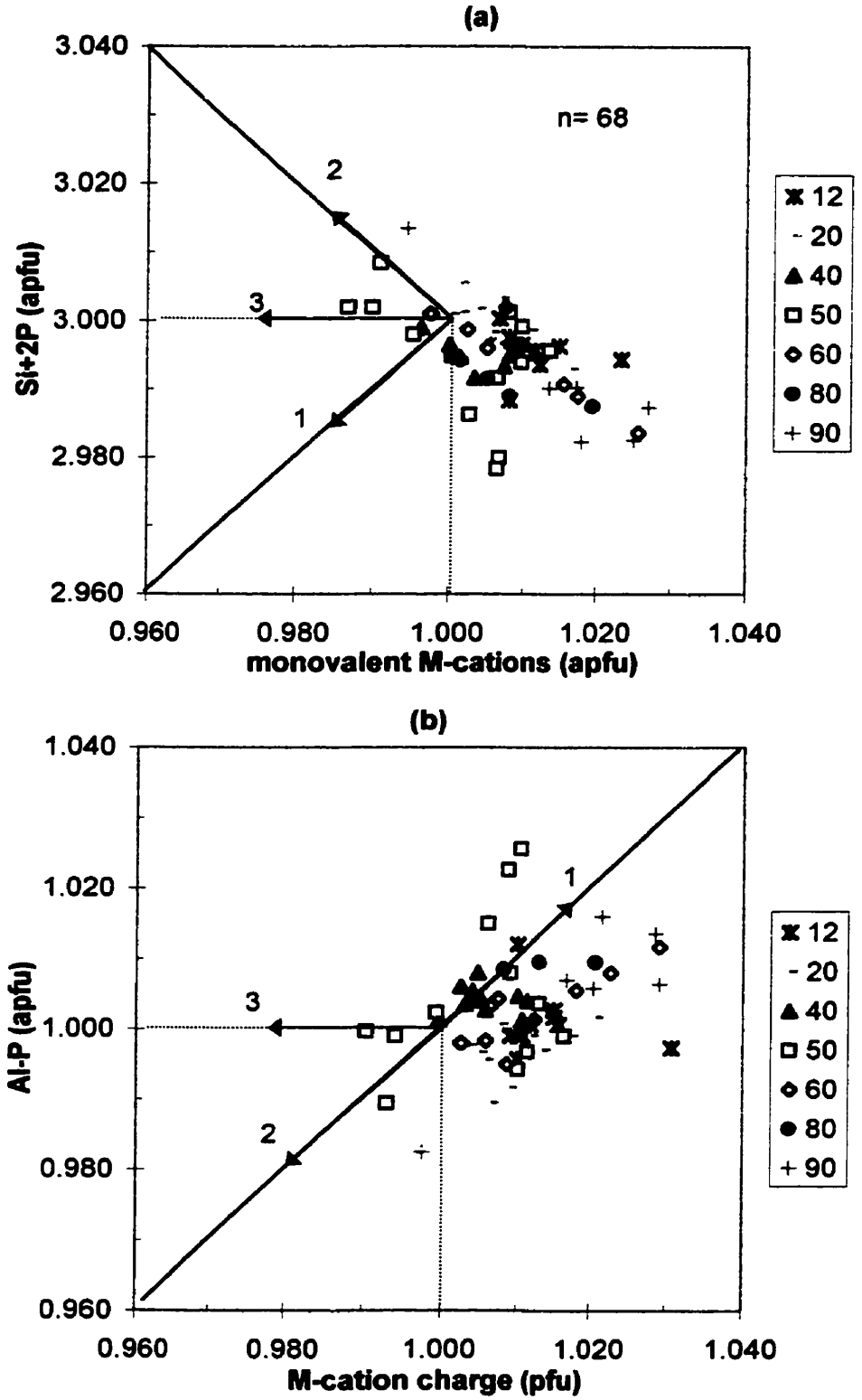


**Figure 6.14** Stoichiometry and charge balance in blocky microcline-perthite: (a) Si+2P *vs.* $\Sigma M$; (b) Al-P *vs.* $M+$, diagonal line indicates $M+ - TO^{2-} = 0$; [1] Plagio -clase substitution trend, [2] vacancy trend, [3] *M*-cation deficiency trend.

In the virtual absence of Ca, this is at least in part real due to minor Ba and Sr, which do not collectively exceed 0.004 *apfu*.

*Structural state*

Xray powder-diffraction data for Type 1 blocky microcline are presented in Table 6.7, with corresponding correlation matrix including unit-cell dimensions against compositional data, in Table 6.8. On the c-b plot (Figure 6.15a), data points cluster nearest the maximum-microcline end-member but are shifted upwards slightly towards the Rb-dominant feldspar series. Data points from different zones within the cluster (Figure 6.15b) show no particular trends, with the possible exception of zone (40) data which, on average, indicate a greater degree of disorder than samples from other zones. A good correlation exists ($R^2$=0.89) between unit-cell volume and atomic Rb+Cs contents (Figure 6.16a); however, triclinicity and atomic Rb+Cs (Figure 6.16b) are poorly correlated ($R^2$= -0.37).

**6.2 'Late' K(Rb) – feldspars** (Types 2 to 6)

The other feldspar Types-2 to -6 are described separately below in terms of colour, texture, and composition. For the most part, these individual types are much less abundant than the blocky K-feldspar, and are found only in specific zones. They do, however, cover most of the spectrum of the general subsolidus paragenetic sequence of feldspars (*e.g.* Černý, 1994; Teertstra, 1997), and some of them may share some degree of temporal, if not spatial, overlap. For this reason, and for the sake of easy comparisons, the individual data series for each of the 'late' feldspar types are presented on the same compositional charts and tables. Table 6.9 lists representative

**Table 6.7:** Blocky K-feldspar (Type 1) unit-cell parameters.

| Sample | Zone | a (Å) | b (Å) | c (Å) | α (°) | β (°) | γ (°) | V (Å$^3$) | Δ |
|---|---|---|---|---|---|---|---|---|---|
| 94-10-R | 10 | 8.589(3) | 12.969(2) | 7.224(1) | 90.58(2) | 115.94(2) | 87.81(3) | 723.1 | 0.914 |
| SLE-18 | 12 | 8.596(2) | 12.967(1) | 7.2244(7) | 90.64(1) | 115.98(1) | 87.70(2) | 723.4 | 0.959 |
| SLW-1C | 12 | 8.593(2) | 12.968(1) | 7.224(1) | 90.61(2) | 115.97(1) | 87.74(2) | 723.2 | 0.954 |
| 12-15-2B | 20 | 8.593(3) | 12.967(1) | 7.224(1) | 90.59(2) | 115.98(2) | 87.78(2) | 723.1 | 0.954 |
| 12-15-2C | 20 | 8.599(3) | 12.969(2) | 7.225(1) | 90.58(3) | 115.95(2) | 87.76(3) | 724.0 | 0.955 |
| 76-23-N | 20 | 8.594(3) | 12.972(2) | 7.225(1) | 90.64(2) | 115.95(2) | 87.78(3) | 723.7 | 0.906 |
| 76-23-O | 20 | 8.588(3) | 12.966(2) | 7.222(1) | 90.56(2) | 115.95(2) | 87.81(2) | 722.5 | 0.949 |
| 78-21-H | 20 | 8.590(2) | 12.965(1) | 7.222(1) | 90.47(2) | 115.97(2) | 87.92(2) | 722.7 | 0.936 |
| L-12-E | 20 | 8.579(4) | 12.965(2) | 7.222(2) | 90.56(3) | 115.95(3) | 87.79(4) | 721.7 | 0.956 |
| 86-07-T | 40 | 8.599(2) | 12.967(1) | 7.222(1) | 90.58(2) | 115.98(1) | 87.85(2) | 723.4 | 0.908 |
| 92-11-L | 40 | 8.614(3) | 12.970(2) | 7.220(1) | 90.53(3) | 115.98(2) | 87.99(3) | 724.7 | 0.839 |
| 94-10-K | 40 | 8.595(3) | 12.970(2) | 7.222(1) | 90.59(2) | 115.97(2) | 87.85(3) | 723.2 | 0.888 |
| C-045-Q | 40 | 8.602(2) | 12.971(1) | 7.2220(8) | 90.61(2) | 115.98(1) | 87.81(2) | 723.9 | 0.909 |
| C-107-E | 40 | 8.604(2) | 12.970(1) | 7.2225(8) | 90.57(2) | 115.98(1) | 87.85(2) | 724.0 | 0.909 |
| 10-25-4 | 47 | 8.618(2) | 12.970(1) | 7.2223(7) | 90.58(2) | 116.02(1) | 87.96(2) | 725.0 | 0.864 |
| 10-25-3c | 50 | 8.605(2) | 12.9658(7) | 7.2247(7) | 90.58(1) | 115.97(1) | 87.89(1) | 724.1 | 0.887 |
| 12-15-1A | 50 | 8.609(4) | 12.968(2) | 7.223(1) | 90.60(2) | 116.00(2) | 87.83(3) | 724.2 | 0.912 |
| 12-15-1AB | 50 | 8.599(2) | 12.966(1) | 7.2224(7) | 90.59(2) | 115.96(1) | 87.83(2) | 723.5 | 0.909 |
| 94-10-G | 50 | 8.608(3) | 12.968(1) | 7.222(1) | 90.60(2) | 115.97(2) | 87.91(2) | 724.4 | 0.856 |
| C-C | 50 | 8.602(2) | 12.971(1) | 7.2250(8) | 90.60(2) | 115.99(1) | 87.77(2) | 724.1 | 0.954 |
| 12-15-4 | 60 | 8.606(2) | 12.970(1) | 7.2250(9) | 90.58(2) | 115.98(2) | 87.81(2) | 724.4 | 0.935 |
| C-090-J | 60 | 8.614(3) | 12.968(2) | 7.225(1) | 90.59(3) | 115.98(2) | 87.83(2) | 725.0 | 0.909 |
| C-096-I | 60 | 8.608(3) | 12.969(2) | 7.224(1) | 90.58(3) | 116.00(2) | 87.84(2) | 724.4 | 0.911 |
| C-S | 60 | 8.609(2) | 12.971(1) | 7.2247(7) | 90.62(2) | 115.98(1) | 87.76(2) | 724.7 | 0.932 |
| C-M | 63 | 8.604(1) | 12.9705(6) | 7.2249(6) | 90.59(1) | 115.97(1) | 87.78(1) | 724.3 | 0.934 |
| 10-25-1 | 80 | 8.621(1) | 12.9714(6) | 7.2246(4) | 90.603(9) | 116.010(8) | 87.83(1) | 725.5 | 0.906 |
| 10-25-2 | 80 | 8.617(2) | 12.968(1) | 7.2221(9) | 90.57(2) | 115.99(2) | 87.89(2) | 725.0 | 0.886 |
| 12-15-19 | 80 | 8.606(3) | 12.969(1) | 7.225(1) | 90.60(3) | 115.98(2) | 87.80(2) | 724.3 | 0.915 |
| 12-15-10 | 90 | 8.611(2) | 12.971(1) | 7.2250(7) | 90.61(2) | 115.99(1) | 87.77(2) | 724.8 | 0.933 |
| 12-15-17 | 90 | 8.612(3) | 12.968(1) | 7.225(1) | 90.55(3) | 115.98(2) | 87.84(2) | 724.9 | 0.928 |
| 96-11-B | 99 | 8.593(3) | 12.967(2) | 7.222(1) | 90.55(3) | 115.99(2) | 87.87(3) | 722.9 | 0.911 |
| | | | | | | | | | |
| max | | 8.621 | 12.978 | 7.227 | 90.64 | 116.02 | 87.99 | 725.8 | 0.96 |
| min | | 8.579 | 12.965 | 7.220 | 90.47 | 115.94 | 87.70 | 721.7 | 0.84 |
| **average** | | **8.603** | **12.969** | **7.224** | **90.58** | **115.98** | **87.83** | **724.0** | **0.92** |
| stdev | | 0.010 | 0.003 | 0.002 | 0.03 | 0.02 | 0.06 | 0.9 | 0.03 |

**Table 6.8:** Correlation matrix of blocky K-feldspar (Type 1) compositions and unit-cell parameters.

| | a | b | c | α | β | γ | V | Δ |
|---|---|---|---|---|---|---|---|---|
| a | 1 | 0.478 | 0.130 | 0.135 | **0.736** | 0.364 | **0.973** | -0.531 |
| b | 0.478 | 1 | 0.329 | 0.454 | 0.270 | -0.142 | **0.609** | -0.198 |
| c | 0.130 | 0.329 | 1 | 0.486 | 0.026 | **-0.660** | 0.301 | **0.520** |
| α | 0.135 | 0.454 | 0.486 | 1 | 0.077 | **-0.649** | 0.235 | 0.135 |
| β | **0.736** | 0.270 | 0.026 | 0.077 | 1 | 0.284 | **0.635** | -0.305 |
| γ | 0.364 | -0.142 | **-0.660** | **-0.649** | 0.284 | 1 | 0.230 | **-0.819** |
| V | **0.973** | **0.609** | 0.301 | 0.235 | **0.635** | 0.230 | 1 | -0.450 |
| Δ | -0.531 | -0.198 | **0.520** | 0.135 | -0.305 | **-0.819** | -0.450 | 1 |
| Ba | -0.172 | -0.071 | 0.085 | -0.118 | -0.060 | -0.090 | -0.160 | 0.165 |
| Li | 0.189 | -0.215 | -0.189 | 0.065 | 0.083 | 0.197 | 0.121 | -0.272 |
| K/Rb | **-0.841** | -0.316 | -0.201 | -0.171 | **-0.683** | -0.176 | **-0.810** | 0.314 |
| K/Na | 0.454 | 0.316 | 0.256 | 0.243 | 0.367 | -0.068 | 0.474 | -0.080 |
| Rb/Cs | -0.304 | -0.299 | -0.238 | -0.059 | -0.189 | 0.071 | -0.344 | 0.009 |
| K/Cs | **-0.745** | -0.315 | -0.190 | -0.095 | **-0.593** | -0.147 | **-0.724** | 0.255 |
| P2O5 | 0.170 | -0.110 | **-0.555** | -0.211 | 0.249 | **0.642** | 0.054 | **-0.636** |
| SIO2 | **-0.697** | -0.217 | 0.020 | 0.105 | -0.459 | -0.403 | **-0.658** | 0.451 |
| AL2O3 | -0.155 | -0.227 | **-0.540** | -0.065 | -0.080 | 0.356 | -0.243 | -0.390 |
| NA2O | -0.235 | -0.090 | -0.159 | -0.376 | -0.181 | 0.256 | -0.232 | -0.061 |
| K2O | **-0.804** | -0.345 | -0.026 | 0.094 | **-0.595** | -0.448 | **-0.771** | 0.481 |
| RB2O | **0.895** | 0.432 | 0.179 | 0.106 | **0.636** | 0.266 | **0.883** | -0.393 |
| CS2O | **0.695** | 0.400 | 0.328 | 0.137 | **0.531** | 0.016 | **0.711** | -0.107 |
| $Rb^{+}+Cs^{+}$ | **0.897** | 0.438 | 0.202 | 0.109 | **0.639** | 0.245 | **0.888** | -0.370 |
| Si+2P/Al+Fe-P | -0.387 | -0.096 | -0.005 | -0.064 | -0.133 | -0.107 | -0.377 | 0.208 |
| Al-P | 0.368 | 0.071 | -0.038 | 0.063 | 0.125 | 0.123 | 0.350 | -0.227 |
| Si+2P | -0.387 | -0.148 | -0.128 | -0.074 | -0.127 | -0.027 | -0.401 | 0.114 |
| Σ*M* | 0.087 | 0.212 | 0.460 | 0.039 | -0.098 | -0.295 | 0.189 | 0.306 |
| *M*+ | 0.130 | 0.204 | 0.479 | 0.039 | -0.034 | -0.274 | 0.225 | 0.299 |
| *M** | -0.162 | 0.121 | 0.432 | -0.010 | -0.122 | -0.326 | -0.068 | 0.422 |
| East | 0.078 | 0.086 | 0.130 | 0.091 | -0.012 | -0.027 | 0.110 | 0.018 |

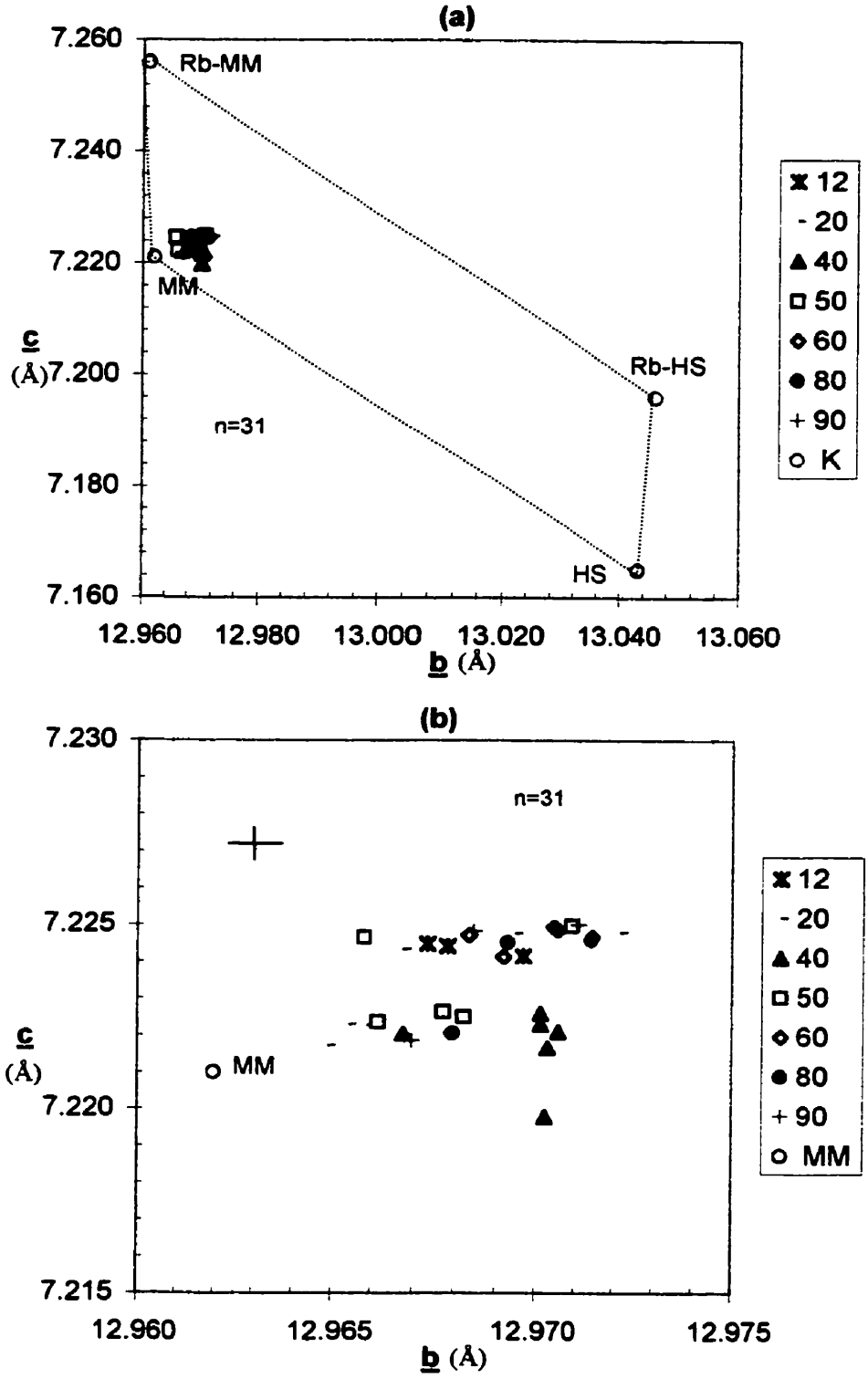


**Figure 6.15** Blocky K-feldspar (Type 1) unit-cell dimensions. Open circles represent ideal ordered to disordered, and Rb-dominant to K-dominant b-c parameters from Cerny et al., 1985b. Cross-hair represents average error.

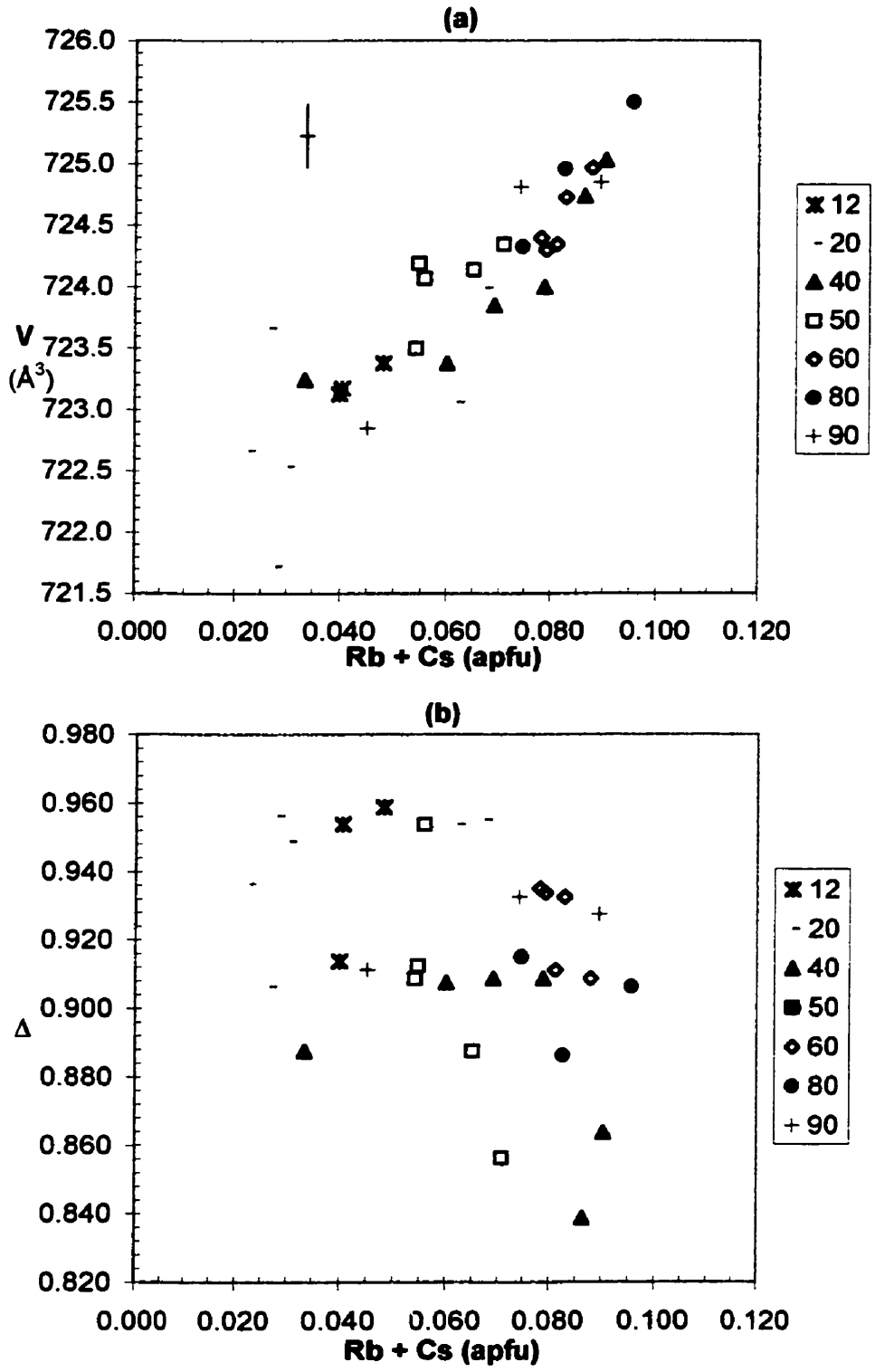


**Figure 6.16** Blocky K-feldspar (Type 1) unit-cell parameters (volume and triclinicity) vs. atomic contents (Rb + Cs) Cross-hair represents average standard analytical error.

**Table 6.9:** Representative compositions (wt%) and formula (apfu) of late K-(Rb)-feldspar (Types 2-6) (EMPA data)

| Sample | BL-jar2 | LM-1 | PM1-8a | pa101-26 | A-10 | pa101-10 | polIC-2 | polIC-4 | ADPV-1 | AD10-4 |
|---|---|---|---|---|---|---|---|---|---|---|
| Type | 2 | 2 | 3 | 3 | 4 | 4 | 5 | 5 | 6 | 6 |
| P2O5 | 0.25 | 0.12 | 0.15 | 0.00 | 0.01 | 0.00 | 0.00 | 0.00 | 0.01 | 0.00 |
| SIO2 | 63.93 | 63.91 | 62.50 | 62.66 | 62.59 | 56.53 | 61.83 | 63.62 | 65.13 | 66.23 |
| AL2O3 | 18.24 | 18.40 | 18.22 | 17.76 | 17.80 | 16.06 | 18.09 | 18.13 | 17.97 | 18.32 |
| MGO | 0.00 | 0.00 | 0.00 | 0.01 | 0.00 | 0.00 | 0.00 | 0.00 | 0.00 | 0.00 |
| CAO | 0.00 | 0.00 | 0.00 | 0.00 | 0.00 | 0.03 | 0.00 | 0.00 | 0.00 | 0.00 |
| MNO | 0.00 | 0.00 | 0.00 | 0.00 | 0.01 | 0.01 | 0.00 | 0.00 | 0.00 | 0.00 |
| FE2O3 | 0.00 | 0.01 | 0.02 | 0.01 | 0.00 | 0.00 | 0.00 | 0.00 | 0.01 | 0.00 |
| SRO | 0.06 | 0.02 | 0.05 | 0.06 | 0.06 | 0.18 | 0.00 | 0.00 | 0.03 | 0.00 |
| BAO | 0.00 | 0.02 | 0.00 | 0.04 | 0.01 | 0.00 | 0.00 | 0.00 | 0.06 | 0.00 |
| PBO | 0.00 | 0.01 | 0.01 | 0.01 | 0.01 | 0.00 | 0.00 | 0.00 | 0.01 | 0.00 |
| NA2O | 0.31 | 0.15 | 0.18 | 0.05 | 0.03 | 0.03 | 0.05 | 0.06 | 0.03 | 0.01 |
| K2O | 15.00 | 15.60 | 14.71 | 13.20 | 13.54 | 1.79 | 12.18 | 13.83 | 16.79 | 15.20 |
| RB2O | 2.36 | 2.20 | 3.68 | 6.15 | 5.76 | 24.84 | 9.09 | 5.68 | 0.02 | 0.00 |
| CS2O | 0.33 | 0.18 | 0.31 | 0.10 | 0.26 | 1.43 | 0.34 | 0.05 | 0.00 | 0.00 |
| TOTAL | 100.49 | 100.60 | 99.83 | 100.05 | 100.08 | 100.90 | 101.58 | 101.37 | 100.05 | 99.76 |
| P5+ | 0.010 | 0.005 | 0.006 | 0.000 | 0.000 | 0.000 | 0.000 | 0.000 | 0.000 | 0.000 |
| SI4+ | 2.985 | 2.982 | 2.969 | 2.997 | 2.993 | 2.994 | 2.972 | 2.994 | 3.014 | 3.035 |
| AL3+ | 1.003 | 1.012 | 1.020 | 1.001 | 1.004 | 1.002 | 1.025 | 1.005 | 0.980 | 0.990 |
| MG2+ | 0.000 | 0.000 | 0.000 | 0.001 | 0.000 | 0.000 | 0.000 | 0.000 | 0.000 | 0.000 |
| CA2+ | 0.000 | 0.000 | 0.000 | 0.000 | 0.000 | 0.002 | 0.000 | 0.000 | 0.000 | 0.000 |
| MN2+ | 0.000 | 0.000 | 0.000 | 0.000 | 0.000 | 0.000 | 0.000 | 0.000 | 0.000 | 0.000 |
| FE3+ | 0.000 | 0.000 | 0.001 | 0.000 | 0.000 | 0.000 | 0.000 | 0.000 | 0.000 | 0.000 |
| SR2+ | 0.002 | 0.001 | 0.001 | 0.002 | 0.002 | 0.006 | 0.000 | 0.000 | 0.001 | 0.000 |
| BA2+ | 0.000 | 0.001 | 0.000 | 0.001 | 0.000 | 0.000 | 0.000 | 0.000 | 0.001 | 0.000 |
| PB2+ | 0.000 | 0.000 | 0.000 | 0.000 | 0.000 | 0.000 | 0.000 | 0.000 | 0.000 | 0.000 |
| NA+ | 0.028 | 0.013 | 0.017 | 0.005 | 0.003 | 0.003 | 0.005 | 0.005 | 0.003 | 0.001 |
| K+ | 0.893 | 0.928 | 0.892 | 0.805 | 0.826 | 0.121 | 0.747 | 0.830 | 0.991 | 0.889 |
| RB+ | 0.071 | 0.066 | 0.112 | 0.189 | 0.177 | 0.846 | 0.281 | 0.172 | 0.000 | 0.000 |
| CS+ | 0.007 | 0.004 | 0.006 | 0.002 | 0.005 | 0.032 | 0.007 | 0.001 | 0.000 | 0.000 |
| $\Sigma T$ | 3.998 | 3.999 | 3.995 | 3.998 | 3.997 | 3.996 | 3.997 | 3.999 | 3.995 | 4.025 |
| $TO_2$ | 0.994 | 1.007 | 1.015 | 1.001 | 1.003 | 1.002 | 1.025 | 1.005 | 0.980 | 0.990 |
| Si+2P/Al-P | 3.023 | 2.972 | 2.938 | 2.994 | 2.984 | 2.988 | 2.900 | 2.979 | 3.075 | 3.066 |
| $\Sigma M$ | 0.999 | 1.011 | 1.027 | 1.001 | 1.011 | 1.002 | 1.040 | 1.008 | 0.994 | 0.890 |
| $M+$ | 1.002 | 1.014 | 1.030 | 1.007 | 1.015 | 1.018 | 1.040 | 1.008 | 0.999 | 0.890 |
| $M^*$ | 0.009 | 0.007 | 0.015 | 0.006 | 0.012 | 0.016 | 0.015 | 0.003 | 0.018 | -0.100 |

-atomic contents normalized to 8 oxygens

Type 2: granular microcline veins (60)

Type 3: metasomatic microcline veins in pollucite (80)

Type 4: adularian (K-Rb) feldspar; metasomatic along vein margins of type 3 (80)

Type 5: metasomatic clusters in pollucite (80) (unpub. data, Teertstra pre-1995)

Type 6: adularia crystals in leaching cavities (40),(50)

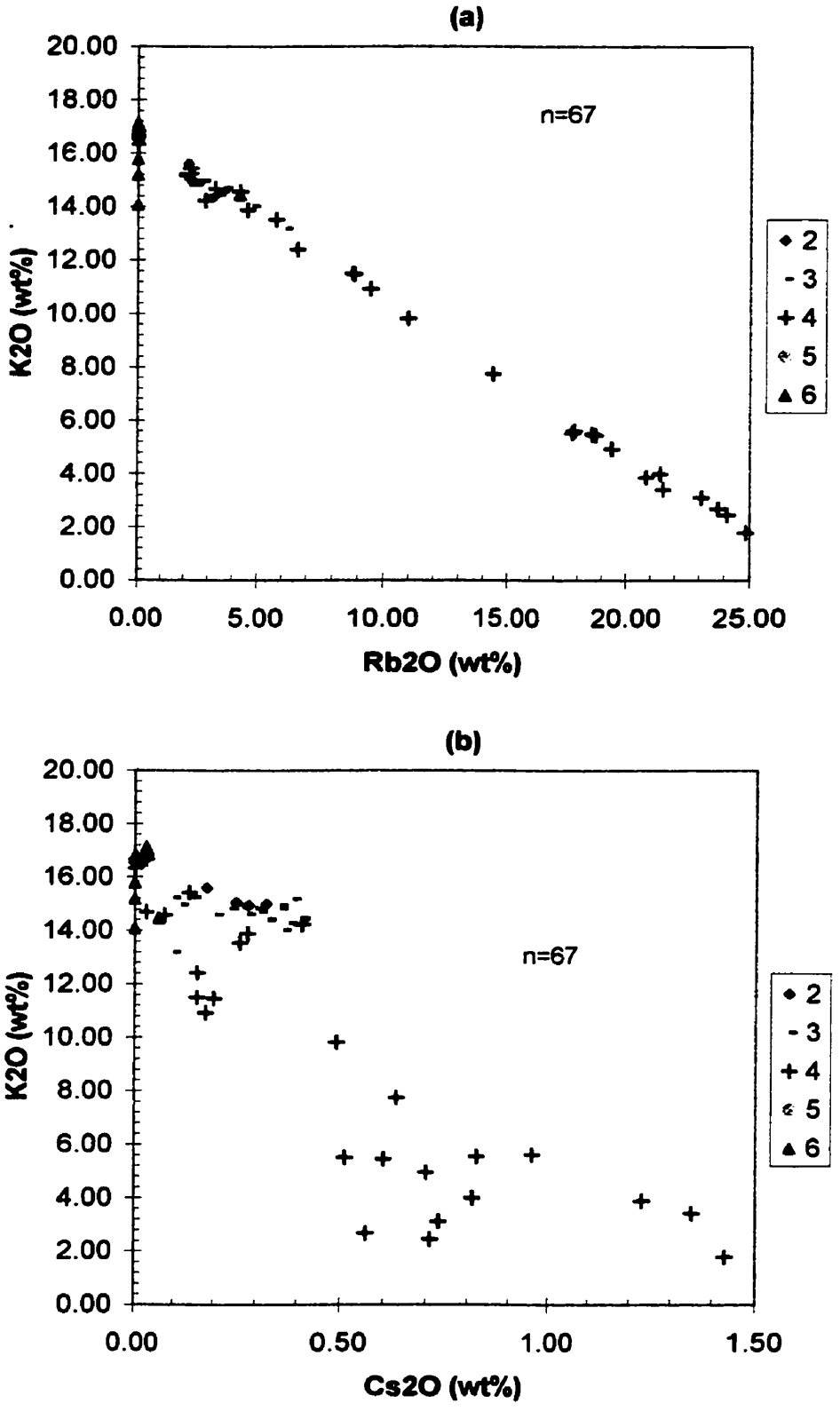


**Figure 6.17** Bivariate oxide plots (EMPA) of late K-feldspars (Types 2,3,4,6).

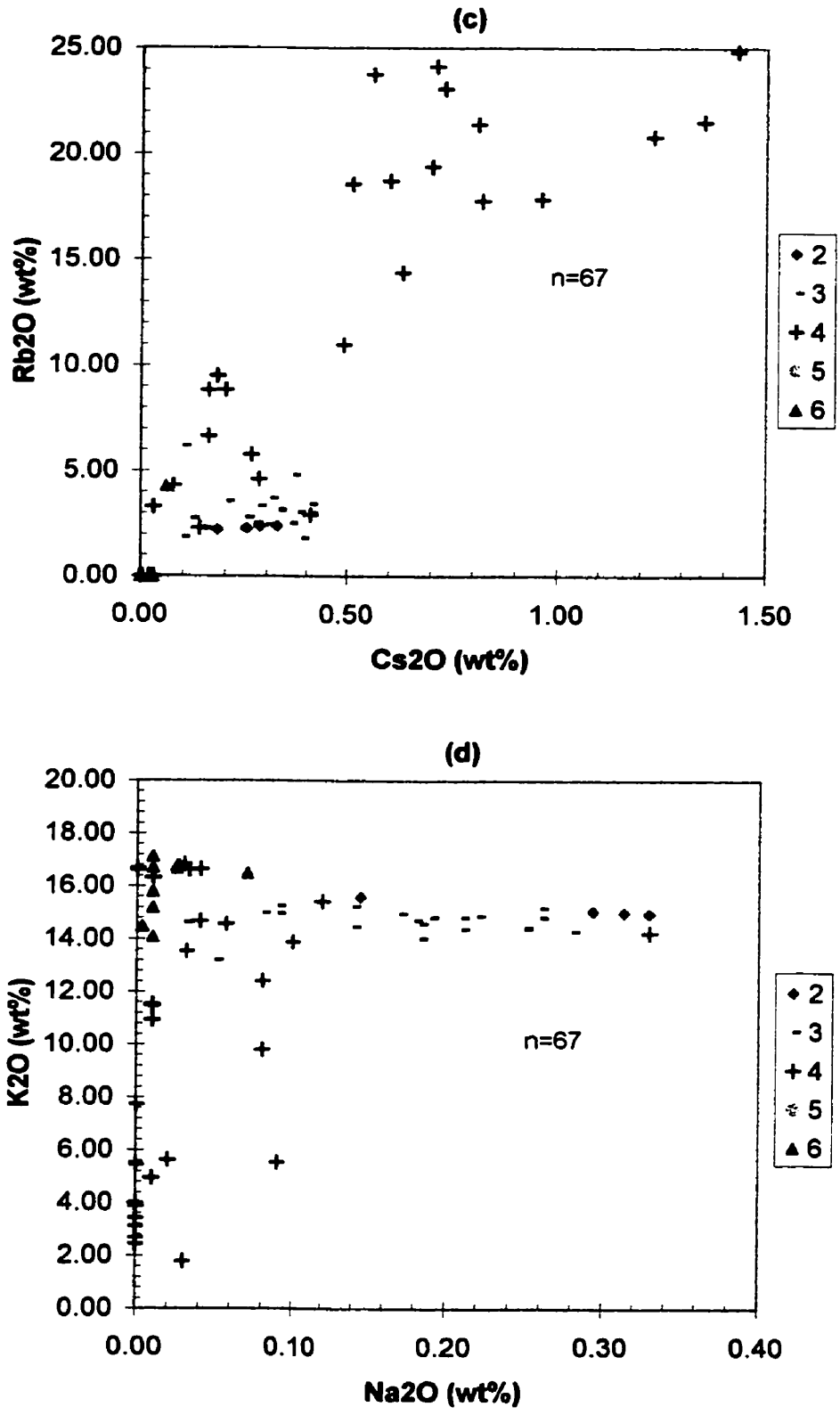


**Figure 6.17** Bivariate oxide plots (EMPA) of late K-feldspars (Types 2,3,4,6).

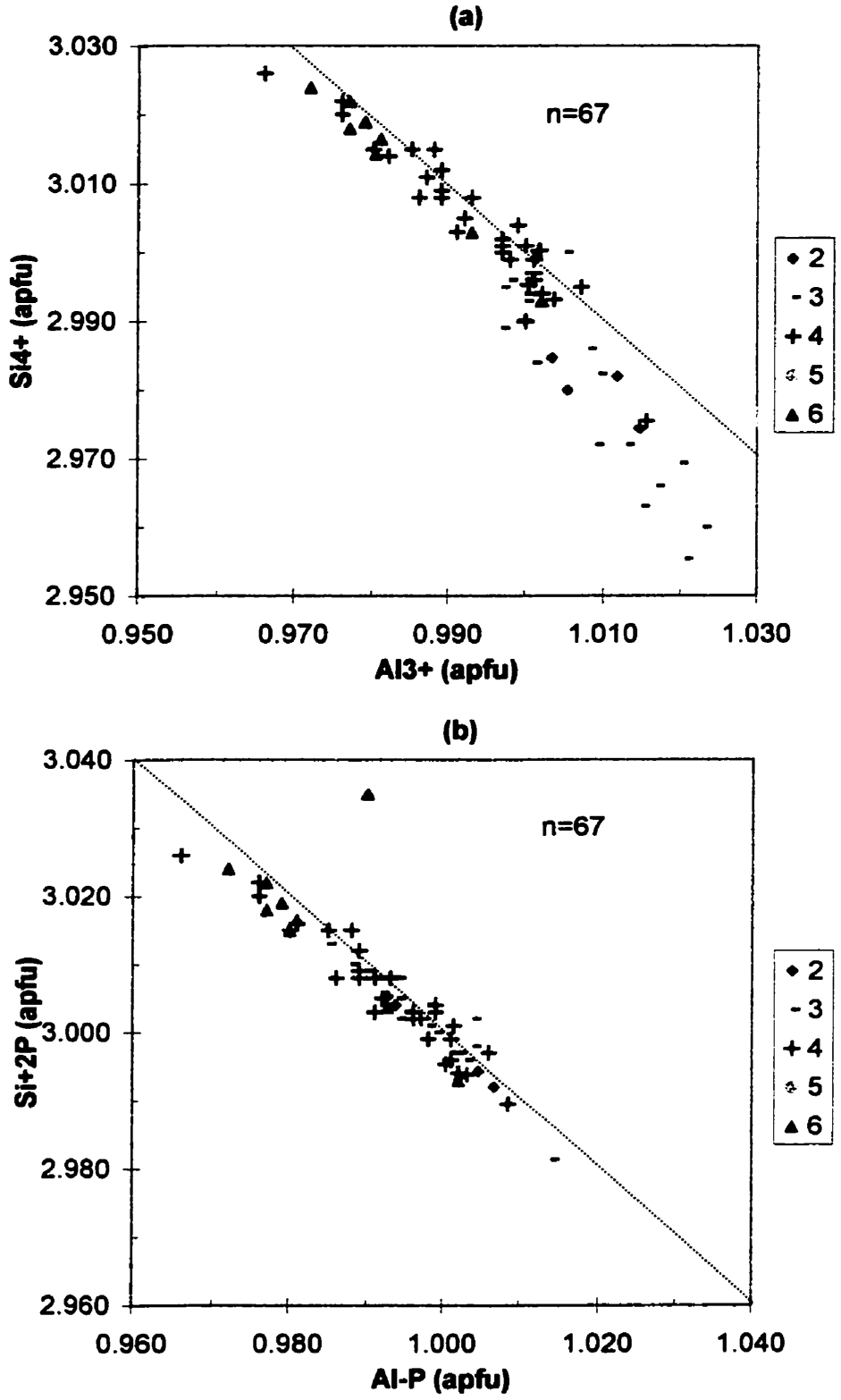


**Figure 6.18** **(a)** Si and Al atomic contents of late K-feldspars. **(b)** Corrected for berlinite substitution. In both diagrams, dashed diagonal represents sum of tetrahedral cations ( $\sigma T = 4.000$).

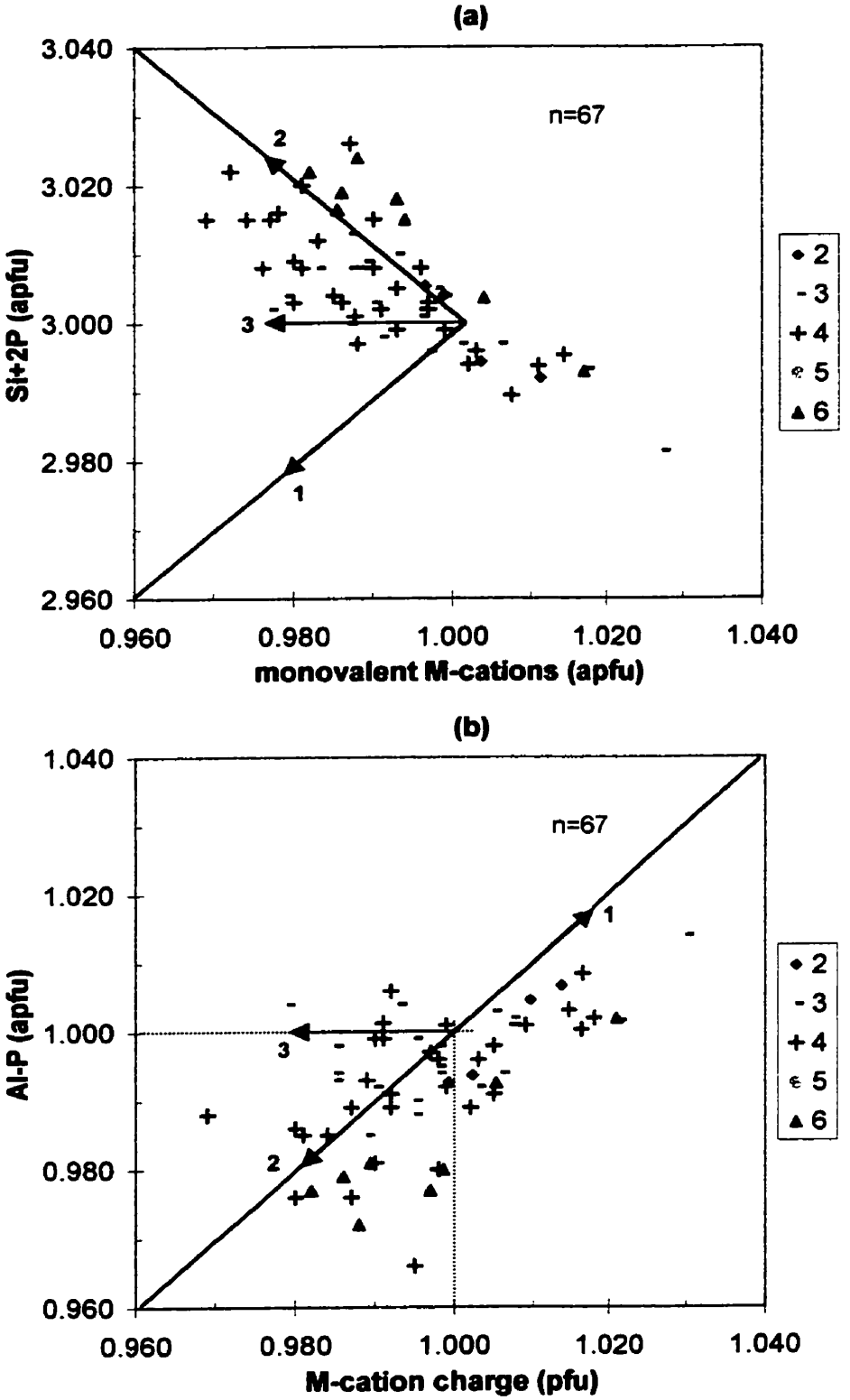


**Figure 6.19** Stoichiometry and charge balance in late K-feldspars. Diagonal line in (b) indicates *M*+ - *TO2*- = 0; [1] Plagioclase substitution trend, [2] vacancy substitution trend, [3] *M*-cation deficiency trend.

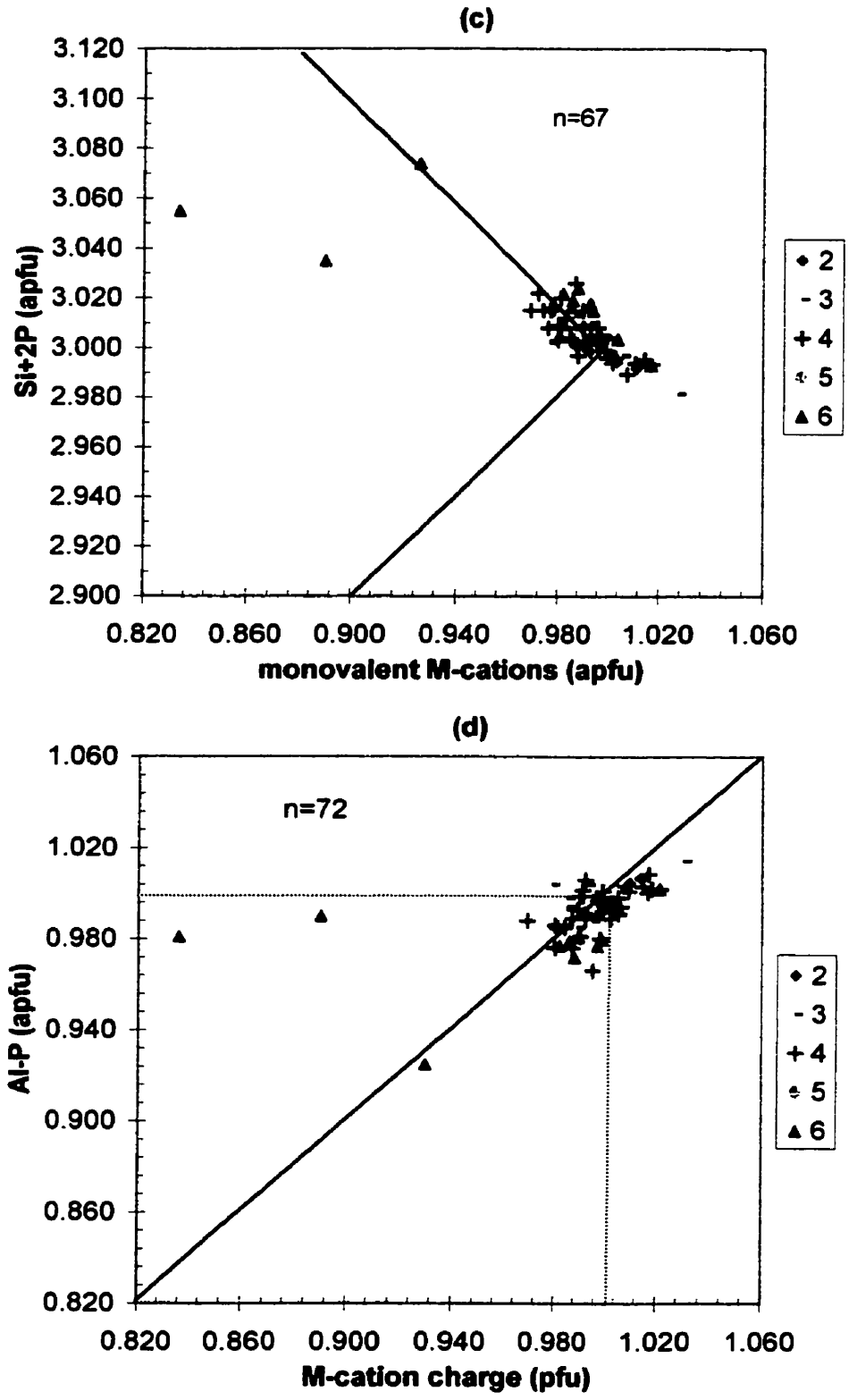


**Figure 6.19** Same data but greater range than in Figures 18a and 18b. Note extreme variations in the three adularia compositions along the vacancy and *M*-cation deficiency trends.

**Table 6.10:** Some unit-cell dimensions for late K(Rb)-feldspar varieties.

| Sample | Type | a (Å) | b (Å) | c (Å) | α (°) | β (°) | γ (°) |
|---|---|---|---|---|---|---|---|
| 5 | 3 | 8.609(2) | 12.971(3) | 7.225(2) | 90.62(3) | 115.98(2) | 87.79(2) |
| 7 | 6 | 8.591(1) | 13.042(2) | 7.169(1) | 90 | 115.99(1) | 90 |
| 12 | 6 | 8.603(2) | 13.050(4) | 7.171(2) | 90 | 115.93(3) | 90 |
| 13 | 6 | 8.596(2) | 13.040(3) | 7.166(2) | 90 | 115.97(2) | 90 |
| 15 | 6 | 8.597(2) | 13.038(3) | 7.172(3) | 90 | 115.99(2) | 90 |

5,7 from Teertstra (1997)

12, 13, 15 from Černý and Chapman (1984)

compositions of Types 2 to 6. Bivariate oxide-content diagrams for K, Rb, Cs, and Na are presented in Figures 6.17a to d. Crystal-chemical data are presented in Figures 6.18a,b and Figures 6.19 a,b. A limited number of unit-cell parameters for Types 3 and 6 from the literature are presented in Table 6.10.

**Type 2:** *granular non-perthitic microcline veins in zone (60)*

Granular K-feldspar from zone (60) occurs in veins of varying sizes, as medium-grained beige to pale-grey subhedral to anhedral grains. The veins generally pinch and swell with thicknesses between 10 and 30 cm, and contain predominantly K-feldspar, locally lined with muscovite (sericite), quartz and various pink to orange equant phosphates, and minor Ta/Nb oxides. Some of the grey samples (*e.g.* Figure 6.20) consist of matrix-supported pseudo-hexagonal prisms of K-feldspar, some larger than 5 cm in diameter. The matrix consists of a dark-bluish-grey, fine-grained assemblage of quartz, sericite and local minor Bi-sulfides. Most samples, except sample BL-Jar1, are non-perthitic.

*Composition*

Only 4 EMPA-determined compositions for this feldspar type are available; each composition represents an average of 2-5 analytical points. Potassium and rubidium vary inversely (Figure 6.17a) with $K_2O$ varying from 15.60 to 14.96 wt% and $Rb_2O$ from

2.20 to 2.36 wt%. This coincides with an increase in $Cs_2O$ from 0.10 to 0.41 wt% (Figure 6.17b,c). Individual $Na_2O$ values are some of the highest in Figure 6.17d. Potassium and sodium appear inversely proportional, with $Na_2O$ varying between 0.15 and 0.33 wt%.

Phosphorus incorporation via the berlinite substitution is significant (Figures 6.18a,b) with $P_2O_5$ varying between 0.12 to 0.31 wt%. Si+2P/Al-P varies from 2.972 to 3.027. Taking analytical error into account, the distribution of data points in Figures 6.19a,b indicate that the type-2 feldspars are close to ideal stoichiometry. A slight shift along the vacancy substitution vector [2] is well within analytical error.

**Type 3:** *metasomatic microcline veins in pollucite (80)*

This K-feldspar type (Figure 6.21) occurs as pink cleaveable, or occasionally microcrystalline microcline in veinlets and veins up to 4 mm wide, which fill fractures in, and replace pollucite in zone (80). The veins also commonly contain variable quantities of grey to white albite, quartz, and muscovite or lepidolite; the latter giving the vein a purplish hue. Other minerals observed in BSE images include apatite, spodumene, calcite, and local Ta/Nb (Sn) oxides.

*Composition*

Twenty-one non-averaged EMPA-determined compositions are available for this feldspar type. Potassium and rubidium vary inversely (Figure 6.17a) with $K_2O$ varying from 15.25 to 13.20 wt%, and $Rb_2O$ from 1.80 to 6.15 wt%. This coincides with an increase in $Cs_2O$ from 0.10 to 0.41 wt% (Figure 6.17b,c). Individual $Na_2O$ contents (Figure 6.17d) show a wide spread of generally low values between 0.03 and 0.28 wt%.

Phosphorus incorporation via the berlinite substitution is significant (Figures 6.18a,b), with $P_2O_5$ varying between 0.00 and 0.51 wt%. Si+2P/Al-P varies from 2.938 to 3.056. There is a relatively wide distribution of data points in Figures 6.19 a,b, with the mid-point of the trends roughly centered over the ideal stoichiometric values. The relatively shallow trends in Figures 6.19a,b, along vectors [2] and [3], suggest the presence of both vacancy and light *M*-cation substitutions. The average *M*-cation deficiency (*M**) is, however, only 0.000 +/- 0.010, with individual values as low as -0.026.

*Structural state*

Only one unit-cell refinement for this feldspar variety was encountered in the relevant literature for Tanco (Table 6.10). Teertstra (1997) reported this sample as a vein microcline in pollucite, and determined unit-cell dimensions by Rietveld refinement.

**Type 4:** *adularian (K-Rb) feldspar*

This feldspar type occurs as microscopic selvedges, which seem to have locally recrystallized from the type-3 K-feldspar (Figure 6.22), and partially replaced pollucite along the margins of the type-3 veins (Teertstra, 1997).

*Composition*

Thirty individual compositions are available for this feldspar type. Potassium and rubidium vary inversely (Figure 6.17a) and exhibit the greatest range of contents compared to all the other feldspar types. $K_2O$ varies from 16.83 to 1.79 wt% with a concomitant increase in $Rb_2O$ from 0.00 to 24.84 wt%. This coincides with a general increase in $Cs_2O$ from 0.00 to 1.43 wt% (Figure 6.17b), along a relatively steep $Rb_2O$ *vs.* $Cs_2O$ trend (Figure 6.17c). With one exception, individual $Na_2O$ contents (Figure 6.17d) are very low, with values between 0.00 and 0.11 wt%.

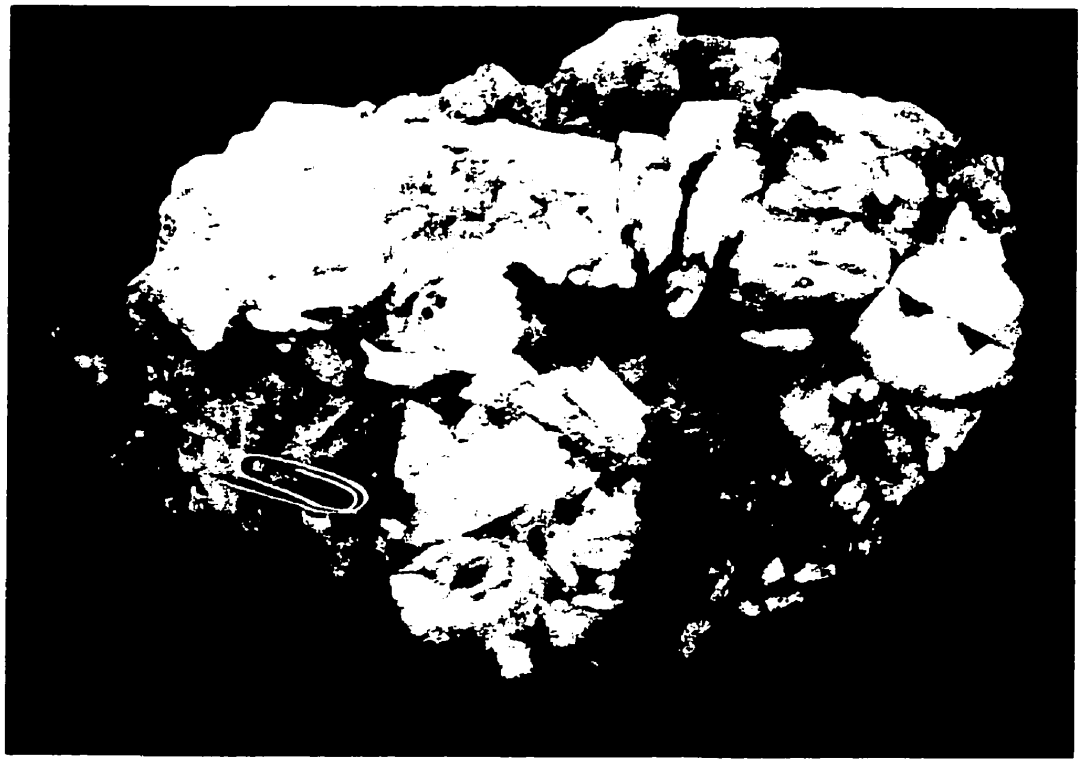

**Figure 6.20** Hand sample of granular non-perthitic microcline (Type 2) veins (white), hosted in quartz (grey-brown). Veins comprise an aggregate of quasi-hexagonal microcline individuals lined with fine-grained muscovite (yellow) and Bi-sulphides (black).


**Figure 6.21** Hand sample of metasomatic microcline vein assemblage in pollucite from zone (80). Central parts of veins comprise mostly pink K-feldspar (Type-3), with non-visible adularian (Type 4) K-feldspar and albite (Types D,E) occurring along vein margins, and in veinlets normal to the main vein structure. Finely dispersed lepidolite contributes purplish hue.

Phosphorus incorporation via the berlinite substitution is not significant (Figures 6.18a,b) with 90% of samples containing less than 0.05% $P_2O_5$. Si+2P/Al-P varies from 2.963 to 3.133. There is a wide distribution of data points in Figures 6.19 a,b, with the trends more-or-less passing through the ideal stoichiometric values. Similarities are observed with the Type-3 trends in Figures 6.19a,b, along vectors [2] and [3], suggesting the presence of both vacancy and light *M*-cation substitutions. The extent of the substitutions (particularly along vector [2]) is greater than for all other feldspar types. The average *M*-cation deficiency (*M**) is 0.003 +/- 0.011, with individual values as low as -0.021.

**Type 5:** *metasomatic clusters of adularian (K>Rb) feldspar in pollucite (80)*

This feldspar type occurs within metasomatic clusters in zone (80), as microscopic aggregates of subhedral adularian crystals associated with minor quartz and clay minerals (Figure 6.23). In most cases, the clusters are closely associated with sericitic veinlets, which cross-cut pollucite, and contain minor quantities of anhedral spodumene and clay minerals.

*Composition*

Compositional data on the Type-5 feldspar is limited to unpublished data of Teertstra (pre-1995). An analysis of crystal-chemical results indicates significant analytical error as a result of poor EMPA standard calibration (P. Černý, personal comm., 2001). Results are however, useful qualitatively. $Rb_2O$ varies between 0 and 15.4 wt%, and $Cs_2O$ varies between 0 and 0.71 wt%, indicating similarly high (albeit not as extreme) contents in comparison to Rb and Cs bearing feldspar of Type-4.

**Type 6:** *adularia crystals in leaching cavities*

Ćerný and Chapman (1972, 1984) define adularia as a morphologically distinct variety of end-member K-feldspar, characteristic of low-temperature hydrothermal or diagenetic paragenesis. The strict definition of adularia specifies a euhedral crystal form, with Na-poor composition closely approaching $Or_{100}$. For the purposes of this thesis, I adhered to the strict morphological definition of adularia, which applies only to milky-white to pink, sub-millimeter, euhedral crystals collected from drusy aggregates in leaching cavities from zones (50) and (40) (Figure 6.24). These feldspar aggregates are commonly associated with cookeite, cesian analcime, montmorillonite-illite, and rarely sulfides, and sulfosalts. Adularia locally forms oriented overgrowths on albite (Černý, 1972), and radial coatings on relict spodumene. A few crystals appeared zoned under back-scattered electrons (Figure 6.25). Teertstra (1997) reported outer dark margins up to 50μm wide, and found them to be considerably *M*-cation deficient as far as EMPA-determined compositions were concerned.

*Composition*

Eleven compositions are available for this feldspar type; of these, 5 compositions are averages of 2-5 point determinations. Rubidium and Cs contents (Figures 6.17a,b,c) are consistently below detection, except for one heterogeneous sample which contained an average of 4.28 wt% $Rb_2O$, and 0.06 wt% $Cs_2O$. $K_2O$ varies from 17.15 to 14.09 wt%. $Na_2O$ contents (Figure 6.17d) are very low, with most values between 0.00 and 0.03 wt%; one sample attained a value of 0.07.

Phosphorus content is essentially nil. Si/P varies from 2.987 to 3.323 (Figure 6.18). There is a relatively wide scatter of data points in Figures 6.19 a,b. In Figure 6.19c, extreme displacements of three points along vectors [2] and [3] are observed. The two

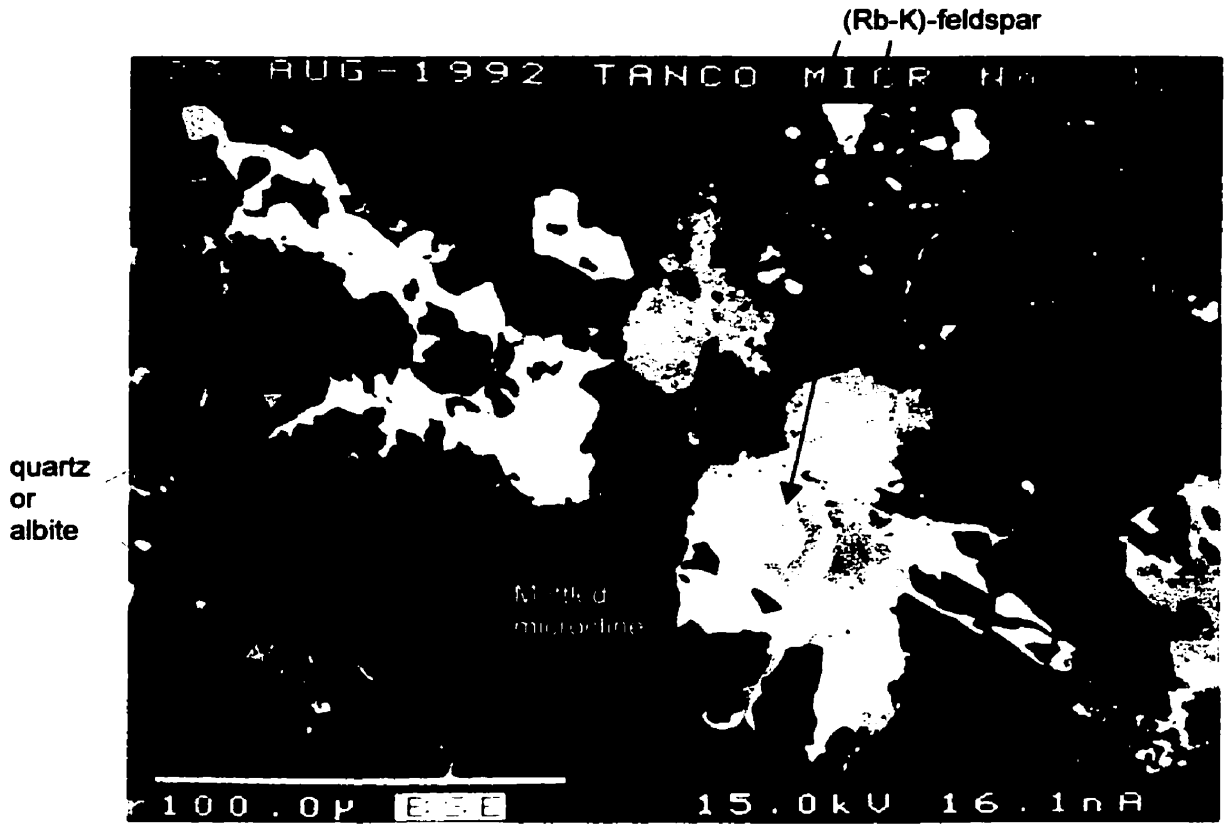


**Figure 6.22** BSE image of (K-Rb)-feldspar veining pollucite in zone (80). Dark mottled microcline (Type 3) indicates low to variable Rb contents. Brighter regions indicate increasing Rb (Cs) contents in adularian (Rb-K)-feldspar (Type-4). (Image from Teertstra, 1997)

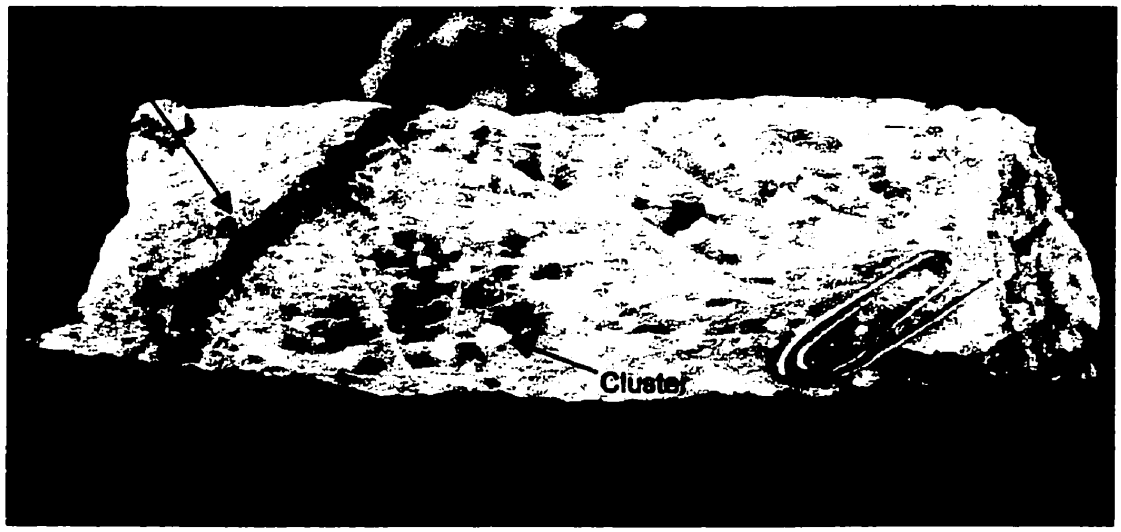


**Figure 6.23** Hand sample of pollucite from zone (80) containing adularian (Type-5) clusters (white). Most clusters occur along network of white sericite-albite veinlets.

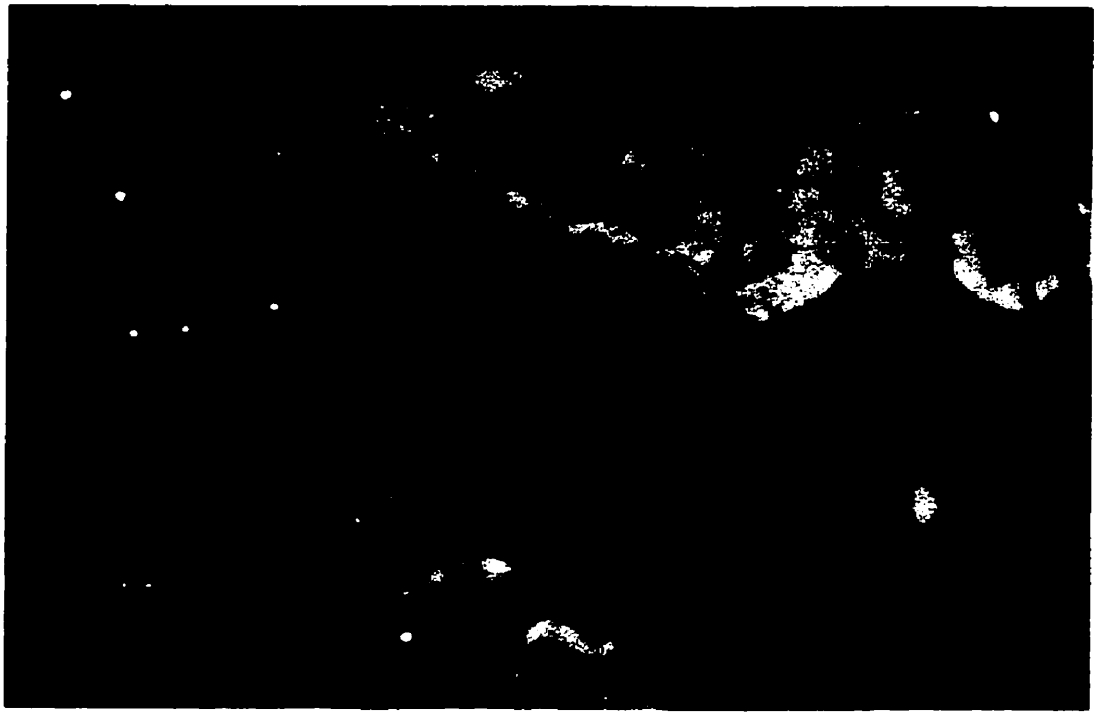

**Figure 6.24** Photograph of drusy overgrowths of adularia +/- Cs analcime, plus very-fine-grained micas and clays, on albite or relict spodumene in a vug from zone (50). Field of view is about 4mm.

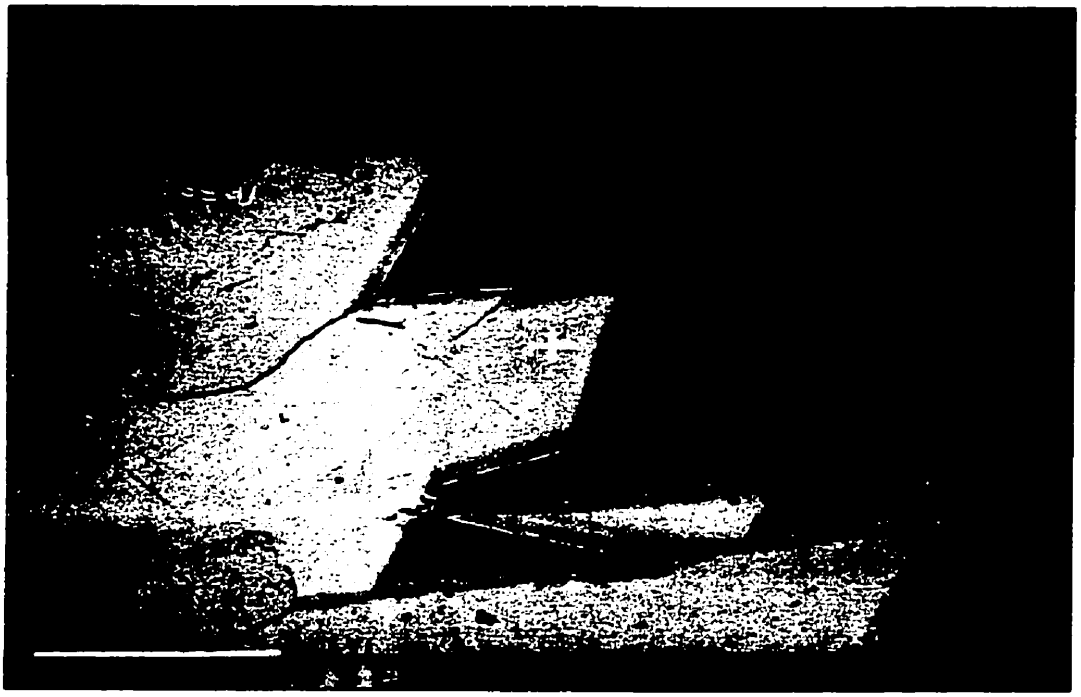

**Figure 6.25** BSE image of zoned euhedral adularia crystal from zone (50). Dark rim is representative of low average atomic weight, probably indicative of elevated H+ (see text for further information).

extreme compositions along vector [3] are the results of analyses of a dark, outer rim of a zoned adularia sample (*e.g.* Figure 6.25). $M^*$ values for these two samples are –0.100 and –0.145, indicating very significant *M*-cation deficiency. Teertstra (1997) speculated that the outer dark rims on adularia crystals, observed in BSE images, could be indicative of H+ substitution in the *M*-site; follow-up analysis by SIMS or hydrogen-ion extraction are still required to support this hypothesis.

*Structural state*

Černý (1972) and Teertstra (1997) refined unit-cell dimensions of Type-6 adularia, which corresponded to the high-sanidine structure with virtually total (Si, Al) disorder (Table 6.10).

## CHAPTER 7: MINERALOGY OF TANCO ALBITE

Based on morphological and textural characteristics, six different types of albite are recognized in the Tanco pegmatite (Table 6.1; Types A-F). The first two types, aplitic albite (Type A) and cleavelanditic albite (Type B), are essential rock-forming mineral varieties, which collectively comprise 26% of the volume of Tanco (Stilling 1998). The remaining types have very low abundances, and generally occur as significant components of replacement or metasomatic assemblages.

Representative compositions of albite (Types A,B) of individual zones, are summarized in Table 7.1. A complete listing of albite compositions determined by EMPA is found in Appendix IV. As noted in chapter 5 and Appendix I, analytical results for Fe, Ti, Mg, Cs, and F were consistently below detection. Subsequent listings of analytical data and discussion of all albite types will be limited to the following suite of elements: Na, K, Rb, Ca, Sr, Mn, Al, Ga, Si, and P. Histograms illustrating the contents of selected oxides and average compositions by zone for both aplitic albite and cleavelandite are presented in Figures 7.1-7.3 and Figures 7.4, 7.5. Corresponding statistics for $P_2O_5$, CaO, and $K_2O$ are listed in Table 7.2.

**Type A:** *aplitic albite* (10,20,30,40,50,60,70,80)

Aplitic albite typically comprises a mosaic of very fine-grained, equidimensional, subhedral crystals (Figure 7.6) intimately associated with a variety of accessory minerals, and is found in all zones except (90). There are three general morphological occurrences: 1) Large lenses (meters to 10's of meters) of massive bluish or purplish to white aplitic albite containing significant disseminated to coarse-grained quartz [*e.g.* all of zone (30)], and minor, randomly dispersed to weakly banded (Li)-muscovite, apatite, tourmaline, and (Ta, Nb, Sn) oxide minerals. 2) Moderate-size lenses [*e.g.*, in zones (20)

and (60)], decimeters to meters thick, of white to bluish or purplish aplitic 'line rock' composed of linear to bulbous arrays of accessory-rich and accessory-free layers. Accessory minerals include significant mm-sized, equant, euhedral apatite and/or bluish-black, 1-2 mm long, euhedral tourmaline columns, muscovite or lepidolite, and minor Ta-Nb, and/or Sn oxides. Subhedral, cm-scale tourmaline and white cesian-beryl crystals commonly occur in contact with smoky quartz (Figure 7.7). 3) Small lenses (mm's-cm's) of white, bluish, greenish, or orange-hue aplitic albite as part of matrix assemblages in all zones. Colour reflects type and quantity of accessory minerals. Local orange staining may be caused by Fe-hydroxide staining.

*Chemical Composition*

Phosphorus in aplitic albite ranges from 0.03 to 0.38 wt% $P_2O_5$ (Table 7.2). The overall distribution (Figure 7.1a) is bimodal, with a distinctly higher frequency between 0.09 and 0.12 wt% $P_2O_5$, and a smaller peak between 0.30-0.33 wt%. Ninety-one percent of all individual EMPA-determined compositions are above the detection limit of 0.073 wt%, with 11% of compositions greater than 0.30 wt% $P_2O_5$. Average $P_2O_5$ by zone (Figure 7.5a), does not vary significantly above or below 0.15 wt % except for zones (40) and (80), which attain average values of 0.20 and 0.21 wt%, respectively.

Calcium ranges from 0.02-0.19 wt% CaO (Table 7.2). The overall distribution (Figure 7.2a) is close to Gaussian, with a broad profile and a maximum frequency between 0.03 and 0.05 wt% CaO. There is a paucity of values between 0.12 and 0.16 wt%, and only two samples with compositions greater than 0.16 wt%. Average CaO contents by

**Table 7.1:** Representative compositions (wt%) and formula (APFU) of albite from Tanco, Manitoba (EMPA data)

| Sample | SLW-3C | L-12-M | C-096-U | C-033-O | C-E | 92-11-H | 92-11-P | Poll-6 | 12-15-22 |
|---|---|---|---|---|---|---|---|---|---|
| Zone | (12) | (20) | (30) | (40) | (50) | (60) | (70) | (80) | (90) |
| P2O5 | 0.03 | 0.12 | 0.20 | 0.20 | 0.22 | 0.12 | 0.00 | 0.16 | 0.05 |
| SIO2 | 67.77 | 68.63 | 68.69 | 68.46 | 68.54 | 68.11 | 67.85 | 67.84 | 68.77 |
| AL2O3 | 19.43 | 19.84 | 19.61 | 19.71 | 19.65 | 19.50 | 19.25 | 19.58 | 19.22 |
| MGO | 0.00 | 0.00 | 0.00 | 0.00 | 0.00 | 0.00 | 0.00 | 0.00 | 0.00 |
| CAO | 0.03 | 0.05 | 0.03 | 0.09 | 0.07 | 0.05 | 0.06 | 0.05 | 0.03 |
| MNO | 0.01 | 0.02 | 0.01 | 0.01 | 0.01 | 0.01 | 0.02 | 0.01 | 0.01 |
| FE2O3 | 0.02 | 0.01 | 0.01 | 0.00 | 0.01 | 0.00 | 0.04 | 0.01 | 0.00 |
| SRO | 0.02 | 0.03 | 0.03 | 0.02 | 0.02 | 0.01 | 0.02 | 0.02 | 0.03 |
| BAO | 0.00 | 0.02 | 0.00 | 0.00 | 0.02 | 0.03 | 0.02 | 0.05 | 0.01 |
| PBO | 0.01 | 0.01 | 0.01 | 0.00 | 0.01 | 0.00 | 0.00 | 0.01 | 0.00 |
| NA2O | 11.75 | 11.86 | 11.71 | 11.61 | 11.73 | 11.74 | 11.66 | 11.60 | 11.74 |
| K2O | 0.08 | 0.06 | 0.05 | 0.06 | 0.06 | 0.06 | 0.08 | 0.05 | 0.07 |
| RB2O | 0.04 | 0.05 | 0.04 | 0.05 | 0.05 | 0.05 | 0.06 | 0.05 | 0.06 |
| CS2O | 0.00 | 0.00 | 0.01 | 0.01 | 0.01 | 0.00 | 0.00 | 0.00 | 0.00 |
| TOTAL | 99.15 | 100.69 | 100.39 | 100.22 | 100.38 | 99.67 | 99.04 | 99.43 | 99.97 |
| P5+ | 0.001 | 0.004 | 0.008 | 0.007 | 0.008 | 0.004 | 0.000 | 0.006 | 0.002 |
| SI4+ | 2.988 | 2.980 | 2.987 | 2.983 | 2.983 | 2.986 | 2.995 | 2.981 | 3.004 |
| AL3+ | 1.010 | 1.015 | 1.005 | 1.012 | 1.008 | 1.008 | 1.002 | 1.014 | 0.990 |
| MG2+ | 0.000 | 0.000 | 0.000 | 0.000 | 0.000 | 0.000 | 0.000 | 0.000 | 0.000 |
| CA2+ | 0.001 | 0.002 | 0.001 | 0.004 | 0.003 | 0.002 | 0.003 | 0.002 | 0.001 |
| MN2+ | 0.000 | 0.001 | 0.000 | 0.000 | 0.000 | 0.000 | 0.001 | 0.000 | 0.000 |
| FE3+ | 0.001 | 0.000 | 0.000 | 0.000 | 0.000 | 0.000 | 0.002 | 0.000 | 0.000 |
| SR2+ | 0.001 | 0.001 | 0.001 | 0.001 | 0.001 | 0.000 | 0.001 | 0.001 | 0.001 |
| BA2+ | 0.000 | 0.000 | 0.000 | 0.000 | 0.000 | 0.001 | 0.001 | 0.001 | 0.000 |
| PB2+ | 0.000 | 0.000 | 0.000 | 0.000 | 0.000 | 0.000 | 0.000 | 0.000 | 0.000 |
| NA+ | 1.005 | 0.998 | 0.987 | 0.981 | 0.990 | 0.998 | 0.998 | 0.989 | 0.994 |
| K+ | 0.005 | 0.003 | 0.003 | 0.003 | 0.003 | 0.003 | 0.004 | 0.003 | 0.004 |
| RB+ | 0.002 | 0.002 | 0.001 | 0.001 | 0.001 | 0.002 | 0.002 | 0.001 | 0.002 |
| CS+ | 0.000 | 0.000 | 0.000 | 0.000 | 0.000 | 0.000 | 0.000 | 0.000 | 0.000 |
| $\Sigma T$ | 3.998 | 4.000 | 4.000 | 4.003 | 3.999 | 3.998 | 3.997 | 4.001 | 3.995 |
| $TO_{2-}$ | 1.010 | 1.011 | 0.998 | 1.005 | 1.000 | 1.003 | 1.003 | 1.008 | 0.988 |
| Si+2P/Al-P | 2.961 | 2.957 | 3.009 | 2.983 | 2.999 | 2.985 | 2.986 | 2.968 | 3.044 |
| $\Sigma M$ | 1.011 | 1.003 | 0.991 | 0.986 | 0.995 | 1.003 | 1.003 | 0.993 | 1.000 |
| $M+$ | 1.014 | 1.009 | 0.995 | 0.995 | 1.002 | 1.008 | 1.011 | 1.000 | 1.003 |
| $M^*$ | 0.004 | -0.002 | -0.002 | -0.010 | 0.002 | 0.005 | 0.008 | -0.008 | 0.015 |

-atomic contents normalized to 8 oxygens

-each value represents average of 3-6 data points

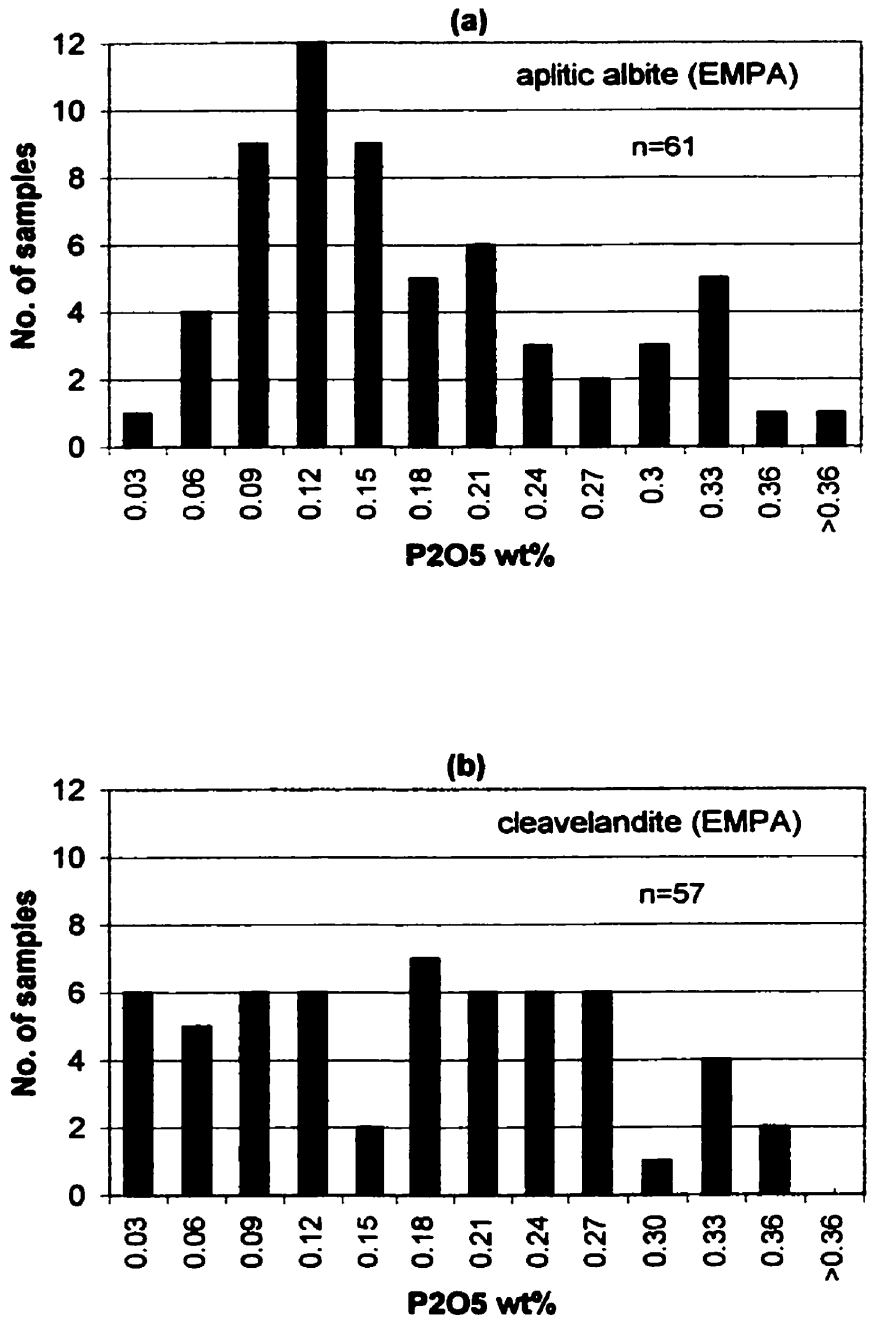


**Figure 7.1** Albite histograms for selected oxides: (a) Type-A; (b) Type-B.

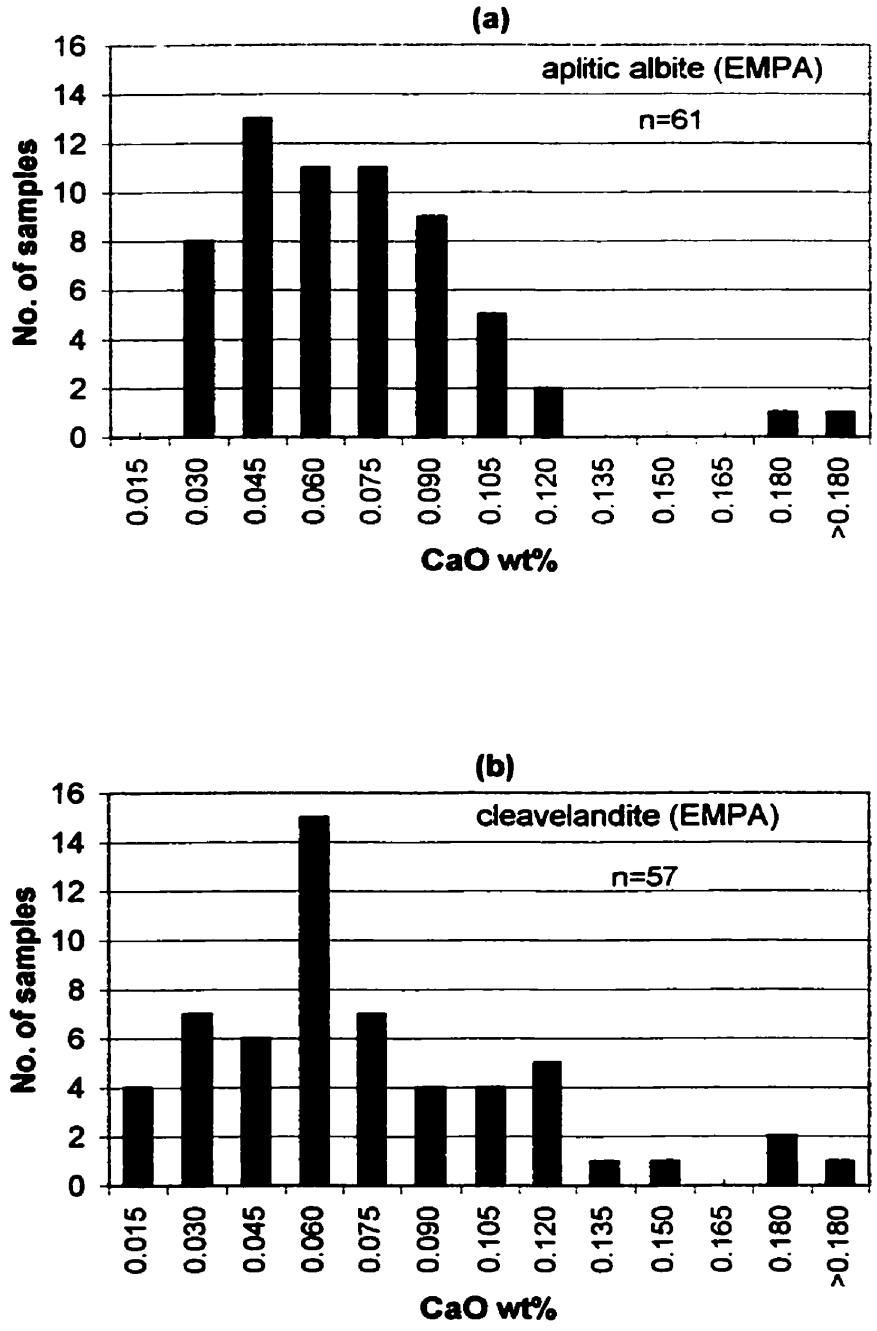


**Figure 7.2** Albite histograms for selected oxides: (a) Type-A; (b) Type-B.

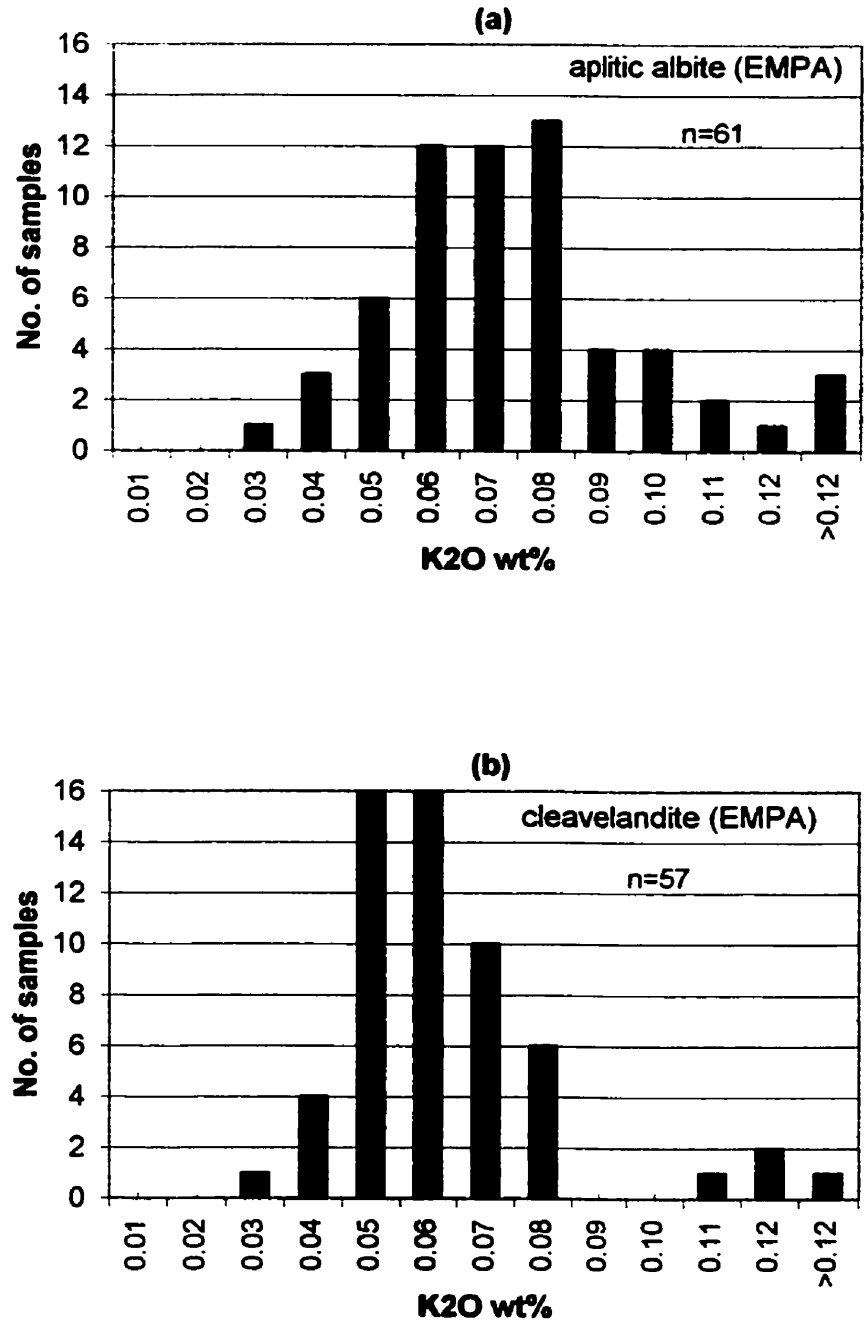


**Figure 7.3** Albite histograms for select oxides: (a) Type-A; (b) Type-B.

**Table 7.2:** Selected oxide (wt%) statistics, per zone, for albite (Types A & B)

**P2O5 - aplitic albite**

| Zone | 10 | 20 | 30 | 40 | 50 | 60 | 70 | 80 | 90 |
|---|---|---|---|---|---|---|---|---|---|
| n | 5 | 11 | 14 | 13 | 4 | 11 | | 3 | |
| max | 0.30 | 0.31 | 0.31 | 0.38 | 0.25 | 0.31 | | 0.29 | |
| min | 0.03 | 0.08 | 0.05 | 0.04 | 0.10 | 0.04 | | 0.15 | |
| average | 0.15 | 0.15 | 0.13 | 0.20 | 0.14 | 0.15 | | 0.21 | |
| STDEV | 0.11 | 0.07 | 0.07 | 0.12 | 0.08 | 0.07 | | 0.07 | |

**P2O5 - cleavelandite**

| Zone | 10 | 20 | 30 | 40 | 50 | 60 | 70 | 80 | 90 |
|---|---|---|---|---|---|---|---|---|---|
| n | 1 | 15 | | 21 | 10 | 3 | 2 | 3 | 2 |
| max | | 0.32 | | 0.35 | 0.35 | 0.24 | 0.23 | 0.16 | 0.17 |
| min | | 0.02 | | 0.01 | 0.06 | 0.02 | 0.00 | 0.03 | 0.05 |
| average | 0.30 | 0.17 | | 0.18 | 0.18 | 0.12 | 0.11 | 0.07 | 0.11 |
| STDEV | | 0.09 | | 0.10 | 0.09 | 0.11 | 0.16 | 0.08 | 0.09 |

**CaO - aplitic albite**

| Zone | 10 | 20 | 30 | 40 | 50 | 60 | 70 | 80 | 90 |
|---|---|---|---|---|---|---|---|---|---|
| n | 5 | 11 | 14 | 13 | 4 | 11 | | 3 | |
| max | 0.17 | 0.19 | 0.10 | 0.10 | 0.04 | 0.11 | | 0.08 | |
| min | 0.03 | 0.03 | 0.03 | 0.02 | 0.03 | 0.03 | | 0.07 | |
| average | 0.08 | 0.07 | 0.06 | 0.06 | 0.03 | 0.07 | | 0.07 | |
| STDEV | 0.06 | 0.04 | 0.02 | 0.03 | 0.00 | 0.03 | | 0.00 | |

**CaO - cleavelandite**

| Zone | 10 | 20 | 30 | 40 | 50 | 60 | 70 | 80 | 90 |
|---|---|---|---|---|---|---|---|---|---|
| n | 1 | 15 | | 21 | 10 | 3 | 2 | 3 | 2 |
| max | | 0.20 | | 0.17 | 0.11 | 0.05 | 0.06 | 0.05 | 0.06 |
| min | | 0.01 | | 0.01 | 0.02 | 0.02 | 0.05 | 0.01 | 0.03 |
| average | 0.09 | 0.08 | | 0.07 | 0.07 | 0.04 | 0.06 | 0.03 | 0.05 |
| STDEV | | 0.06 | | 0.04 | 0.03 | 0.02 | 0.01 | 0.02 | 0.03 |

**K2O - aplitic albite**

| Zone | 10 | 20 | 30 | 40 | 50 | 60 | 70 | 80 | 90 |
|---|---|---|---|---|---|---|---|---|---|
| n | 5 | 11 | 14 | 13 | 4 | 11 | | 3 | |
| max | 0.12 | 0.10 | 0.11 | 0.13 | 0.08 | 0.13 | | 0.13 | |
| min | 0.05 | 0.04 | 0.04 | 0.04 | 0.06 | 0.03 | | 0.05 | |
| average | 0.08 | 0.08 | 0.07 | 0.07 | 0.07 | 0.07 | | 0.09 | |
| STDEV | 0.03 | 0.02 | 0.02 | 0.02 | 0.01 | 0.03 | | 0.04 | |

**K2O - cleavelandite**

| Zone | 10 | 20 | 30 | 40 | 50 | 60 | 70 | 80 | 90 |
|---|---|---|---|---|---|---|---|---|---|
| n | 1 | 15 | | 21 | 10 | 3 | 2 | 3 | 2 |
| max | | 0.12 | | 0.13 | 0.11 | 0.06 | 0.08 | 0.07 | 0.07 |
| min | | 0.04 | | 0.03 | 0.04 | 0.05 | 0.05 | 0.05 | 0.06 |
| average | 0.03 | 0.06 | | 0.06 | 0.06 | 0.06 | 0.06 | 0.06 | 0.06 |
| STDEV | | 0.02 | | 0.02 | 0.02 | 0.01 | 0.02 | 0.01 | 0.00 |

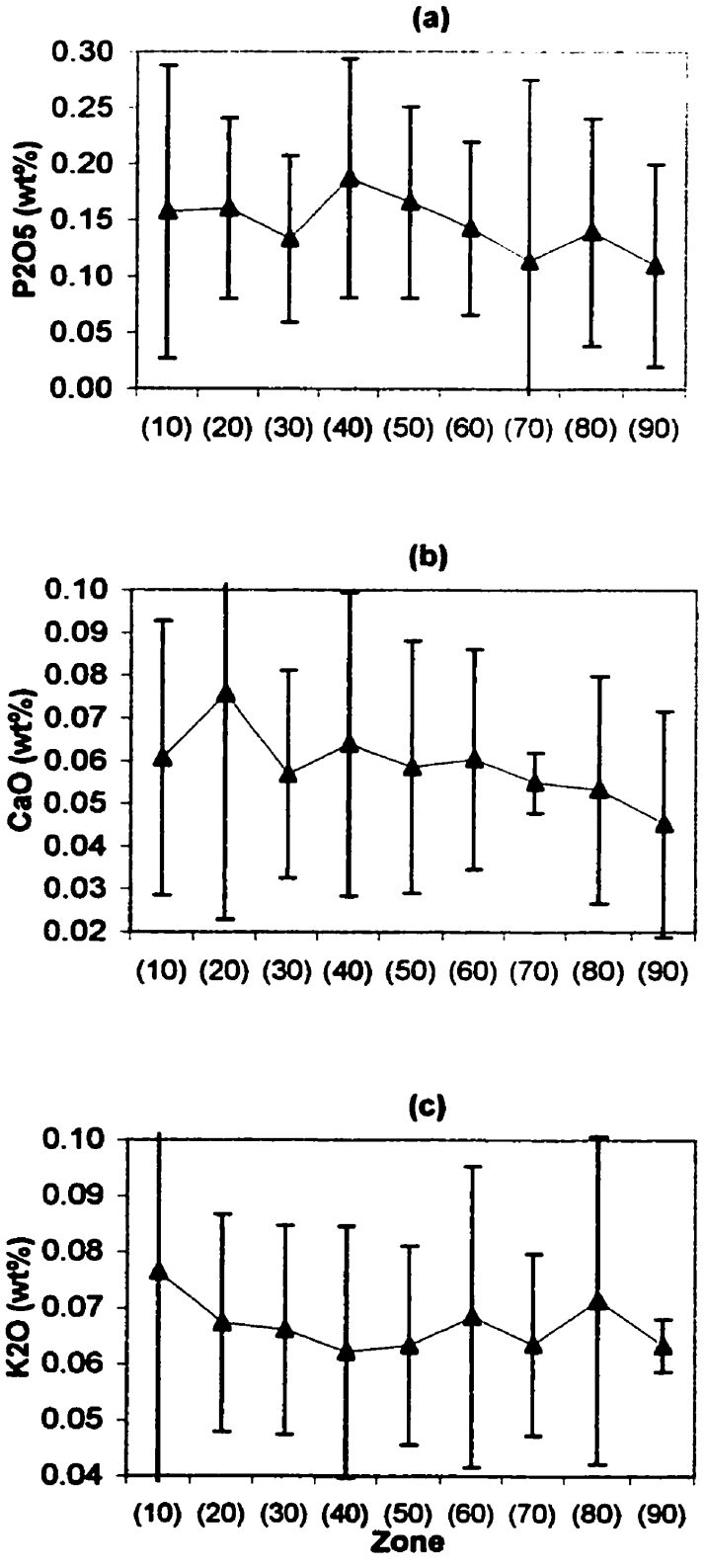


**Figure 7.4** Average oxide contents per zone (EMPA data) collectively for all albite Types A+B. Deviation: +/- 1σ

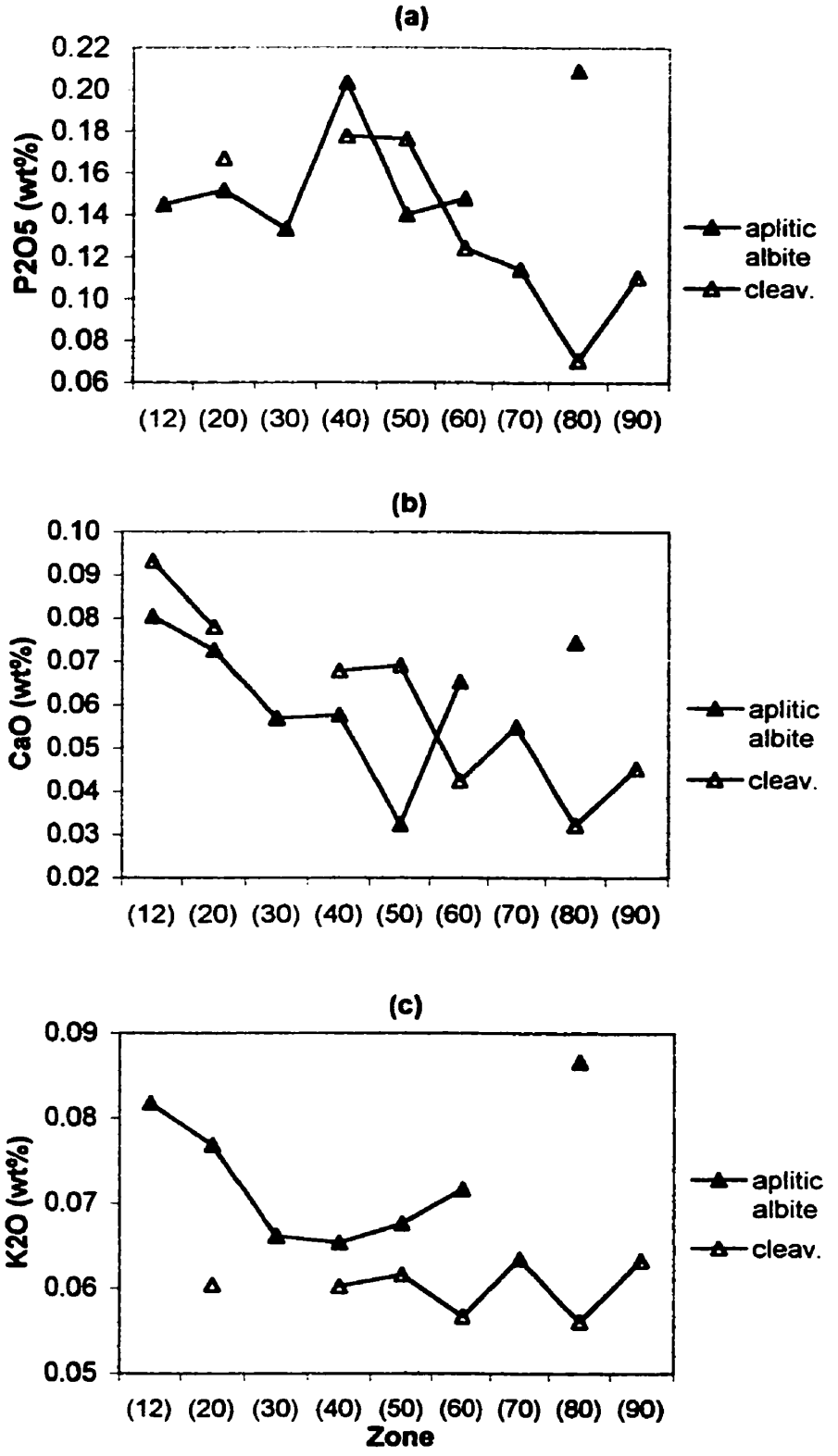


**Figure 7.5** Average oxide contents per zone (EMPA data) for aplitic albite (Type A), and cleavelandite (Type B).

zone (Figure 7.5b) drop steadily from a maximum of 0.08 wt% in zone (10) to a minimum of 0.03 wt% in zone (50). Subsequent CaO averages increase irregularly inwards from zone (50), with a second maximum average of 0.07 wt% attained in zone (80).

Potassium ranges from 0.03-0.13 wt% $K_2O$ (Table 7.2), with a Gaussian distribution (Figure 7.4A) and steadily declining average $K_2O$ from outer to inner zones (Figure 7.5c). Only the maximum average of 0.09 wt% $K_2O$ in zone (80) is inconsistent with this trend.

**Type B:** *cleavelandite* (10,20,40,50,60,70,80,90)

Cleavelandite occurs as white to light-grey, subparallel to radiating plates up to 10 cm in length, that form aggregates consisting almost entirely of albite, locally with minor muscovite, lithiophilite, and Sn-Ta-Nb-oxide minerals. In zone (20), cleavelandite like platy albite is commonly in contact with quartz, euhedral schorl, and books of euhedral muscovite to form the characteristic 'leopard-rock' texture (Figure 7.8). A similar mineral assemblage and texture is found in zone (40), commonly with lithiophilite but almost always without schorl. In zones (40) and (50), radial rims of cleavelandite commonly form in contact with large amblygonite-montebrasite crystals, microcline-perthite and spodumene + quartz intergrowth after petalite. Cleavelandite in zones (60) and (90) is commonly associated with lepidolite. In zones (70) and (80), cleavelandite is only found in transitional mineral assemblages with adjacent zones.

*Chemical Composition*

Phosphorus in cleavelandite ranges from below detection to 0.35 wt% $P_2O_5$ (Table 7.2). There is a remarkably uniform frequency distribution in Figure 7.1b. Twelve percent of cleavelandite compositions are greater than 0.30 wt% $P_2O_5$.

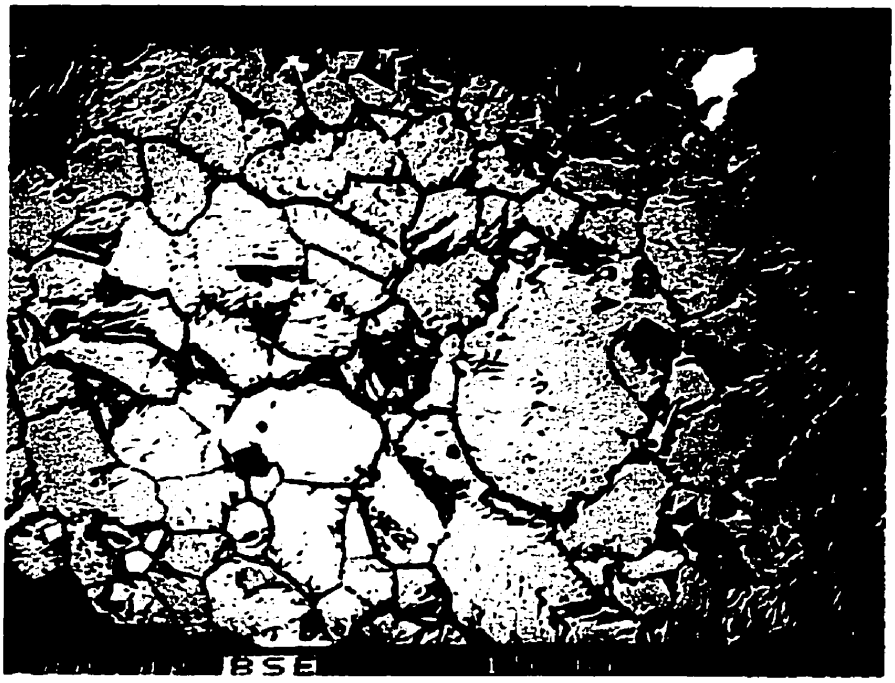


**Figure 7.6** BSE image of aplitic albite showing individual subhedral grains of relatively uniform sizes. Field of view is 500 μm.

**Figure 7.7** Line rock with bulbous aplitic albite apophyses and haloes of black tourmaline (schorl) and fine grained Ta/Nb oxides, in contact with smoky quartz and white euhedral crystals of cesian-beryl. Upper-right corner consists of white cleavelandite, intergrown with radiating tourmaline partially altered to mica. Location: near contact between zones (60) and (30).

**Figure 7.8** Hand sample of 'leopard rock' from zone (20). Assemblage comprises coarse columnar black schorl, coarse blebs of grey quartz, and a network of medium-platy white cleavelandite, plus minor fine-grained muscovite, aplitic albite (top left), and K-feldspar (pink patches).

Averages in Figure 7.5a attain a maximum of 0.18 wt% $P_2O_5$ in zones (40) and (50), and then gradually decline towards inner zones.

Calcium ranges from 0.01 to 0.29 wt% CaO (Table 7.2). The distribution (Figure 7.2b) is close to Gaussian, centered on a distinct frequency peak between 0.05 and 0.06 wt%. Calcium averages by zone (Figure 7.5b) decrease steadily from 0.09 wt% CaO in zone (10), to 0.04 wt% in zone (60). Subsequent averages vary irregularly, with a minimum average of 0.03 occurring in zone (80).

Potassium ranges from 0.03 to 0.13 wt% $K_2O$ (Table 7.2), with a tight Gaussian data distribution (Figure 7.3b), and constant average compositions by zone (Figure 7.5c), close to 0.06 wt% $K_2O$.

**Other trace-element contents in albite** *(Types A,B)*

Lithium content of albite, determined by SIMS, is considerably lower than that of Type-1 K-feldspar (Table 7.3), with a range between 0.11 to 1.66 ppm.

Average Sr and Mn contents (Appendix IV) in 'primary' albite are invariably below EMP detection limits (Appendix I: SrO = 0.059 wt%, MnO = 0.025 wt%). Twenty-three percent of individual point values for SrO were above this limit (K-feldspar: 47%), and 34% of point values for Mn were above this limit (K-feldspar: 4%). Existing data for SrO range from 0.00 to 0.06, averaging 0.02 wt%; MnO varies between 0.00 to 0.02, averaging 0.01 wt%. Most if not all Sr can be assumed radiogenic, migrated from Rb-rich phases (see comments on Sr in Chapter 6).

Beryllium is very low in albite (0.2 to 6.7 ppm; Table 7.3), comparable to concentrations in blocky K-feldspar (Table 6.6).

Gallium was determined at Ecole Polytechnique for cleavelandite and comparable coarse varieties. Gallium values slightly increase from 46 to 125 ppm with increasing Al, but average zone contents vary erratically (see Chapter 8, Figures 8.2a,b, 8.3i).

Boron concentration is very low, ranging from 0.8 to 10.2 ppm (Table 7.3). The spread of data overlaps with that determined for Type-1 K-feldspar (Table 6.6).

**Crystal-chemistry** ***(aplitic albite and cleavelandite)***

Deviation from ideal Si/Al ratio, due to the berlinite substitution (Figure 7.9), is not as prominent as in K-feldspar (Figures 6.12a,b). Atomic ranges of Si and Al (Figure 7.9a) are also smaller with Si ranging from ~3.00 to 2.955 apfu, and Al ranging from 1.00 to 1.03 apfu. Correcting for the berlinite substitution results in almost perfect stoichiometry (Figure 7.9b) with average Si+Al+P = 4.000 +/- 0.002. The (Si+2P)/(Al-P) ratio varies from 2.928 to 3.044, with an average of 2.974 +/- 0.020. The tetrahedral framework charge ($TO^{2-}$) determined as *Al-P* (Figures 7.9b,7.10a,b), ranges from 0.995-1.018 apfu with an average of 1.006 +/- 0.005. This is nearly perfectly balanced by the *M*-cation charge (*M+*) (Figures 7.11b, 7.13a,b), with a range of 0.984 to 1.027 pfu, and an average of 1.005 +/- 0.007.

The distribution of data points parallel to vector [2] in Figures 7.11, 7.12, and 7.13 suggests possible vacancy substitution. Shifts along the *M*-cation deficiency trends, vector [3], are generally not significant. The average *M*-cation deficiency as determined

**Table 7.3:** Individual albite SIMS analyses.

| Sample | grain | Zone | Type | Li (ppm wt) | B (ppm wt) | Be (ppm wt) |
|---|---|---|---|---|---|---|
| L-12-M | M-1 | 20 | A | 1.60 | 2.4 | 2.7 |
| L-12-M | M-2 | 20 | A | 0.96 | 1.7 | 1.48 |
| 95-08-N | N-1 | 20 | B | 1.66 | 1.35 | 0.25 |
| 95-08-N | N-2 | 20 | B | 0.53 | 10.2 | 3.9 |
| C-096-U | U-1 | 30 | A | 0.43 | 7.2 | 6.4 |
| C-096-U | U-2 | 30 | A | 0.13 | 7.8 | 1.5 |
| C-033-P | P-1 | 40 | A | 0.34 | 6.2 | 3.0 |
| C-033-P | P-2 | 40 | A | 0.38 | | 3.5 |
| C-033-W | W-1 | 40 | B | 0.36 | 4.8 | 4.4 |
| C-033-W | W-2 | 40 | B | 0.23 | 4.4 | 5.7 |
| L-12-G | G-2 | 50 | A | | 8.5 | 2.2 |
| L-12-G | G-1 | 50 | A | 0.60 | 4.9 | 6.0 |
| C-045-I | I-2 | 50 | B | 0.18 | 1.6 | 0.62 |
| C-045-I | I-1 | 50 | B | 0.12 | 0.82 | 0.19 |
| C-045-M | M-1 | 60 | A | 0.11 | 6.6 | 2.5 |
| C-045-M | M-2 | 60 | A | 0.16 | 8.2 | 5.3 |
| C-033-U | U-1 | 60 | B | 0.3 | 2.4 | 1.02 |
| C-033-U | U-2 | 60 | B | 0.29 | 1.6 | 0.81 |
| 12-15-15 | 15-2 | 80 | B | 1.3 | 1.96 | 1.4 |
| 12-15-15 | 15-1 | 80 | B | 1.17 | 1.03 | 0.26 |
| 1C-10 | 10-1 | 90 | B | 0.97 | 6.5 | 3.3 |
| 1C-10 | 10-2 | 90 | B | 1.16 | 9.7 | 6.7 |
| | | max | | 1.66 | 10.2 | 6.7 |
| | | min | | 0.11 | 0.8 | 0.2 |
| | | **average** | | **0.62** | **4.8** | **2.9** |
| | | 1σ | | 0.51 | 3.1 | 2.1 |

by the equation ($M^* = M^+ - TO^{2-}$) is -0.002 +/- 0.007; minimum $M^*$ is –0.017 pfu. Both the $\square Si_4O_8$ and *M*-cation deficiency trends are within the limits of analytical error. However, a significant shift is observed along the plagioclase-type substitution vector [1]. This is consistent with slightly elevated contents of divalent *M*-cations ($Ca^{2+}$ = 0.000 to 0.010, $\bar{x}$ = 0.003 apfu +/- 0.001; and Ca+Ba+Sr = 0.001 to 0.011, $\bar{x}$ = 0.004 +/-.002).

Figures 7.10, 7.12, and 7.13 each contain two mutually complementary diagrams {a,b}, one depicting variations in crystal-chemistry by zone, the other, variations in crystal-chemistry by mineral type (*i.e.* aplitic albite *vs.* cleavelandite). Data shown in Figures 7.10b, 7.12b, and 7.13b indicate that there are no significant crystal-chemical differences between aplitic albite and cleavelandite, except that aplitic albite, in general, exhibits a slightly greater range of values.

**Structural state** *(aplitic albite and cleavelandite)*

X-ray powder-diffraction data for albite Types A+B are presented in Table 7.4. On the c-b plot (Figure 7.14) data points cluster tightly around the ideal low-albite endpoint. Data points within the cluster differentiated by zone (Figure 7.14b), and by albite variety (Figure 7.14c) show no significant trends. 1σ-standard deviations of the albite unit-cell dimensions (Table 7.4) fall within average analytical errors and preclude any meaningful correlations amongst the different unit-cell dimensions, or in comparison to trace-element contents.

**Type C:** *saccharoidal albite* **(40,50)**

Saccharoidal albite is defined as a very fine-grained paragenetically late variety of albite that typically forms in the interior parts of pegmatite dykes, and displays metasomatic contacts with neighboring pegmatite minerals. To date, no unequivocally identifiable

saccharoidal albite has been found in the Tanco pegmatite. Aplitic albite from zone (30) can be texturally similar, and occasionally displays replacement-like embayments into minerals of adjacent zones. Also, somewhat coarser-grained albite locally replaces K-feldspar and spodumene + quartz pseudomorphs after petalite in zones (40) and (50). However, some bulbous masses and embayments resembling metasomatic replacement could also be generated by inwardly moving crystallization fronts, that reacted and partly resorbed adjacent mineral assemblages, by magmatic processes involving constitutional zone refining (Morgan and London, 1999).

Distinguishing between aplitic albite and saccharoidal albite in the field can be difficult, particularly when the only samples available are from drill core. For these reasons, saccharoidal albite was not sampled as a separate category in this study, but samples resembling this variety were ranked with the perceptually and spatially closest type, A or B.

**Type D:** *metasomatic albite* **veins in pollucite zone (80)**

Off-white to medium-grey veins of granular to tabular albite, a few to 20 mm across, form locally a polygonal network in pollucite of zone (80), texturally similar to the network composed of the non-perthitic microcline veins (K-feldspar, Type 3) (Černý and Simpson, 1978). This generation of albite, associated with minor quartz, was so far not analyzed.

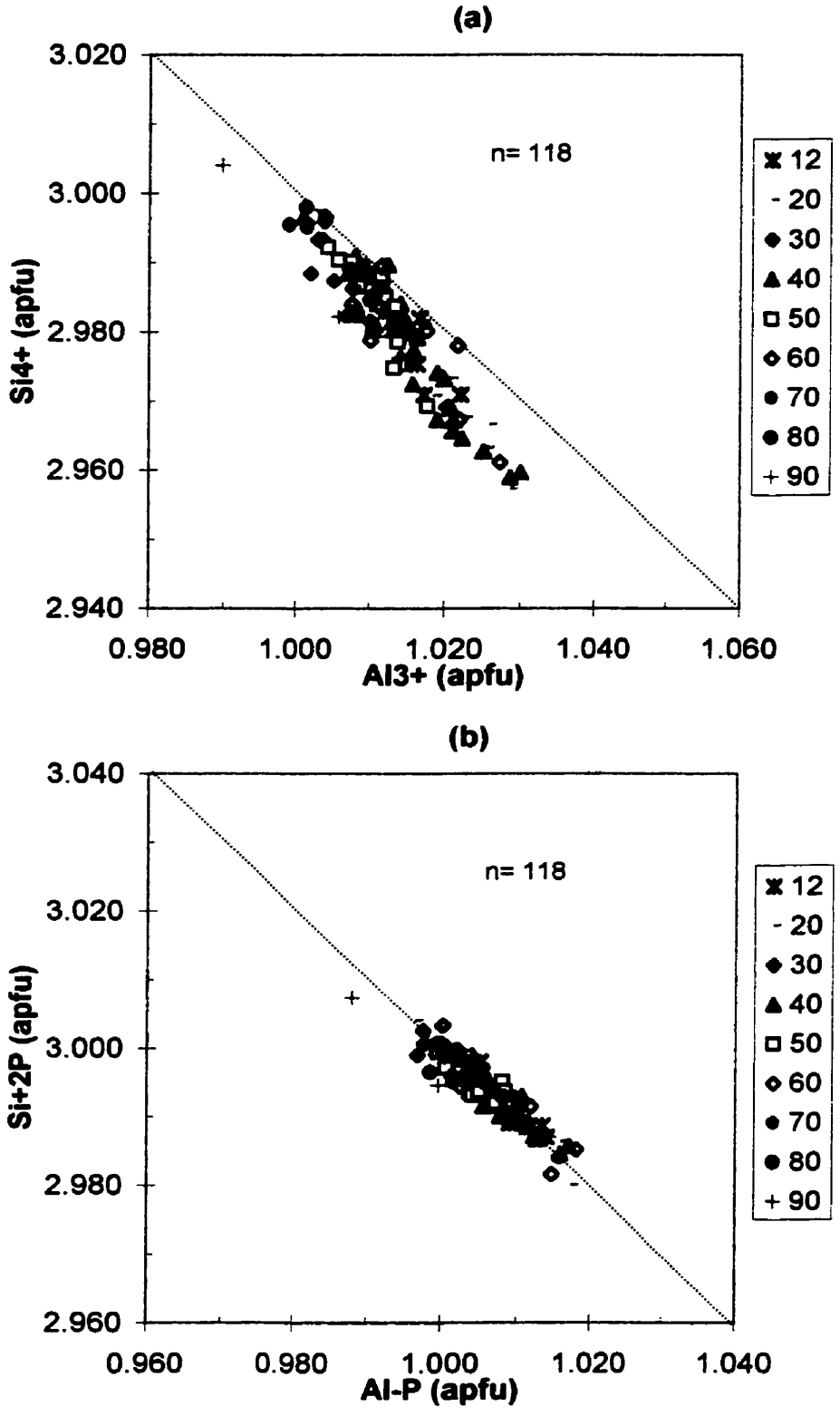


**Figure 7.9** **(a)** Si and Al atomic contents in albite (Types A+B). **(b)** corrected for berlinite substitution. In both diagrams, dashed diagonal represents sum of tetrahedral cations *($\Sigma T = 4.000$)*.

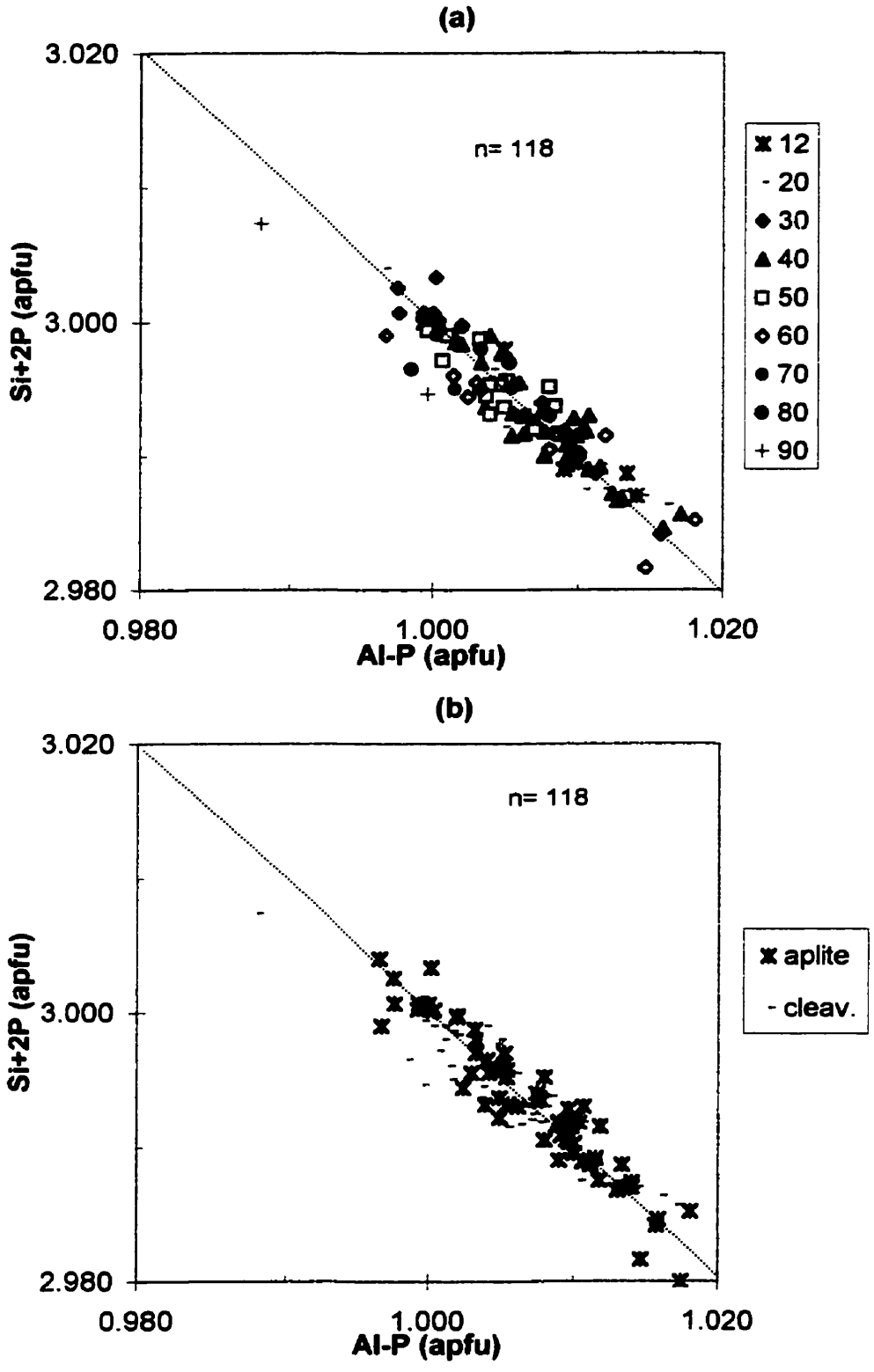


**Figure 7.10** Tetrahedrally coordinated cations in albite: **(a)** designated by zone (Types A + B); **(b)** designated by mineral variety (Types A,B). Compare scale change to Fig. 7.9. Diagonal line represents *($\Sigma T = 4.000$)*.

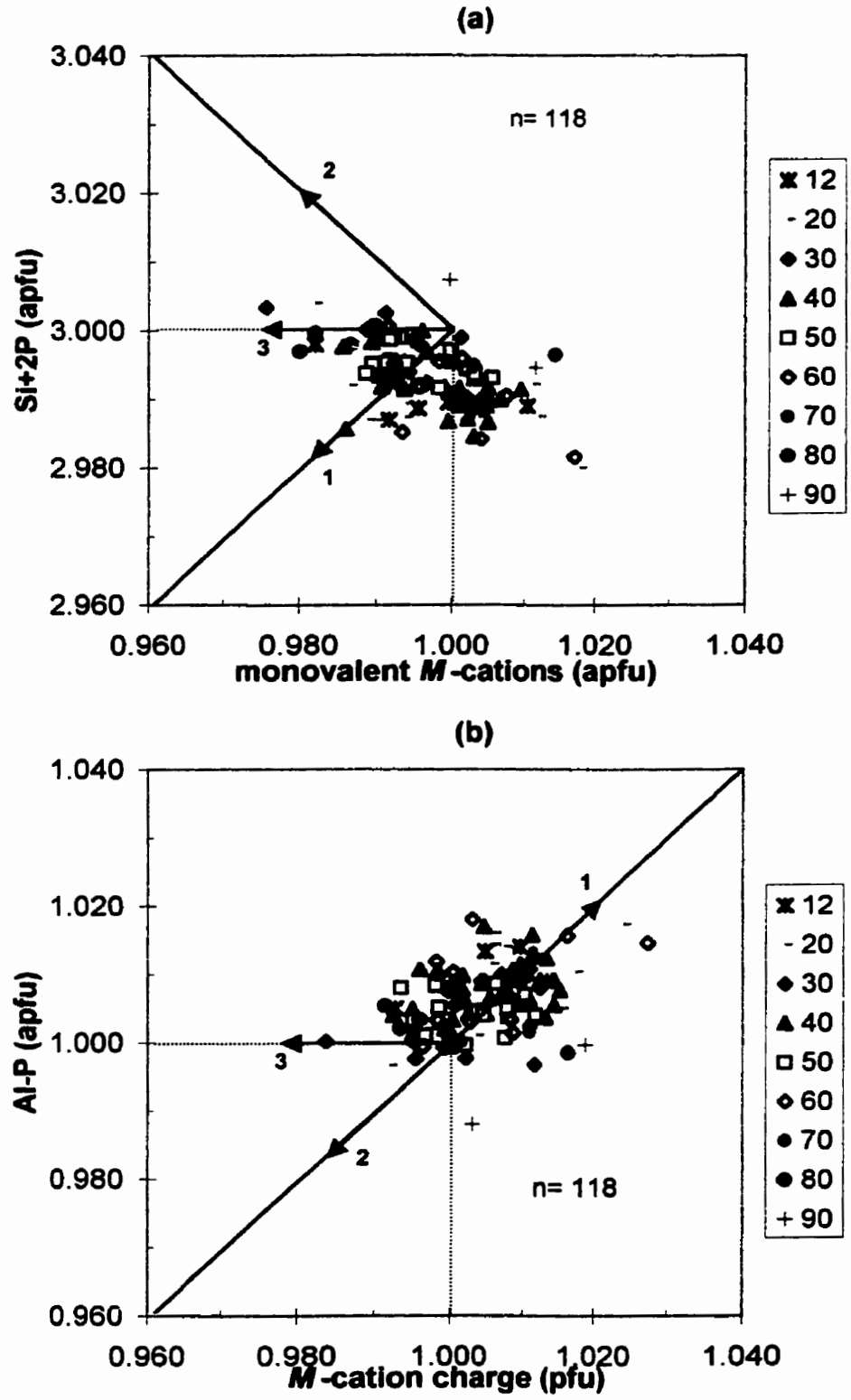


**Figure 7.11** Stoichiometry and charge balance in albite (Types A+B): (**a**) *Si+2P vs.* Σ*M*; (**b**) Al-P vs. *M+*, diagonal line indicates *M+ - TO2-* = 0. [**1**] plagioclase substitution trend, [**2**] vacancy substitution trend, [**3**] *M*-cation deficiency trend.

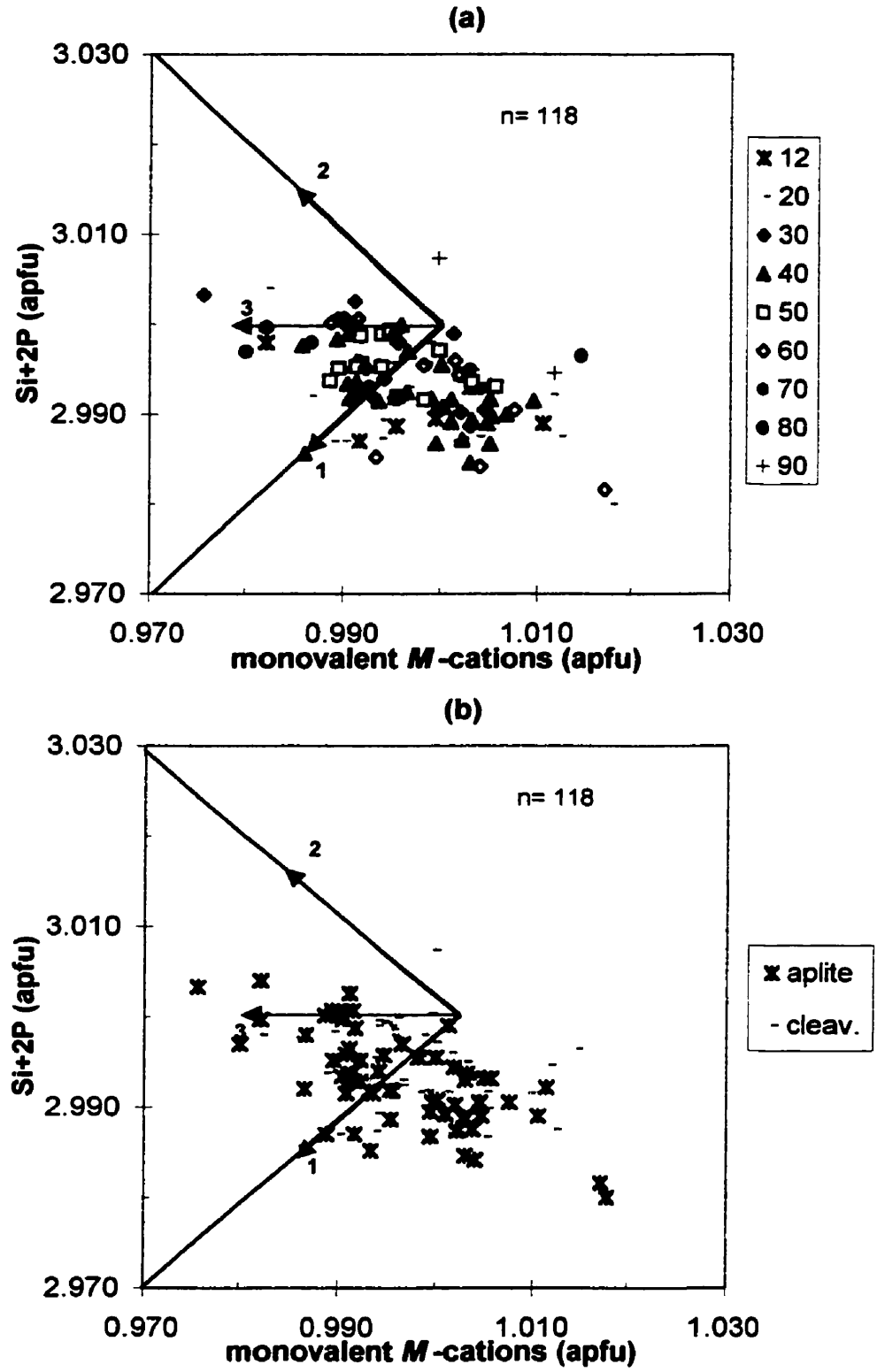


**Figure 7.12** Stoichiometry in albite: **(a)** designated by zone (Types A + B); **(b)** designated by mineral variety (Types A,B). Compare scale change from Fig. 7.11. Substitution vectors as in Figure 7.11a.

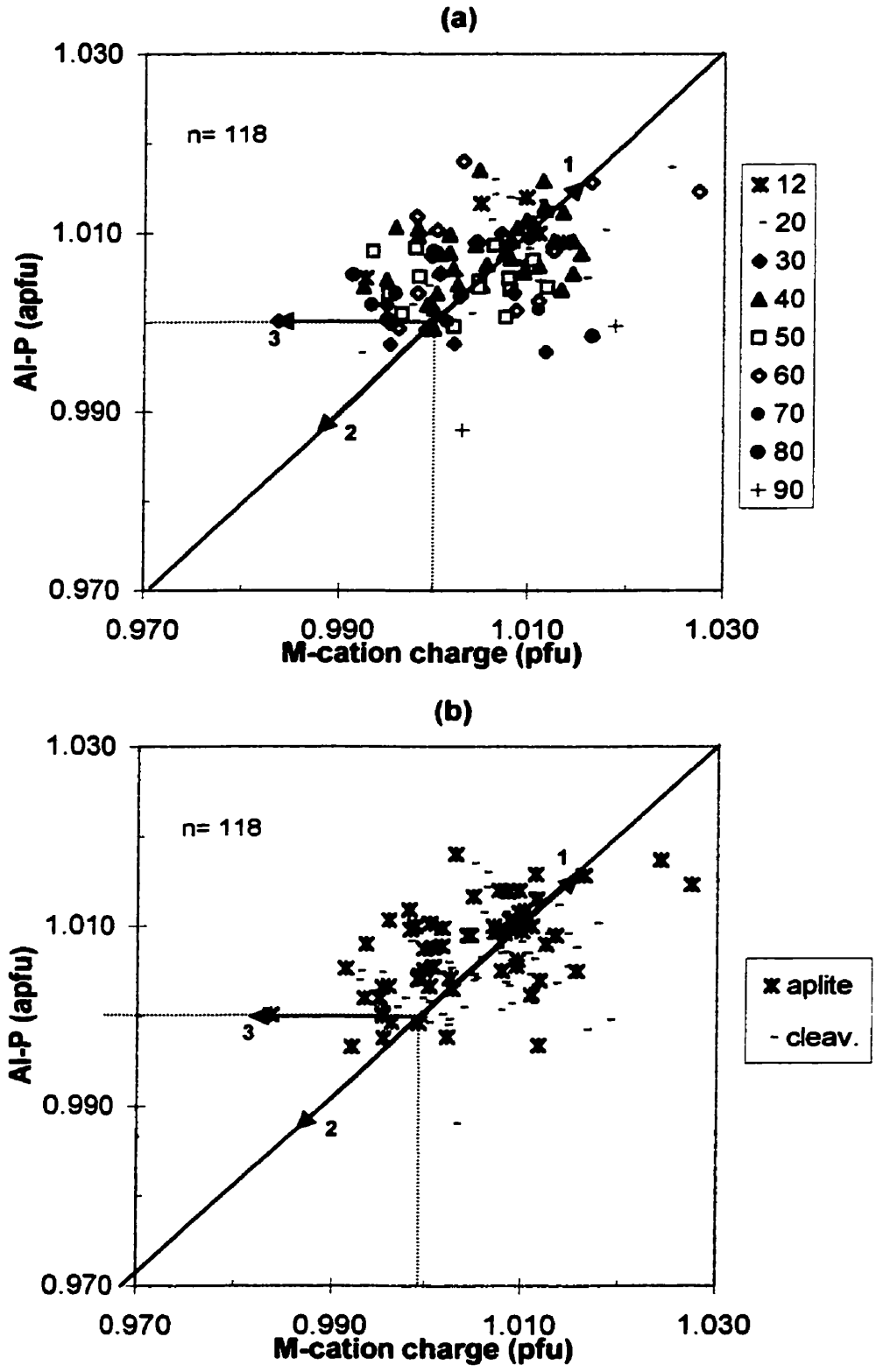


**Figure 7.13** *T*-cation charge ($TO^{2-}$=Al-P) vs. *M*-cation charge ($M^{+}$) in albite (Types A+B). (a) designated by zone; (b) designated by mineral variety. Compare scale change from Fig. 7.11. Substitution vectors as in Fig. 7.11b.

**Table 7.4:** Albite (Types A,B) unit-cell parameters.

| Sample | Zone | Type | a (Å) | b (Å) | c (Å) | α (°) | β (°) | γ (°) | V (Å$^3$) |
|---|---|---|---|---|---|---|---|---|---|
| SLW-3C | 12 | A | 8.138(1) | 12.787(1) | 7.1589(9) | 94.223(8) | 116.59(2) | 87.76(1) | 664.3 |
| SLE-24 | 12 | B | 8.139(2) | 12.786(2) | 7.162(1) | 94.28(1) | 116.65(2) | 87.73(2) | 664.3 |
| 76-05-H | 20 | A | 8.140(1) | 12.7863(9) | 7.1610(7) | 94.248(6) | 116.62(1) | 87.74(1) | 664.5 |
| L-12-M | 20 | A | 8.139(3) | 12.789(2) | 7.158(2) | 94.19(2) | 116.61(3) | 87.76(3) | 664.4 |
| 95-08-N | 20 | B | 8.139(4) | 12.786(3) | 7.161(2) | 94.23(2) | 116.63(4) | 87.70(4) | 664.4 |
| L-12-D | 20 | B | 8.142(3) | 12.788(2) | 7.162(2) | 94.25(2) | 116.62(3) | 87.75(3) | 664.8 |
| 76-23-J | 30 | A | 8.133(3) | 12.785(2) | 7.158(2) | 94.25(1) | 116.58(3) | 87.71(2) | 663.7 |
| C-096-U | 30 | A | 8.139(2) | 12.782(2) | 7.159(1) | 94.25(1) | 116.62(3) | 87.73(2) | 664.0 |
| 12-15-11 | 30 | A | 8.138(3) | 12.790(3) | 7.160(2) | 94.26(2) | 116.60(4) | 87.71(3) | 664.5 |
| 12-15-13 | 30 | A | 8.138(2) | 12.791(1) | 7.162(1) | 94.26(1) | 116.62(2) | 87.73(2) | 664.6 |
| L-12-K | 40 | A | 8.136(2) | 12.792(2) | 7.158(2) | 94.25(1) | 116.57(3) | 87.70(2) | 664.6 |
| C-033-O | 40 | B | 8.138(2) | 12.787(2) | 7.160(1) | 94.24(1) | 116.58(2) | 87.71(2) | 664.5 |
| C-033-X | 40 | B | 8.136(1) | 12.7870(8) | 7.1614(7) | 94.272(8) | 116.61(1) | 87.71(1) | 664.3 |
| C-045-S | 40 | B | 8.147(3) | 12.792(2) | 7.160(1) | 94.20(1) | 116.61(2) | 87.80(2) | 665.3 |
| 86-07-P | 50 | A | 8.141(2) | 12.789(2) | 7.162(1) | 94.25(1) | 116.64(2) | 87.74(2) | 664.7 |
| L-12-G | 50 | A | 8.136(2) | 12.787(1) | 7.160(1) | 94.26(1) | 116.61(2) | 87.73(2) | 664.1 |
| B-06-B | 50 | B | 8.138(2) | 12.786(1) | 7.156(1) | 94.24(1) | 116.58(2) | 87.77(2) | 664.0 |
| C-E | 50 | B | 8.140(3) | 12.792(2) | 7.157(2) | 94.22(2) | 116.62(3) | 87.72(3) | 664.5 |
| C-045-M | 60 | A | 8.138(2) | 12.783(2) | 7.160(2) | 94.24(1) | 116.60(3) | 87.72(2) | 664.1 |
| C-107-F | 60 | A | 8.136(2) | 12.785(2) | 7.158(1) | 94.28(1) | 116.61(2) | 87.70(2) | 663.9 |
| 92-11-H | 60 | B | 8.137(3) | 12.789(3) | 7.166(3) | 94.29(3) | 116.65(4) | 87.69(4) | 664.6 |
| C-033-U | 60 | B | 8.139(2) | 12.782(1) | 7.162(1) | 94.30(1) | 116.61(2) | 87.67(2) | 664.3 |
| C-K | 63 | B | 8.139(1) | 12.786(1) | 7.1588(9) | 94.235(8) | 116.59(2) | 87.76(1) | 664.3 |
| C-F | 70 | B | 8.140(2) | 12.791(1) | 7.155(1) | 94.218(9) | 116.58(2) | 87.76(2) | 664.4 |
| 12-15-15 | 80 | B | 8.139(3) | 12.787(2) | 7.160(2) | 94.23(1) | 116.58(3) | 87.70(2) | 664.5 |
| Poll-4 | 80 | B | 8.139(3) | 12.787(2) | 7.156(1) | 94.23(1) | 116.60(3) | 87.72(2) | 664.0 |
| 1C-10 | 90 | B | 8.139(1) | 12.786(1) | 7.1594(9) | 94.270(8) | 116.60(2) | 87.72(1) | 664.4 |
| | | | | | | | | | |
| max | | | 8.147 | 12.792 | 7.166 | 94.30 | 116.65 | 87.80 | 665.3 |
| min | | | 8.133 | 12.782 | 7.155 | 94.19 | 116.57 | 87.67 | 663.7 |
| **average** | | | **8.139** | **12.787** | **7.160** | **94.25** | **116.61** | **87.73** | **664.4** |
| stdev | | | 0.003 | 0.003 | 0.002 | 0.03 | 0.02 | 0.03 | 0.3 |

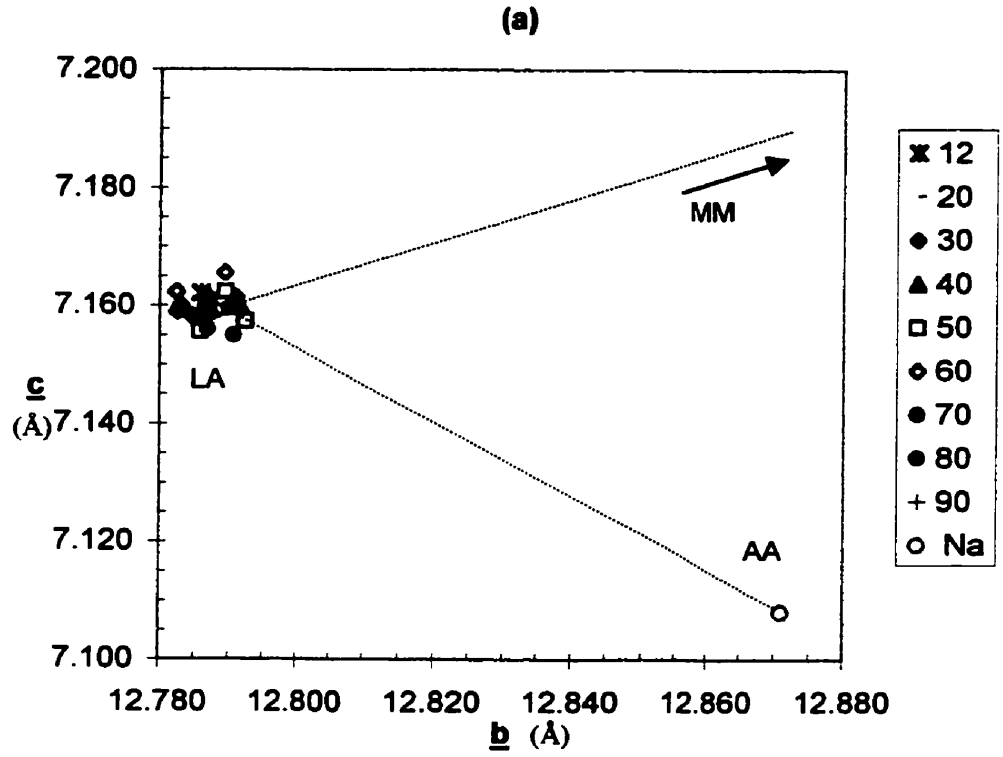


**Figure 7.14** Albite (Types A,B) unit-cell parameters. AA-analbite, LA-low albite (open circle parameters from Černý et al., 1985b)

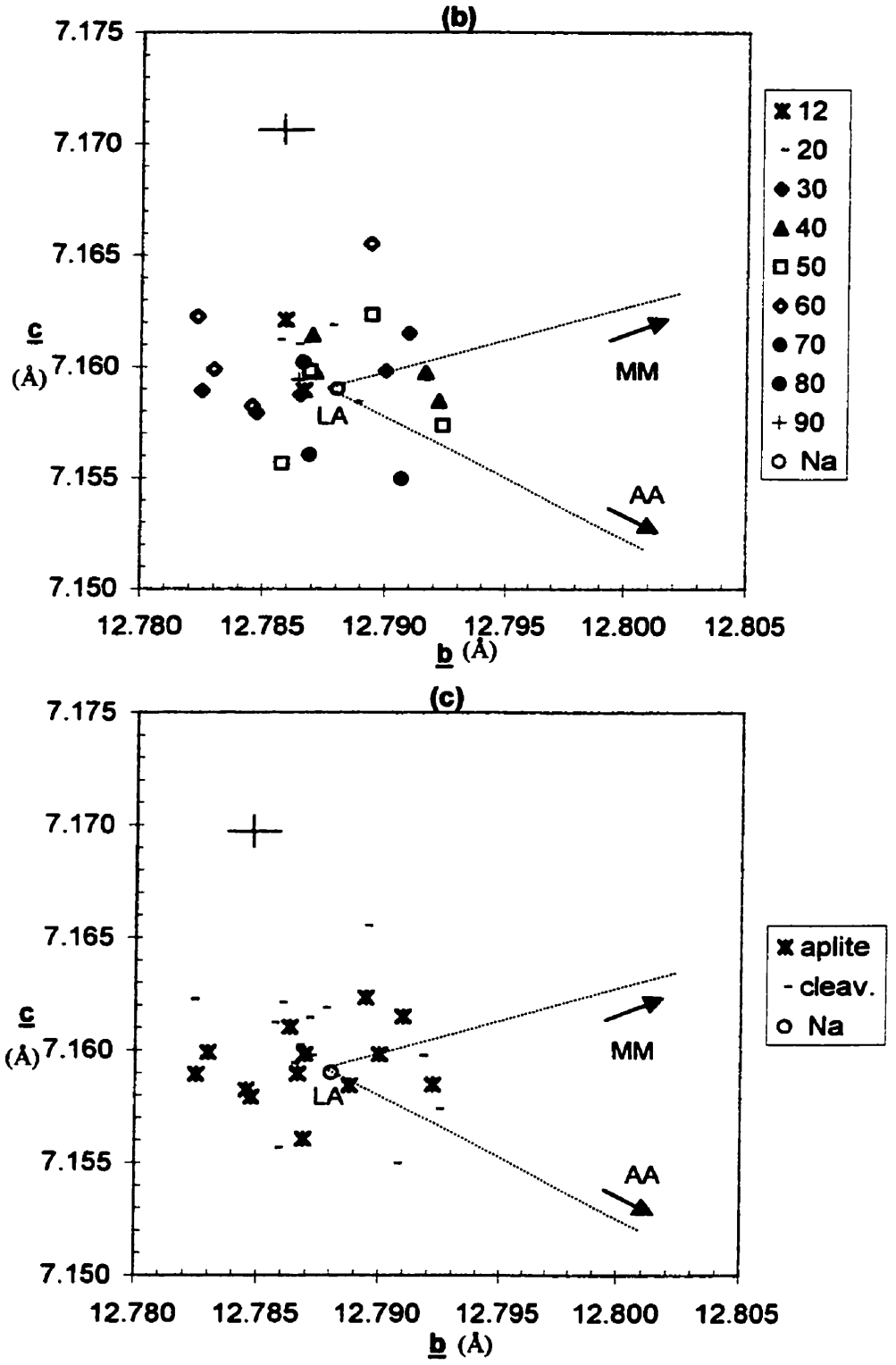


**Figure 7.14** Albite (Types A,B) unit-cell dimensions. (b) designated by zone (c) designated by mineral type (A or B)
Cross-hairs represent average standard error (+/- 1σ).

**Type E: anhedral albite associated with Type-4 K-Rb-feldspar**

This albite is closely associated with Type-4 K-Rb-feldspar, metasomatic after microcline Type-3 and adjacent pollucite along the contacts of these two phases in zone (80). However, the abundance of its anhedral to dendritic grains is much lower than that of the K-Rb phases. This feldspar was not quantitatively analyzed, but identified as such by Teertstra (1997, Fig. 4.20A, 4.20B)

**Type F:** *albite crystals* in leaching cavities zones (40) (50)

Tiny tabular crystals of albite, flattened parallel to {010} and less than 2mm in maximum dimension, are associated with Type-6 adularia, cookeite, cesian analcime, apatite and clay minerals in leaching cavities of zones (40) and (50). P. Vanstone (personal comm., 2001) reported the occurrences of two cavities in the upper portions of zone 50 (45?), "Both cavities were lined with albite crystals, quartz crystals, and an irregular overcoating of brown apatite. There were apatite textures reminiscent of possibly petalite and tourmaline or spodumene. In both cases, the cavities were in a mass of cleavelandite and the albite crystals may have been, in part, terminations of the enclosing cleavelandite blades." Černý (1972) observed that, "Albite is rather rare, and is found only where the matrix surrounding the secondary assemblage contains cleavelandite. Thus, it seems to be formed only by recrystallization, more or less *in situ*. Albite forms platy crystals flattened on {010}, with {001} and {10 $\bar{1}$} predominant over prismatic faces. Simple albite twins are most common, occasionally lamellar twinning parallel to {010} is also observed, and the extinction angles of these polysynthetic twins on {010} suggest the possible presence of other twinning laws. The crystals are usually etched and exhibit a silky dull luster. Oriented overgrowths of adularia on {001} and {10 $\bar{1}$} are common."

Unit-cell dimensions and optical properties from a single sample indicate essentially pure low albite (Ćerný, 1972), with the following cell parameters: $\underline{a}$ = 8.138(3) (Å), $\underline{b}$ = 12.786(4) (Å), $\underline{c}$ = 7.158(1) (Å), $\alpha$ = 94.24(2)°, $\beta$ = 116.62(1)°, $\gamma$= 87.74(2)° , V ($Å^3$) = 664.0 (0.2).

# CHAPTER 8: GEOCHEMICAL EVOLUTION

This chapter presents bulk-geochemical considerations beginning with those of blocky K-feldspar (Type 1) and albite (Types A and B), followed by late K-(Rb)-feldspars (Types 2-6). For the Type-1 K-feldspar, emphasis is placed on the spatial distribution of minor and trace-elements by: i) comparing average compositions in the different individual zones, and ii) assessing compositional variations within single zones along north-south and east-west transects, and finally iii) assessing compositional variability within single large crystals. For albite (Types A and B), and K(Rb)-feldspar (Types 2-6), emphasis is placed on the compositional ranges of the respective types.

Geochemical variations by zone for blocky K-feldspar (Type 1), and albite (Types A,B) are presented in Figures 8.1a-r, and Figures 8.2a-d, respectively, followed by a summary of average elemental ratios by zone, in Figures 8.3a-k. Variations in K-feldspar compositions and element ratios, within individual zones, along the 9700N east-to-west transect, and along the two north-to-south transects (10200E, 9100E), are presented for zone (20) (Figures 8.4a-h, 8.5a-h, 8.6a-h), and for zone (40) (Figures 8.7a-h, 8.8a-h, 8.9a-h). Finally, Figures 8.10a-f, show compositional variations within single K-feldspar crystals: one from zone (20), and two from zone (50).

## 8.1 Geochemical evolution across pegmatite zones

*Blocky K-feldspar (Type 1)*

The distribution of minor and trace-elements in bulk K-feldspar of Type 1 changes gradually throughout the primary zonal sequence from (10) to (90). Tables 8.1 and 8.2 list data for some of the ratios, *i.e.* K/Rb, K/Cs, Rb/Cs, K/Na, K/Ba, Ba/Rb, Rb/Tl, Cs/Tl, and Al/Ga, which are particularly useful in characterizing the geochemical evolution of K-

feldspar from highly evolved granitic pegmatites. The behavior of K/Rb in granitic systems is well understood, and especially useful. Barring significant metasomatism or other alteration, a smooth decreasing K/Rb trend is a universal indicator of progressive fractional crystallization at a multitude of scales (Černý *et al.*, 1985, Černý, 1994).

At Tanco, individual values range from 0.68 to 3.47 wt% Rb, and 371 to 4170 ppm Cs (Figure 8.1a). Average K/Rb, for individual zones at Tanco, vary between 8.2 and 3.8 (Table 8.1) with individual samples ranging from 14.2 to 2.8 (Appendix V). Average K/Cs per zone varies between 117 and 39, with individual samples ranging between 262 and 23.5. Compositions from individual zones cluster rather tightly in Figures 8.1b,c. Significant overlap among the different zones is evident, especially with compositions from zones (10) and (20); but, on average, compositions from outer- to inner zones plot sequentially along decreasing K/Rb and K/Cs trends (Figures 8.1c, 8.3a,b). From zone (10) to (50), Rb/Cs (Figures 8.1d, 8.3c) remains relatively constant at 14.4 +/- 3.1; however, the ratio drops significantly and attains a distinctly lower average of 10.3 +/- 2.7 for zones (60) to (90).

Bulk K-feldspar contents of P and Li in Tanco are 400 to 3300 ppm, and 40 to 900 ppm, respectively, and show somewhat similar trends when plotted against K/Rb (Figures 8.1 e,f). Maximum contents (and averages, Figure 6.7) are encountered for P in zone (40), and for Li in zone (50). The P distribution (Figure 8.1e) is noteworthy; compositions from zones (20) (40) and (50) form an early arcuate increase, followed by a broad flat-lying trend, comprised mostly of compositions from zones (50) (60) (80) and (90), which extends to P contents much lower than those from zone (20). This indicates that P-depletion occurred sometime during, or shortly after, the consolidation of zone (50),

**Table 8.1:** Blocky K-feldspar statistics for selected ratios (bulk composition)

**K/Rb**

| Zone | (10) | (20) | (40) | (50) | (60) | (80) | (90) |
|---|---|---|---|---|---|---|---|
| n | 8 | 38 | 29 | 17 | 14 | 3 | 5 |
| max | 12.3 | 14.2 | 11.0 | 6.6 | 6.4 | 4.0 | 7.0 |
| min | 5.4 | 4.8 | 3.5 | 3.4 | 2.8 | 3.3 | 3.5 |
| average | 7.2 | 8.2 | 6.2 | 5.7 | 4.6 | 3.8 | 4.6 |
| 1σ | 2.4 | 2.4 | 2.2 | 0.9 | 0.7 | 0.4 | 1.4 |

**K/Cs**

| Zone | (10) | (20) | (40) | (50) | (60) | (80) | (90) |
|---|---|---|---|---|---|---|---|
| n | 8 | 38 | 29 | 17 | 14 | 3 | 5 |
| max | 152 | 262 | 178 | 117 | 71 | 44 | 157 |
| min | 65 | 54 | 37 | 49 | 29 | 37 | 24 |
| average | 111 | 117 | 85 | 84 | 45 | 39 | 65 |
| 1σ | 32 | 51 | 34 | 18 | 11 | 4 | 53 |

**Rb/Cs**

| Zone | (10) | (20) | (40) | (50) | (60) | (80) | (90) |
|---|---|---|---|---|---|---|---|
| n | 8 | 38 | 29 | 17 | 14 | 3 | 5 |
| max | 20.6 | 22.3 | 17.6 | 17.8 | 17.4 | 11.2 | 22.3 |
| min | 10.1 | 9.3 | 9.0 | 12.0 | 6.5 | 9.3 | 5.7 |
| average | 14.7 | 14.2 | 13.6 | 15.0 | 10.2 | 10.5 | 12.9 |
| 1σ | 3.7 | 3.6 | 2.6 | 2.0 | 2.8 | 1.0 | 6.1 |

**K/Na**

| Zone | (10) | (20) | (40) | (50) | (60) | (80) | (90) |
|---|---|---|---|---|---|---|---|
| n | 8 | 38 | 29 | 17 | 14 | 3 | 5 |
| max | 7.6 | 14.6 | 17.1 | 14.2 | 50.1 | 15.6 | 43.3 |
| min | 3.6 | 3.6 | 3.7 | 6.1 | 6.1 | 10.8 | 6.1 |
| average | 5.5 | 7.3 | 8.8 | 9.5 | 15.0 | 13.3 | 16.0 |
| 1σ | 1.5 | 2.6 | 3.5 | 2.0 | 10.0 | 2.4 | 15.6 |

**K/Ba**

| Zone | (10) | (20) | (40) | (50) | (60) | (80) | (90) |
|---|---|---|---|---|---|---|---|
| n | 8 | 38 | 29 | 17 | 14 | 3 | 5 |
| max | 1768 | 20025 | 52051 | 30184 | 12582 | 5175 | 8178 |
| min | 386 | 465 | 772 | 1154 | 311 | 472 | 1029 |
| average | 917 | 4664 | 10510 | 9381 | 2919 | 2053 | 3212 |
| 1σ | 538 | 4717 | 11634 | 9248 | 3252 | 2703 | 2870 |

**Ba/Rb**

| Zone | (10) | (20) | (40) | (50) | (60) | (80) | (90) |
|---|---|---|---|---|---|---|---|
| n | 8 | 38 | 29 | 17 | 14 | 3 | 5 |
| max | 0.0284 | 0.0206 | 0.0072 | 0.0046 | 0.0135 | 0.0079 | 0.0068 |
| min | 0.0040 | 0.0003 | 0.0001 | 0.0001 | 0.0003 | 0.0008 | 0.0005 |
| average | 0.0116 | 0.0049 | 0.0021 | 0.0016 | 0.0043 | 0.0052 | 0.0026 |
| 1σ | 0.0078 | 0.0055 | 0.0023 | 0.0015 | 0.0042 | 0.0039 | 0.0025 |

**Table 8.2:** Blocky K-feldspar statistics for selected ratios (bulk composition)
(unpublished data, P. Cerny)

**Rb/Tl**

| Zone | (10) | (20) | (40) | (50) | (60) | (80) |
|---|---|---|---|---|---|---|
| n | 1 | 20 | 7 | 14 | 9 | 3 |
| max | | 188 | 136 | 146 | 148 | 287 |
| min | | 82 | 102 | 54 | 75 | 148 |
| average | 118 | 119 | 126 | 91 | 103 | 215 |
| 1σ | | 21 | 12 | 22 | 24 | 70 |

**Cs/Tl**

| Zone | (10) | (20) | (40) | (50) | (60) | (80) |
|---|---|---|---|---|---|---|
| n | 1 | 20 | 7 | 14 | 9 | 3 |
| max | | 14.7 | 8.0 | 14.6 | 15.4 | 25.1 |
| min | | 3.2 | 5.3 | 2.6 | 8.3 | 16.8 |
| average | 9.7 | 6.9 | 7.0 | 7.9 | 12.1 | 19.8 |
| 1σ | | 3.1 | 1.1 | 2.8 | 2.5 | 4.6 |

**Al/Ga**

| Zone | (10) | (20) | (40) | (50) | (60) |
|---|---|---|---|---|---|
| n | 1 | 13 | 7 | 14 | 8 |
| max | | 2156 | 2935 | 3342 | 1303 |
| min | | 993 | 1261 | 906 | 897 |
| average | 1478 | 1417 | 1671 | 1680 | 1116 |
| 1σ | | 288 | 581 | 806 | 164 |

which incidentally corresponds to the sudden stabilization of large volumes of amblygonite-montebrasite in zones (40) and (particularly) (50). A similar but less conspicuous depletion in Li, also apparent in compositions from zones (60) (80) and (90) (Figure 8.1f), could be related to the extensive crystallization of petalite and spodumene which culminated in zone (50). Cesium does not generally occur in petalite or spodumene in appreciable quantities (Stilling 1998), and evidently exhibits independent geochemical behavior, relative to Li, in the presence of these minerals (Figure 8.1g). Cesium increases in K-feldspar from zone (10) to (50); the latter of which contains huge accumulations of pollucite (80), and continues to increase in zones (60), (80), and (90).

Thallium contents in K-feldspar increase steadily from 60 ppm to 320 ppm (Figures 8.1h,i,k), in a zonal sequence from (10) to (50), followed by a decreasing trend through (60) to a minimum of about 100 ppm in (80). K-feldspar from zones (60) and (80) contains considerably less Tl than the maximum, averaging slightly less than 200 ppm. Rb/Tl values from zones (20) and (40) increase along overlapping trends with decreasing K/Rb (Figure 8.1j) in K-feldspar. This is followed by an abrupt change to decreasing Rb/Tl with constant to slightly decreasing K/Rb in zone (50), and a return to increasing Rb/Tl in (60) and (80). In terms of zonal averages, Rb/Tl is relatively constant in zones (10), (20) and (40) with values of 118, 119, and 126 ppm respectively, but values drop in zones (50) and (60) with averages of 91 and 103 ppm (Figure 8.3e, Table 8.2). Data are not available for zone (90). From Figures 8.1h,i,k it is evident that Tl attains maximum values in zone (50). With decreasing K/Rb, the relative increase in rubidium is greater than Tl in zones (20) and (40), as is evident by the negative slope in Figure 8.1j; however, the reverse is true in zones (50) and (60). Cs and Tl increase synchronously in zones (20) (40) and (50), however, Tl decreases in zones (60) and (80) at about constant Cs (Figures 8.1h). Consequently, Cs/Tl is about constant at

decreasing K/Rb in zones (20), (40) and (50), but increases in zones (60) and (80) (Figures 8.1l, 8.3f).

The ranges of the low Ca and Ba contents are consistently broad in most zones (Figure 8.1m,n), and show virtually no correlation with K/Rb. K/Ba values of most zones significantly overlap with each other (Figure 8.1o), however, zonal averages (Figure 8.3g) indicate an overall increase in K/Ba from zone (10) to (20) and (40), followed by a decrease in the succession (50) (60) and (80). The Ba/Rb average-per-zone profile (Figure 8.3h) is a well-defined mirror image of the K/Ba profile (Figure 8.3g), with high Ba/Rb average values in zones (10) and (80), and corresponding low values in zones (40) and (50).

There is a systematic increase in K/Na with decreasing K/Rb (Figure 8.1p, Table 8.1), with maximum individual values of 50 and 43 occurring in zones (60) and (90), respectively. The calculated zonal averages (Table 8.1, Figure 8.3d), are consistent with the observed decrease in volume of albite lamellae in perthite from outer to inner zones (Table 6.2), and with the decrease in Na in the K-feldspar phase (Figure 6.11b).

Gallium contents in Tanco K-feldspar samples from zones (10) (20) (40) (50) and (60) range from 31 to 116 ppm Ga (Figure 8.1q), with Al/Ga varying between 3300 and 900 (Figure 8.1k). Considering compositions from all zones, the Al vs. Ga distribution seems to be random (Figure 8.1q); however, Al and Ga values from zones (10) (20) and (40) appear to form a broad sublinear trend with a positive slope. Average Al/Ga values per zone increase in zonal sequence from zone (20) to (50): 1417,1671,1680, followed by a drop to a low of 1116 in zone (60) (Figure 8.3i, Table 8.2).

*Albite (Types A,B)*

Compositional variability in Tanco albite is much less pronounced than in K-feldspar; consequently, relatively few geochemical plots are presented.

Gallium contents in Tanco albite samples from zones (10) (20) (40) (50) and (60) range from 46 to 125 ppm Ga (Figure 8.2a), with Al/Ga varying between 2220 and 828 (Figure 8.2b). There is a somewhat pronounced linear Al vs. Ga trend (Figure 8.2a) with maximum Al and Ga values occurring in zone (60). For both the cleavelanditic albite and blocky K-feldspar varieties, the self-aligning Al/Ga vs. Ga trends are simple and to a degree overlapping, with the albite data showing generally lower Al/Ga values, and at the lower end of the range, slightly higher Ga values, as shown in Figures 8.2b and 8.1r. These figures also show that the progress from high to low Al/Ga does not follow any simple zonal sequence. Individual zones show extensive mutual overlaps and local reversals. The data for albite and K-feldspar show the same pattern of average zonal variations, with Al/Ga decreasing from (10) to (20) and from (50) to (60), but increasing from (20) to (50) (Figure 8.3i). There is no simple explanation for this trend, as competing minerals such as petalite, amblygonite, and pollucite have the same or lower Al/Ga values, and the abundances of Ga-rich micas are very low in zones (40) and (50) (Černý, 1982; Černý *et al.*, 1998).

Calcium and P are the only other trace-elements that occur above detection limits in a statistically meaningful number of albite samples. A plot of Na/Ca vs. P (Figures 8.2c,d) shows a very poor inverse relation, with no particular systematic shifts in favour of any given zone or mineral variety.

## 8.2 Geochemical variations within individual zones

This section describes the distribution of minor- and trace-elements within individual zones (20), (40) and (60) along east-west and north-south transects (Figure 3.4). A standard set of elements and element ratios has been selected for mutual comparison of all sections; this includes K/Rb, K/Cs, Rb/Cs, K/Na, P, Li, K/Ba and Ba/Rb. A sufficient number of samples from zone (20) (Figure 8.4) were available, allowing for comparisons between hangingwall and footwall compositions. In Figures 8.4-8.8, I have preserved the original coordinate system (measured in feet) used by Tanco mine geologists and engineers.

*Zone (20): East-West fence (9700N)*

Figures 8.4a-h depict geochemical variations in zone (20), along a 1 km length of the E-W transect (9700N). The most obvious variations are observed in a general west-to-east decrease in K/Rb and K/Cs; two compositions at the easternmost limit break this trend with significantly above-average values. From a statistical viewpoint, the spread of data (standard deviations) along the K/Rb and K/Cs trends (Figures 8.3a,b) is relatively consistent. P, Li, and K/Na trends are perceptibly concave-down (Figures 8.4e,f,d). The K/Ba and Ba/Rb trends (Figures 8.4g,h), suggest a slight easterly enrichment in Ba.

*Zone (20): North-South fences (10200E, 9100E)*

The two parallel north-south fences, 10200E (Figures 8.5 a-h) and 9100E (Figures 8.6 a-h), stretch over the length of 370 m and 350 m, respectively. In practically all cases, geochemical trends are either flat, or consist of highly variable and randomly distributed values.

*Zone (20): Hangingwall vs. Footwall geochemistry*

In almost all cases, hangingwall and footwall compositions mutually overlap to such an extent that no significant differences are suggested (Figures 8.4, 8.5, 8.6). However, one exception is apparent: Rb/Cs hangingwall values, along the north-to-south 10200E transect (Figure 8.5c), are significantly lower than footwall values. This transect is the only one that passes through a lengthy section of the pollucite zone (80), from 9350N to 9800N.

*Zone (40): East-West fence (9700N)*

Compositions along this fence are presented in Figures 8.7a-h. K/Rb, K/Cs, and Rb/Cs trends are almost horizontal, but a slight downward trend to the west might be indicated. If so, these trends are opposite to those indicated for zone (20) (Figure 8.4). K/Rb and K/Cs trends could be considered slightly concave-up, whereas K/Na and P are notably concave-down (Figures 8.7d,e). The overall shapes (Figures 8.7d,e) are similar to the respective configurations in zone (20) (Figures 8.4d,e). Li, K/Ba, and Ba/Rb (Figures 8.7e-h), all exhibit random, 'shot-gun'-like patterns.

*Zone (40): North-South fences (10200E, 9100E)*

Compositions along the 10200E, and 9100E fences are presented in Figures 8.8a-h and 8.9a-h, respectively. K/Rb, K/Cs, and Rb/Cs trends are essentially flat but with relatively low averages and small variations relative to the other trends so far discussed. The K/Rb and K/Cs trends, along 10200E (Figures 8.8a,b), are distinctly lower than the same trends along the 9100E fence. P contents along the 10200E transect (Figure 8.8e) are highly variable relative to those along the 9100E transect (Figure 8.9e). The reverse is true for Li, which has relatively consistent values along the 10200E transect (Figure 8.8f).

*Zone (60): East-West fence (9700N)*

Twelve data points at 5 different locations were available from zone (60). K/Rb and K/Cs trends are flat, with K/Rb averaging 4.7 +/- 0.9 and K/Cs averaging 42 +/- 8. The only other notable trend is Ba/Rb, which shows a steady increase from west to east, from approximately 0.001 to 0.012.

## 8.3 Evolution of single crystals of K-feldspar

Figures 8.10a-f show compositional variations along the length of three giant K-feldspar crystals: one from zone (20), and two from zone (50).

Four samples (1A-1D) were collected along the mid-section length of a vertically oriented club-shaped K-feldspar (crystal 12-15-2, Appendix V) from zone (20). Sample 1A was collected near the bottom, narrowest section of the crystal (1 cm width); sample 1D was collected 4m higher near the 80 cm wide termination. The matrix surrounding the crystal consisted of a mineral assemblage of fine-medium grained albite, quartz, tourmaline and muscovite, with localized aplitic albite. The proportion of muscovite seems to increase upwards in the matrix adjacent to the crystal.

Five samples (2A-2E) came from a vertically oriented 5m-long K-feldspar in zone (50) (crystal 12-15-1, Appendix V) with a uniform width of 60 cm. Both sides of the crystal were in contact with coarse-grained spodumene + quartz intergrowth (squi), and minor assemblages containing fine to medium-grained albite, amblygonite, quartz and Ta/Nb oxides. The crystal was largely continuous except for a small horizontal fracture near the middle sample, which facilitated a 20 cm dextral offset.

The other five samples (3A-3E) were collected from a horizontal 5m-long K-feldspar from zone (50) (crystal 10-25-3, Appendix V). Width variation is slight along the 5m length, with a maximum width of 1m observed near sample 3E. Small fractures commonly cross-cut the crystal at near right-angles. Fine, euhedral albite laths along cleavage faces were widespread, and were particularly abundant near samples 3B and 3C.

In terms of compositional trends, only K/Rb varied systematically along the length of the 3 crystals (decreasing trends in Figure 8.10a). Crystal (10-25-3) is the only one that has similar K/Rb and K/Cs profiles. For the two crystals from zone (50), concave-down profiles are common in the single element plots of P, Li, and Ca. The trends of Ca are reciprocal to those of K/Na, suggesting a dependency of Ca on the albite content (substantial in K-feldspar as exsolved perthitic lamellae, and/or as granular contamination).

### 8.4 Geochemistry of the late K(Rb)-feldspar (Types 2-5) (EMPA)

The range of K/Rb for the late feldspar types is extreme (Figure 8.11a,b). Rubidium in most adularia samples (Type 6) is very low resulting in extremely high to undefined K/Rb ratios. The granular microcline and metasomatic microcline (Types 2,3) have moderate to low K/Rb ratios, and Cs contents similar to those of the blocky K-feldspar (Type 1). Adularian (K-Rb)-feldspar (Type 4) contains low to extremely high Rb, resulting in K/Rb values between 6 and 0.07, and low to extremely high Cs (b.d.l. to 13500 ppm). Six out of twenty Type-4 samples contained no detectable Rb, and essentially no Cs.

Phosphorus generally decreases with decreasing K/Rb (Figure 8.11b). Maximum P values occur in Types-2 and -3 (Type 2: 500-1400 ppm), (Type 3: 50-2200 ppm). Type-4 contents are generally low, with 90% of values below 150 ppm, and 50% of values

below detection. Type-6 samples have the lowest overall P contents, with nine out of eleven values below detection.

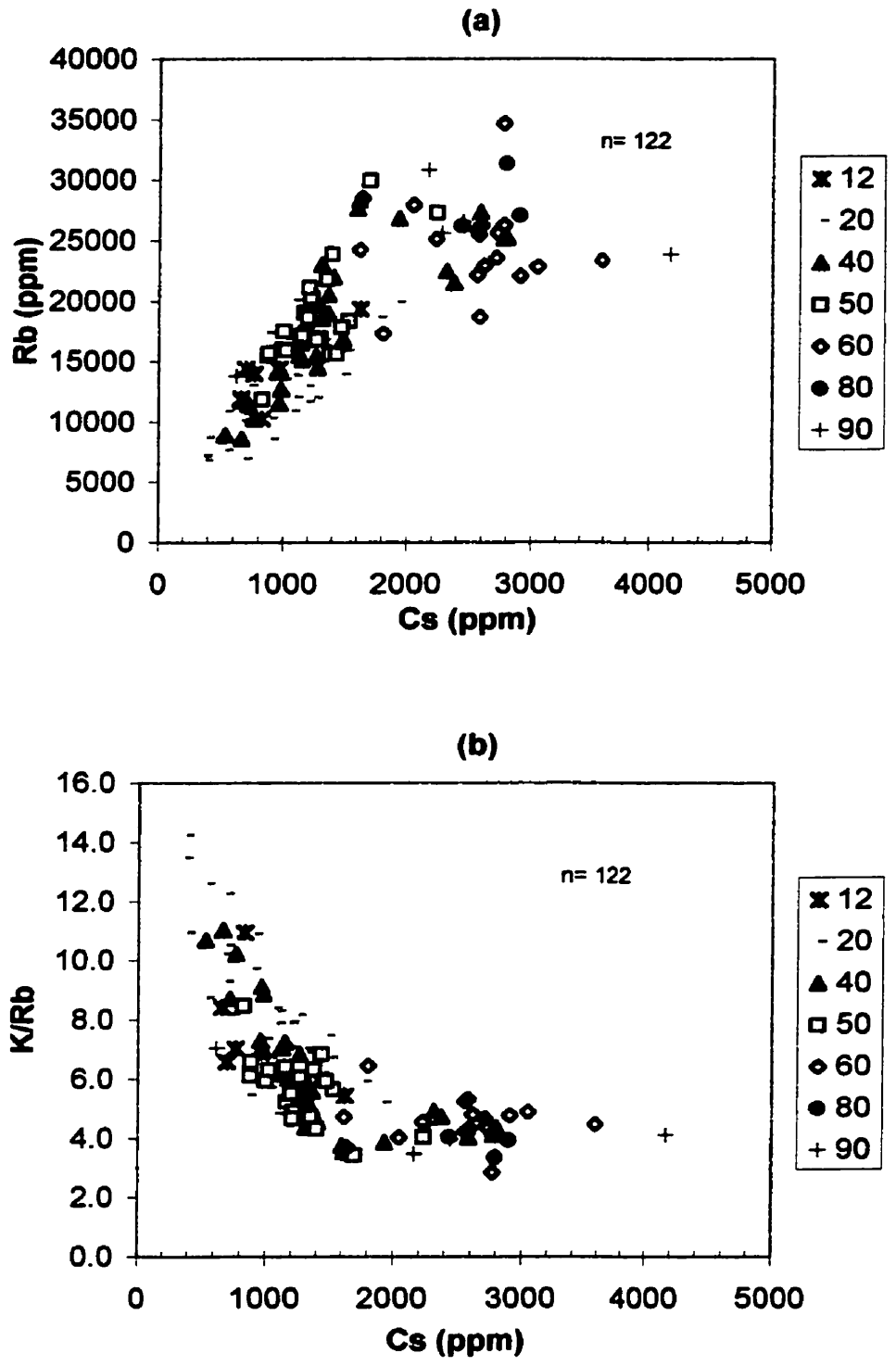


**Figure 8.1** Bulk chemistry of microcline-perthite (Type 1) designated by zone.

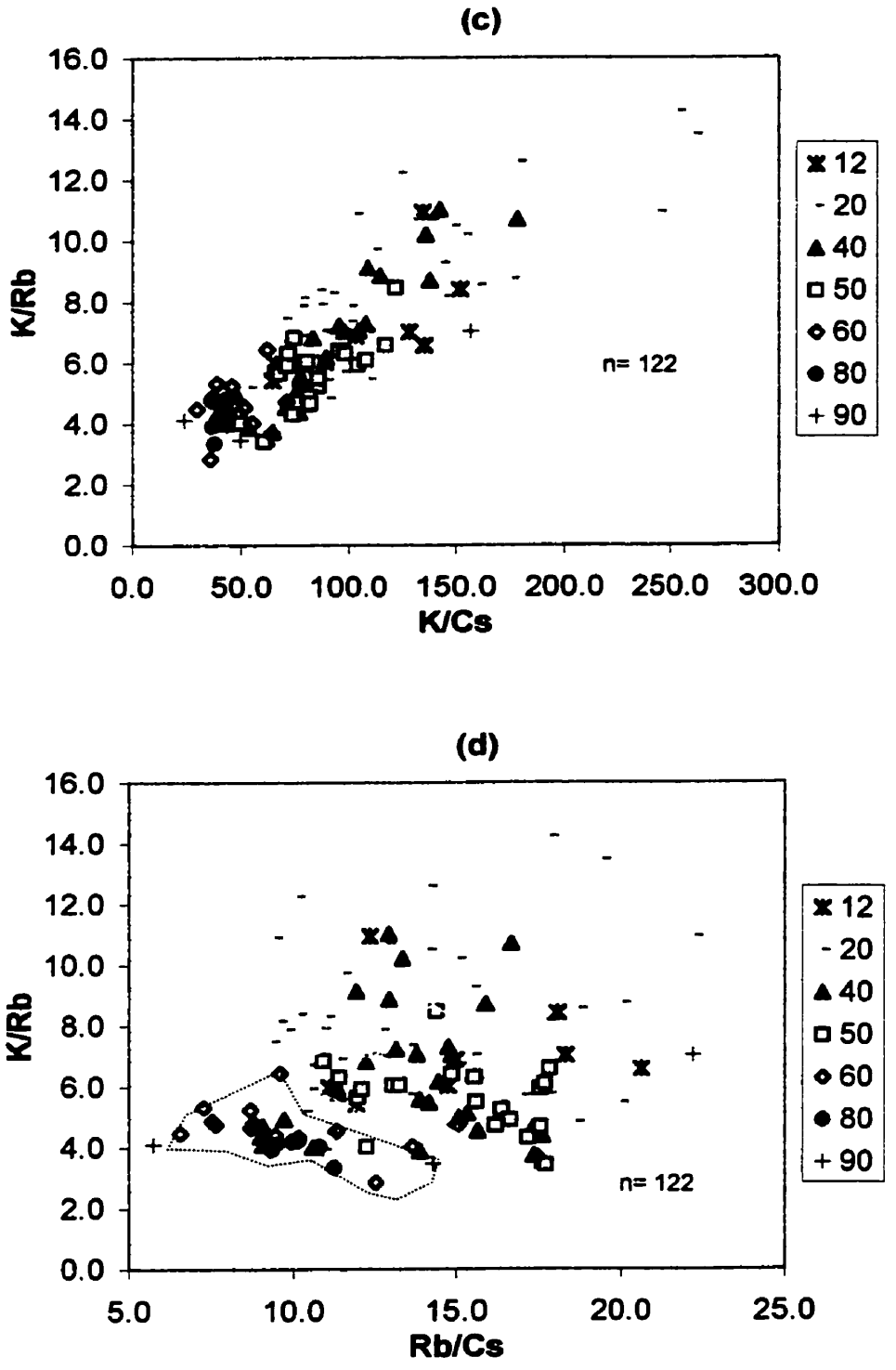


**Figure 8.1** Bulk chemistry of microcline-perthite (Type 1) designated by zone.

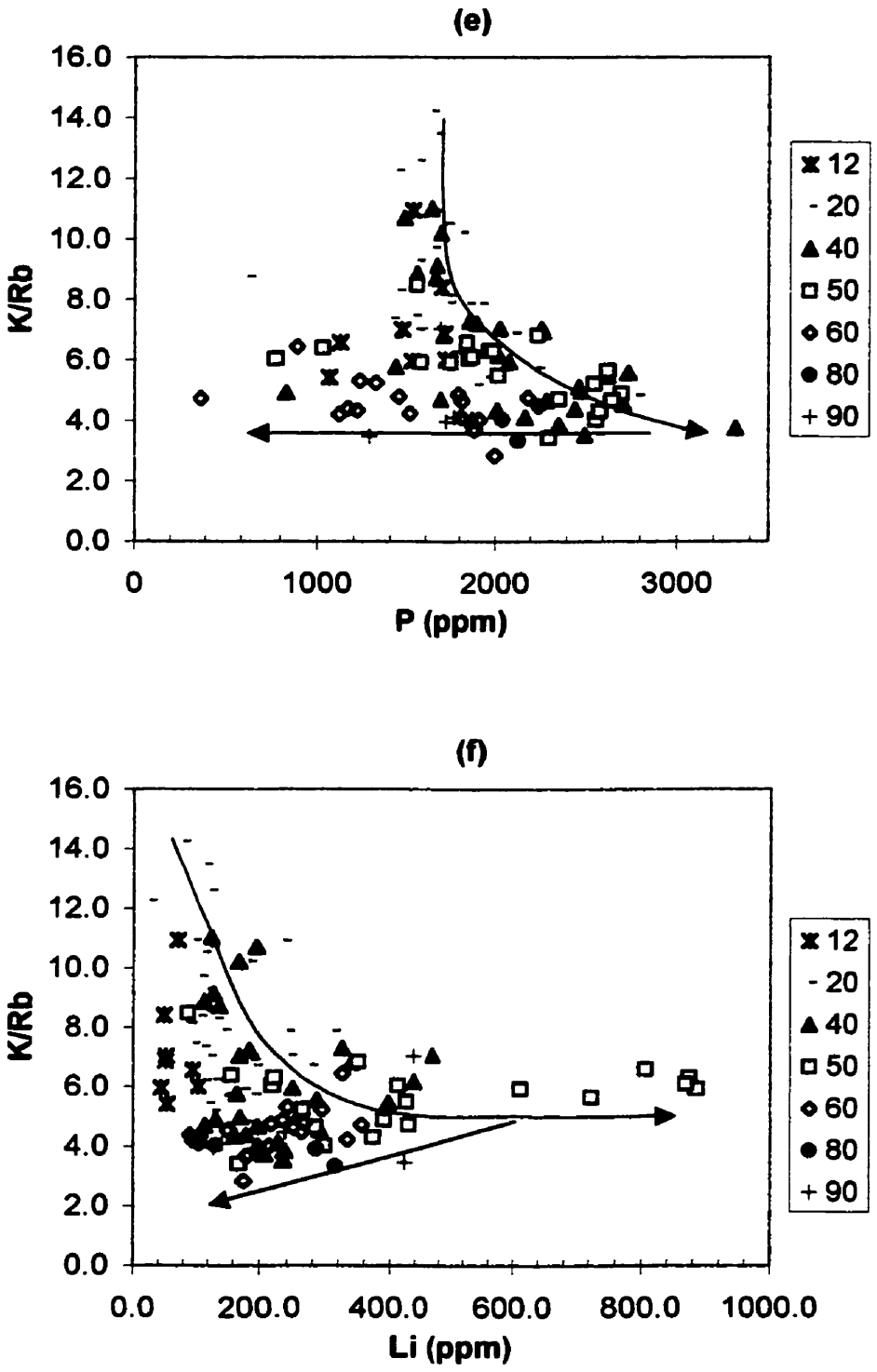


**Figure 8.1** Bulk chemistry of microcline-perthite (Type 1) designated by zone.

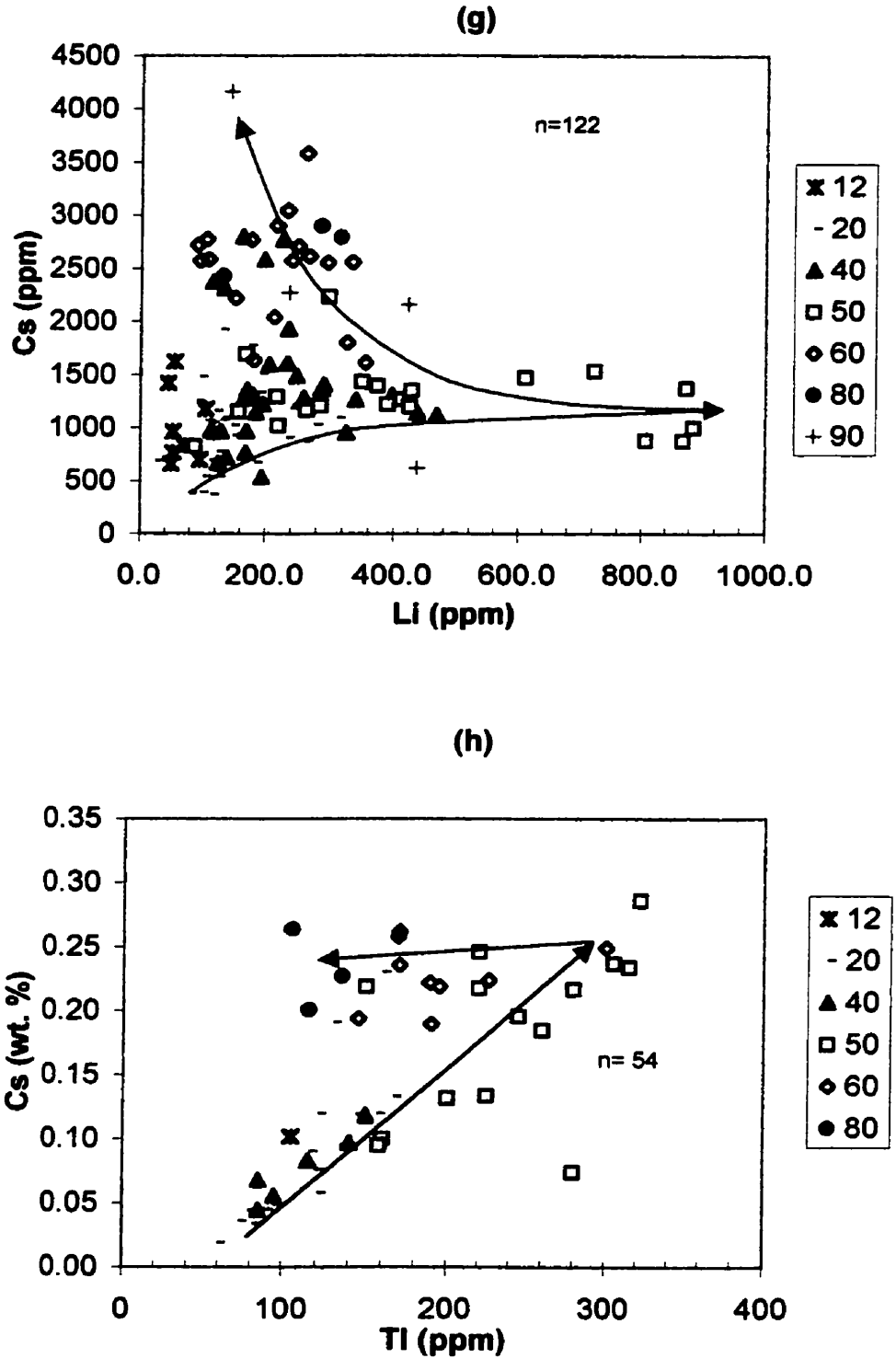


**Figure 8.1** Bulk chemistry of microcline-perthite (Type 1) designated by zone.

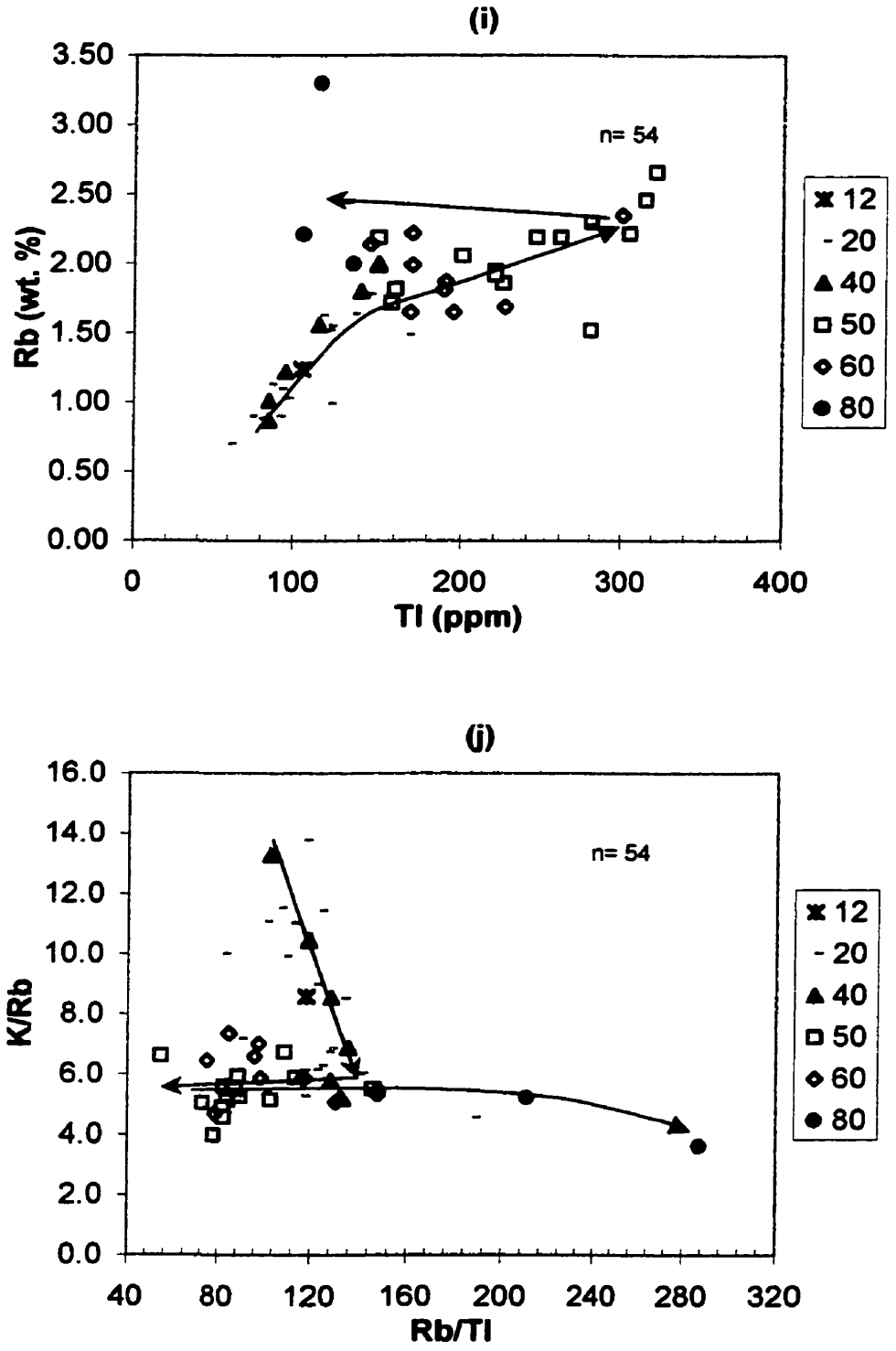


**Figure 8.1** Bulk chemistry of microcline-perthite (Type 1) designated by zone.

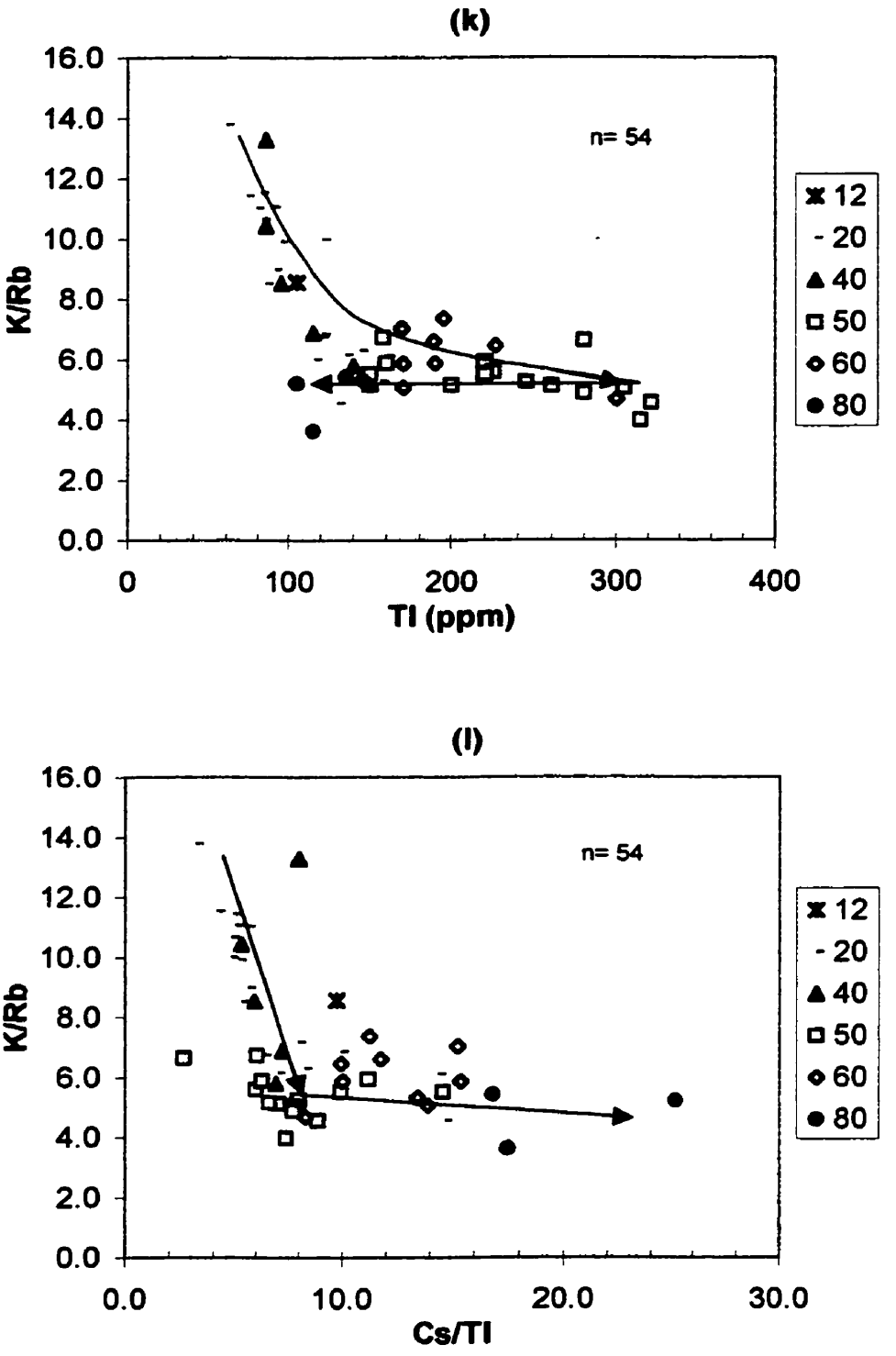


**Figure 8.1** Bulk chemistry of microcline-perthite (Type 1) designated by zone.

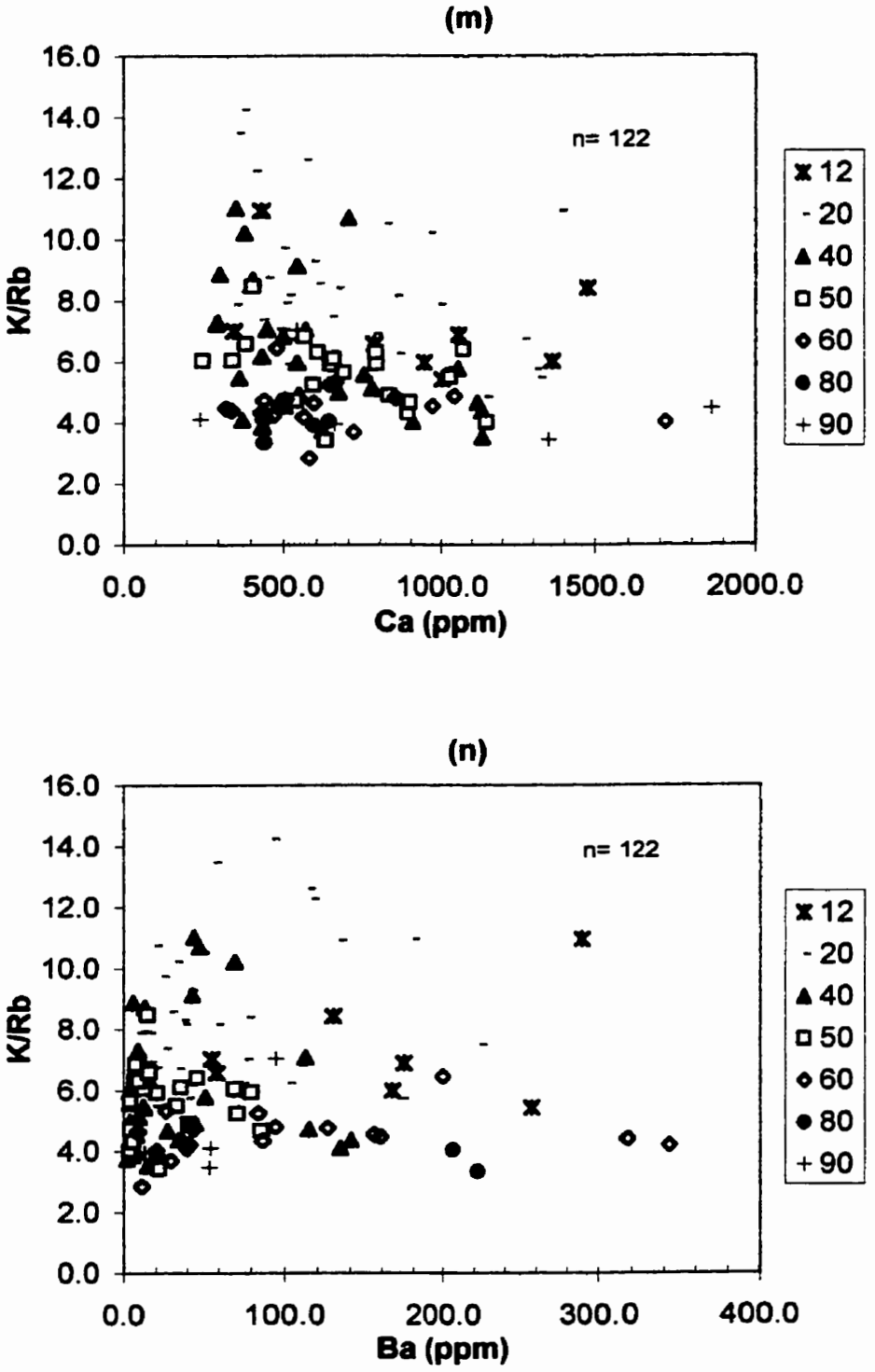


**Figure 8.1** Bulk chemistry of microcline-perthite (Type 1) designated by zone.

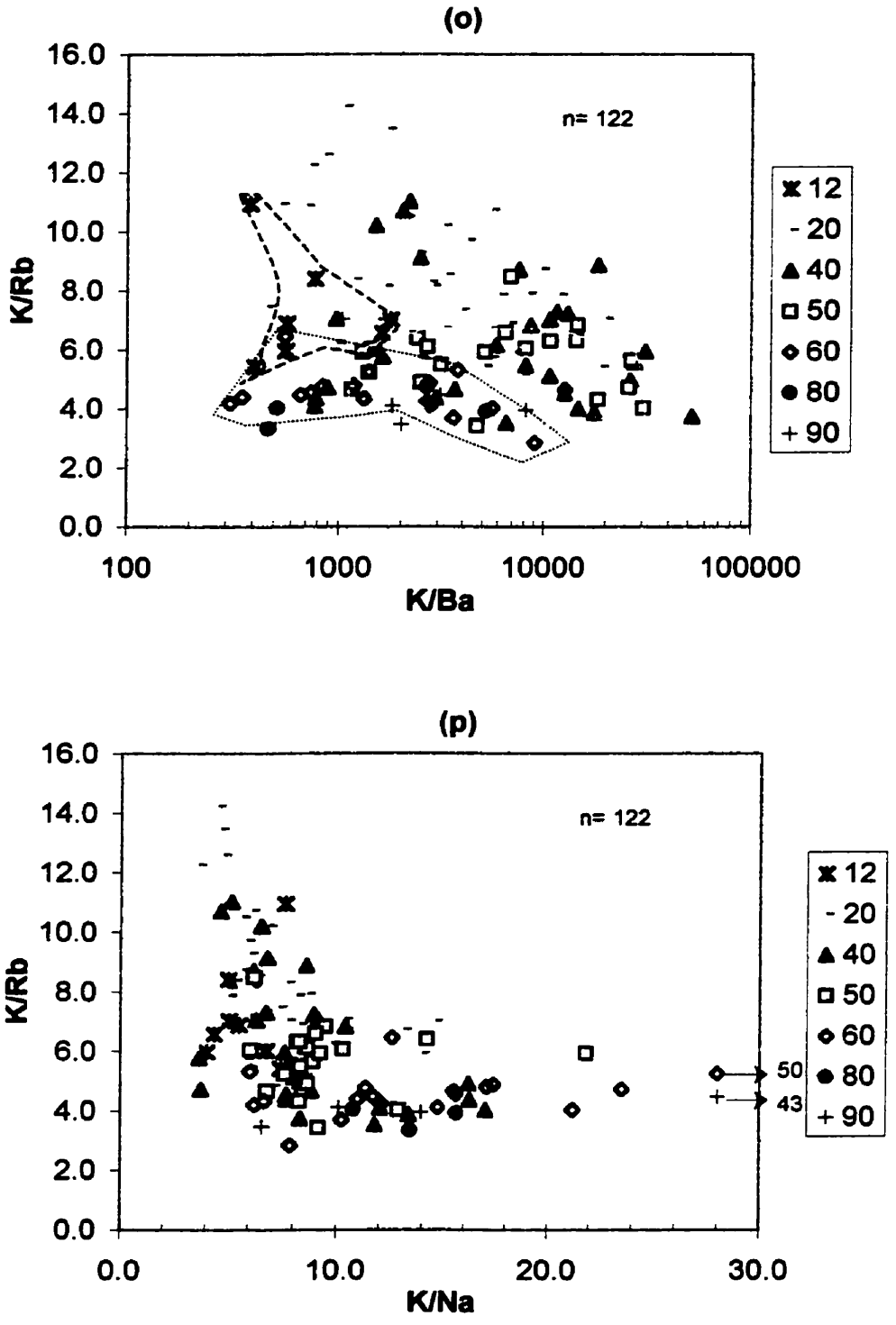


**Figure 8.1** Bulk chemistry of microcline-perthite (Type 1) designated by zone.

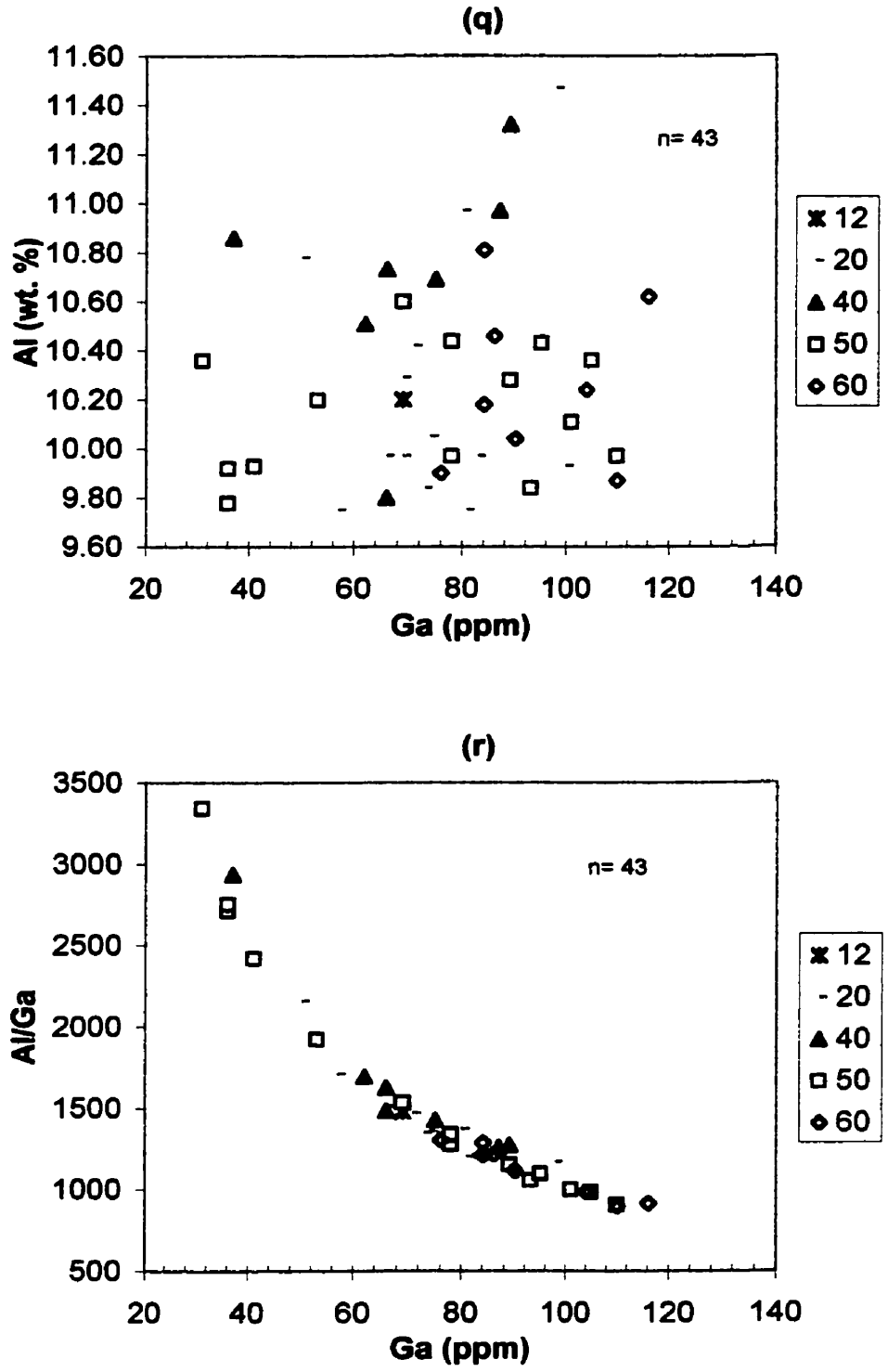


**Figure 8.1** Bulk chemistry of microcline-perthite (Type 1) designated by zone.

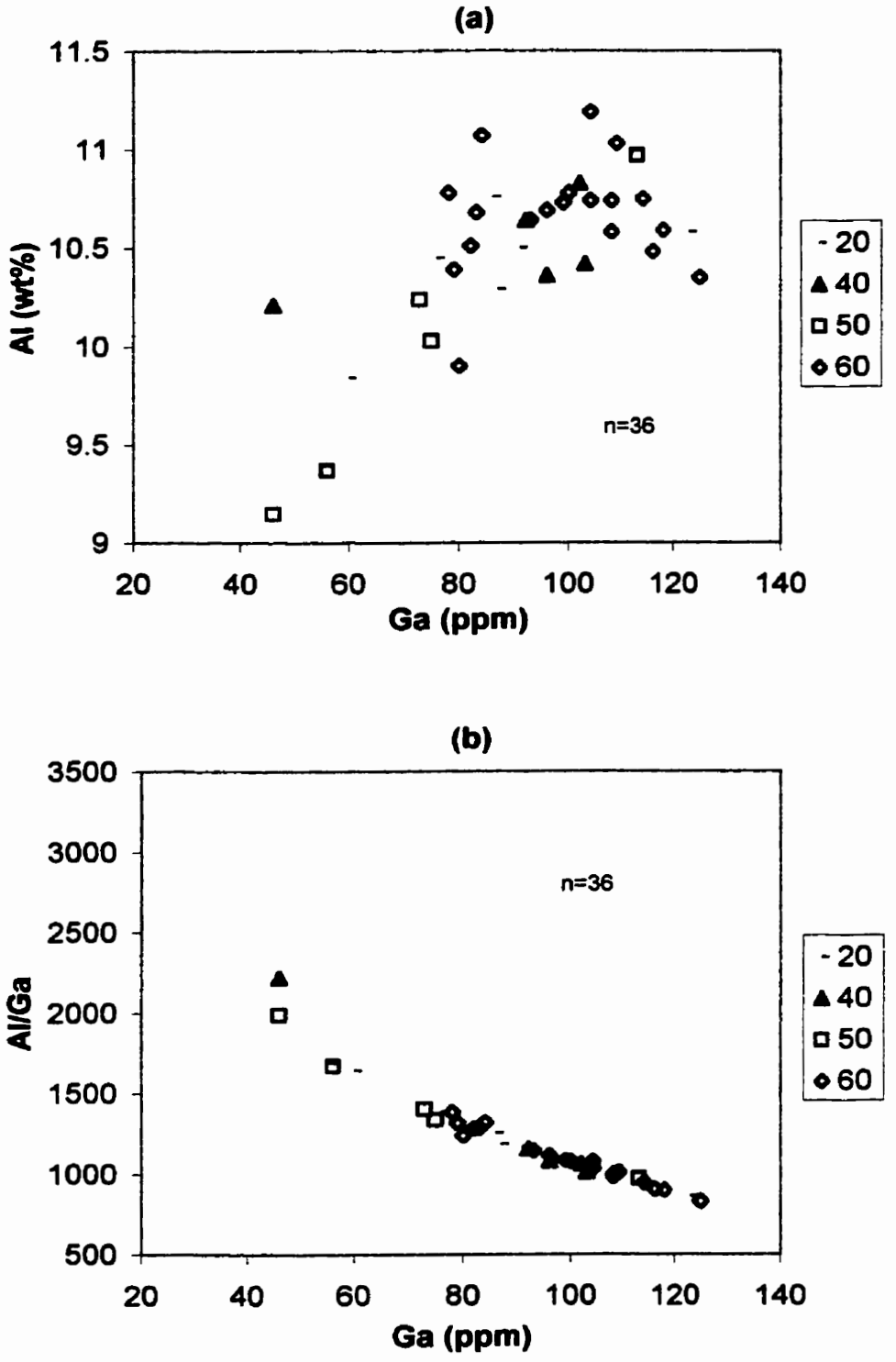


**Figure 8.2** Bulk chemistry of albite (Type B) designated by zone

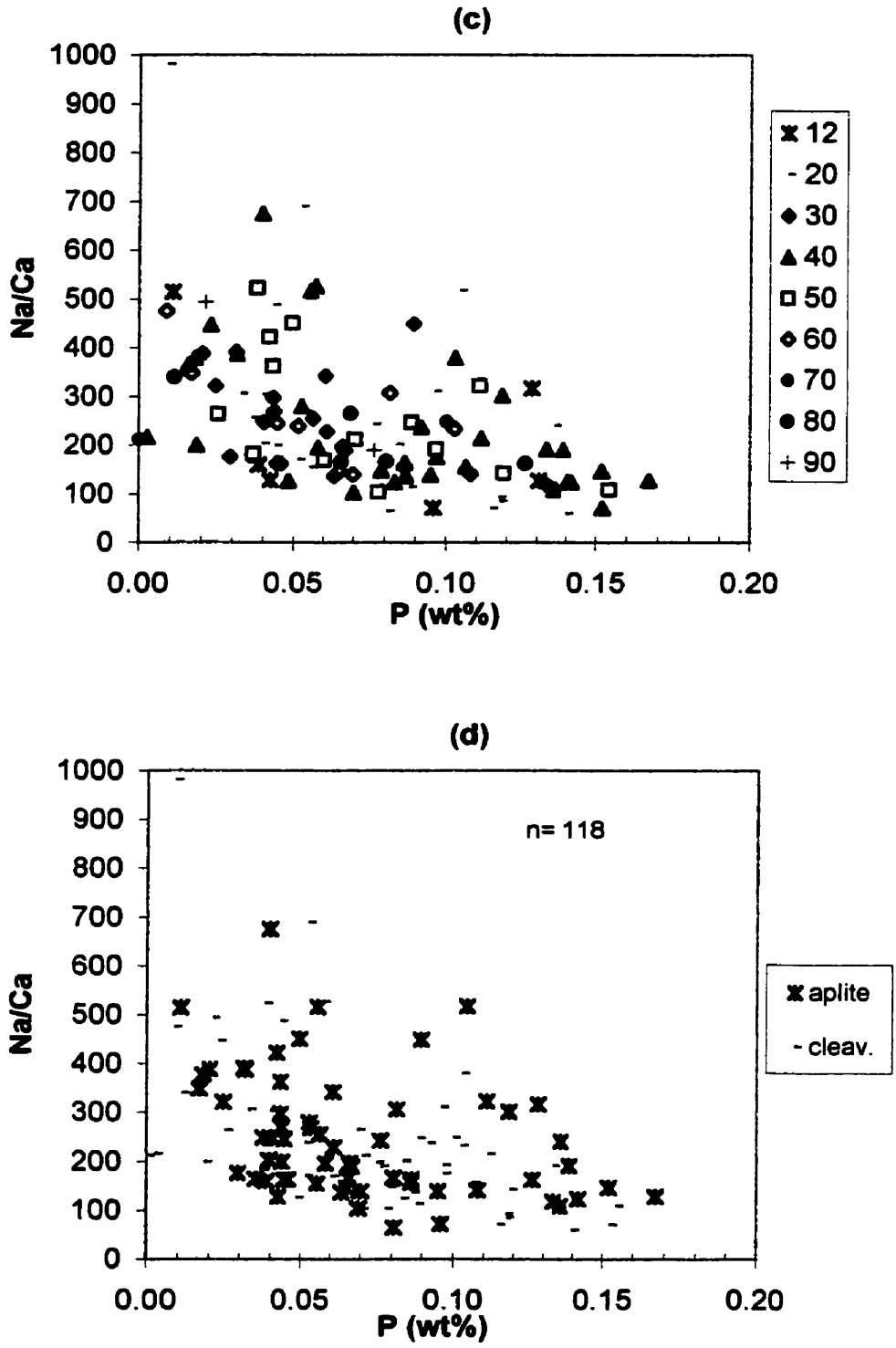


**Figure 8.2** Bulk chemistry of albite (Types A+B): (c) designated by zone, (d) designated by type

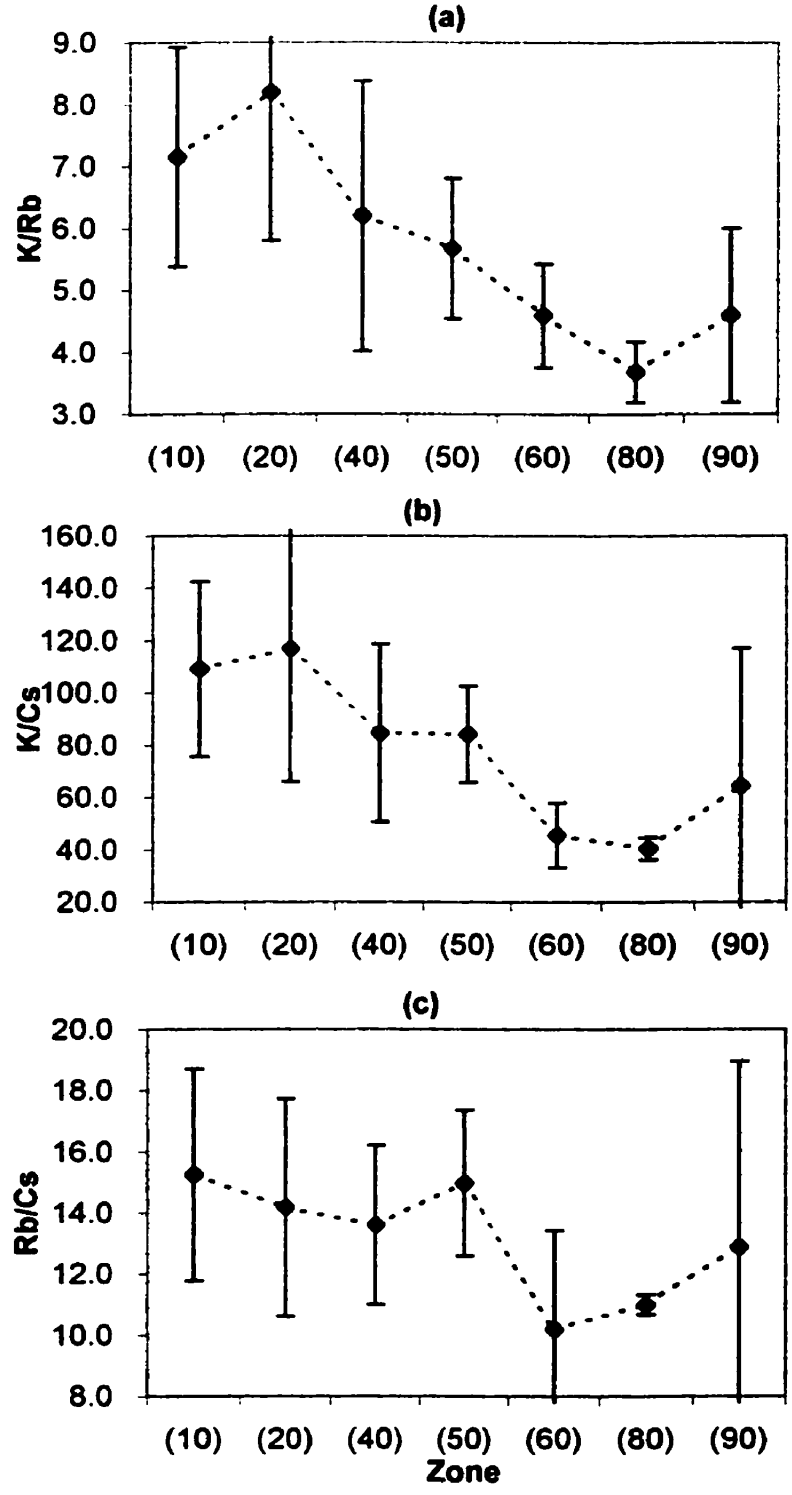


**Figure 8.3** Average bulk chemistry of microcline-perthite (Type 1) designated by zone. Deviations: +/-1 σ

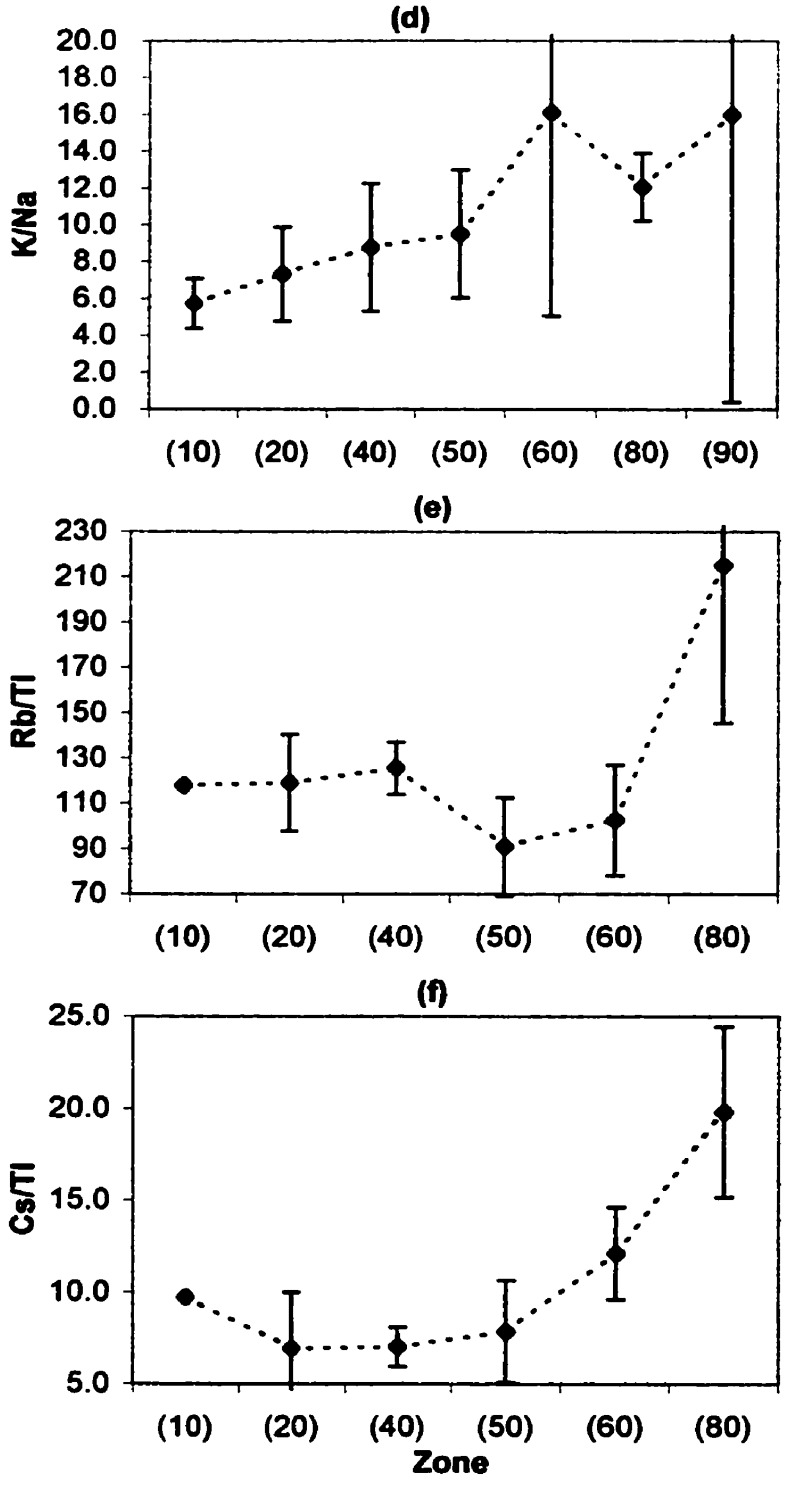


**Figure 8.3** Average bulk chemistry of microcline-perthite (Type 1) designated by zone. Deviations: +/-1 σ

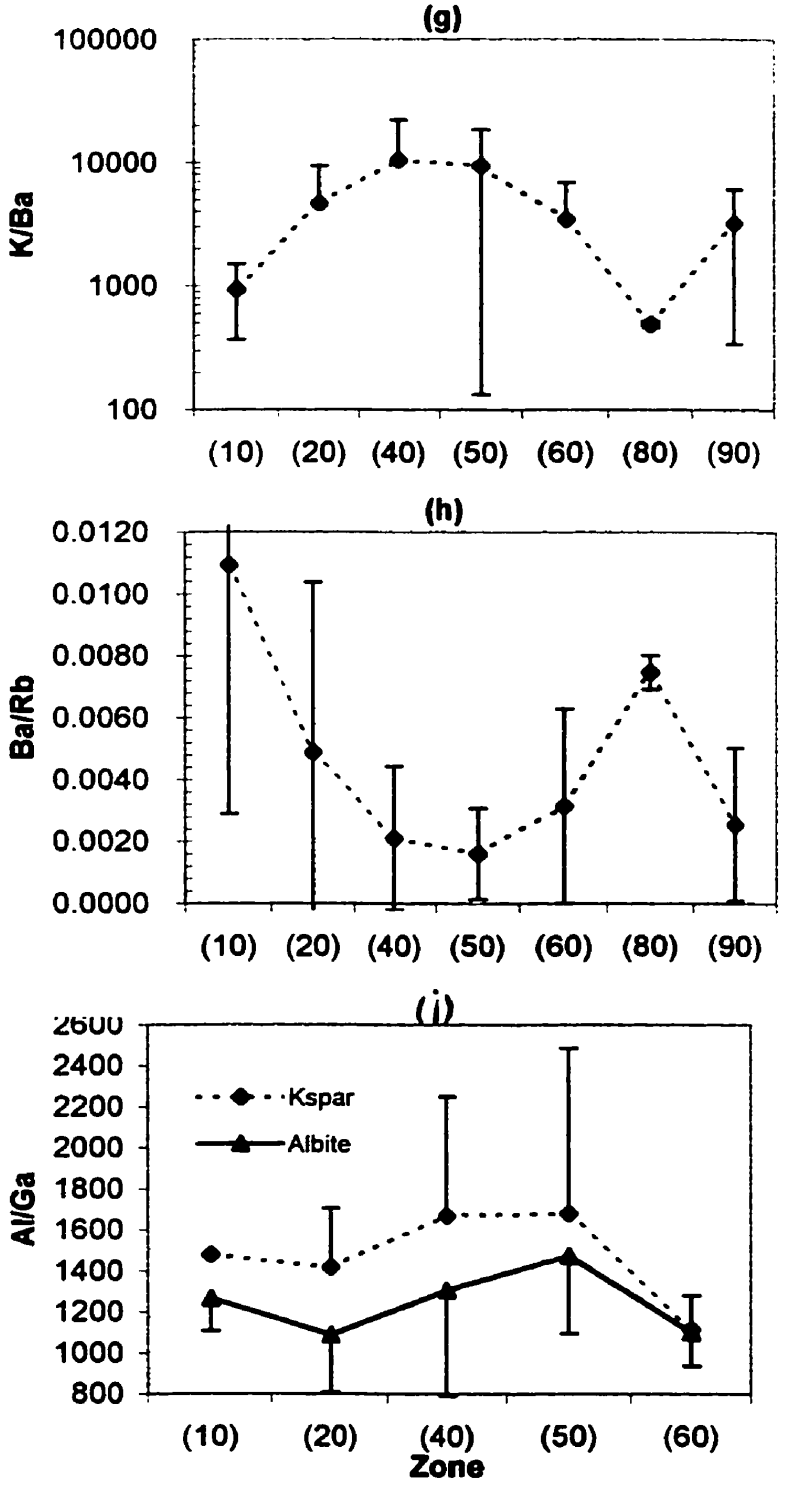


**Figure 8.3** (g),(h) Average bulk chemistry of microcline-perthite (Type 1) (i) Al/Ga bulk chemistry in K-feldspar (Type 1) and albite (Type B). Deviations: +/-1 σ

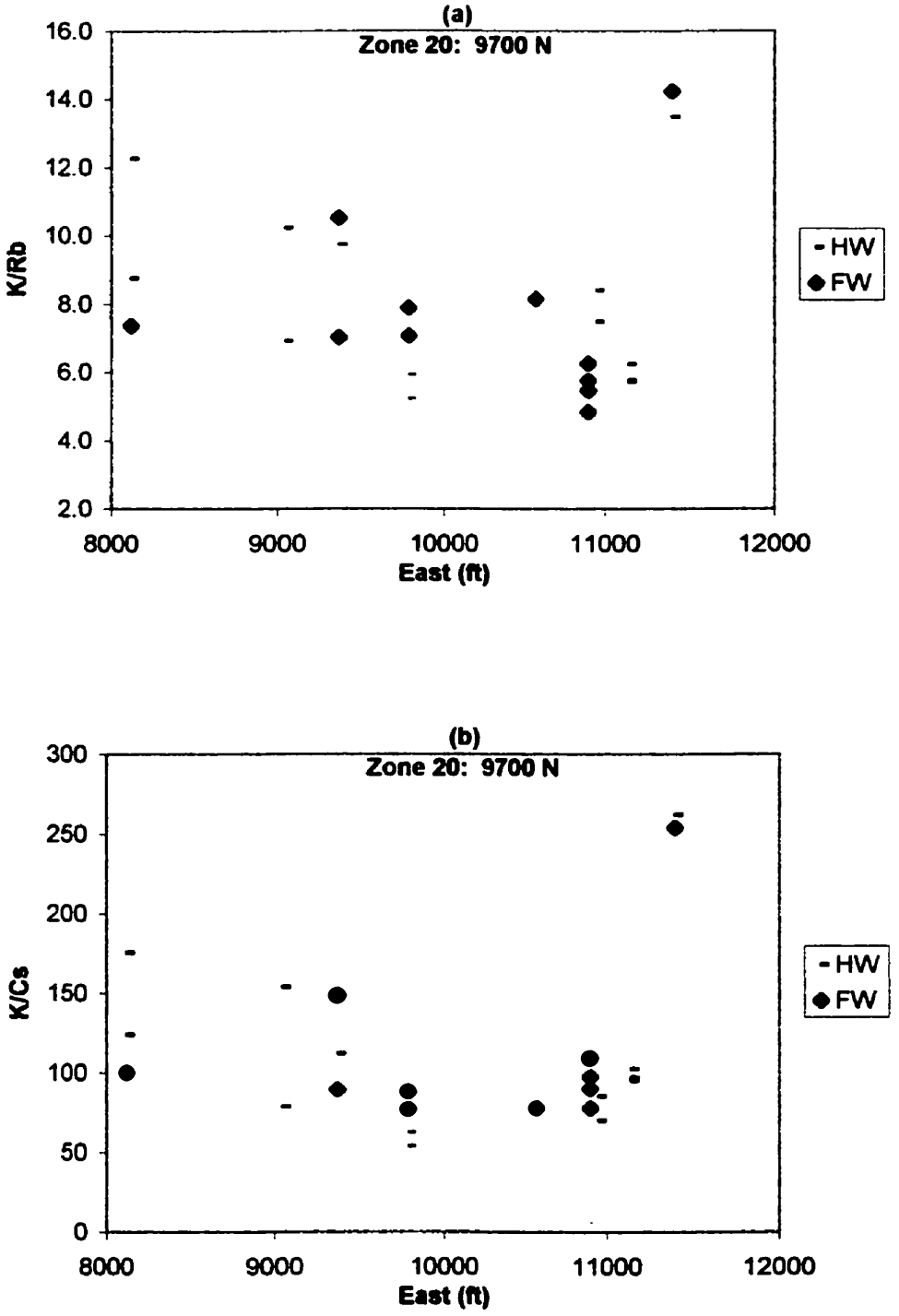


**Figure 8.4** Bulk chemistry of microcline-perthite (Type 1), from hangingwall (HW) and footwall (FW) locations of zone (20).

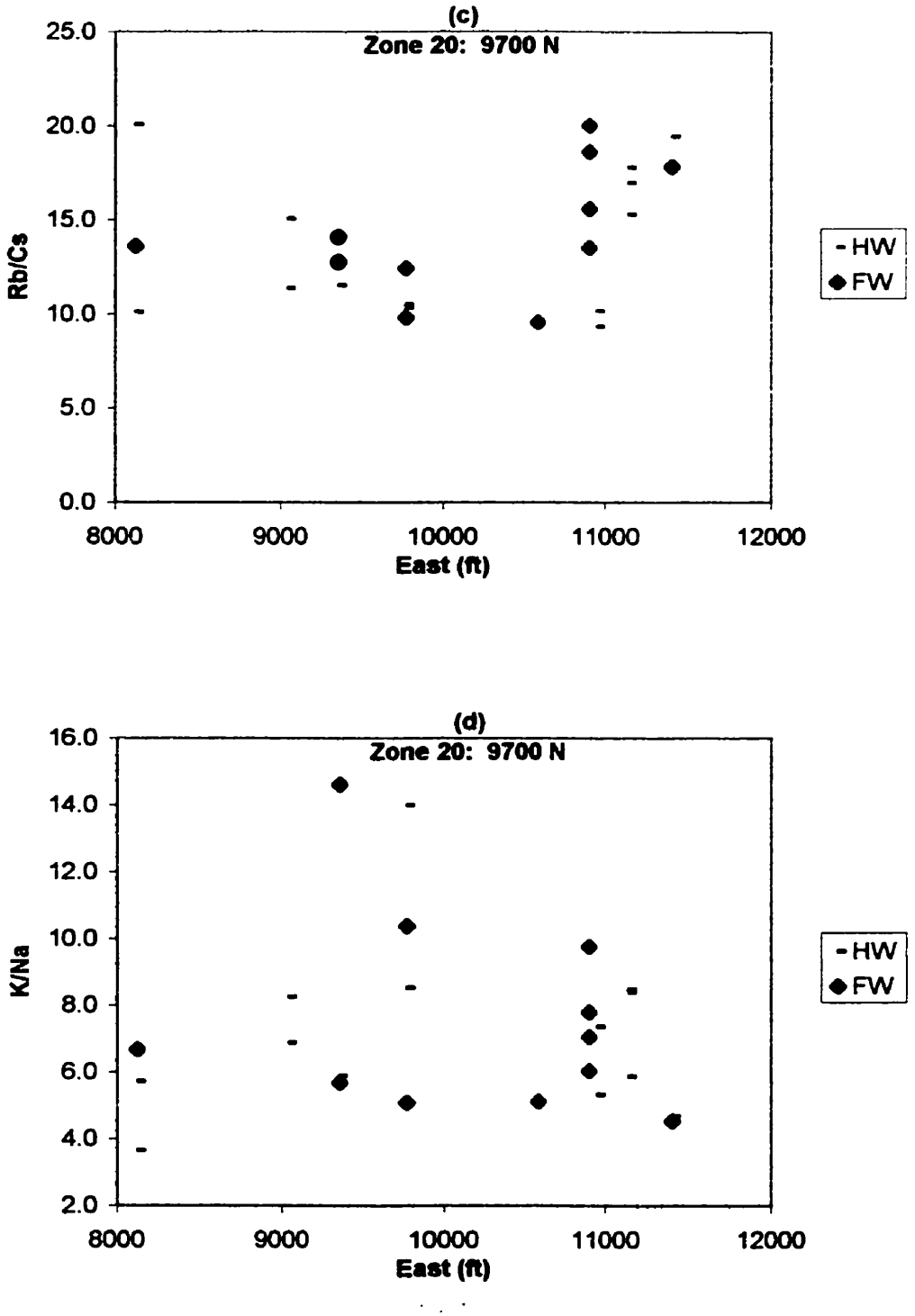


**Figure 8.4** Bulk chemistry of microcline-perthite (Type 1), from hangingwall (HW) and footwall (FW) locations of zone (20).

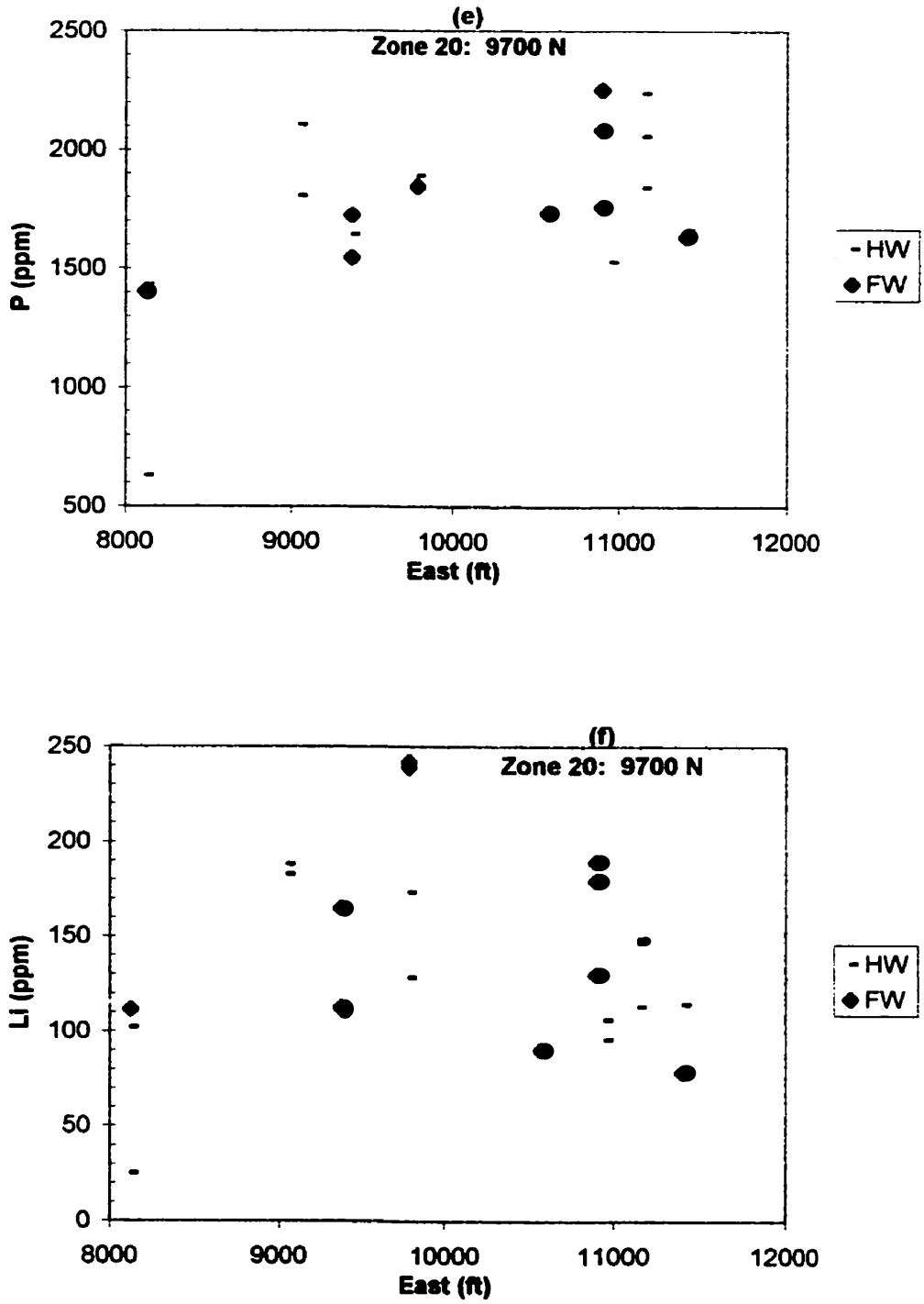


**Figure 8.4** Bulk chemistry of microcline-perthite (Type 1), from hangingwall (HW) and footwall (FW) locations of zone (20).

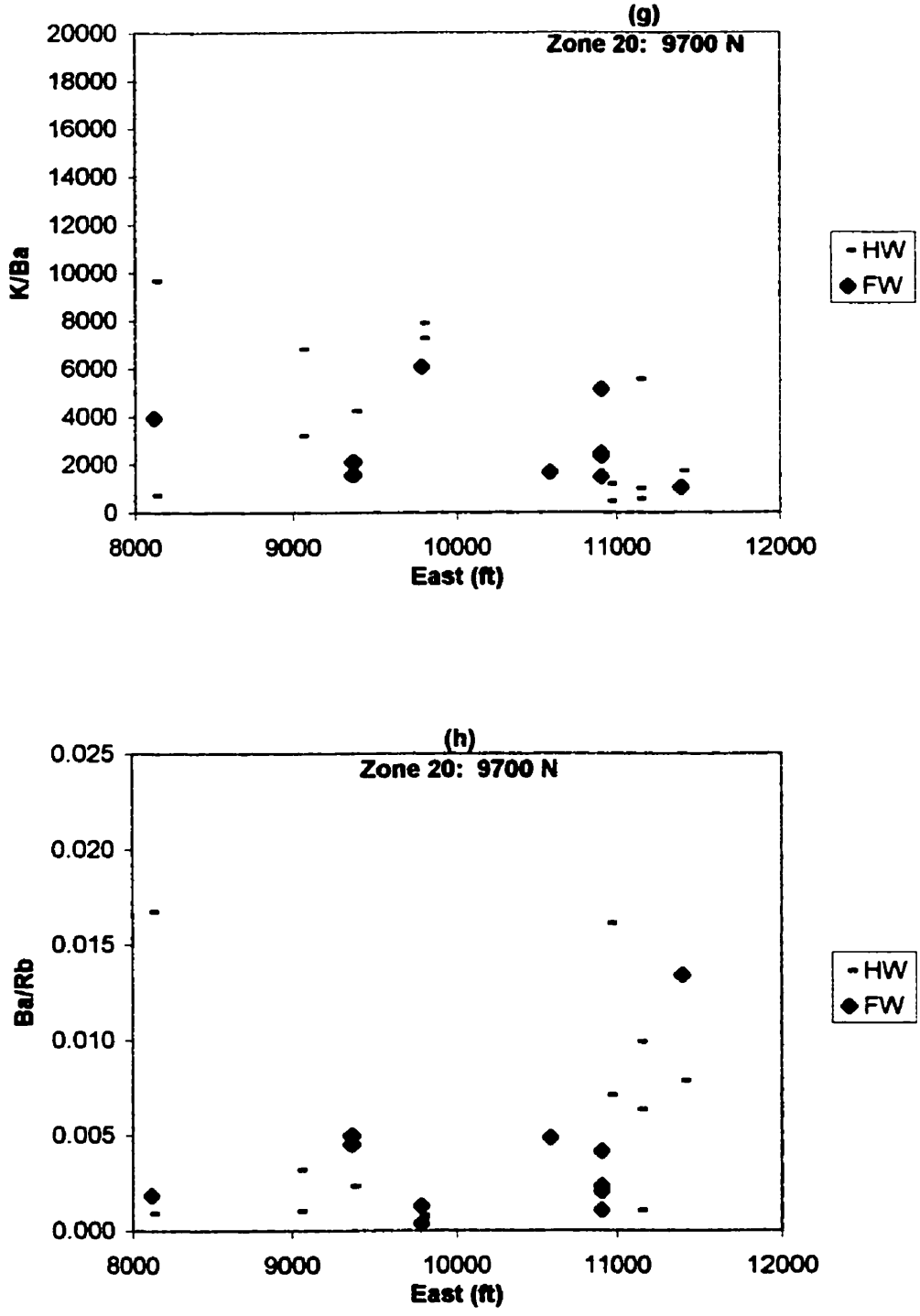


**Figure 8.4** Bulk chemistry of microcline-perthite (Type 1), from hangingwall (HW) and footwall (FW) locations of zone (20).

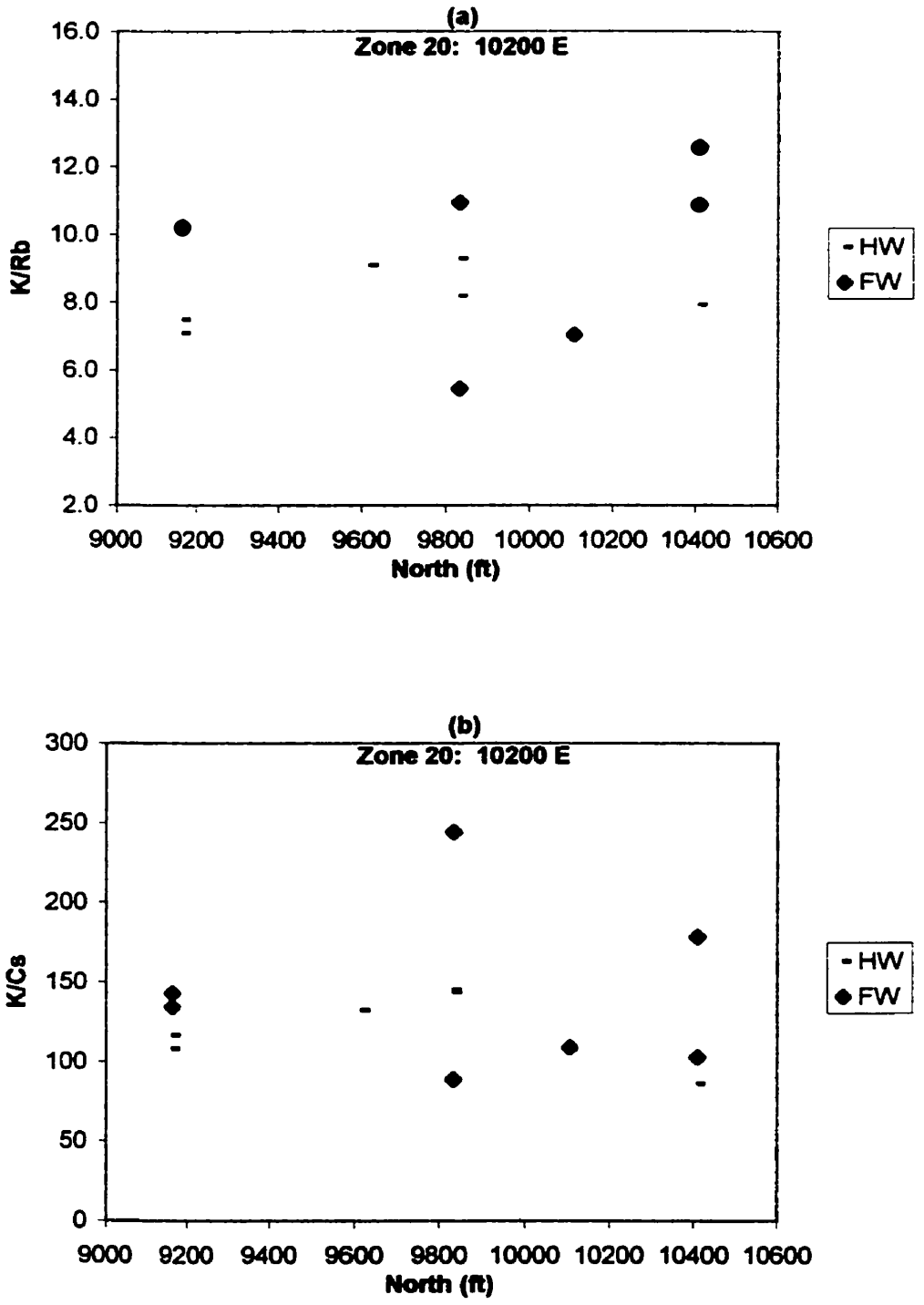


**Figure 8.5** Bulk chemistry of microcline-perthite (Type 1), from hangingwall (HW) and footwall (FW) locations of zone (20).

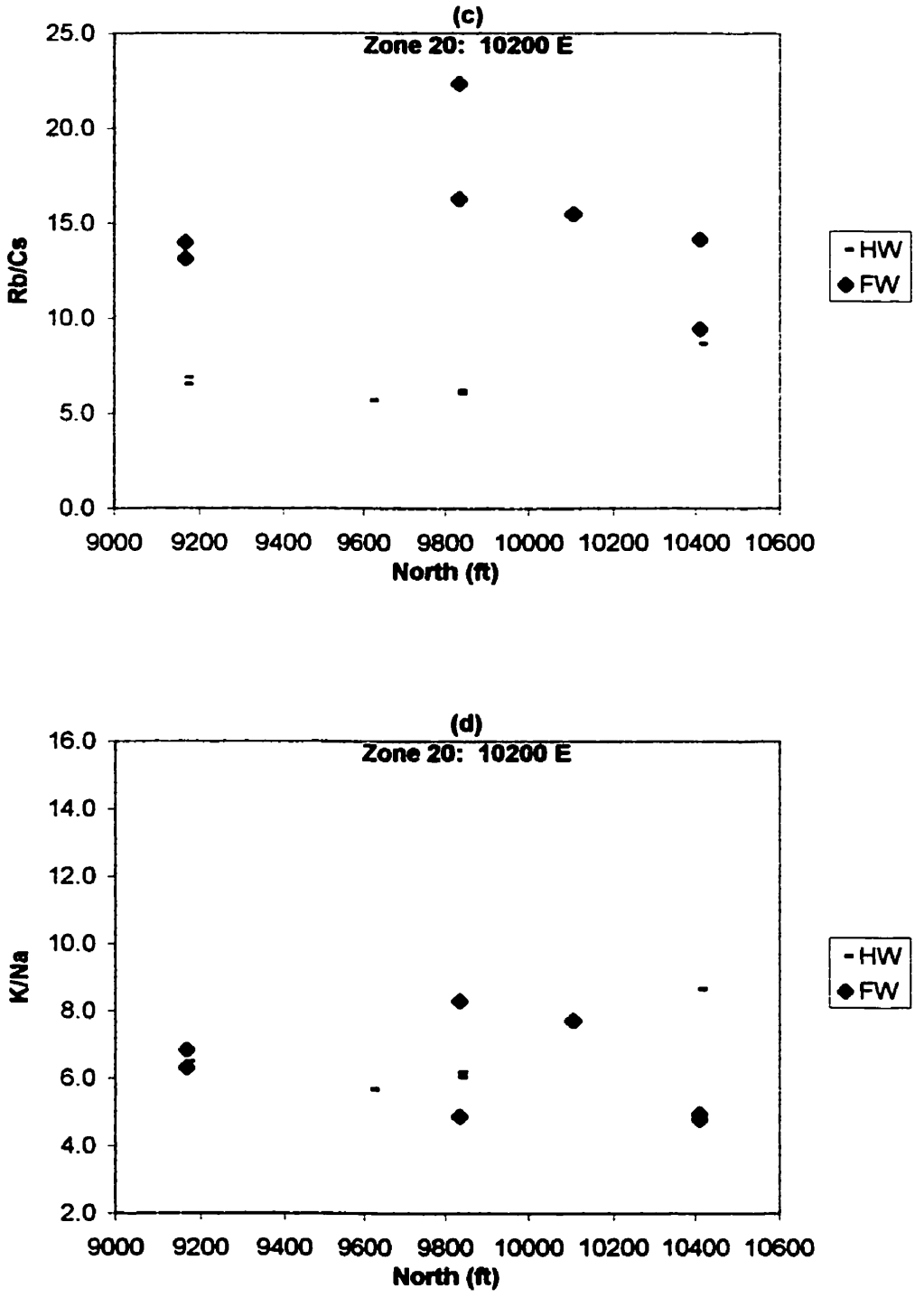


**Figure 8.5** Bulk chemistry of microcline-perthite (Type 1), from hangingwall (HW) and footwall (FW) locations of zone (20).

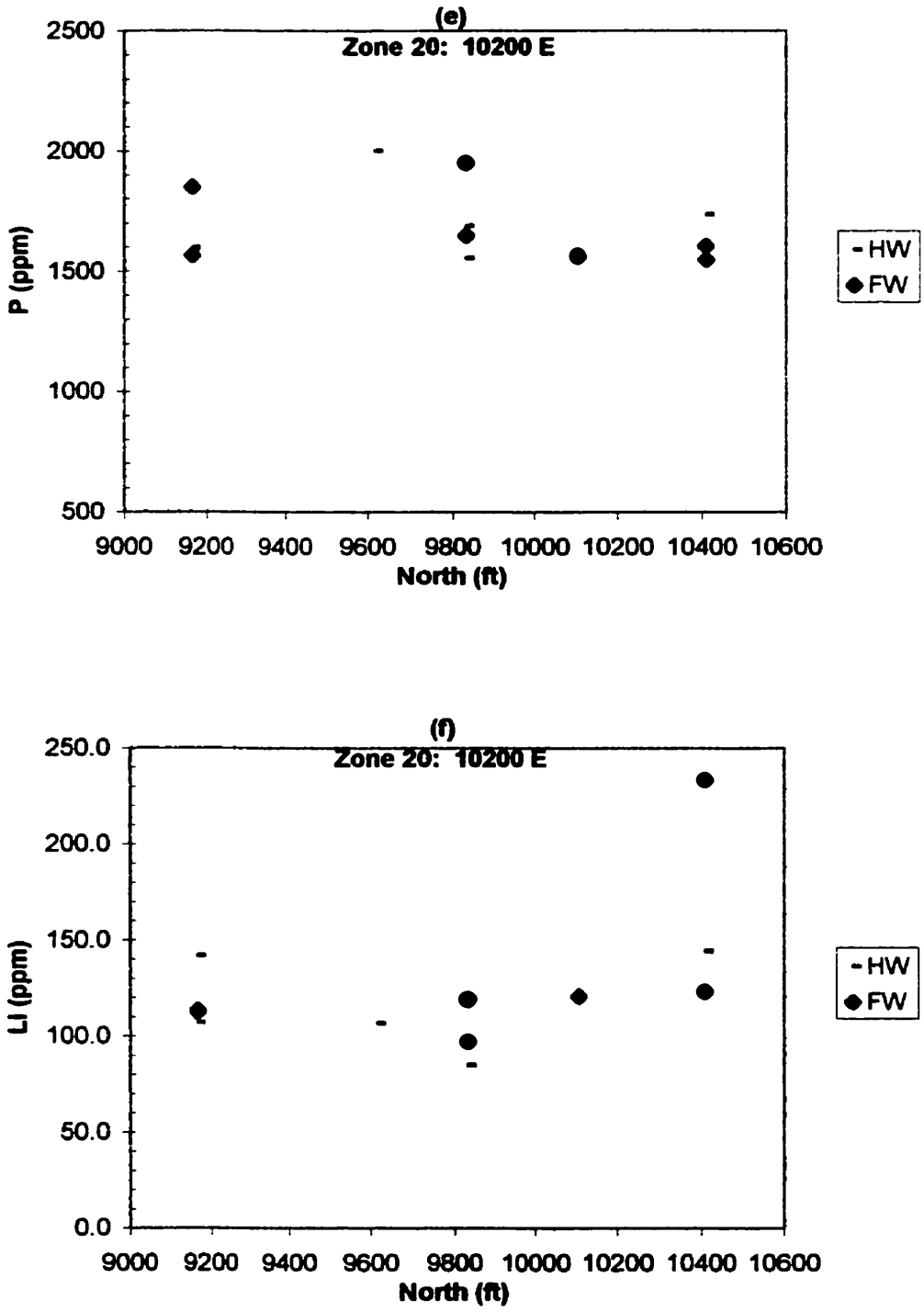


**Figure 8.5** Bulk chemistry of microcline-perthite (Type 1), from hangingwall (HW) and footwall (FW) locations of zone (20).

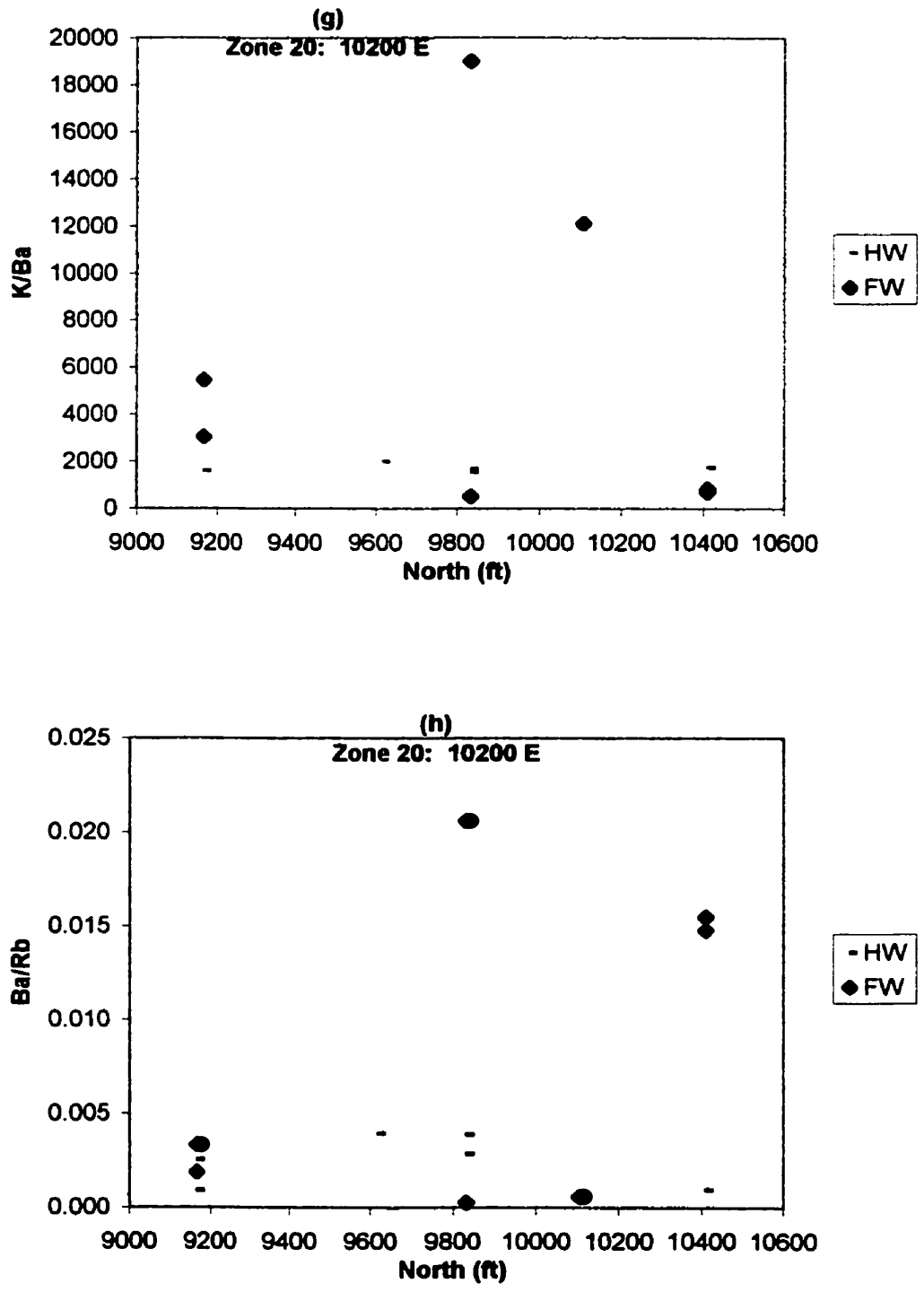


**Figure 8.5** Bulk chemistry of microcline-perthite (Type 1), from hangingwall (HW) and footwall (FW) locations of zone (20).

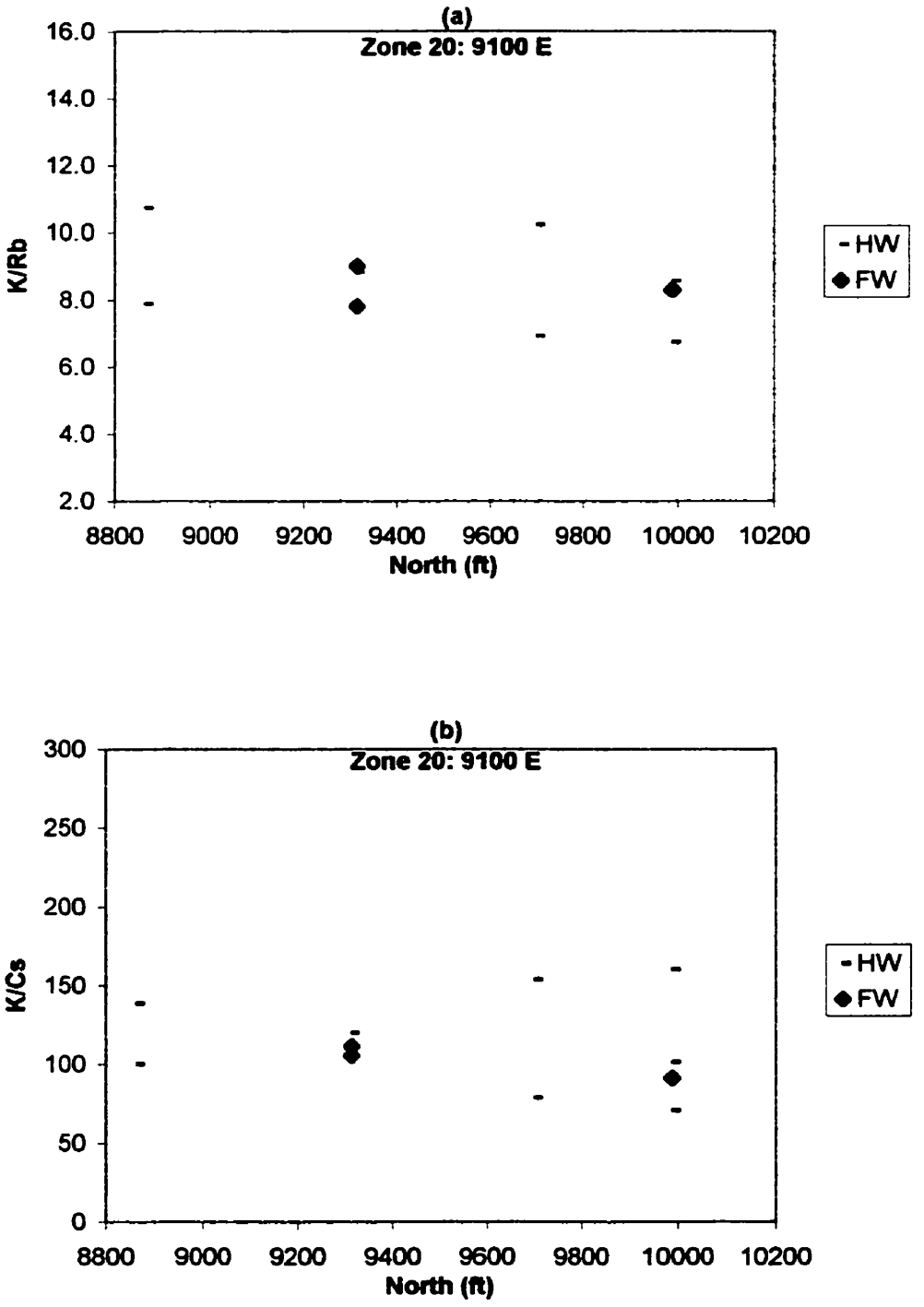


**Figure 8.6** Bulk chemistry of microcline-perthite (Type 1), from hangingwall (HW) and footwall (FW) locations of zone (20).

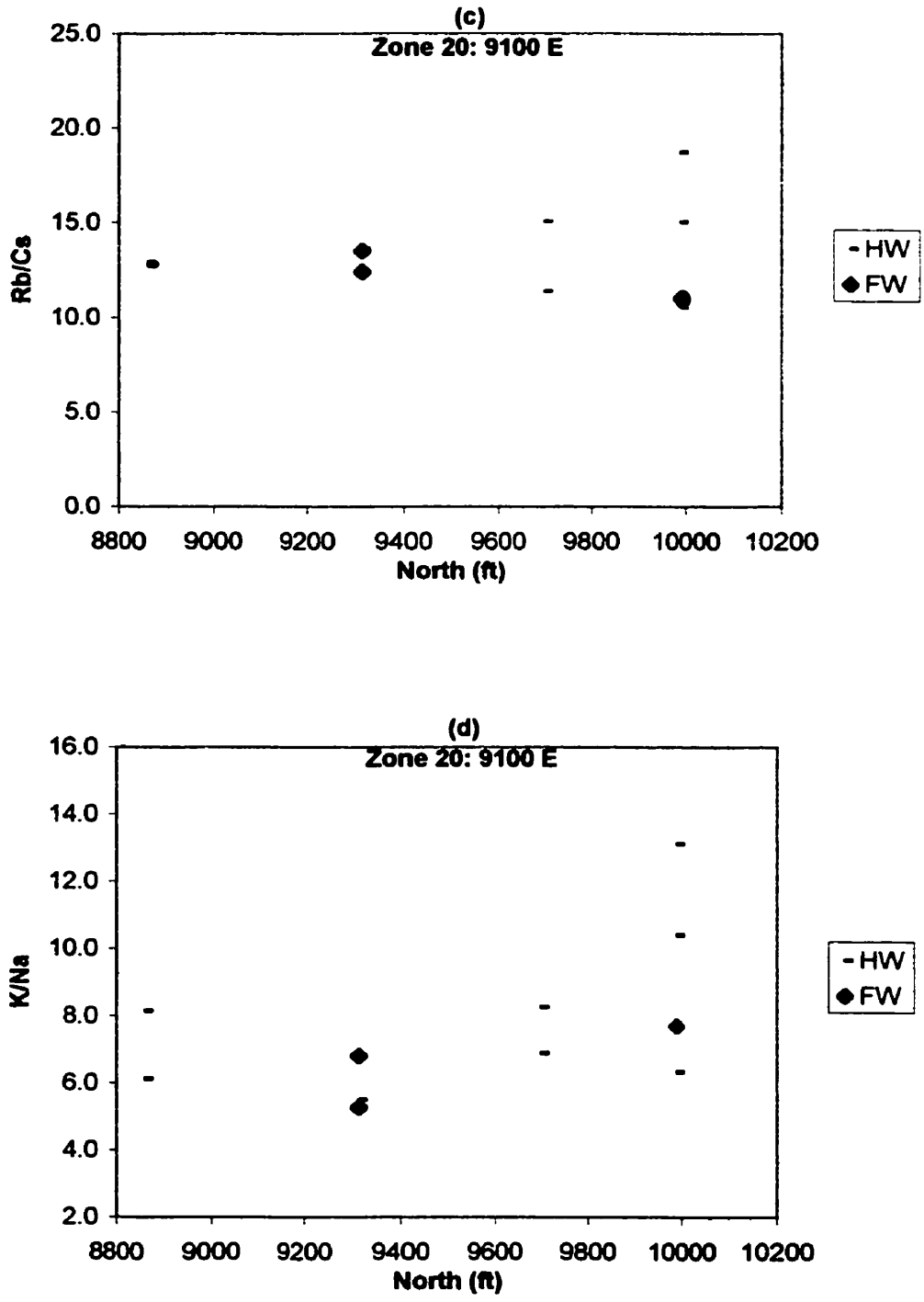


**Figure 8.6** Bulk chemistry of microcline-perthite (Type 1), from hangingwall (HW) and footwall (FW) locations of zone (20).

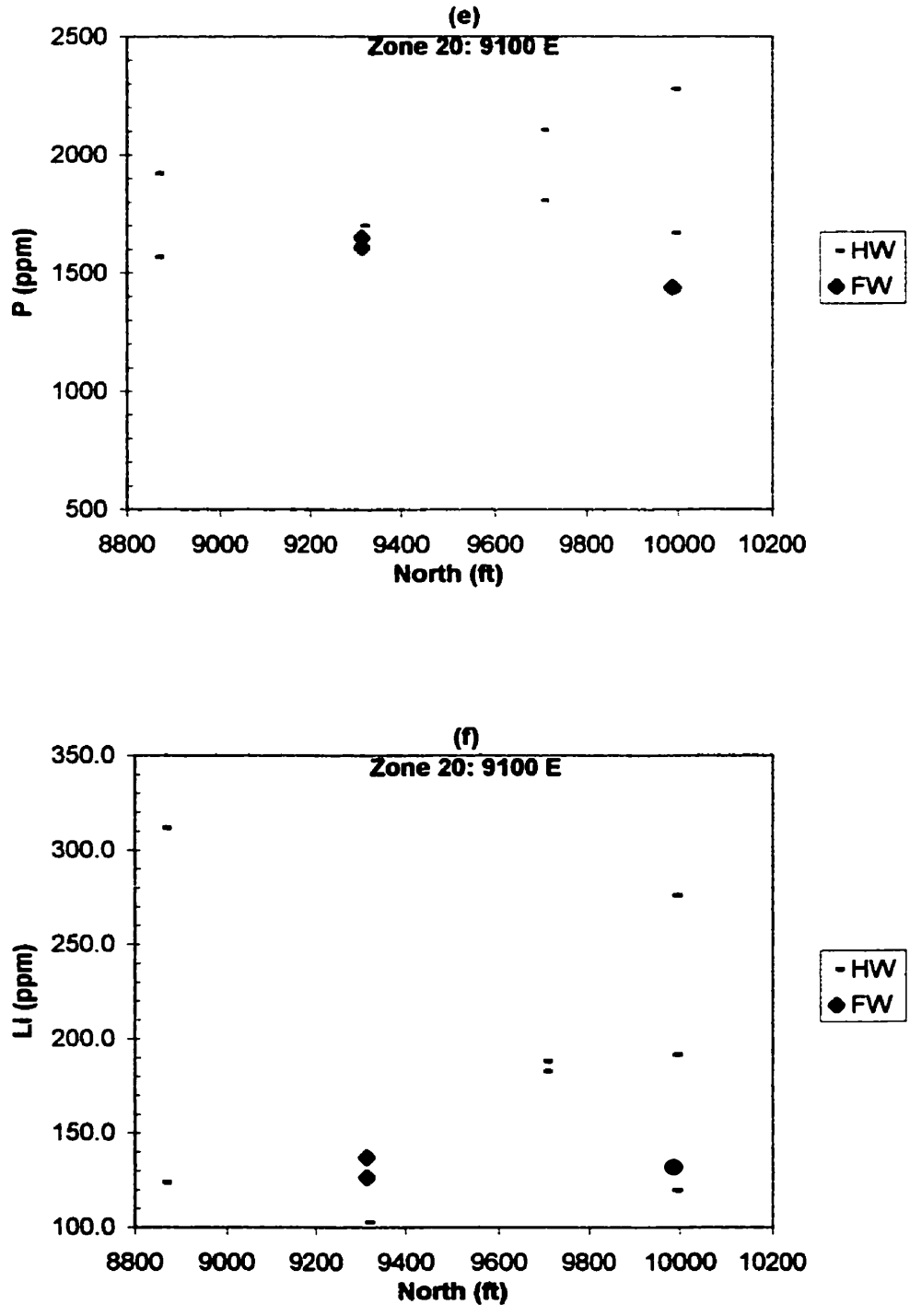


**Figure 8.6** Bulk chemistry of microcline-perthite (Type 1), from hangingwall (HW) and footwall (FW) locations of zone (20).

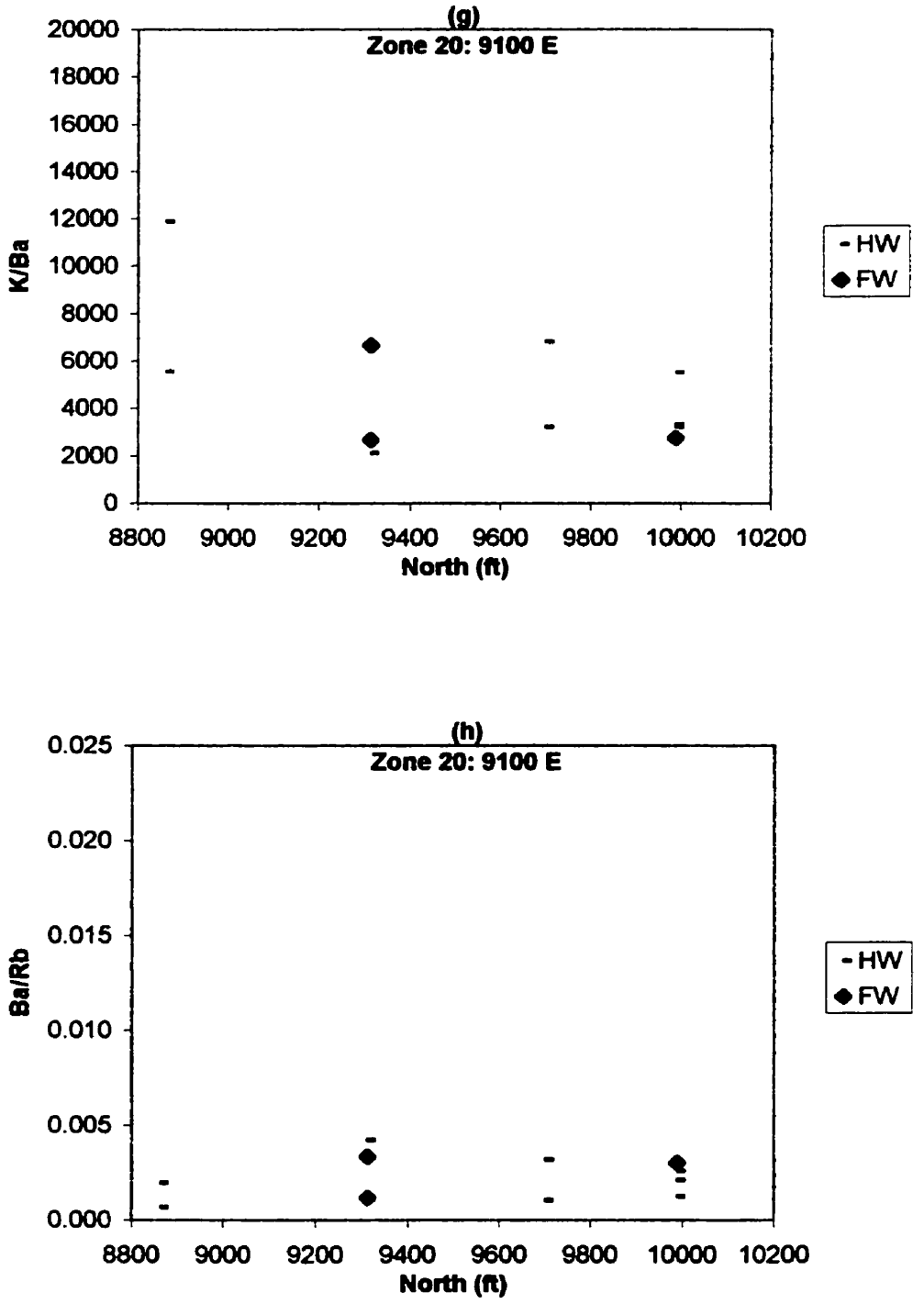


**Figure 8.6** Bulk chemistry of microcline-perthite (Type 1), from hangingwall (HW) and footwall (FW) locations of zone (20).

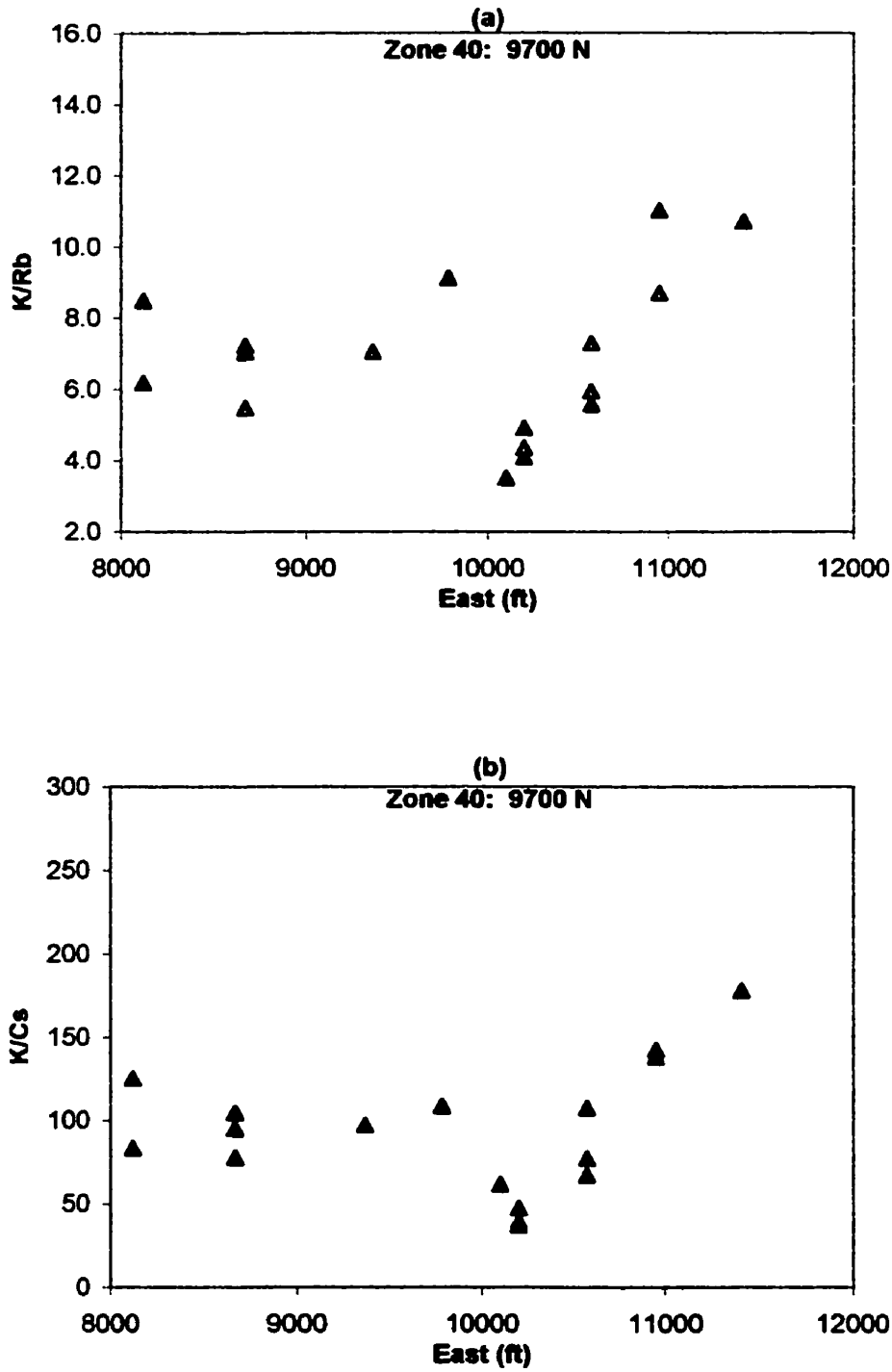


**Figure 8.7** Bulk chemistry of microcline-perthite (Type 1) from zone (40)

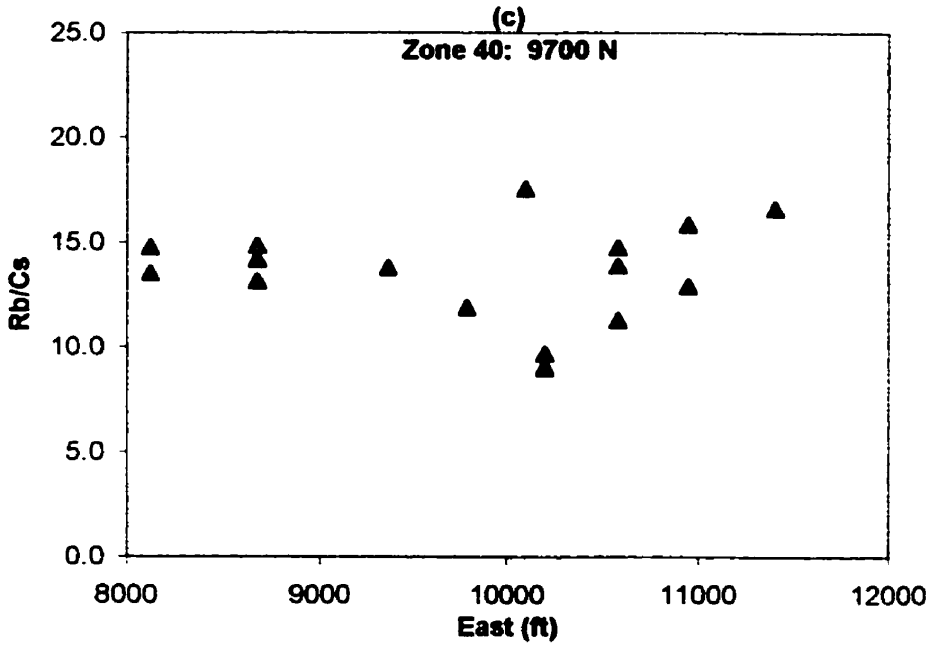


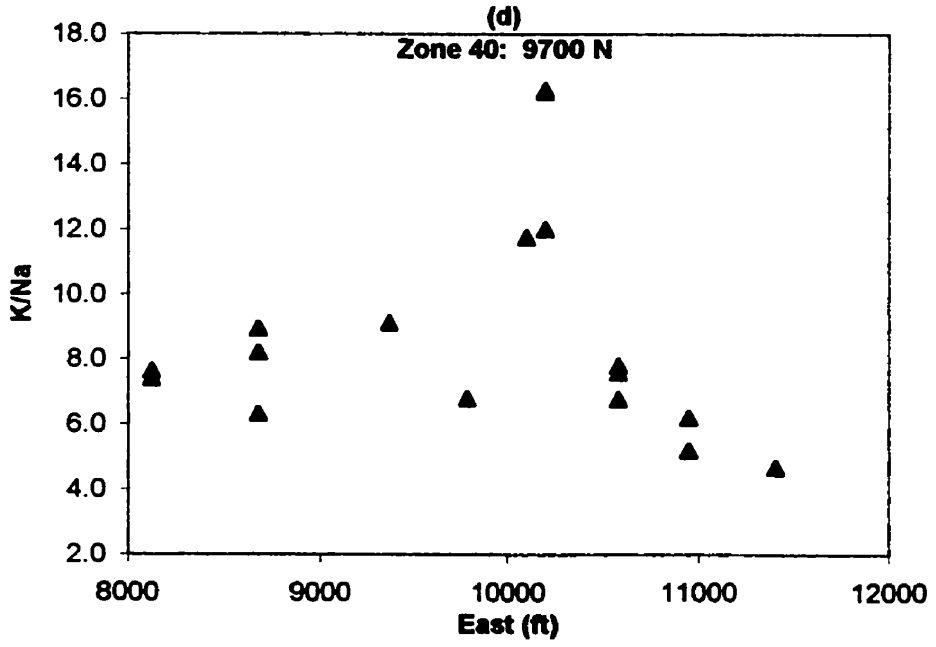


**Figure 8.7** Bulk chemistry of microcline-perthite (Type 1) from zone (40)

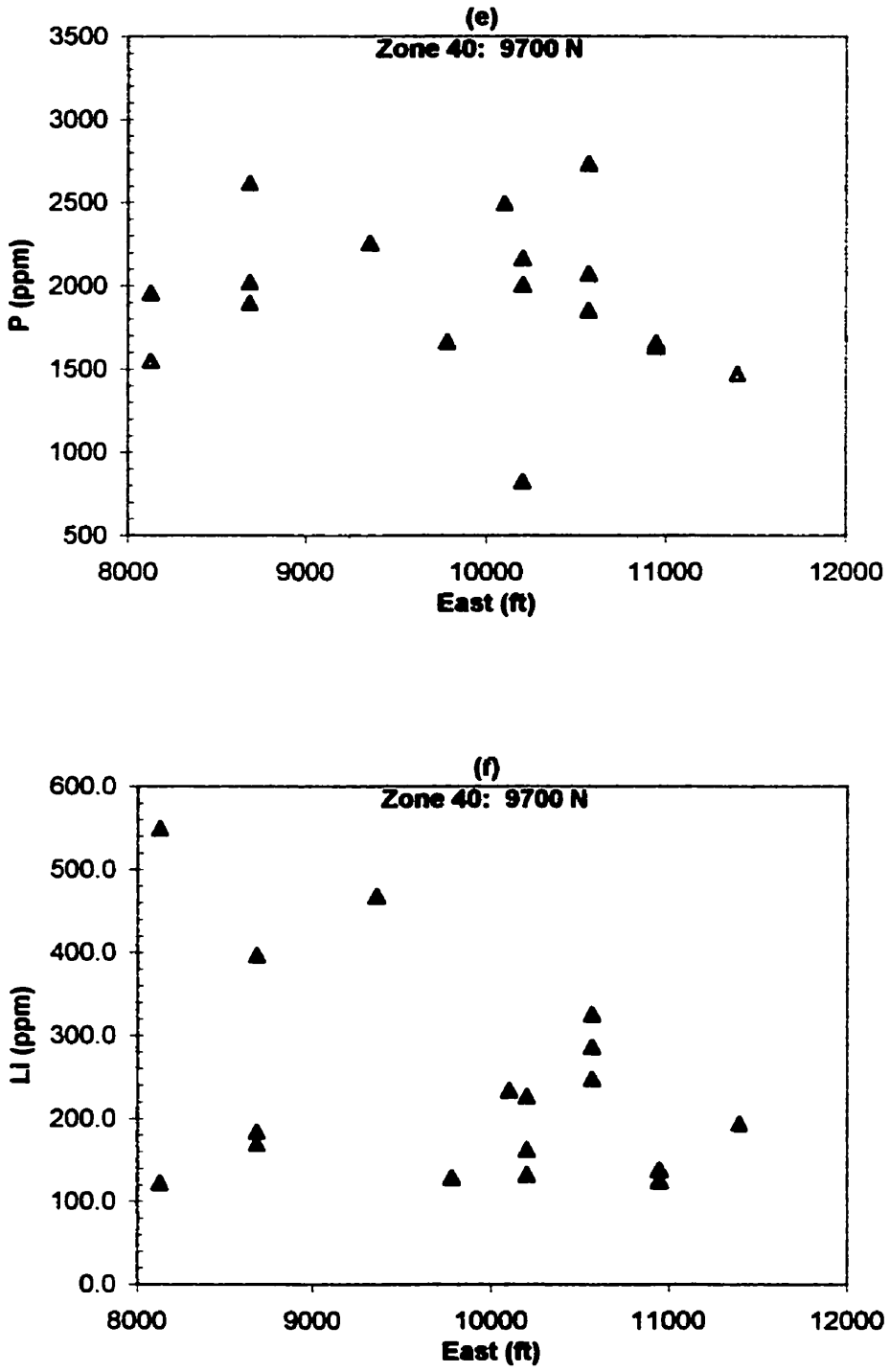


**Figure 8.7** Bulk chemistry of microcline-perthite (Type 1) from zone (40)

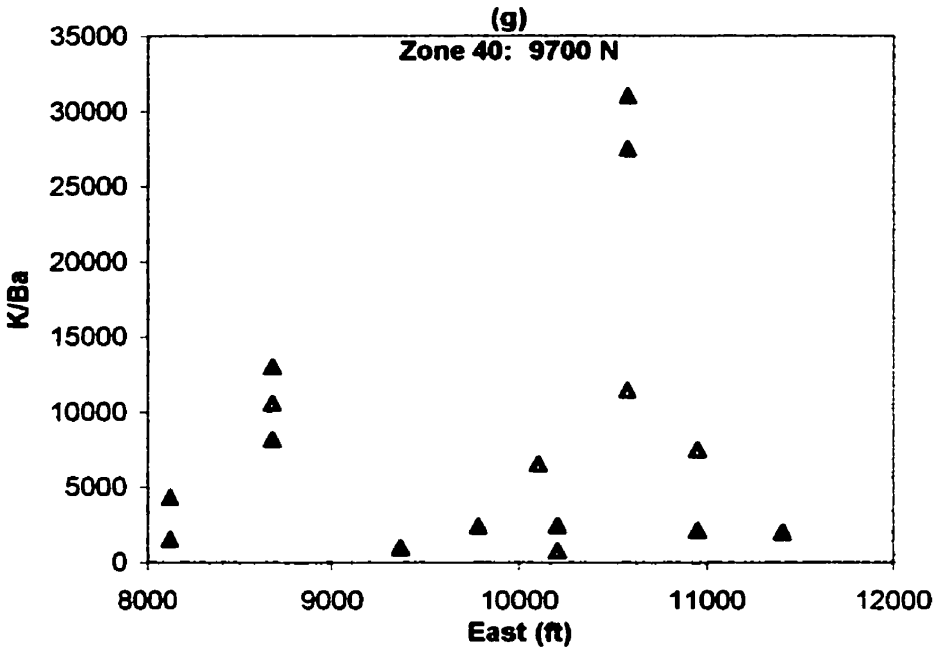


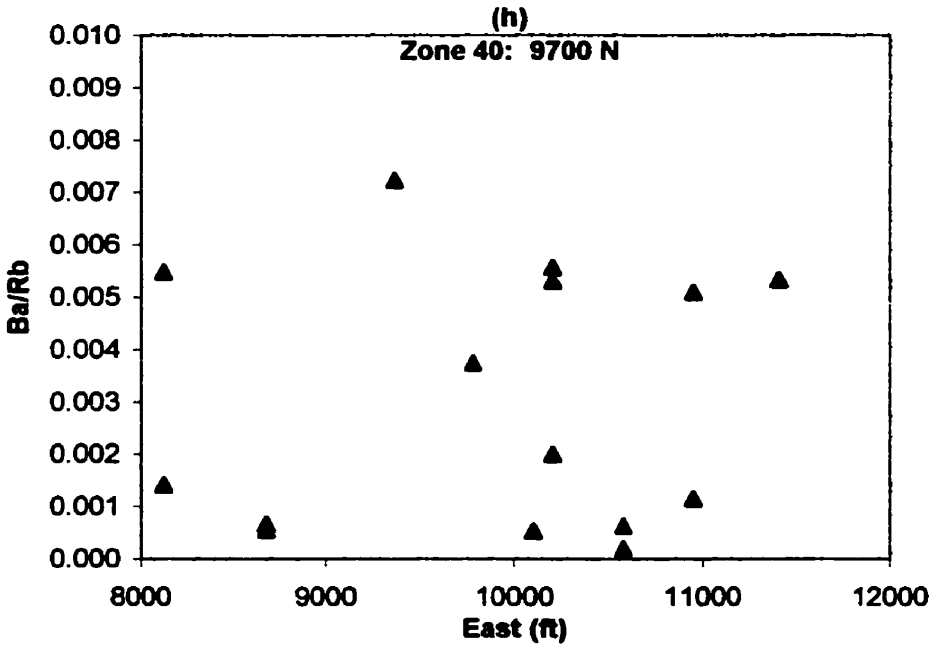


**Figure 8.7** Bulk chemistry of microcline-perthite (Type 1) from zone (40)

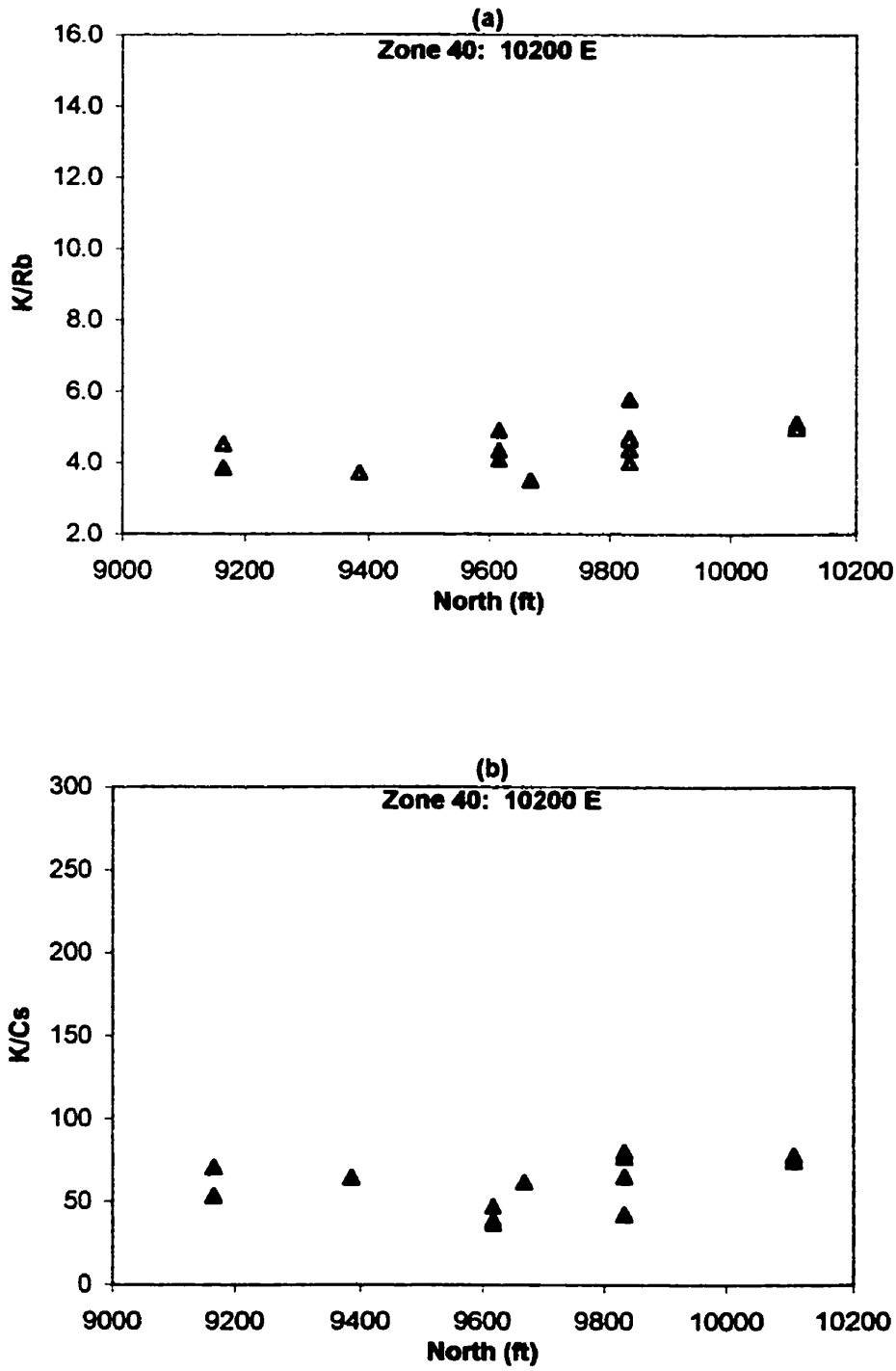


**Figure 8.8** Bulk chemistry of microcline-perthite (Type 1) from zone (40)

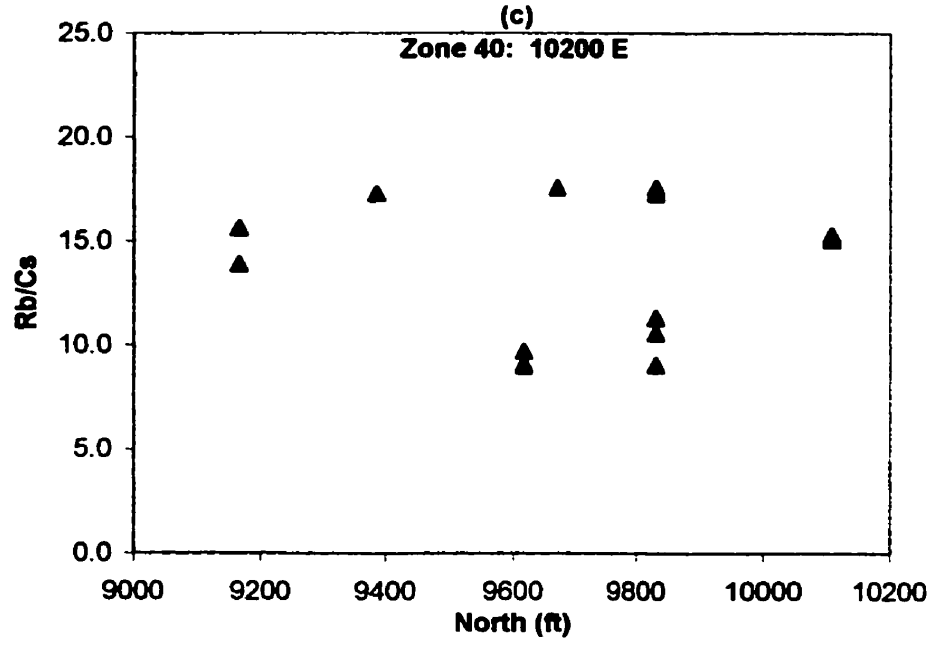


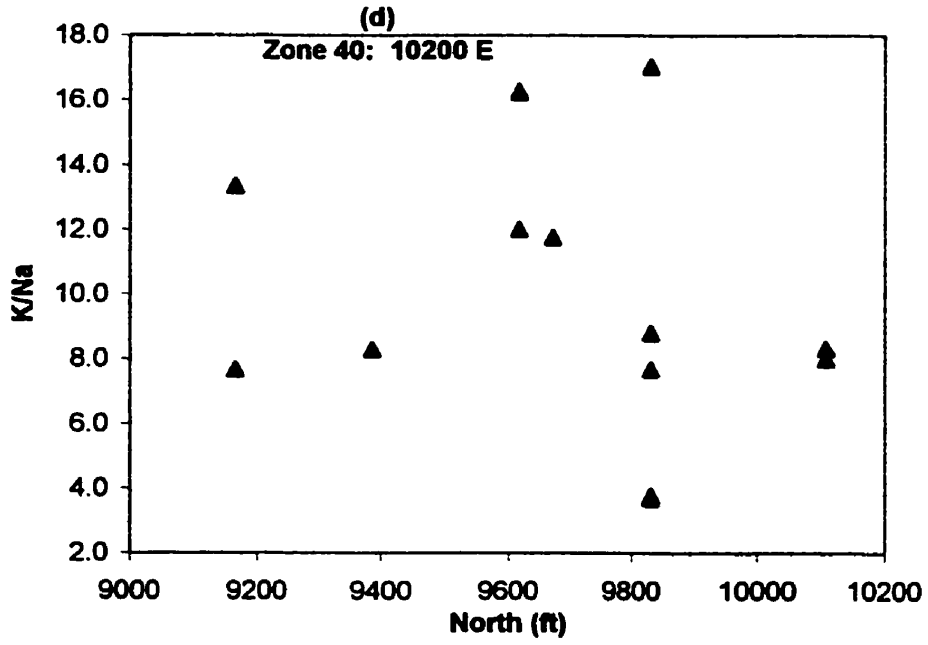


**Figure 8.8** Bulk chemistry of microcline-perthite (Type 1) from zone (40)

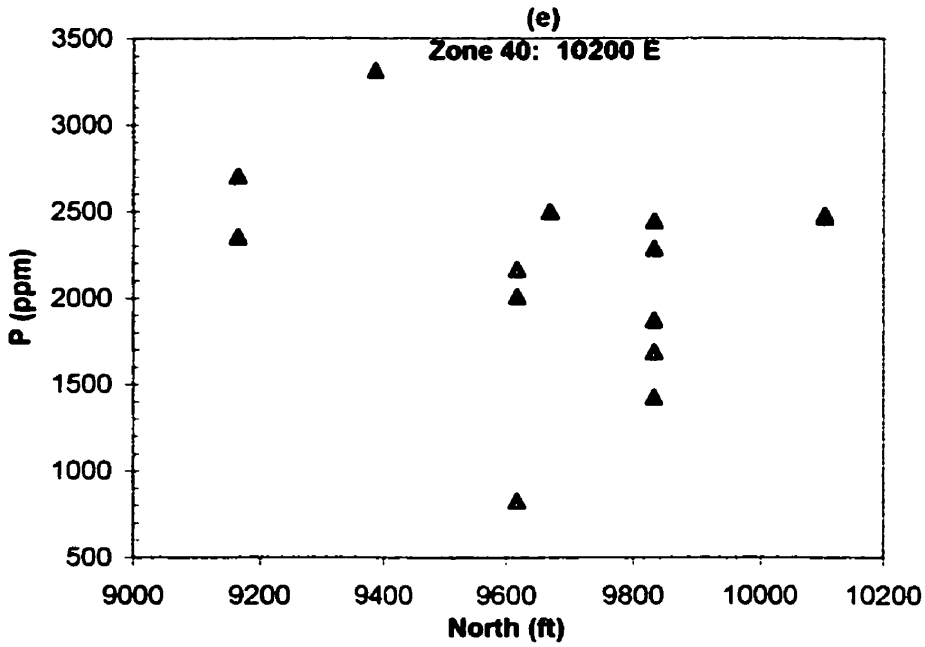


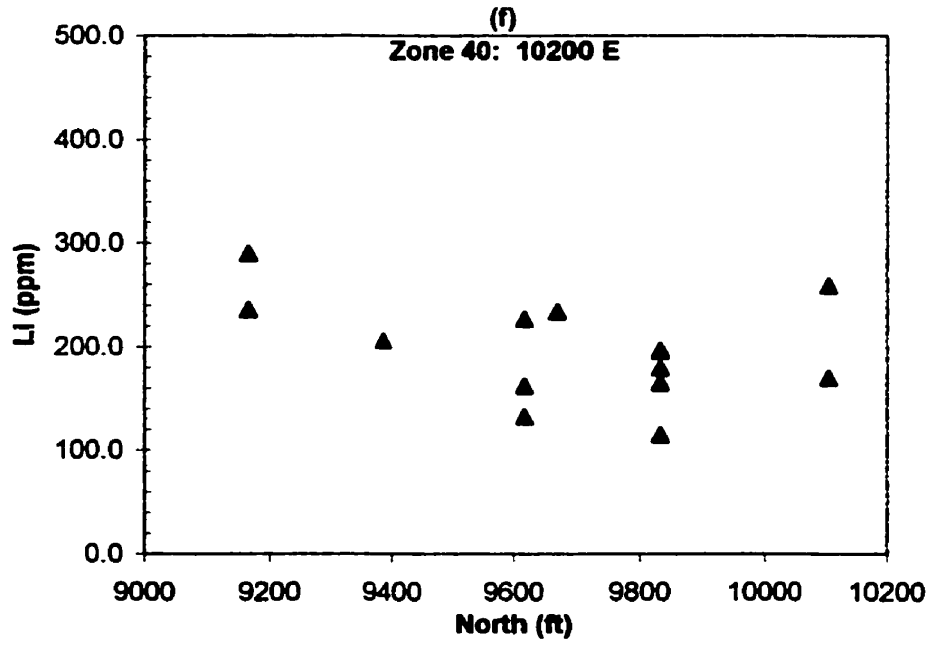


**Figure 8.8** Bulk chemistry of microcline-perthite (Type 1) from zone (40)

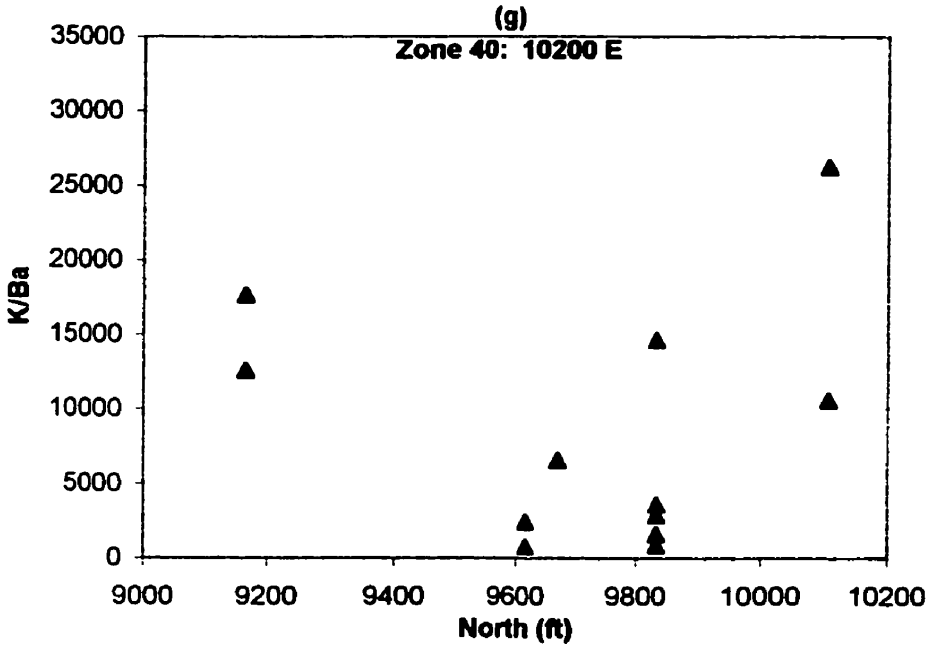


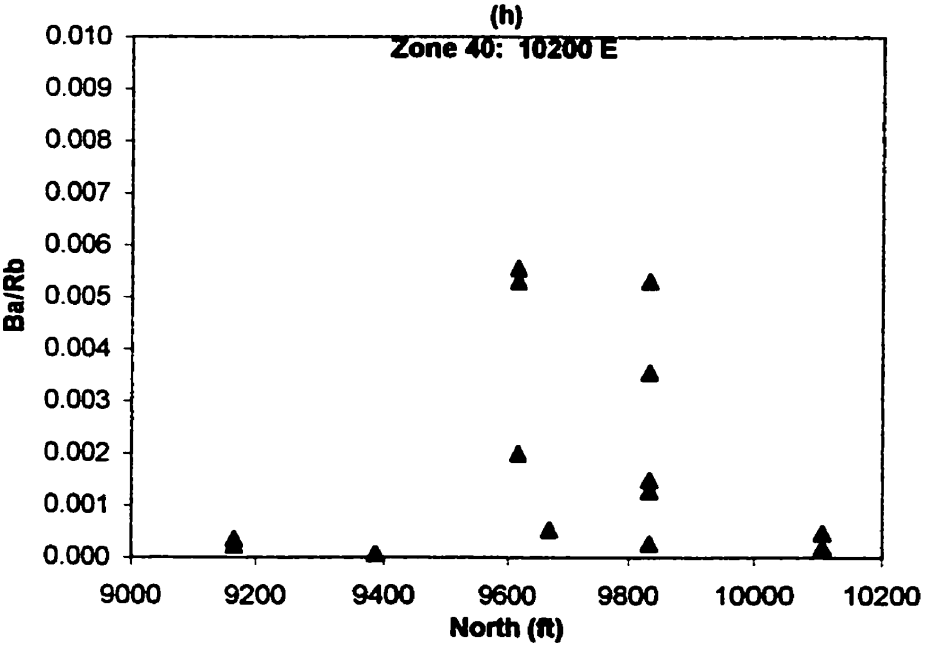


**Figure 8.8** Bulk chemistry of microcline-perthite (Type 1) from zone (40)

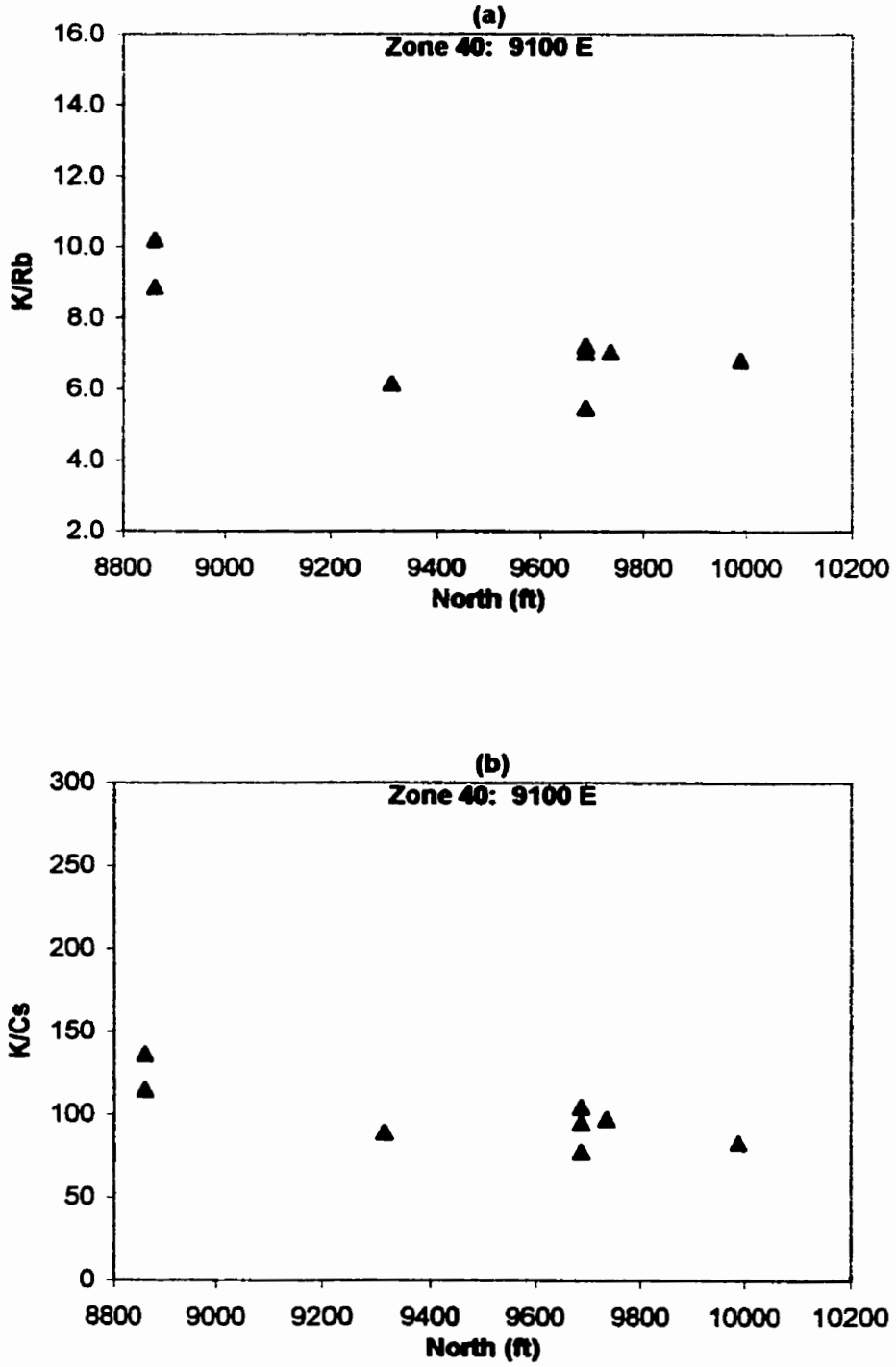


**Figure 8.9** Bulk chemistry of microcline-perthite (Type 1) from zone (40)

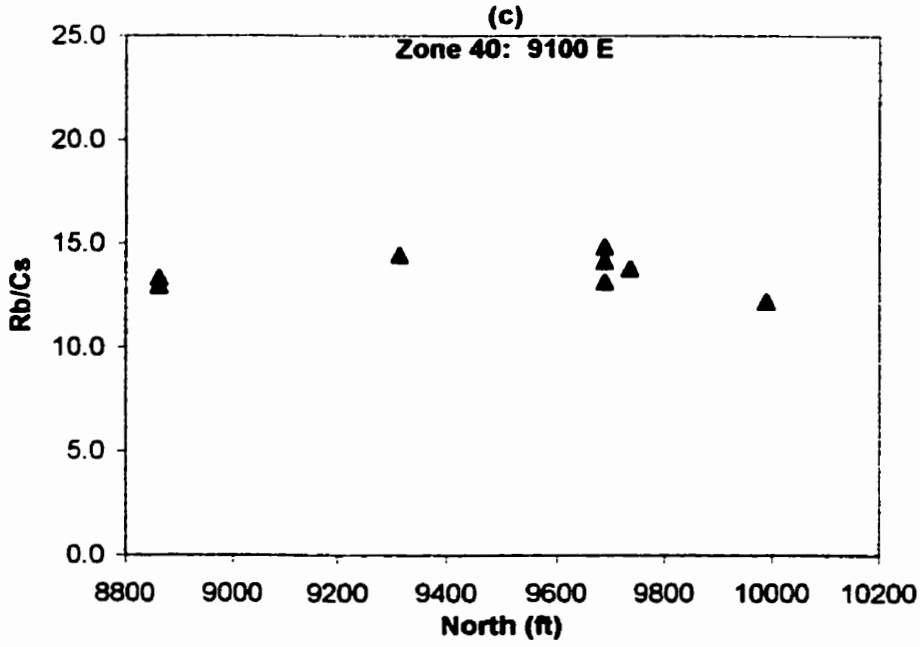


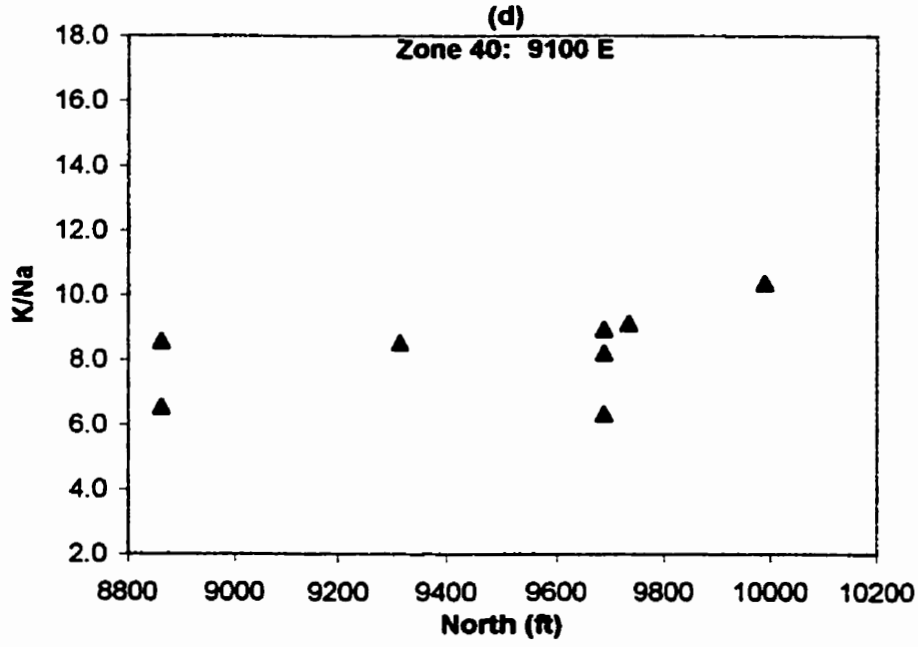


**Figure 8.9** Bulk chemistry of microcline-perthite (Type 1) from zone (40)

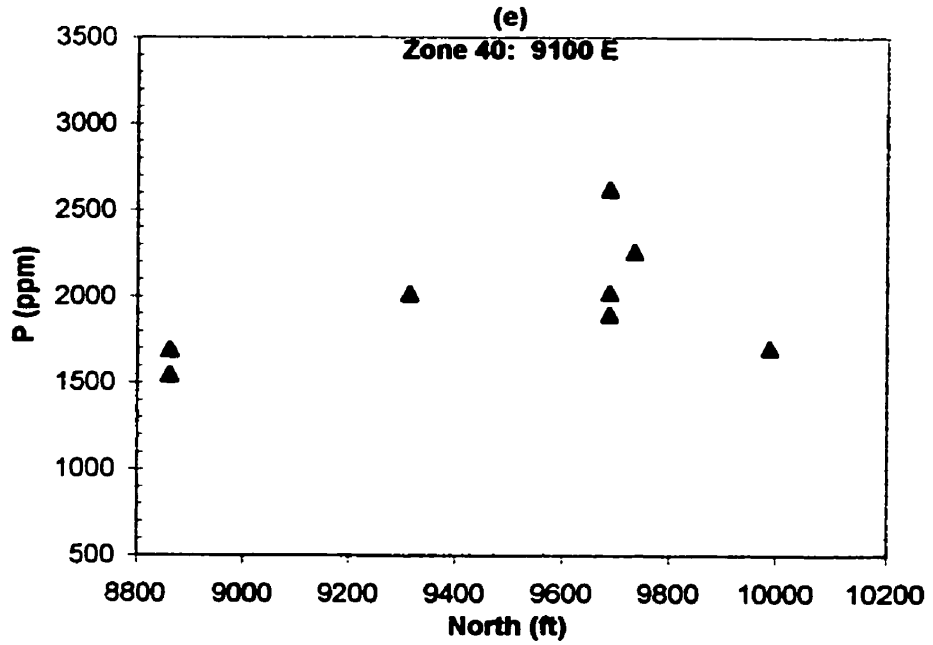


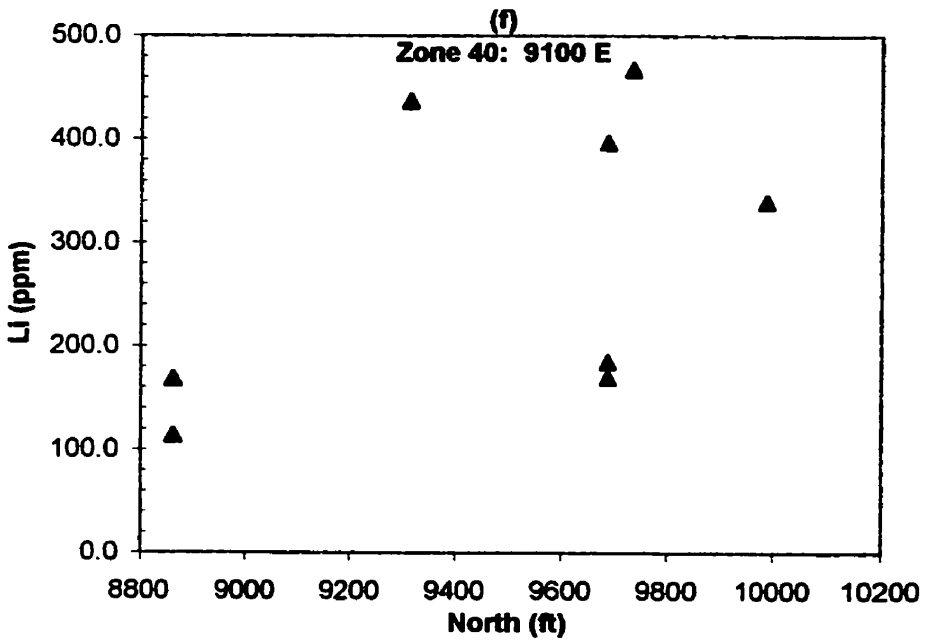


**Figure 8.9** Bulk chemistry of microcline-perthite (Type 1) from zone (40)

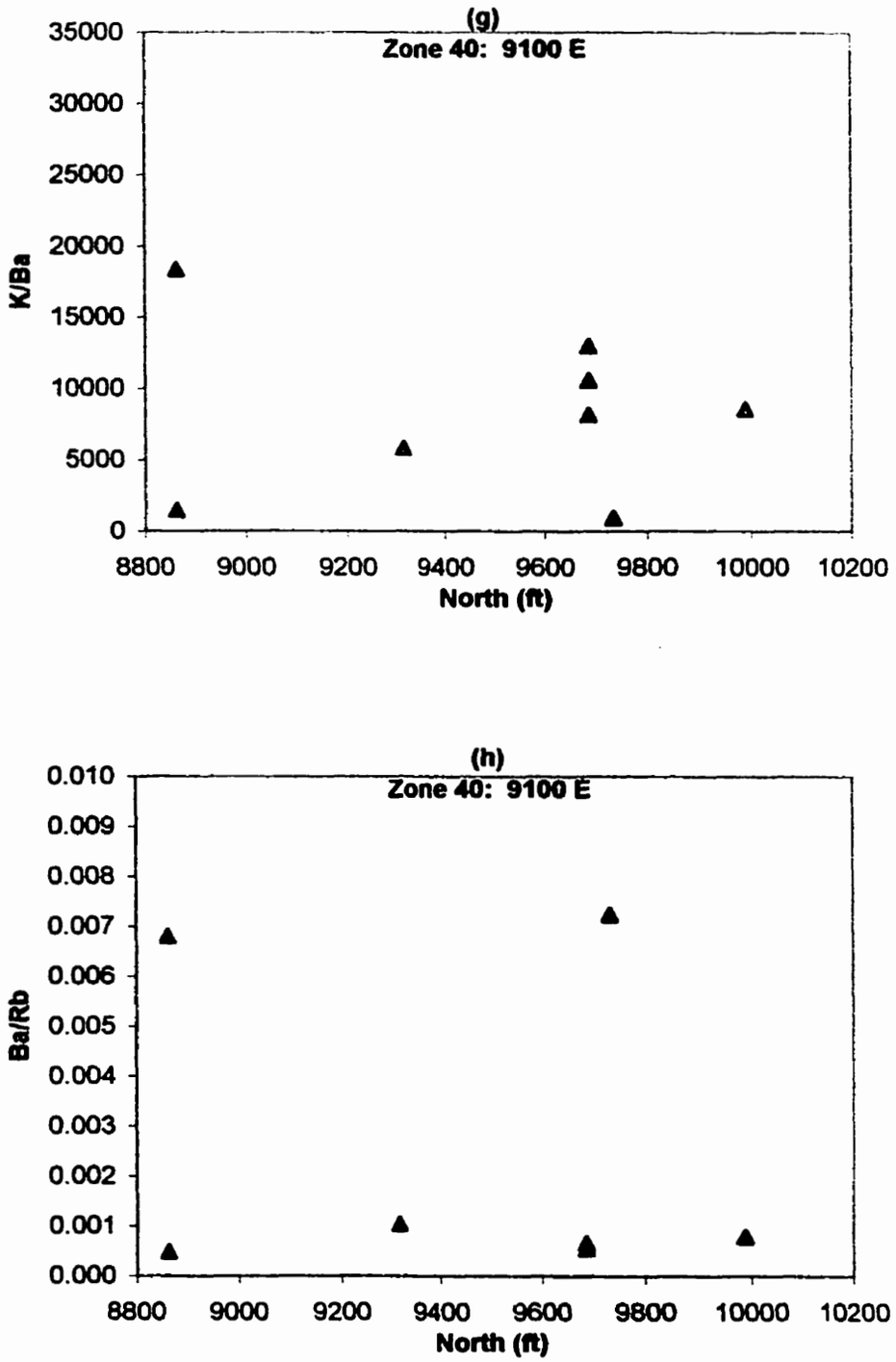


**Figure 8.9** Bulk chemistry of microcline-perthite (Type 1) from zone (40)

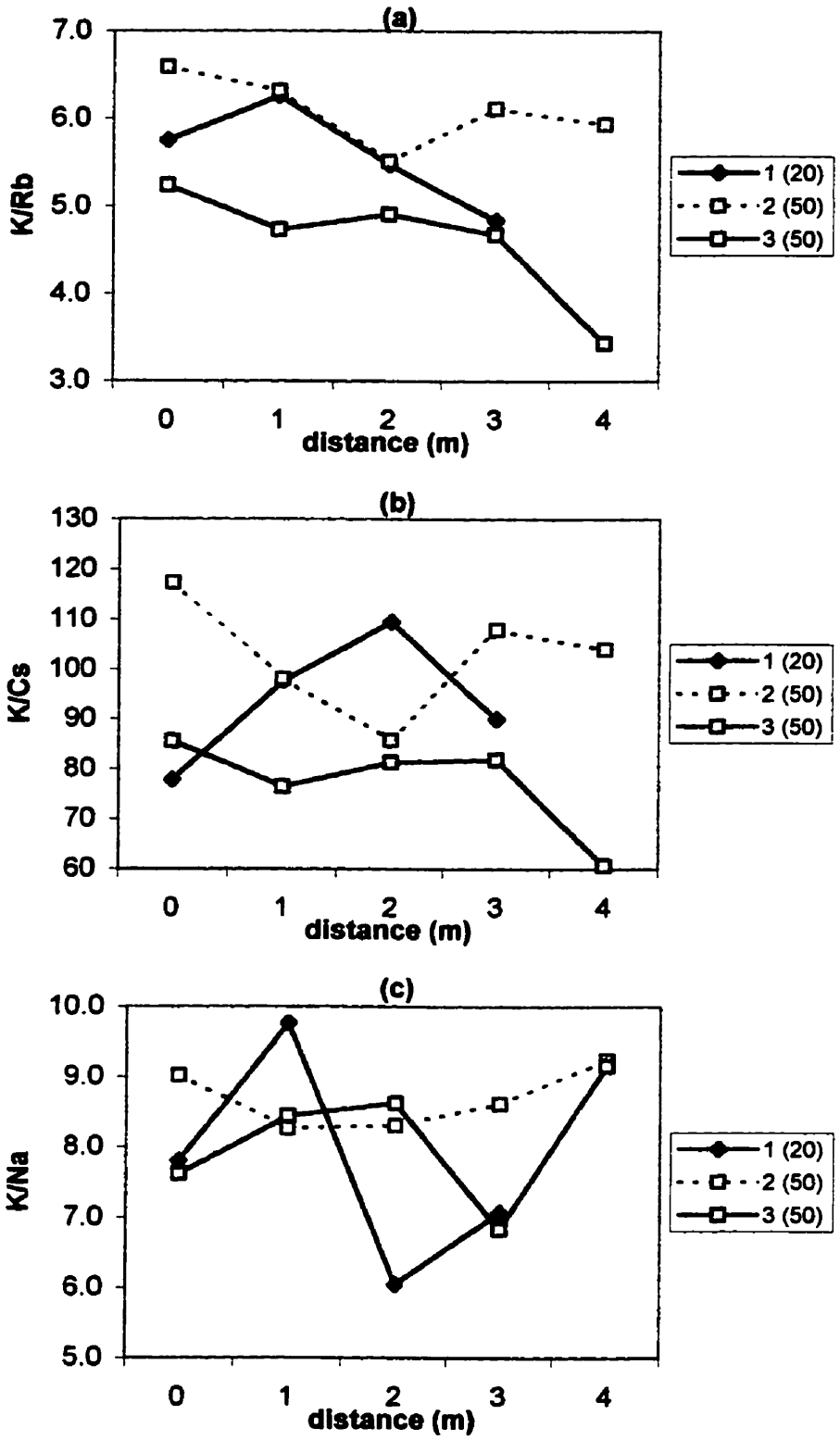


**Figure 8.10** Microcline-perthite single crystal geochemistry. Numbers in legend refer to individual crystals (see text) up to 5 m in length, followed by zonal designation.

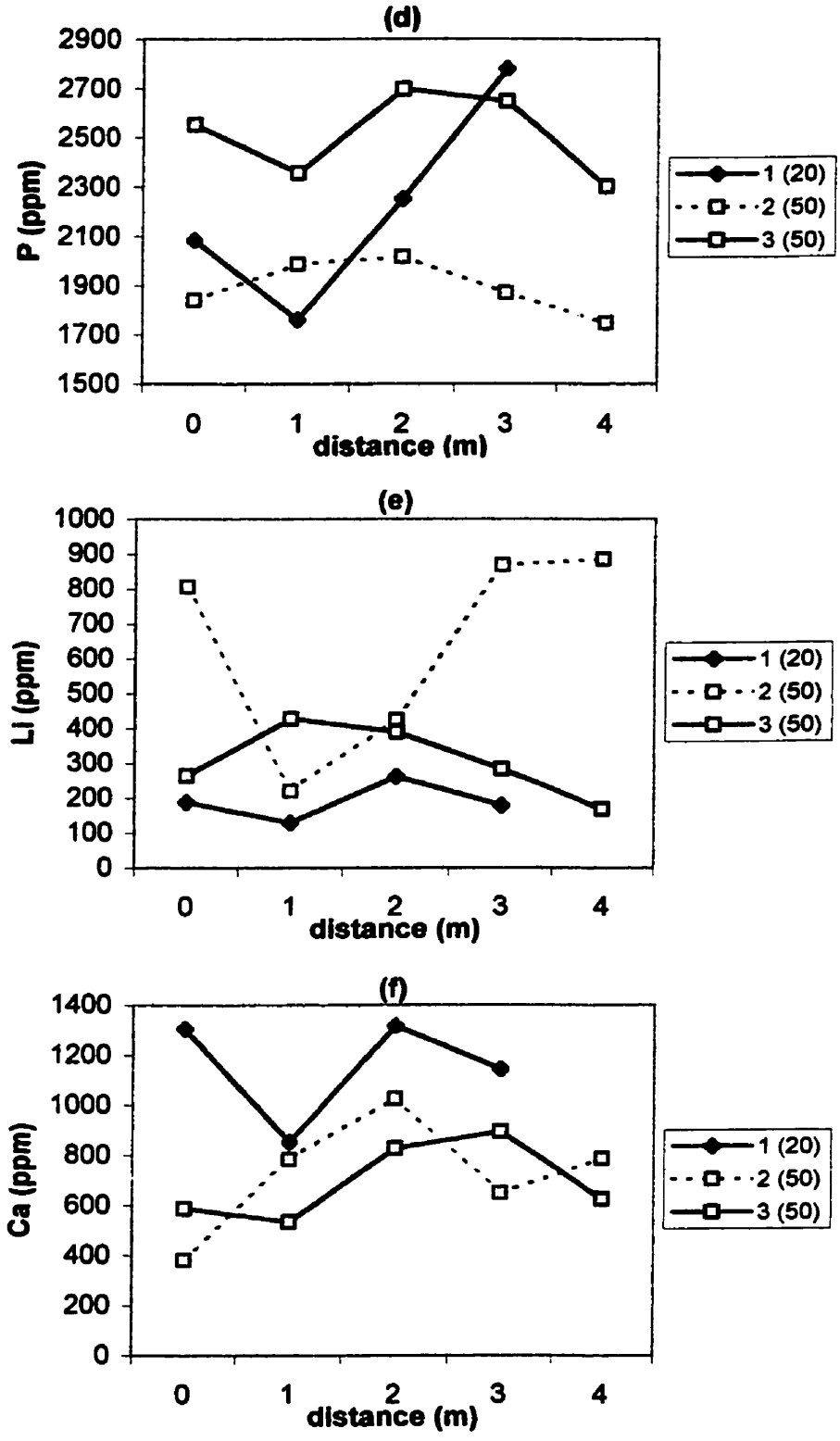


**Figure 8.10** Microcline-perthite single crystal geochemistry. Numbers in legend refer to individual crystals (see text) up to 5 m in length, followed by zonal designation.

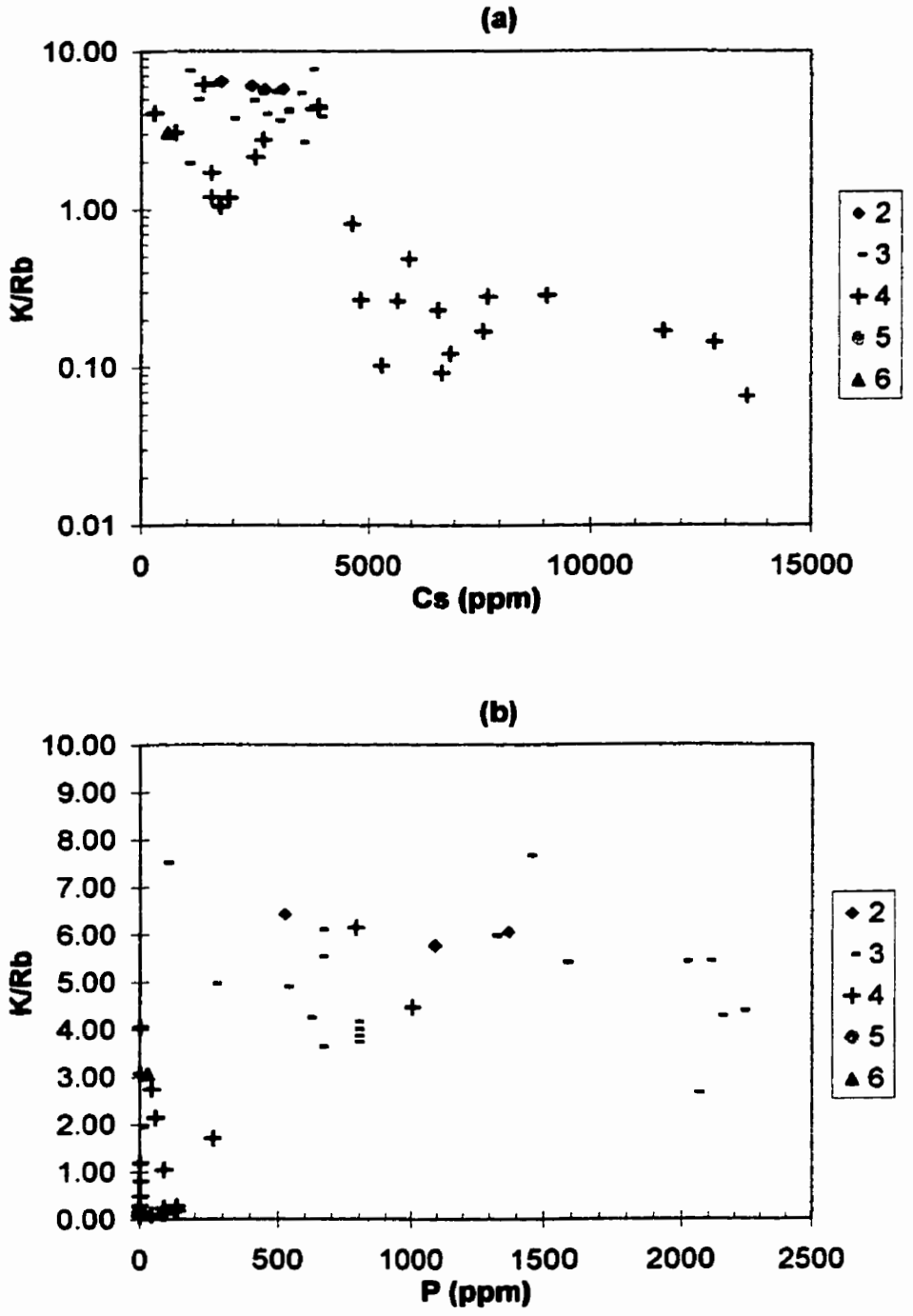


**Figure 8.11** Geochemistry (EMPA) of late K (Rb)-feldspar (Types 2,3,4,6)

# CHAPTER 9: DISCUSSION

Feldspars in highly evolved granitic pegmatites are notoriously understudied, despite the fact that they comprise the majority of the modal volume of pegmatites, and represent a significant geochemical reservoir of major-, minor- and trace-elements. The feldspar paragenetic sequence (Figure 6.1) records geochemical and textural variations throughout the entire cooling history, from high-temperature primary crystallization, to subsolidus readjustments, and finally hydrothermal alteration and replacement stages. The relative modal abundances of the different feldspar types in the different zones (Figure 9.1) link the feldspars to the volumetric parameters of the individual zones, and to the bulk composition of the pegmatite.

## 9.1 Paragenetic relations of the feldspars

The author has purposely avoided the use of genetic terms such as 'primary' and 'secondary', because rock-forming processes in Tanco inevitably involved a series of complex and overlapping events, starting with primary magmatic crystallization, followed by superposed processes involving late-stage fracture filling and local solution-reprecipitation; and finally by metasomatic to hydrothermal alterations involving recrystallization, leaching and replacement. For the most part, overall textural features and contact relations of minerals in zones (20) (40) (50) and (80) indicate genesis by primary magmatic crystallization. More problematic are the distinctive textural and mineralogical features observed in zones (30), (70), (80), and (90). There is a long history of debate concerning internal pegmatite units, and whether they formed as replacement assemblages (Crouse *et al.*, 1979, Burnham and Nekvasil, 1986), from supercritical hydrous fluids (Jahns and Burnham, 1969; Jahns, 1982, Thomas *et al.*, 1988), or by primary magmatic crystallization from $H_2O$-undersaturated melt (London,

1987; London *et al.*, 1989; Černý, 1992). In consideration of textural and paragenetic features observed at Tanco, the more recent experimental and petrological investigations by the latter group support a predominantly primary magmatic origin of Type-1 feldspars at Tanco.

**Table 9.1:** Paragenetic sequence and modal abundances of feldspar types per zone.

| *Zone* | **K(RB)-feldspar Types** | **modal abundance** | **Albite Types** | **modal abundance** |
|---|---|---|---|---|
| **10** 0.1% | **1** blocky microcline- perthite | 0.1% | **A** aplitic albite<br>**B** cleavelandite | 63%<br>3% |
| **20** 30.8% | **1** blocky microcline- perthite | 15% | **A** aplitic albite<br>**B** cleavelandite | 10%<br>30% |
| **30** 2.7% | | | **A** aplitic albite | 67% |
| **40** 28.8% | **1** blocky microcline- perthite | 24% | **A** aplitic albite<br>**B** cleavelandite<br>**C** saccharoidal albite | 5%<br>20%<br>1-10% |
| | **6** adularia crystals | 0.1% | **F** albite crystals | <0.1% |
| **50** 13.1% | **1** blocky microcline- perthite | 25% | **A** aplitic albite<br>**B** cleavelandite<br>**C** saccharoidal albite | 2%<br>5%<br>0.1-1% |
| | **6** adularia crystals | 0.1% | **F** albite crystals | <0.1% |
| **60** 13.6% | **1** blocky microcline- perthite | 50% | **A** aplitic albite<br>**B** cleavelandite | 15%<br>5% |
| | **2** granular non-perthitic microcline | 0.X% | | |
| **70** 7.5% | **1** blocky microcline- perthite | 2.0% | **A** aplitic albite<br>**B** cleavelandite | 0.1%<br>0.2% |
| **80** 1.3% | **1** blocky microcline- perthite | 2.5% | **A** aplitic albite<br>**B** cleavelandite | 1%<br>4% |
| | **3** metasomatic microcline<br>**4** adularian (K-Rb) feldspar<br>**5** adularian (K>Rb) feldspar | 0.X%<br>0.0X%<br>0.0X% | **D** metasomatic albite<br>**E** anhedral albite | 0.3%<br>0.1% |
| **90** 2.1% | **1** blocky microcline- perthite | 10% | **B** cleavelandite | 8% |

-Percentages in column 1 refer to volume % of each zone within the pegmatite.
-Zonal volume %, Type-1 and Type-A+B abundances from Stilling (1998).

Of all the feldspar types so far discussed, blocky microcline-perthite (Type 1) displays features most consistent with a primary authigenic origin. Based on crystal morphology and typical phenocrystic occurrences relative to associated albite-rich matrix assemblages, K-feldspar formed first in the feldspar paragenetic sequence (Table 6.1). Textural features, in most cases, suggest aplitic albite and cleavelandite also formed as major components of primary mineral assemblages; however, sporadic occurrence of a mineral assemblage containing albite and significant abundances of fine-grained micas, quartz and rare accessory minerals also exhibit replacement-like features, suggestive of a metasomatic origin.

The fine grain-size of aplitic albite is inevitably a product of rapid nucleation, the onus for which is thought to be related to the removal of silicate-network-modifying components [*i.e.* B, F, Li, $H_2O$, (P); 'chemical-quench', London, 1987]. Jahns and Burnham (1969) proposed a 'pressure-quench' mechanism for the generation of line-rock, in which rapid nucleation occurred as a result of sudden and periodic chamber depressurization related to the rupture of host lithologies under pressure from an exsolved hydrous-fluid phase. Kleck (1996) advocated gravitational settling as a viable mechanism. Recent studies and experimental work concerning textural aspects of pegmatites of the Pala district favour the development of line-rock by diffusion-controlled oscillatory nucleation, involving the progression of a crystallization front through liquid melt (Webber, 1997), or a crystallization front that drives forward a highly fluxed, hydrous-melt boundary layer through a solid or semi-solid precursor (constitutional zone-refining; Morgan and London, 1999).

The variable textures and associations of aplitic albite in Tanco (Chapters 3,7) probably represent more than one mode of genesis. Textural features of large to medium sized

aplite bodies are suggestive of a primary origin, however, the origin of smaller, more localized occurrences of 'saccharoidal' albite are less certain.

Despite the common occurrence of cleavelandite in pegmatites, hardly any work has been done on its distribution or morphology. This variety of albite is found almost exclusively in pegmatites, in a wide range of associations, including large-volume matrix assemblages in wall and interior zones, and substrate platforms for rare gem minerals in gem-bearing miarolitic cavities (*e.g.* Pala district, elbaite, morganite). Laurs *et al.* (1998) interpreted cleavelandite associated with F-rich mica and elbaite in miarolitic cavities of granitic pegmatites in northern Pakistan as the result of local rupture of miarolitic cavities. The other reported occurrence of non-pegmatite cleavelandite involves a peralkaline complex [*i.e.* Khibiny Alkaline Complex, Kola Peninsula (Yakovenchuk *et al.*, 1999)]; here, cleavelandite, consisting of subparallel and radiating laths up to 1-2 cm long, is associated with microcline, astrophyllite, loparite and aegirine. Textural relations between cleavelandite and the primary aluminosilicates indicate its metasomatic origin involving Na-rich fluid interaction with a primary nepheline syenite (A. Chakhmouradian, personal comm., 2001).

The distribution of cleavelandite as a major rock-forming mineral throughout Tanco suggests that it is contemporaneous to slightly later than aplitic albite in the sequence of primary crystallization. In rare cases where aplitic albite and cleavelandite coexist, cleavelandite laths commonly nucleate and radiate outward from within an aplitic substrate, although in some cases the reverse is observed, with aplitic albite capping terminations of cleavelanditic laths. Except for the difference in texture, relatively few general statements can be made about the mineralogical affinities of aplitic albite *vs.*

cleavelandite, nor does there seem to be a discernible pattern of relative abundances of the two varieties from zone to zone.

Modal abundances of early albite and K-feldspar throughout the zonal sequence (Table 9.1 and Figure 5.3) indicate a general increase in K-feldspar from outer zones (10) and (20) through (40) and (50) to zone (60), with a concurrent relative decrease in albite modal compositions. Zones (30) (70) (80) and (90) generally do not adhere to this trend; zone (30) is particularly notable because it is composed almost entirely of aplitic albite. Zone (60) is also distinctive because the modal abundance of K-feldspar is higher than expected for inner-intermediate zones of highly evolved granitic pegmatites. It also has characteristically variable and irregular textural features. Some sections are similar in texture to parts of zones (40) or (50), with coarse-grained K-feldspar or amblygonite or petalite, enveloped by typical medium-grained matrix assemblages. However, common occurrences of green to yellow to lavender, fine-grained microcline-, quartz- and mica-rich assemblages (MQM), usually associated with Ta-Nb rich mineralization, occur as metre-scale bands, and large irregular bodies dispersed throughout the more typical medium-to-coarse-grained lithologies. Textural relations between the different assemblages are ambiguous, and difficult to explain in terms of primary magmatic crystallization processes alone. Textural complexities are compounded along transitional boundary layers between zone (60) and lepidolite zone (90). Detailed petrographic and isotopic studies are warranted to adequately describe and interpret the variable features of zone (60), and its relation to adjacent zones, particularly (90).

The majority of highly evolved rare-element pegmatites, which contain petalite or spodumene in their most evolved zones, also contain considerably higher proportions of albite, rather than K-feldspar, associated with the Li-Al-silicate minerals (*e.g.* Separation

Rapids pegmatite field, Ontario, Breaks and Tindle, 1997). This is one reason why zone (60) is of notable interest. Descriptions in the literature of similar units, from other pegmatite localities of the same family and type, are rare. Mineral-assemblage classification systems conceived by Cameron *et al.* (1949) and Norton (1983) do not clearly distinguish a pegmatite assemblage containing predominantly K-feldspar, with subordinate to minor mica, quartz, albite, and petalite (spodumene). Norton (1983) assigned the Tanco zone (60) to his assemblage 7, which he called a perthite-quartz unit. Other localities within which he recognized assemblage 7 (*e.g.* Bikita, Zimbabwe, Peerless, South Dakota) lacked many of the subordinate minerals present in Tanco zone (60).

Similar mineral assemblages within central portions of pegmatite bodies have been described in the Mongolian Altai pegmatite No. 3 (Wang *et al.*, 1981), and the Hugo and Tin Mountain pegmatites in South Dakota (Walker *et al.*, 1986; Norton, 1983, 1994). The second intermediate zone of the Tin Mountain pegmatite is composed primarily of large crystals of Or-rich perthite, with a medium-grained matrix containing albite, muscovite and quartz. Maximum reported Cs, Rb and Or contents of bulk K-feldspar from this pegmatite (1500, 10400 ppm, and $Or_{80}Ab_{20}An_0$ respectively) occur in this zone, a feature analogous to K-feldspar compositions from zone (60) of Tanco, and close to those from zone IX of the Mongolian Altai No. 3 pegmatite (see Table 9.2 below). No data are available for the Hugo pegmatite.

*Late K(Rb) feldspar sequence*

To the best of my knowledge, the late veins of non-perthitic granular microcline (Type 2) in zone (60) have not been previously recognized or studied at any other locality. Chemical compositions are not too dissimilar from run-of-the-mill blocky K-feldspar

(Type-1) of zone (60), but it is clear that this feldspar and associated mineral assemblages formed as late-stage fracture fillings. Based on textural and chemical characteristics, it is interpreted as a locally derived late K-feldspar; however, with the information gathered so far, it is not possible to speculate on the characteristics or nature of its parent medium.

The metasomatic microcline (Type 3) veins in pollucite in zone (80) and the intimately associated adularian (Type 4) (K-Rb)-feldspars are known from several other localities (Teertstra, 1997), but are generally not well understood. The intimate co-existence of K- and Rb- dominant feldspar (Figures 6.18, 6.19) within the vein assemblages described previously by Teertstra (1997) is likely a product of both exsolution and recrystallization by hydrothermal alteration from a proximal Rb-bearing host. Evidence is generally lacking for derivation from long-range migration of a Rb-rich aqueous fluid (Teertstra, 1997). Based on relatively high-temperature experimental work in the ternary Na-K-Rb feldspar system, Lagache (1998) found no apparent thermodynamic evidence for microcline-rubicline immiscibility at subsolvus conditions below 450°C at 100MPa; however, she did speculate that substantial Cs could promote immiscibility.

The association of the adularian clusters (Type-5) and adularia crystals (Type-6) with various secondary minerals (calcite, cookeite, cesian analcime, montmorillonite-illite, apatite) indicates a hydrothermal origin within the eucryptite stability field (~350 to 200 °C, and 2 to 1 kbar, Teertstra, 1998; Černý, *et al.*, 1998). Adularia composition characteristically approaches pure end-member K-feldspar, of which samples analysed in this study are no exception. The $Or_{100}$ composition is expected at T<300 °C, based on extrapolations of experimentally-derived solvus curves (Bachinski and Muller, 1971; Smith and Parsons, 1974). Besides minute substitutions of Ba and Sr into the structure,

the only other significant stoichiometric deviation from $KAlSi_3O_8$ is due to the $\square Si_4O_8$ substitution (Teertstra, 1997). Coprecipitated minerals, including cookeite, Cs-analcime, and a variety of Rb and Cs rich micas and clay minerals, indicate widespread subsolidus activity of Rb and Cs (Teertstra, 1997) at the time of adularia formation.

## 9.2 General chemical composition of Tanco feldspars

Chemical compositions of feldspars from other similar pegmatites belonging to the same family and type are spotty in the literature. Nevertheless, a survey of Tanco K-feldspar compositions indicates that microcline-perthite (Type 1) attains some of the highest rare-alkali contents ever recorded in similar feldspars from other rare-element granitic pegmatites (Table 9.2). At tetrahedral sites, P and Ga also attain significant contents in both K-feldspar and albite. Specific references and comparisons to feldspars from other localities, as well as compositional contrasts to granite-hosted feldspars, are presented below.

### 9.2.1 Composition of microcline-perthite (Type 1)

*Lithium*

Granitic rocks typically contain less than 100 ppm Li (Černý *et al.*, 1985a). Lithium contents in feldspars from a variety of petalite- or pollucite-bearing pegmatites are presented in Table 9.2. The highest values of 469 and 418 ppm were reported from Siberia (Makagon and Shmakin, 1988) and Red Cross Lake, Manitoba (Černý *et al.*, 1994), respectively; however, more typical values range from 100 to 200 ppm (Table 9.2; Černý *et al.*, 1985).

**Table 9.2:** Rare-alkali contents in K-feldspar from various rare-element complex pegmatites (spodumene or petalite subtype), locally pollucite-bearing.

| Sub-type | Zone | *n* | Li (ppm) | Rb (%) | Cs (ppm) | Tl (ppm) | K/Rb | Rb/Cs | Rb/Tl | Location |
|---|---|---|---|---|---|---|---|---|---|---|
| | III | | 75 | 0.32 | 260 | 41 | 34.1 | | | Mongolian Altai Pegmatite No. 3 (Shmakin, 1992) |
| | III-IV | | 120 | 0.25 | 140 | 34 | 41.6 | | | |
| | III-IV | | 110 | 0.32 | 200 | 44 | 33.1 | | | |
| | IX | | 240 | 0.66 | 2700 | 95 | 16.5 | | | |
| | IX | | 130 | 0.62 | 2200 | 190 | 17.6 | | | |
| | V | | 107 | 0.64 | 1226 | | 18.8 | | | Mongolian Altai Pegmatite No. 3 (Wang *et al.* 1981) |
| | VII | | 107 | 0.62 | 2452 | | 21.3 | | | |
| | IX | | 130 | 0.66 | 2547 | | 18.9 | | | |
| | II | | | 0.153 | 60 | 10 | 69.1 | | 153 | Mongolian Altai Pegmatite No. 3 (Solodov, 1962) |
| | III | | | 0.289 | 50 | 25 | 36.3 | | 116 | |
| | IX | | | 0.550 | 2580 | 61 | 20.4 | | 90 | |
| petalite | upper | *21* | 100-500 | 1.12-3.00 | 1360-3920 | | 10-3.66 | 9.0-5.6 | | Siberia (Makagon and Shmakin, 1988) |
| petalite | lower | *10* | 175-390 | 0.94-1.90 | 460-1670 | | 12.2-6.5 | 27.6-11.3 | | |
| | Ta-Cs-Li | | 256<br>469 | 1.62<br>2.18 | 3300<br>1700 | | 6.8<br>4.7 | 4.9<br>12.8 | | |
| petalite | | *81* | 50-208 | 0.10-2.08 | 40-2970 | 15-238 | 106-5.2 | 54.2-3.7 | | Russia (Shmakin, 1997) |
| with pollucite | | *30* | 81-317 | 0.47-2.64 | 450-2287 | 89-1155 | 21.9-3.7 | 13.7-2.0 | | |
| petalite (w. poll.) | | *17* | | | | | 11.5-5.8 | 41-15 | | Utö, Sweden (Smeds and Černý, 1989) |
| petalite (w. poll.) | | | | | 5100-5600 | | 8.6-3.4 | | | Varuträsk, Sweden (Smeds and Černý, 1989; Quensel, 1956) |
| spod. (w. poll) | 2 | *3* | | 0.89-1.04 | 957-1500 | | 12.1-9.8 | 9.7-6.7 | | Tin Mountain, South Dakota (Walker *et al.*, 1986) |
| average data | spod. (w. poll) | *19* | 53 | 1.08 | 1282 | | 9 | 9 | | Tot Lake, NW Ontario (Breaks, 1989) |
| extreme data | pet. (w. poll) | | 418 | 4.98 | 4244 | 402 | 1.9 | | 122 | Red Cross Lake, NE Manitoba (Černý *et al.*, 1994) |
| average data | spod. | *3* | 148 | 2.59 | 786 | | 4.2 | | | Volta Grande, Brazil (Lagache and Quéméneur, 1997) |

Lithium contents determined by ICP range from a minimum of 25 ppm to a maximum of 1600 ppm (0.005 - 0.34 wt% $Li_2O$), but most data fall between 180 to 420 ppm. A series of seven or eight samples extend to Li contents greater than 980 ppm; only one sample contains more than this value. These are some of the highest Li contents ever reported in K-feldspar, although some of the extreme contents are likely influenced by microinclusions of Li-bearing micaceous minerals and clay particles contained within bulk samples (Černý *et al.*, 1985a; Černý, 1994).

Individual Li contents determined by SIMS (37-214 ppm) are, on average, considerably lower than those determined by ICP. This supports the contention that contamination from inclusions or alteration may have boosted the Li values determined by wet-analysis on bulk samples.

*Sodium*

Consolidation of hydrous and volatile-rich pegmatites at subsolvus conditions is generally conducive to the development of perthite texture to such an extent that nearly all available Na is incorporated into the plagioclase phase. Under such conditions, Na in the K-feldspar phase does not seem to exceed trace-element concentrations.

Bulk compositions of Tanco microcline-perthite (Type 1) range from 0.31 to 3.6 wt% $Na_2O$ with an overall average of 1.8 wt%. EMPA-determined compositions of the K-feldspar phase range from 0.15 to 0.78 wt% $Na_2O$ and average 0.32 wt%.

*Rubidium*

Granites typically average from 190 to 276 ppm Rb, with K/Rb between 300 and 160 (Černý *et al.*, 1985a). Černý (1994) reported that Rb contents routinely attain

concentrations between 10000 to 25000 ppm (1.1-2.7 wt% $Rb_2O$) in K-feldspars of complex rare-element pegmatites. The highest recorded value of 5.87 wt% $Rb_2O$ (4.98 wt% Rb), came from a blocky perthitic microcline from the pollucite-bearing Red Cross Lake pegmatite, NE Manitoba (Černý *et al.*, 1985b; Table 9.2).

Rubidium contents at Tanco (0.73-3.19 wt% $Rb_2O$) are at the higher end of the 'normal' range for similar pegmatites (Table 9.2).

*Cesium*

Cesium contents in granitoid rocks are poorly documented, but are significantly lower than Rb contents. Estimates of <1 to 10 ppm, and K/Cs close to 3000 have been suggested for granitoid rocks (including batholithic biotite granites) (Černý *et al.*, 1995a). Černý (1994) reported that Cs routinely attains concentrations of 2000-3000 ppm (0.21-0.38 wt% $Cs_2O$) in K-feldspars from complex rare-element pegmatites. The highest values of 5600 and 4244 ppm (Table 9.2) were reported from Varuträsk, Sweden (Quensel, 1956), and Red Cross Lake, Manitoba (Černý *et al.*, 1985b), respectively.

The distribution of Cs contents at Tanco is distinctly bimodal, with maximum peak frequencies occurring between 0.03 and 0.06, and 0.30 and 0.33 wt% $Cs_2O$; the highest single value is 0.38 wt % (3580 ppm).

*Thallium*

Thallium contents in K-feldspar from granites typically range from 0.7 to 5.0 ppm, with reported values up to 30 ppm (Sahl, 1974). Data for the Mongolian Altai No. 3 pegmatite (Table 9.2) typically are in the range 10-100 ppm. Extreme values include 1155 ppm

from a pollucite-bearing pegmatite in Russia (Shmakin, 1997), and 402 ppm from Red Cross Lake, MB (Černý *et al.*, 1994).

There is a continuous range of Tl contents in the Tanco K-feldspar from 80 to 330 ppm.

*Beryllium*

The range in Be values (0.1 – 5.8 ppm) in blocky K-feldspar (Type 1) at Tanco, falls within the mid- to lower-end of typical ranges of Be contents found in K-feldspars from various granitoids and pegmatites compiled in Smith and Brown (1988).

*Calcium*

Similarly to sodium, there is a disparity between bulk and microprobe-determined analyses of calcium in K-feldspar, which can be attributed to albite having a greater affinity for Ca.

Bulk analyses of Tanco microcline-perthites (Type 1) yielded 0.034 to 0.26 wt% CaO with an overall average of 0.095 wt%. Only 1% of EMP analyses of the K-feldspar phase are above the detection limit of 0.025 wt%.

*Strontium*

Strontium is considered relatively compatible with the K-feldspar structure, having a crystal-melt distribution coefficient greater than 3 in granitic systems (Icenhower and London, 1996). Under simple fractional crystallization, one would expect Sr to be consumed early in the sequence of primary feldspar crystallization, which should be observed as a decreasing trend from outer to inner zones. However, a plot of Sr *vs.* Rb of Tanco K-feldspar (Figure 6.10) indicates that total present-day Sr is radiogenic (see

pg. 77). All Sr was apparently fractionated out before the beginning of consolidation of the Tanco pegmatite.

*Barium*

Whole-rock Ba contents in granitoid rocks vary over 3 orders of magnitude, with higher contents associated with more primitive rocks. Late granitic differentiates commonly contain 900 to 300 ppm, with K-feldspar as the primary Ba-bearing mineral phase (Černý *et al.*, 1985a). Appreciably differentiated granitic pegmatites consistently contain less than 100 ppm Ba, but variations amongst different localities suggest that bulk Ba values are largely regionally specific (Černý *et al.*, 1985a).

Barium values in the Tanco K-feldspar range between 2 and 340 ppm, with 80% of values below 100 ppm.

*Manganese and Lead*

Mn and Pb contents of the Tanco K-feldspar both fall far below EMPA detection limits, with only 4% and 14% of individual point analyses above detection limits of 0.025 and 0.041 oxide wt%, respectively.

*Boron*

Boron is present in very low concentrations varying from 1.0 to 10.2 ppm (Table 6.6). This is in remarkable contrast to the B content of Tanco micas (Margison, 2001).

*Gallium*

Gallium in most igneous rocks varies between <1 and ~ 40 ppm, with Al/Ga in granitic rocks varying from 8000 to about 2000 (Černý *et al.*, 1985a). The highest Ga content in

K-feldspar from Red Cross Lake, MB (Wang *et al.*, 1988) was reported as 140 ppm, with an Al/Ga value of 812.

Tanco K-feldspars range from 46 to 125 ppm Ga, with Al/Ga varying between 2220 and 828.

*Phosphorus*

Granitic rocks typically contain between 0.01 and 0.21 wt% $P_2O_5$ (London *et al.*, 1990). London *et al.* (1990) reported P contents for 1500 feldspar analyses collected from 59 peraluminous pegmatite localities. The sample distribution was bimodal, with peak $P_2O_5$ contents of 0.2 wt% and 0.4 wt%. Individual compositions ranged from below detection to 1.20 wt% $P_2O_5$, with approximately 60% of the data greater than 0.30 wt%.

The distribution of Tanco $P_2O_5$ contents (Figure 6.6a) is Gaussian, with a peak frequency between 0.30 and 0.35 wt% $P_2O_5$. Individual P contents attain values up to 0.57 wt% $P_2O_5$, with 76% of contents greater than 0.30 wt% $P_2O_5$.

### 9.2.2 Compositions of late K-Rb feldspar (Types 4,5,6)

Teertstra (1997) reported several dozen compositional ranges of vein and cluster adularian (K-Rb) feldspars in pollucite bodies from various localities around the world, including Maine, Connecticut, Massachusetts, Colorado, California, Quebec, Ontario, Zimbabwe, Namibia, Finland, Sweden, Madagascar, Siberia, Nová Ves u Českého, Krumlova and China.

At Tanco, the Type-4 adularian Rb-K-feldspar exhibited the greatest range of Rb contents, varying from 0.00 to 24.84 wt% $Rb_2O$. The highest ever Rb content in a feldspar (26.2 wt% $Rb_2O$) was reported by Teertstra (1997) in a Type-4 feldspar from the Kola Peninsula.

The distinctive morphology, composition and range of structural state of adularia is discussed by Černý and Chapman (1986,1984). Compositionally, adularia is generally distinguished by low to subordinate trace-element contents: Na<1.5, Rb<0.37, Sr<0.25, Ba<1.7 wt%. Compositions of Tanco adularia crystals (Type 6) are considerably below these maxima. Non-ideal stoichiometry suggests substantial vacancy substitution, and possibly light-element substitution in the form of $H_2O$ $(OH)^-$, or $(H_3O)^+$ (Teertstra, 1997).

### 9.2.3 Albite compositions

Compositional data for pegmatitic albite are even more scarce than K-feldspar data, presumably because trace-elements contents are much less pronounced, thus limiting their usefulness as indicators of petrologic processes.

*Potassium*

$K_2O$ contents in 8 albite samples from interior zones of the Mongolian Altai No. 3 pegmatite range from 0.10 to 0.75 wt% (Wang *et al.*, 1981).

$K_2O$ in the Tanco albite ranges from 0.03 to 0.13 wt% with an overall average of 0.07 wt%.

*Beryllium*

Smith and Brown (1988) remarked that, in general, plagioclases tend to contain more Be than co-existing alkali feldspar. The range in SIMS-determined Be in Tanco albite (0.2 to 6.7 ppm; Table 7.3) largely overlaps with the range of K-feldspar contents (Table 6.6).

*Calcium*

CaO contents in 8 albite samples from interior zones of the Mongolian Altai No. 3 pegmatite range from 0.11 to 0.30 wt% (Wang *et al.*, 1981).

CaO in the Tanco albite ranges from 0.01 to 0.20 wt% with an overall average of 0.06 wt%.

*Strontium*

Strontium is somewhat enriched albite of primitive pegmatites, but very low in highly fractionated ones.

In the Tanco pegmatite, Sr in albite is suspected excess radiogenic (see pg. 77)

*Barium*

Černý *et al.* (1984) reported up to 330 ppm Ba in albite from the geochemically primitive Vežná pegmatite in the Czech Republic. Average Ba contents in albite from spodumene-bearing pegmatites in Russia range from 3 to 6 ppm (Shmakin, 1997).

Ba values in the Tanco albite ranges from 4 and 515 ppm, with an overall average of 151 ppm.

*Manganese, Lead, Gallium*

Data on these elements are difficult to find. Ga and Mn tend to be slightly enriched in albite as opposed to K-feldspar.

Mn and Pb contents in Tanco albite determined by EMPA exceede the respective limits of detection of 0.025 and 0.041 oxide wt%, in only 34% and 20% of individual point analyses. Maximum average sample values obtained include 0.02 wt% MnO, and 0.03 wt% PbO.

Ga in Tanco albite of zones (10) (20) (40) (50) and (60) was determined by wet-chemistry and ranged between 46 and 125 ppm, with an overall average of 92 ppm.

*Boron*

Boron concentration in Tanco albite is very low, ranging from 0.8 to 10.2 ppm (Table 7.3). The spread of data overlaps with that determined for Type-1 K-feldspar (Table 6.6).

*Phosphorus*

Average $P_2O_5$ contents in albite from granitic bodies in Cornwall, England (London, 1992a) range from 0.184 wt% (biotite granite), to 0.099 wt% (tourmaline muscovite granite), and 0.351 wt% (topaz lithium mica granites). Phosphorus contents from more than 200 plagioclase feldspars from various peraluminous LCT pegmatites, are reported by London *et al.* (1990); values range from below detection to 0.57 wt% $P_2O_5$, and form a distinctly bimodal distribution. The highest content recorded to date is 1.06 wt% $P_2O_5$ (Martin *et al.*, 1993).

$P_2O_5$ contents of the Tanco albite range from below detection to 0.40 wt% $P_2O_5$, with aplitic albites exhibiting a bimodal distribution.

### 9.3 Trace-element distributions in K-feldspar *vs.* albite

Of the minor and trace-elements listed and analysed in both primary K-feldspar and albite, P, Rb and Cs are relatively enriched in K-feldspar, whereas Ca, Ga and possibly Mn are more enriched in albite. Ba and Sr seem to be slightly enriched in K-feldspar but cover similar ranges of values for both minerals.

The SIMS-determined data indicate that B and Be are equally distributed between K-feldspar and albite, but Li strongly prefers the former.

At the present limits of detection, and at all spatial scales examined, trace-element composition in albite does not vary significantly, except for the zonal variations in Ca, K and P. However, geochemical variation in the K-feldspar types is highly significant, particularly variation between zones. Ca, Mg, Ti, Mn and F are consistently below limits of detection. Strontium is radiogenic in origin, and of no petrologic significance (*cf.* p.77, 86; also Clark and Černý, 1987). Ba is highly variable, but generally close to the limit of EMPA detection in all zones except (10) and (80). Due to the relatively high distribution coefficient of Ba [$D(Ba)^{Fsp/glass}$ =15-20 for Or-rich feldspar in peraluminous melt (Icenhower and London, 1996)], it is fractionated from the melt early, and occurs at detection limit throughout most of the zonal sequence.

### 9.4 Spatial trace-element distributions in K-feldspar

The distribution of minor and trace-elements within individual zones [(20) (40) and (60)] along east-west and north-south transects generally leads to ambiguous, and/or contradictory conclusions. The most statistically sound and persuasive trends occur along the zone (20)-9700N transect, and show a general west-to-east decrease in K/Rb and K/Cs. There is also evidence in zones (20) and (60) for an easterly increase in Ba. Also, concave-down trends are suggested for P, Li and K/Na in zone (20), and for P and K/Na in zone (40). No systematic trends were observed along the north-south transects. Only one hangingwall-footwall compositional difference in zone (20) is significant: Rb/Cs hangingwall values are significantly lower than footwall values along the 10200E transect, which cuts across the largest area of the main pollucite body.

### 9.5 Trace-element distributions in single K-feldspar crystals

Single-crystal compositions indicates a systematic decrease in K/Rb with growth of giant K-feldspar crystals in zones (20) and (50). The trends of Ca are reciprocal to those of K/Na, suggesting a dependency of Ca on the albite content. Overall, compositional variations along the three crystals examined are generally insignificant, and are close to being random for elements other than Rb.

### 9.6 Geochemical trends of Li, P, Rb, Tl and Cs

Variation of trace-element contents in K-feldspar is controlled by a variety of intrinsic and extrinsic factors. Distribution coefficients $D[X]^{Kf/melt}$ for a given trace-element (X) between K-feldspar and the evolving melt are controlled mainly by intrinsic factors related to the relative incompatibility of the substituting element. In the case of Li, Rb, Tl and Cs, differences in ionic radii and electronegativity (relative to K) are the most important considerations (Table 9.3). In the case of phosphorus, incorporation of P is

controlled by the berlinite substitution ($P^{5+} + Al^{3+} = 2Si^{4+}$). This mechanism requires availability of excess Al, thus partly explaining high P contents of K-feldspars from peraluminous intrusions (London *et al.*, 1990).

**Table 9.3:** Ionic radii and electronegativities of common M-cation trace-elements in K-feldspar.

| | Z | Ionic Radius (Å) (8-coordinated) | Electronegativity (Pauling's) |
|---|---|---|---|
| $Li^+$ | 3 | 1.06 | 0.98 |
| $K^+$ | 19 | 1.65 | 0.82 |
| $Rb^+$ | 37 | 1.75 | 0.82 |
| $Tl^+$ | 81 | 1.73 | 1.62 |
| $Cs^+$ | 55 | 1.88 | 0.79 |

Source: WebElements™ Professional edition, http://www.webelements.com/webelements

Extrinsic factors which could account for trace-element variability include i) heterogeneous melt compositions during primary crystallization, ii) changes in distribution coefficients in response to evolving P,T,x conditions during primary crystallization, iii) precipitation of other minerals which effectively remove the trace-element at local to deposit scales, and iv) reequilibration/recrystallization at subsolidus to hydrothermal conditions.

The general trends of increasing Li, Rb, Tl and Cs from outer to inner zones (Figure 8.1) generally reflect the relative incompatibility differences with respect to K as a function of differences in ionic radii and electronegativity (Table 9.2). Specific details of the geochemical behavior of different trace-elements in feldspars from pegmatites are discussed by Černý *et al.* (1985a) and Černý (1994). Geochemical plots involving these

elements (Chapter 8) are consistent with a relative incompatibility sequence Rb < Tl ≅ Li < Cs. However, a detailed survey of the plots involving K, Li, Rb, Tl and Cs in chapters 6 and 8 reveals more complex trends, not explainable by differences in compatibility alone. Simple fractional crystallization should result in steady sequential increase in rare-alkalis and P. Analysis of the compositional data reveals obvious bimodal distributions for Li and Cs, and possibly for Rb. Phosphorus is essentially unimodal for K-feldspar, but distinctly bimodal for albite. Divergent geochemical trends and inflections also are common and are indicative of episodic changes in the behavior of the evolving paragenetic sequence in time and space.

*i) Heterogeneous melt compositions*

In terms of extrinsic factors (mentioned above) which affect the trace-element signatures of the evolving compositions of melt and feldspar, the first (heterogeneous melt composition), is beyond the scope of the present work. Explaining the large-scale spatial distribution of zones in the pegmatite requires a joint understanding of the bulk composition, mineralogy and petrology of the pegmatite as a whole.

*ii) Effects of evolving P,T,x on the primary crystallization sequence*

Changes in P, T and x conditions include a complex and interconnected series of factors, which, for the most part, operated within a closed system at Tanco. Primary crystallization, initiated at the interface between host rock and melt, would have occurred at some degree of undercooling, and would have progressed inward at variable rates of crystallization and degrees of undercooling (London, 1992; Černý, 1998). It is well known that many distribution coefficients are partial functions of temperature, although recent work by Icenhower and London (1996) precludes a significant $D[X]^{feldspar/melt}$ dependence on temperature in peraluminous melt, where X = Ba, Sr, Rb, and Cs.

The degree of undercooling is an important parameter that promotes pegmatitic textures by disequilibrium crystal growth, facilitated by increasing $H_2O$ and fluxing components B, F, P, and Li in the melt (London, 1992). London (1990) reported that the latter fluxing components are not requisite for disequilibrium crystal growth, "but that they do promote zoning by expanding the liquidus field of quartz, and migration of projected residual melt compositions toward the $NaAlSi_3O_8$ apex (pg. 46)." Eventual saturation with respect to $H_2O$ occurs by 'chemical quench' whereby fluxing components are removed by stabilization of late minerals such as tourmaline, which results in devolitization, followed by rapid nucleation from residual melt-fluid components. Periodic shifts from vapour-undersaturated, disequilibrium growth mechanisms to vapour-saturated conditions can occur at a variety of scales and at different stages of pegmatite consolidation, and would probably have a significant effect on trace-element distributions. Pressure changes are not considered an important parameter driving magmatic consolidation of Tanco, as pressure mostly reflects the depth of emplacement (London, 1986), and consolidation probably occurred very rapidly; *i.e.* < 1000 years (Černý *et al.*, 1998). Local 'pressure-quench' may have operated in association with the development of miarolitc cavities, but these structures are quite rare at Tanco .

The exact relations between the above-mentioned theoretical considerations, and anomalous chemical trends observed in figures from chapters 6,7, and 8 are not completely clear. A good example is the distinct clustering of Cs-enriched K-feldspar compositions from zone (60) +/- (80) and (90) (Figures 6.9b,c). Examination of geochemical data (Figures 8.1f,g,h) shows an accumulation of Cs and Rb in zones (60) (80) and (90), relative to feldspars from zone (50), which are conversely enriched in Li and Tl. The three-stage Rb/Tl trend (Figure 8.1j) is also of considerable interest, but is

presently not understood. Thallium and Rb have almost identical ionic radii, but the distinctly higher electronegativity of Tl has a destabilizing effect on the tetrahedral framework, effectively making Tl more incompatible than Rb (Shaw, 1952). Under conditions of normal fractional crystallization, Rb/Tl is expected to progressively decrease; however, this is clearly not the case, as shown in Figure 8.1j. A gently decreasing trend is shown by zonal averages (Figure 8.3e), but with a prominent increase in zone (80). Large-scale incorporation of Tl into pollucite (Černý 1982), which composes ~75 vol. % of this zone, may possibly explain the Tl-depleted composition of the K-feldspar.

London (1992b) stressed the importance of "the divergence in compositions of residual melt and crystalline phases with increasing concentrations of B, P, and F (p. 531)." Interaction of these elements with alkalis and $H_2O$ lowers liquidus and solidus temperatures, enhances silicate-liquid $H_2O$ miscibility, and controls partitioning and concentration of group-I elements and higher-field-strength cations.

Alternatively, the radical departure of Li and Cs contents in K-feldspar from zone (50) *vs.* zones (60) and (80) (Figure 8.1g), could be related to crystal-chemical constraints. In the case of significant Li incorporation, a shift in lattice parameters to accommodate the much smaller *M*-cation, could conceivably reduce the size of proximal 8-fold *M*-sites, effectively inhibiting incorporation of the very large Cs ion. A corollary to this is related to the suspected Cs-induced theoretical immiscibilty gap in the system albite-orthoclase-(Rb-feldspar) (Lagache, 1998). A detailed analysis of unit-cell data in relation to EMPA and SIMS data is needed to ascertain if there is a link between the incorporation of Li and Cs and unit-cell dimensions of K-feldspar from Tanco; however, the contents of both elements in the Tanco feldspars are too low to induce measurable change.

*iii) Trace-element variability in relation to the precipitation of competing minerals*

The most tangible of the extrinsic factors relates to the precipitation of other trace-element-consuming minerals. The stabilization of amblygonite-montebrasite (40) (50), petalite (spodumene) (50) (60), lepidolite (50) (60) (90), and pollucite (80) (60) at different locations and times in the primary crystallization sequence would have had a distinct effect on the availability of P, Li, Rb, Tl and Cs, not only in relation to local co-precipitating feldspar, but also on the overall trace-element budget for the remainder of the primary sequence of crystallization. Table 9.4 lists average contents of Rb, Tl and Cs in different minerals in different zones.

Solodov (1962) reported that at low concentrations of Rb, Tl and Cs in the melt, white micas incorporate proportionally greater quantities of these elements in comparison to K-feldspar; however, the reverse seems to be true at high concentrations. In consideration of this, and of the low modal abundances of micas in most of the outer zones at Tanco, muscovite probably had a limited affect on the distribution of these rare-alkali elements relative to K-feldspar.

On the other hand, lepidolite is highly enriched in Rb, Tl and Cs in comparison to other white micas and K-feldspar. Limited local accumulations of lepidolite in zones (50) and (60) might control the local distribution of these elements in K-feldspar, as is suggested by the decrease in rate of Rb incorporation relative to rates of Cs and Tl consumption by K-feldspar in zones (50) (60) (80) (Figures 8.1a,i). Zone (90) is predominantly lepidolite and Li-muscovite, and represents a substantial reservoir of Rb, Cs and Tl.

**Table 9.4:** Trace-element contents in potentially competing mineral phases from Tanco.

| | Zone | mode* (vol. %) | $Rb_2O$ (wt.%) | $Tl_2O$ (wt.%) | $Cs_2O$ (wt.%) |
|---|---|---|---|---|---|
| K-feldspar (this study) | 50 | 25 | 2.22 | 0.024 | 0.11 |
| | 60 | 50 | 2.47 | 0.020 | 0.30 |
| | 80 | 2.5 | 2.59 | 0.024 | 0.27 |
| Muscovite** | 50 | 0.1 | 1.74 | 0.011 | 0.22 |
| | 60 | 12 | 1.93 | 0.012 | 0.34 |
| | 80 | 2.0 | 2.67 | nd | 0.25 |
| Lepidolite/ Li-musc.** | 50 | 0.2 | 4.52 | 0.022 | 0.87 |
| | 60 | 0.1 | 4.57 | 0.023 | 0.95 |
| | 80 | 7.0 | 4.04 | 0.021 | 0.81 |
| Beryl* | 50 | 0.1 | 0.07 | nd | 2.92 |
| | 60 | 1.0 | 0.07 | nd | 2.92 |
| | 80 | 0 | - | - | - |
| Pollucite* | 50 | 1.0 | 0.83 | 0.010 | 32.19 |
| | 60 | 0 | - | - | - |
| | 80 | 75 | 0.83 | 0.010 | 32.19 |

*Volume and Tl data, and all Beryl and Pollucite contents from Stilling (1998)

** Rb and Cs data for muscovite and lepidolite from Margison (2001)

*iv) Re-equilibration/recrystallization at subsolidus to hydrothermal conditions.*

Localized redistribution of K, Rb, Cs, P, Li and Na are well-established in relation to the late K(Rb) –feldspar types 3,4,5, and 6 (Teertstra, 1997, Teertstra *et al.*, 1998a). There is also no doubt, based on the omnipresent abundances of maximum microcline-perthite, that very extensive subsolidus re-equilibration has occurred at Tanco. Apatite microinclusions and fracture fillings in K-feldspar from many zones also suggest substantial subsolidus reworking and significant P mobility at low temperature. However, no direct textural proof is available for long-range, across-zone migration of secondary K, Na or albite.

## 9.7 Crystal-chemistry

Figures 6.12b, 6.13a and 6.13b show that the K-feldspar matrix of blocky microcline-perthite displays three slight but persistent deviations from ideal stoichiometry of a virtually $M^{2+}$-free alkali feldspar, $M^{+}AlSi_3O_8$: (i) slight deficiency in tetrahedrally coordinated (Si+Al+P), (ii) apparent excess of alkalis over the single structurally available site (as much as ~0.025 *apfu* for the main cluster of data), and (iii) a lesser excess of Al-P over the ideal value of 1.000 (less than ~0.013 *apfu* for most of the data).

(i) The deficit of tetrahedrally coordinated cations is minor, and within the analytical error. However, it leaves a possibility open for the presence of additional cations. Substantial Ge is highly improbable in framework silicates. Gallium is present but in negligible quantities (Appendix V). Boron was not analyzed for and remains a distinct possibility, although the few data on this element in feldspars from peraluminous pegmatites are not encouraging (tens of ppm, Shearer and Papike, 1986; a few to 600 ppm, Smith and Brown, 1989 from various sources). The recent discovery of substantial B in pegmatitic muscovite (~100 to ~450 ppm B, Shearer and Papike, 1986; 0.04 to 1.10 wt.% $B_2O_3$, Černý *et al.*, 1995), and in muscovite from the Tanco pegmatite investigated here (0.11 to 0.33 wt.% $B_2O_3$, Margison, 2001), suggests the possibility of higher boron concentrations in pegmatitic feldspars. However, our data indicate that the B content of the Tanco feldspars does not exceed 10.2 ppm.

(ii) The apparent excess of *M*-cations and *M*-cation charge may be caused by calibration error: if the Eifel sanidine standard has a higher degree of $\square Si_4O_8$ substitution than established by Teertstra (1997), the plots in Figure 6.14a will

shift along vector 2 and the alkali excess would be eliminated; for example, a current composition of

$$K_{1.015}[Al_{1.005}\ Si_{2.990}]_{\Sigma 3.995}\ O_8 \qquad (1)$$

representative of the alkali-excessive part of the main cluster of data in Figure 6.14a, would change to

$$K_{1.000}[Al_{0.990}\ Si_{3.005}]_{\Sigma 3.995}\ O_8 \qquad (2)$$

by increasing the $\square Si_4O_8$ by 0.015 apfu (Figure 9.1a).

(iii) This substitution would also more than eliminate the apparent excess of Al-P (Figure 9.1b), but it will not affect the apparent surplus of alkalis over the Al-P value and the slight deficit of *T*-cations (see formula 2 above and Figure 9.1b). These imbalances may be eliminated if adequate quantities of B are present in the feldspars examined; 0.12 wt.% $B_2O_3$ is sufficient to complement the *T* cations to full occupancy, and to balance the $T^{3+}$ content of the formula (2) with the *M* cations and their charge:

$$K_{0.999}[Al_{0.989}\ B_{0.010}\ Si_{3.001}]_{\Sigma 4.000}\ O_8 \qquad (3)$$

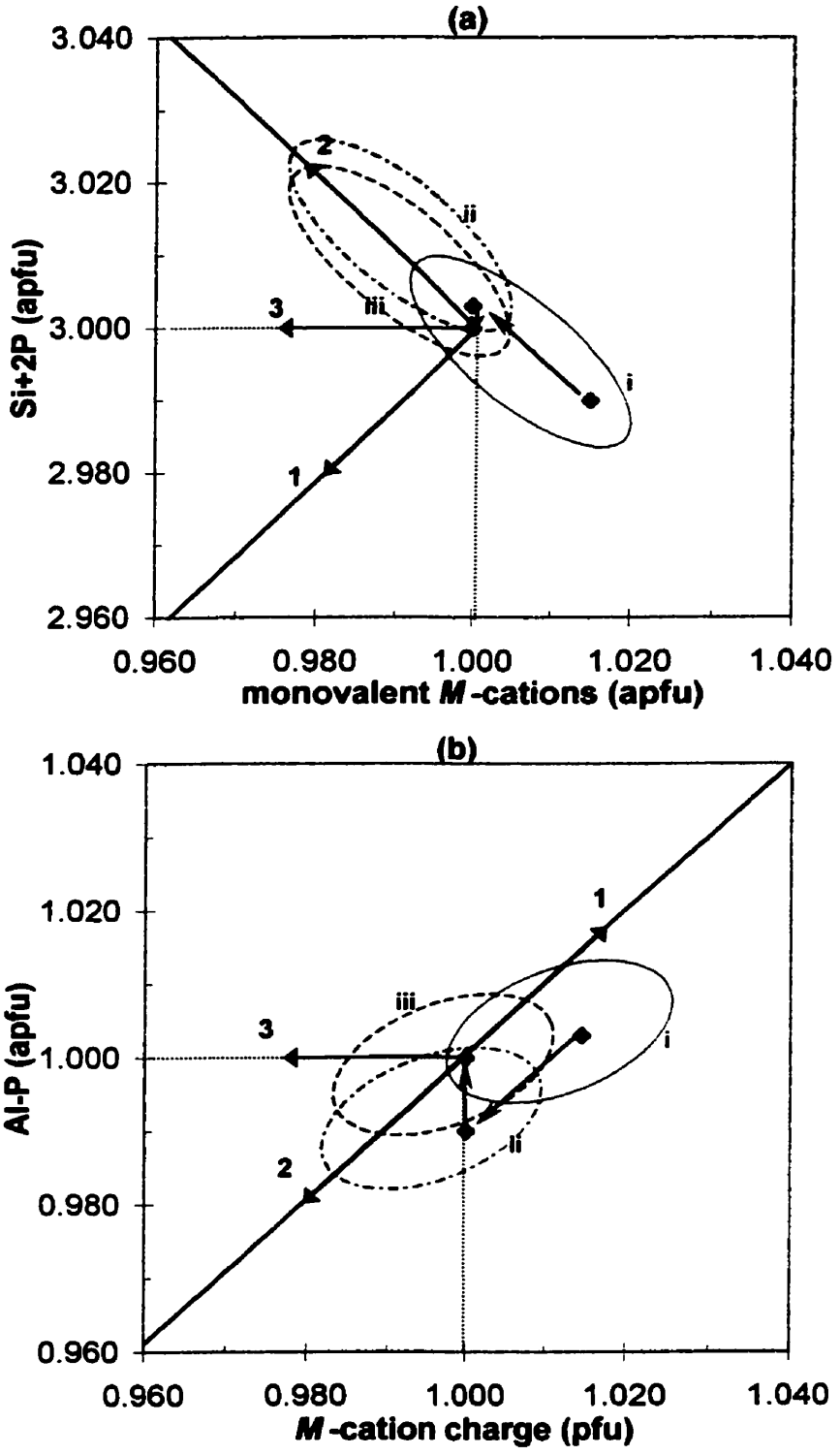


**Figure 9.1** Proposed crystal-chemical data corrections: (i to ii) vacancy shift to correct for possible calibration error of the Eifel sanidine standard; (ii to iii) addition of 0.01 apfu B in place of Si. Solid oval (i) represents field of current data.

Alternatively, solid solution of $T^{3+}$-free alkali silicates in the feldspar structure might be considered, such as the alkali tetrasilicate $K_2Si_4O_9$ (Linthout and Lustenhouwer, 1993), and/or $K\square(\square Si_2)\ O_8^{7-}$ (Kuehner and Joswiak, 1996). However, solid solution of these (and similar) components are not documented structurally, and their potential presence seems to be facilitated by rapid non-equilibrium growth in volcanic rocks of peralkaline composition (Smith and Brown, 1989, Linthout and Lustenhouwer, 1993).

Consequently, there is no unambiguous interpretation available at present for the slight deviations of the blocky feldspar from ideal stoichiometry. The problem requires further experimental study.

### 9.8 Structural states of alkali feldspars

The cluster of albite unit-cell data about the ideal low-albite point on a b-c plot (Figure 7.14) indicates that all of the Tanco albite attained the maximum degree of order. Variations about the ideal are essentially within error and negate the possibility of discerning variability amongst the two albite types (A or B), or by the effects of different trace-element contents, or by zonal provenance.

Unit-cell dimensions of K-feldspar offer slightly more variability than albite. A b-c plot (Figure 6.16) indicates that all Type-1 feldspars are essentially maximum microcline, but with a slight shift in the direction of increased Rb+Cs contents, as is suggested by larger than anticipated unit-cell values. This is supported by a good correlation between unit-cell volume and atomic Rb+Cs content. The degree of order is slightly reduced by increasing contents of Rb+Cs.

## CHAPTER 10: CONCLUSIONS

Trace-element contents in K-feldspar vary significantly, and effectively record relative compositional changes of the evolving melt during primary crystallization. In general, Rb contents increase steadily throughout the sequence of magmatic crystallization. Average K/Rb values per zone decreases steadily, except two zones affected by the presence of substantial amounts of micas, from a maximum of 8.2 to a minimum of 3.8; values for zones (10) and (90) are 7.7 and 4.6, respectively. Individual values range between 14.2 and 2.8. With decreasing K/Rb, the Rb, Tl, Cs contents, and Cs/Tl and K/Na increase, whereas K/Cs and Rb/Cs decrease; Ba, Ca, and Ga vary irregularly. Rb/Tl exhibits a three-step fractionation sequence in which the ratio increases from zone (20) to (40), but decreases from (40) to (50), and increases again to (60) and particularly (80). This last step is possibly influenced by large-scale incorporation of Tl into pollucite.

Phosphorus and Li attain maximum average contents in zones (40) and (50), respectively. Increasing contents from zone (20) to (40) and (50) reflect increasing activity of both components in the residual pegmatite melt, which climaxed early in the primary sequence with the precipitation of amblygonite-montebrasite and petalite in zones (40) and (50). Stabilization of these minerals removed most P and Li from the melt; feldspars in subsequent zones are consequently depleted in Li and P.

SIMS data suggest that some of the Li determined by ICP may be slightly exaggerated, due to impurities and alteration. The X-ppm contents of B and Be are in agreement with those determined at other localities.

Trace-element contents in albite show relatively insignificant variation, not only spatially, but also between the two varieties -- aplitic albite and cleavelandite. A steady decline in average Ca content from outer to inner zones is the only notable trend. By a small margin, average K content in aplitic albite seems to be uniformly higher than in cleavelandite, reflecting the higher crystallization temperature of aplitic albite, and the reduced selectivity of cations during nucleation and growth. The contents of Li, B and Be all are very minor.

Of the minor and trace-elements listed and analysed in both K-feldspar and albite, Rb and Cs each attain extreme contents in K-feldspar relative to albite, P is moderately higher in K-feldspar, whereas Ca, Ga and Mn are higher in albite. Ba and Sr are marginally higher in K-feldspar but generally exhibit similar ranges of values in both minerals. The Sr content of K-feldspar is radiogenic in origin, partly lost, and probably partially incorporated into albite. A strong preference for K-feldspar is shown by Li, whereas B and Be are about equally distributed between K-feldspar and albite.

Crystal-chemical data for K-feldspar and albite indicate almost perfect tetrahedral occupancy and stoichiometry when taking into account the berlinite substitution. However, the stoichiometry of *M*-cations is significantly disturbed, possibly by the presence of light elements and calibration problems (although the deviations are close to analytical error). Of the three substitution-types examined (plagioclase-type, vacancy-type, and apparent light *M*-cation), K-feldspar exhibits a significant shift along the vacancy trend only. Albite exhibits a possible slight vacancy shift, but plagioclase substitution proved to be much more significant.

The distribution of minor and trace-elements within individual zones [(20) (40) and (60)] along east-west and north-south transects, generally leads to ambiguous, and/or contradictory conclusions. The most statistically sound and persuasive trends occur along the zone (20)-9700N transect, and show a general west to east decrease in K/Rb and K/Cs. There is also evidence in zones (20) and (60) for an easterly increase in Ba. Also, concave-down trends are suggested for P, Li and K/Na in zone (20), and for P and K/Na in zone (40). No systematic trends were observed along the north-south transects. Only one hangingwall-footwall compositional difference in zone (20) is significant: Rb/Cs hangingwall values are significantly lower than footwall values along the 10200E transect, which cuts across the largest area of the main pollucite body.

Single-crystal geochemistry indicates a systematic decrease in K/Rb with growth of giant K-feldspar crystals in zones (20) and (50). The trends of Ca are reciprocal to those of K/Na, suggesting a dependency of Ca on the albite content. Overall, compositional variations along the three crystals examined are generally insignificant, and are close to being random for elements other than Rb.

Of the five 'late' K(Rb)-feldspar types examined, both granular non-perthitic microcline in zone (60) (Type 2) and metasomatic microcline in zone (80) (Type 3) have compositional ranges similar to those of blocky K-feldspar (Type 1), but they (virtually) lack perthitic albite and their Rb contents tend to be slightly higher. The adularian (K-Rb) feldspar (Type 4) exhibit the greatest range of Rb and Cs contents, attaining maximum values of 24.84 wt% $Rb_2O$ and 1.43 wt% $Cs_2O$. K *vs.* Rb, K *vs.* Cs, and Rb *vs.* Cs all show well-defined positive correlations. Phosphorus and Na contents are significantly lower than in the Type-2 and -3 feldspar types. Adularia crystals (Type 6)

are almost pure K-feldspar; in all cases except one $Rb_2O$, $Cs_2O$, and $P_2O_5$ contents are below detection limits, and $Na_2O$ contents are less than 0.03 wt%.

Crystal-chemical data for the 'late' K(Rb)-feldspar types indicate near-ideal tetrahedral occupancy and stoichiometry. The negative-vacancy trend is almost as pronounced as the Type-1 deviation form ideal *M*-cation stoichiometry. However, the spread of data along the vacancy trend is much greater than the Type-1 feldspar, particularly for the adularian (Type 4) and adularia (Type 6) varieties. Two adularia (Type 6) compositions show extreme *M*-cation deficiencies. Plagioclase-type substitutions are insignificant.

Unit-cell dimensions indicate highly ordered, near-maximum microcline for all blocky K-feldspar, and for Types-2 and -3 K-feldspar, fully ordered low-albite for Types A, B, and F, and totally disordered high-sanidine structure for adularia crystals of Type-6. (K,Rb)-feldspar of the Types-4 and -5 cannot be examined by conventional methods because the they are found essentially at microscopic scale, intermixed with other mineral species.

## REFERENCES


Baadsgaard, H., and P. Černý, 1993. Winnipeg River pegmatite populations, southeastern Manitoba. Geological Association of Canada-Mineralogical Association of Canada Annual Meeting, Edmonton. Program with abstracts, **18**, A5.

Bachinski, S.W., and G. Müller, 1971. Experimental determinations of the microcline – low albite solvus. *J. Petrol.* **12**: 329-356.

Barker, D.S., 1964. Ammonium in alkali feldspars. *Am. Mineral.* **49**: 851-858.

Barrer, R.M., and N. McCallum, 1953. Hydrothermal chemistry of silicates. Part IV. Rubidium and cesium aluminosilicates. *J. Chem. Soc.* (London), 4029-4053.

Barth, T.F.W., 1969. Feldspars. John Wiley & Sons, Inc., New York. ch. 1.

Borutskaya, V.L., 1975. Synthesis of various rubidium and cesium feldspars. *Dokl. Akad. Nauk SSSR* **222**: 924-927.

Breaks, F.W., 1989. Origin and evolution of peraluminous granite and rare-element pegmatite in the Dryden area, Superior Province of northwestern Ontario. Unpublished Ph.D. thesis, Carleton University, 594p.

Breaks, F.W., and A.G. Tindle, 1997. Rare-Metal Exploration potential of the Separtation Lake Area: an emerging Target for Bikita-Type Mineralization in the Superior Province of NW Ontario. Ontario Geological Survey – Open File Report 5966, 25pp.

Brown, W.L., and I. Parsons, 1994. Feldspars in igneous rocks *in* Feldspars and Their Reactions (I. Parson, ed.), NATO ASI series. Kluwer Academic Publishers, Netherlands, 1994. pp. 449-499.

Bruno, E., and H. Pentinghause, 1974. Substitution of cations in natural and synthetic feldspars *In* The Feldspars, (W.S. MacKenzie and J. Zussman eds.). Manchester University Press, Manchester. pp. 574-609.

Burnham, C.W., and H. Nekvasil, 1986. Equilibrium properties of granitic pegmatite magmas. American Mineralogist, **71**: 239-263.

Cameron, E.N., Jahns, R.H., McNair, A.H., and L.R. Page, 1949. Internal structure of granitic pegmatites. *Econ. Geol. Mon.* **2**: 115.

Černý, P., 1972. The Tanco pegmatite at Bernic Lake, Manitoba. VIII. Secondary minerals from the spodumene-rich zones. *Can. Mineral.* **11**: 714-726.

Černý, P., 1982. The Tanco pegmatite at Bernic Lake, southeastern Manitoba, *In* Granitic pegmatites in science and industry (P. Černý ed.). Mineralogical Association of Canada short course handbook, pp. 527-543.

Černý, P., 1991. Rare-element granitic pegmatites, Part I: Anatomy and internal evolution of pegmatite deposits. *Geosci. Can.* (Ore Deposit Models series) **18**: 49-67.

Černý, P., 1992. Geochemical and petrogenetic features of mineralization in rare-element granitic pegmatites in the light of current research. *Applied Geochemistry* **7**: 393-416.

Černý, P., 1994. Evolution of feldspars in granitic pegmatites *in* Feldspars and Their Reactions (I. Parson, ed.), NATO ASI series. Kluwer Academic Publishers, Netherlands, 1994. pp. 501-540.

Černý, P., 1998. Magmatic vs. Metamorphic derivation of rare-element granitic pegmatites. *Krystalinikum* **24**: 7-34.

Černý, P., and D. London, 1983. Crystal-chemistry and stability of petalite. Tschermak's Mineralogische und Petrographische Mitteilungen, **31**: 81-96.

Černý, P., and F.C. Hawthorne, 1989. Controls on gallium concentration in rare-element granitic pegmatites. Program with abstracts -- Geological association of Canada – Mineralogical association of Canada, annual meeting, Montreal.

Černý, P., and F.M. Simpson, 1978. The Tanco pegmatite at Bernic Lake, Manitoba. X. Pollucite. *Can. Mineral.* **16**: 325-333.

Černý, P., and J. Macek, 1972. The Tanco pegmatite at Bernic Lake, Manitoba. V, Coloured potassium feldspars. *Can. Mineral.* **11**: 679-689.

Černý, P., and R. Chapman, 1984. Paragenesis, chemistry and structural state of adularia from granitic pegmatites. *Bull. Minéral.* **107**: 369-384.

Černý, P., and R. Chapman, 1986. Adularia from hydrothermal vein deposits: extremes in structural state. *Can. Mineral.*. **24**: 717-728.

Černý, P., Ercit, T.S., and P.J. Vanstone, 1996. Petrology and mineralization of the Tanco rar-element pegmatite, southeastern Manitoba. Field trip guidebook A4. Geol. Assoc. Can., Mineral. Assoc. Can. Annual Meeting, Winnipeg, Manitoba, 1-63.

Černý, P., Ercit, T.S., and P.J. Vanstone, 1998. Mineralogy and Petrology of the Tanco rare-element pegmatite deposit. Field trip guidebook B6. International Mineralogical Association, 17$^{th}$ general meeting, Toronto, 1998.

Černý, P., Meintzer, R.E., and A.J. Anderson, 1985a. Extreme fractionation in rare-element granitic pegmatites: selected examples of data and mechanisms. *Can. Mineral.* **23**: 381-421.

Černý, P., Pentinghaus, H. and J. Macek, 1985b. Rubidian microcline from Red

Cross Lake, northeastern Manitoba. *Bull Geol. Soc. Finland* **57**: 217-230.

Černý, P., Smith, J.V., Mason, R.A., and J.S. Delaney, 1984. Geochemistry and petrology of feldspar crystallization in the Věžná pegmatite, Czechoslovakia. *Can. Mineral.* **22**: 631-651.

Černý, P., Trueman, D.L., Ziehlke, D.V., Goad, B.E., and B.J. Paul, 1981. The Cat Lake-Winnipeg River and the Wekusko Lake pegmatite fields, Manitoba. Manitoba department of energy and mines, mineral resources division, Economic geology report ER80-1.

Clark, G.S., 1982. Rubidium-strontium isotope systematics of complex granitic pegmatites. *In* Granitic pegmatites in science and industry (P. Černý ed.). Mineralogical Association of Canada short course handbook, 8, pp. 347-372.

Clark, G.S., and P. Černý, 1987. Radiogenic $^{87}Sr$, its mobility, and the interpretation of Rb-Sr fractionation trends in rare-element granitic pegmatites. *Geochim. et Cosmochim. Acta* **51**: 1011-1018.

Cooper, D.G., 1964. The geology of the Bikita pegmatites; *in* Geology of Some Ore Deposits in Southern Africa, v. 2, p. 441-462.

Crouse, R.A., Černý, P., Trueman, D.L., and R.O. Burt, 1979. The Tanco pegmatite, southeastern Manitoba. Canadian institute of Mining and Metallurgy Bulletin, 1979, No. 2: 1-10.

Crouse, R.A., Černý, P., Trueman, D.L., and R.O. Burt, 1984. The Tanco pegmatite, southeastern Manitoba. *In* CIM Special Volume **29**, The geology of Industrial Minerals in Canada: 169-176.

Deer, W.A., Howie, R.A., and J. Zussman, 1992. The rock-forming minerals, 2nd ed. Addison Wesley Longman Ltd. Edinburough Gate, Harlow, Essex, England. pp. 391-430.

Deubener, J., Sternitzke, M., and G. Müller, 1991. Feldspars $MAlSi_3O_8$ (M = H, Li, Ag) synthesized by low-temperature ion exchange. *Am. Mineral.* **76**: 1620-1627.

Eugster, H.P., and N.L. McIver, 1959. Boron analogues of alkali feldspar and related silicates. *Geol. Soc. Am. Bull.* **70**: 1598-1599.

Faust, G.T., 1936. The fusion relation of iron-orthoclase, with a discussion of the evidence of the existence of an iron-orthoclase molecule in feldspars. *Am. Mineral.* **29**: 753-763.

Fleet, M.E., 1992. Tetrahedral-site occupancies in reedmergnerite and synthetic boron albite ($NaBSi_3O_8$). *Am. Mineral.* **77**: 76-84.

Gasperin, M., 1971. Structure crystalline de $RbAlSi_3O_8$. *Acta Crystallogr.* **B27**: 854-855.

Gaupp, R., Moller, P., and G. Morteani, 1984. Tantal-Pagmatite: Geologische, Petrologiche und Geochemishe Untersuchungen. Monograph series on mineral deposits, **23**. Borntraeger Berlib-Stuttgart, 124 pp.

Ghelis, M., and M. Gasperin, 1970. Evolution des paramètres dans le système $KAlSi_3O_8$ – $RbAlsi_3O_8$. *Compt. Rend. Acad. Sci.* **271**: 1928-1929.

Hallum, M., and H.P. Eugster, 1976. Ammonium silicate stability relations. *Contib. Mineral. Petrol.* **57**: 227-254.

Hautefeuille, P., and A. Perry, 1888. Sur la préparation et les propriétés d'orthose ferrique. *Compt. Rend. Acad. Sci. Paris* **107**: 1150-1152.

Heier, Knut S., and S.R. Taylor, 1959a. Distribution of Ca, Sr and Ba in southern Norwegian pre-Cambrian alkali feldspars. *Geochim. et Cosmochim. Acta* **17**: 286-304.

Heier, Knut S., and S.R. Taylor, 1959b. Distribution of Li, Na, K, Rb, Cs, Pb and Tl in southern Norwegian pre-Cambrian alkali feldspars. *Geochim. et Cosmochim. Acta* **15**: 284-304.

Henderson, C.M.B., 1978. Thermal expansion of alkali-feldspars. II. Rb-sanidine and maximum microcline. *NERC Progress in Experimental Petrol.* 4th report, **11**: 53-57.

Icenhower, J., and D. London, 1996. Experimental partitioning of Rb, Cs, Sr, and Ba between alkali feldspar and peraluminous melt. *Am. Mineral.* **81**: 719-734.

Jahns, R.H., 1982. Internal evolution of granitic pegmatites. *In* Granitic pegmatites in science and industry (P. Černý ed.). Mineralogical Association of Canada short course handbook, 7, pp. 293-346.

Jahns, R.H., and C.W. Burnham, 1969. Experimental studies of pegmatite genesis: I. A model for the derivation and crystallization of granitic pegmatites. *Econ. Geol.* **64**: 843-864.

Kimata, M., 1977. Synthesis and properties of reedmergnerite. *J. Japanese Assoc. Mineral., Petrol. Econ. Geol.* **72**: 162-172.

Kleck, W.D., 1996. Crystal settling in pegmatite magma. *Geol. Assoc. Can. Mineral. Assoc. Can. Abstr. Program.* **21**: A-50.

Kneip, H.J., and F. Liebau, 1994. Feldspars with trivalent non-tetrahedral cations: Experimental studies in the system $NaAlSi_3O_8$ - $CaAl_2Si_2O_8$ – $LaAlSi_3O_8$. *Eur. J. Mineral.* **6**: 87-98.

Kontak, D.J., and R.F. Martin, 1997. Alkali feldspar in the peraluminous South Mountain batholith, Nova Scotia: Trace-element data. *Can. Mineral.* **35**: 959-977.

Kuehner, S.M. and D.J. Joswiak, 1996. Naturally occurring ferric iron sanidine from the Leucite Hills lamproite. *Am. Mineral.* **81**: 229-237.

Lagache, M. and J. Quemeneur, 1997. The Volta Grande Pegmatites, Minas Gerais, Brazil; an example of rare-element granitic pegmatites exceptionally enriched in lithium and rubidium. *Can. Mineral.* **35**:153-165.

Lagache, M., 1998. Le système feldspathique ternaire Na-K-Rb: modélisation et expérimentation. *C.R. Acad. Sci. Paris, Sciences de la terre et des planètes / Earth & Planetary Sciences* **327**: 147-153.

Laurs, B.M., Dilles, J.H., Wairrach, Y., Kauar, A.B., and L.W. Snee, 1998. Geological setting and petrogenesis of symmetrically zoned, miarolitic granitic pegmatites at Stak Nala, Nanga Parbat-Haramosh Masif, northern Pakistan. *Can Mineral.* **36**: 1-47.

Lindqvist, B., 1966. Hydrothermal synthesis studies of potash-bearing sesquioxide-silica systems. *Geol. Fören. i Stockholm Förhr.* **88**: 133-178.

Linthout, K., and W.J. Lustenhouwer, 1993. Ferrian high sanidine in a lamproite from Cancarix, Spain. *Mineral. Mag.* **57**: 289-299.

London, D., Černý, P., Loomis, J.L., and J. Pan, 1990. Phosphorus in alkali feldspars of rare-element granitic pegmatites. *Can. Mineral.* **28**: 771-786.

London, D., 1984. Experimental phase equilibria in the system LiAlSiO4-SiO2-H2O; A petrogenetic grid for lithium-rich pegmatites. *Am. Mineral.* **69**: 995-1004.

London, D., 1986a. The magmatic-hydrothermal transition in the Tanco rare-element pegmatite; Evidence from fluid inclusions and phase equilibrium experiments. *Am. Mineral.* **71**: 376-395.

London, D., 1986b. Formation of tourmaline-rich gem pockets in miarolitic pegmatites. *Am. Mineral.* **71**: 396-405.

London, D., 1987. Internal differentiation of rare-element pegmatites: Effects of boron, phosphorus, and fluorine. *Geochim. et Cosmochim. Acta* **51**: 403-420.

London, D., 1990. Internal differentiation of rare-element pegmatites; A synthesis of recent research. Geological Society of America, Special Paper 246, pp. 35-49.

London, D., 1992a. Phosphorus in S-type magmas: The $P_2O_5$ content of feldspars from peraluminous granites, pegmatites, and rhyolites. *Am. Mineral.* **77**: 126-145.

London, D., 1992b. The application of experimental petrology to the genesis and crystallization of granitic pegmatites. *Can. Mineral.* **30**: 499-540.

London, D., Hervig, R.L., and G.B. VI, Morgan, 1988. Melt-vapor solubilities and element partitioning in peraluminous granite-pegmatite systems; Experimental results with Macusani glass at 200 MPa. *Contib. Mineral. Petrol.* **99**: 360-373.

London, D., Morgan, G.B. VI, and R.L. Hervig, R.L., 1989. Vapor-undersaturated experiments in the system macusanite-H2O at 200 MPa, and the internal differentiation of granitic pegmatites. *Contib. Mineral. Petrol.* **102**: 1-17.

London, D., Wolf, M.B., Morgan G.B., and M.G. Garrido, 1999. Experimental silicate-phosphate equilibria in peraluminous granitic magmas, with a case study of the Alburquerque batholith at Tres Arroyos, Badajoz, Spain. *J. Petrol.* **40**: 215-240.

Long, P.E., 1978. Experimental determination of partition coefficients for Rb, Sr, and Ba between alkali feldspar and silicate liquid. *Geochim. et Cosmochim. Acta* **42**: 833-846.

Mahood, G., and W. Hildreth, 1983. Large partition coefficients for trace-elements in high-silica rhyolites. *Geochim. et Cosmochim.* **47**: 11-30.

Makagon, V.M., and B.M. Shmakin, 1988. Geochemistry of the main formations of granitic pegmatites. Acad. Sci. USSR, Siberia Department, Nauka, Novosgrask.

Margison, S., 2001. Mineralogy and geochemistry of Micas from the Tanco pegmatite... Unpublished M.Sc thesis. University of Manitoba.

Marshall, P.A., 1972. Selected partition ratios in feldspars and micas from Bernic Lake (Chemalloy) pegmatite, Manitoba. M.Sc. thesis, University of Ontario, London, Ont.

Martin R.F., 1971. Disordered authigenic feldspars of the series KAlSi3O8 - KBSi3O8 from southern California. *Am. Mineral.* **56**: 281-291.

Martin, R.F., 1974. Controls of ordering and subsolidus phase relations in the alkali feldspars *In* The Feldspars, (W.S. MacKenzie and J. Zussman eds.). Manchester University Press, Manchester. pp. 574-609.

Martin, R.F., Kontak, D.J., and L.R. Richard, 1993. The significance of P enrichment in alkali feldspar, South Mountain batholith, Nova Scotia, Canada. NATO ASI feldspars and Their Reactions, Abstracts, No. 15.

Mason, R.A., 1980a. Changes in the crystal morphology of synthetic reedmergnerite ($NaBSi_3O_8$) during ordering experiments. *Mineral. Mag.* **43**: 905-908.

Mason, R.A., 1980b. The ordering behavior of reedmergnerite, $NaBSi_3O_8$. *Contrib. Mineral. Petrol.* **72**: 329-333.

Mason, R.A., 1982. Trace-element distributions between the perthite phases of alkali feldspars from pegmatites. *Min. Mag.* **45**: 101-106.

McMillan, P.F., Brown, W.F., and R.E. Openshaw, 1980. The unit-cell parameters of an ordered K – Rb alkali feldspar series. *Am. Mineral.* **65**: 458-464.

Morgan, G.B., and D. London, 1987. Alteration of amphibolitic wallrocks around the Tanco rare-element pegmatite, Bernic Lake, Manitoba. *Am. Mineral.* **72**: 1097-1121.

Morgan, G.B., and D. London, 1999. Crystallization of the Little Three layered pegmatite-aplite dike, Ramona District, California. *Contrib. Mineral. Petrol.* **136**: 310-330.

Morteani, G.B., and R. Gaupp, 1989. Geochemical evaluation of the tantalum potential of pegmatites, *in* Lanthanides, Tantalum and Niobium (P. Moller, P. Černý, and F. Saupe, *eds.)*. Springer-Veriag, 380 pp.

Müller, G., 1988. Preparation of hydrogen and lithium feldspars by ion exchange. *Nature* **332**: 435-436.

Nickel, E.H., 1961. The mineralogy of the Bernic Lake pegmatite, southeastern Manitoba. Department of Mines and Technical Services, Mines Branch, Technical Bulletin, **20**, 38pp.

Norton, J.J., 1983. Sequence of Mineral Assemblages in Differentiated Granitic Pegmatites. *Econ. Geol.* **78**: 854-874.

Norton, J.J., 1994. Structure and bulk composition of the Tin Mountain pegmatite, Black Hills, South Dakota. *Econ. Geol.* **89**: 1167-1175.

Ottolini L., Bottazzi P., Vannucci R., Anal. Chem., 1993, vol. 65, 1960-1968

Partington, G.A., 1995. A review of the geology, mineralization, and geochronology of the Greenbushes Pegmatite, Western Australia. *Economic*

*geology and the Bulletin of the Society of Economic Geologists,* **90**: 616-635.

Paulus, H., and G. Müller, 1988. The crystal structure of a hydrogen-feldspar. *N. Jb. Miner. Mh.* **11**: 481-490.

Penner, A.P., and G.S. Clark, 1971. Rb-Sr age determinations from the Bird River area, southeastern Manitoba. *In* Geoscience studies in Manitoba (A.C. Turnock, ed.), Geological association of Canada, Special Paper, **9**: 105-109.

Pentinghaus, H., and C.M.B. Henderson, 1979. Rubidium-aluminosilikat-Feldspat ($RbAlSi_3O_8$): Stabilität, strukturelle Zustande und Schmelzverhalten: Chemische und thermische Ausdehnung des ($AlSi_3O_8$)-Gerüstes. *Fortschr. Mineral.* **57**: 119-120.

Pouchou, J.L., and F. Pichoir, (1985). "PAP" (phi-rho-Z) procedure for improved quantitative microanalysis. *In* Microbeam Analysis (J.T. Armstrong, ed.). San Francisco Press, San Francisco, California. pp.104-106.

Quensel, P., 1956. The paragenesis of the Varuträsk pegmatite, including a review of its mineral assemblage. *Ark. Min. Geol.* **2**: 9-126.

Ribbe, P.H., 1983. Feldspar mineralogy *in* Reviews in Mineralogy, volume 2, 2nd ed. (Ribbe, P.H. ed.), Mineralogical society of America. Bookcrafters inc., Chelsea Michigan, 1983.

Sahl, K., 1978. Thallium. *In* Handbook of geochemistry, Vol. II/5 (K. Wedepohl, ed.). Springer-Verlag, Berlin, Heidelberg, New York.1978. Chapter 81.

Shaw, D.M., 1951. The geochemistry of thallium. *Geochim. et Cosmochim. Acta* **2**: 118-154.

Shearer C.K., and J.J. Papike, 1986. Distribution of boron in the Tip Top pegmatite, Black Hill, South Dakota. *Geology* **14**: 119-123.

Shmakin, B.M., 1992. New data on the geochemistry and mineralogy of the rare-element pegmatites of Koktokai (Sinezyan, PRC). *Geolchimiya* **6**: 821-

Shmakin, B.M., 1997. Rare-metal pegmatites. *In* Granitic pegmatites, Vol. 2. Novosibirsk, "Nauka", Siberian enterprise RAS.

Smeds, S.-A. and P. Černý, 1989. Pollucite from the Proterozoic petalite-bearing pegmatites of Utö, Stockholm archipelago, Sweden. *Geologiska Föreningens i Stockholms Förhandlingar* **111**: 361-372.

Smith, P. and I. Parsons, 1974. The alkali feldspar solvus at 1 kilobar water-vapour pressure. *Mineral. Mag.* **39**: 747-767.

Smith, V.S., and W.L. Brown, 1988. Feldspar Minerals, volume 1, 2nd ed. Springer-Verlag, Berlin, Heidelberg, New York, London, Paris, Tokyo. ch. 14.

Solodov, N.A., 1962. Distribution of Thallium among the minerals of a zoned pegmatite *In* Geochemistry, The Geochemical Society, No. 7, pp. 738-741.

Stewart, D.B., 1978. Petrogenesis of lithium-rich pegmatites. *Am. Mineral.* **63**: 970-980.

Stilling, A., 1998. The bulk composition of the Tanco pegmatite at Bernic Lake Manitoba, Canada. M.Sc. thesis, University of Manitoba, Winnipeg, MB.

Taylor, B.E., and H. Friedrichsen, 1983. Light stable isotope systematics of granite pegmatites from North America and Norway. *Isotope Geoscience*, **1**: 127-167.

Teertstra, D.K., Černý, P., and F.C. Hawthorne, 1998a. Rubidium feldspars in granitic pegmatites. *Can. Mineral.* **36**: 483-496.

Teertstra, D.K., Černý, P., and F.C. Hawthorne, 1999. Subsolidus rubidium-dominant feldspar from the Morrua pegmatite, Mozambique: paragenesis and

composition. *Mineral. Mag.* **63**: 313-320.

Teertstra, D.K., 1991. Compositional heterogeneity and alteration of pollucite. M.Sc. Thesis, University of Manitoba, Winnipeg, Manitoba, 225 pp.

Teertstra, D.K., 1997. Reactions of (K-Rb)-feldspars from rare-element granitic pegmatites. Ph.D. thesis, Department of Geological Sciences, Winnipeg, Manitoba.

Teertstra, D.K., Hawthorne, F.C., and P. Černý, 1998b. Identification of normal and anomalous compositions of minerals by electron-microprobe analysis: K-rich feldspars as a case study. *Can. Mineral.* **36**: 87-95.

Thomas, A.V., Bray, C.J., and E.T.C. Spooner, 1988. A discussion of the Jahns-Burnham proposal for the formation of zoned granitic pegmatites using solid-liquid-vapour inclusions from the Tanco pegmatite, S.E. Manitoba, Canada. *Transactions of the Royal Society of Edinburgh: Earth Sciences* **79**: 299-315.

Trueman, D.L., 1980. Stratigraphic. structural and metamorphic petrology of the Archean greenstone belt at Bird River, Manitoba. Ph.D. thesis, University of Manitoba, Winnipeg, MB.

Voncken, J.H.L., Konings, R.J.M., Jansen, J.B.H., and C.F. Woensdregt, 1993a. Hydrothermally grown buddingtonite, an anhydrous ammonium feldspar ($NH_4AlSi_3O_8$). *Phys. Chem. Minerals* **15**: 323-328.

Voncken, J.H.L., Konings, R.J.M., Van der Eerden, A.M.J., Jansen, J.B.H., Schuiling, R.D., and C.F. Woensdregt, 1993b. Crystal morphology and X-ray powder-diffraction of the Rb-analogue of high sanidine, $RbAlSi_3O_8$. *N. Jb. Miner. Mh.* **1993**: 10-16.

Waldron, K., Parsons, I., and W.I. Brown, 1983. Solution-redeposition and the orthoclase-microcline transformation: Evidence from granulites and relevance to $^{18}O$ exchange. *Mineral. Mag.* **57**: 697-695.

Walker, F.D.L., Lee, M.R., and I. Parsons, 1995. Micropores and micropermeable texture in alkali feldspars: Geochemical and geophysical implications. *Mineral. Mag.* **59**: 505-534.

Walker, R.J., Hanson, G.N., Papike, J.J., O'Neil, J.R., and J.C. Laul, 1986. Internal evolution of the Tin Mountain pegmatite, Black Hills, South Dakota. *Am. Mineral.*, **71**: 440-459.

Wang, X.J., Černý, P, Chackowsky, L.E., and R. Eby, 1988. The lepidolite-petalite-bearing dikes at Red Cross Lake, Northeastern Manitoba: Extreme enrichment and fractionation of incompatible elements in low-pressure pegmatites. Program with abstracts – Geological association of Canada; Mineralogical association of Canada; Canadian geophysical union, Joint annual meeting, 13, p. A131.

Wang, X.J., Yu, X.Y., Xu, J.G., and Y.Z. Qiu, 1981. Study of pegmatite minerals of Altai Area. Scientific publishing house, Beijing.

Webber, K.L., Falster, A.U., Simmons, W.B., and E.E. Foord. The role of diffusion-controlled oscillatory nucleation in the formation of line rock in pegmatite-aplite dikes. *J. Petrol.* **38**: 1777-1791.

Weitzi, R., and K. Viswanathan, 1971. Rubidium plagioclase durch Kation enaustausch. *Fortschr. Mineral.* **49**: 63.

Wones, D.R., and D.E. Appleman, 1963. Properties of synthetic triclinic KFeSi3O8, iron-microcline, with some observations on the iron-microcline – iron-sanidine transition. *J. Petrol.* **4**: 131-137.

Yakovenchuk, V.N., Ivanyuk, G.Yu., Pakhomovskiy, Ya.A. and Men'shikov, Yu.P., 1999. Minerals of the Khibina Complex. Zemlya Press, Moscow (in Russ.). 320 pp.

## Appendix I: Analytical techniques and statistics

Elements sought, limits of detection (LOD), analytical precision, and percent detection*

| Mineral | All | | All | | Albite | Kspar | Kspar |
|---|---|---|---|---|---|---|---|
| Statistic | LOD | Precision | LOD | Precision | % detection | % detection | % detection |
| Analysis | EMPA | EMPA | ICP/AA | ICP/AA | EMPA | EMPA | ICP/AA |
| | wt.% | +/- | wt.% | +/- | | | |
| SiO2 | 0.060 | 1% | | | 100% | 100% | |
| Al2O3 | 0.045 | 1% | | 5% | 100% | 100% | |
| TiO2 | 0.057 | 1% | | | 0% | 0% | |
| Fe2O3 | 0.086 | 1% | | | 1% | 0% | |
| FeO | | | | | | | |
| MnO | 0.025 | 1% | | | 34% | 4% | |
| MgO | 0.010 | 1% | | | 1% | 1% | |
| CaO | 0.025 | 1% | 0.0040 | 5% | 98% | 1% | 100% |
| BaO | 0.087 | 1% | 0.00033 | 5% | 12% | 11% | 99% |
| SrO | 0.059 | 1% | 0.00059 | 5% | 23% | 47% | 100% |
| Li2O** | 21 ppb | 10% | 0.0011 | 5% | | | 100% |
| Na2O | 0.049 | 1% | 0.16 | 15% | 100% | 100% | 100% |
| K2O | 0.036 | 1% | 0.18 | 5% | 99% | 100% | 100% |
| Rb2O | 0.057 | 1% | 0.055 | 5% | 81% | 100% | 100% |
| Cs2O | 0.032 | 1% | | | 5% | 93% | 100% |
| P2O5 | 0.073 | 1% | 0.020 | 5% | 91% | 99% | 100% |
| B2O3** | 45 ppb | 10% | | | | | |
| BeO** | 27 ppb | 10% | | | | | |
| H2O+ | | | | | | | |
| H2O- | | | | | | | |
| F | 0.069 | 1% | | 5% | 6% | 16% | |
| Sc2O3 | | | | | | | |
| SnO2 | | | | | | | |
| Nb2O5 | | | | | | | |
| Ta2O5 | | | | | | | |
| UO2 | | | | | | | |
| PbO | 0.041 | 1% | | 5% | 20% | 14% | |
| WO3 | | | | | | | |
| ZnO | | | | | | | |
| ZrO2 | | | | | | | |
| HfO2 | | | | | | | |
| Tl2O | | | | | | | |
| Ga2O3 | | | 0.0034 | 5% | | | 99% |
| Sb2O3 | | | | | | | |

* percent detection refers to the percentage of individual analytical contents that surpassed the limit of detection (LOD) for a given oxide.

** Left justified elements analysed by SIMS.

**Appendix II: Average mineral compositions in zone 10**

| Mineral | Albite | Albite | K-feldspar | K-feldspar | K-feldspar |
|---|---|---|---|---|---|
| Analysis | EMPA | | ICP/AA | EMPA** | |
| | Brown (2001) | Stilling (1998) | Brown (2001) | Brown (2001) | Stilling (1998) |
| Mode | | 66.0% | | | 0.0% |
| n | 6 | | 8 | 10 | |
| SiO2 | 67.66 | 67.61 | | 63.63 | |
| Al2O3 | 19.53 | 20.12 | | 18.39 | |
| TiO2 | | | | | |
| Fe2O3 | 0.01 | | | 0.00 | |
| FeO | | | | | |
| MnO | 0.00 | | | 0.00 | |
| MgO | 0.00 | | | 0.00 | |
| CaO | 0.06 | 0.64 | 0.129 | 0.00 | |
| BaO | 0.02 | | 0.017 | 0.02 | |
| SrO | 0.03 | | 0.016 | 0.03 | |
| Li2O** | | | 0.014 | 0.011 | |
| Na2O | 11.62 | 11.44 | 2.5 | 0.28 | |
| K2O | 0.08 | | 12.2 | 15.67 | |
| Rb2O | 0.04 | | 1.60 | 1.69 | |
| Cs2O | 0.00 | | 0.108 | 0.11 | |
| P2O5 | 0.16 | 0.2 | 0.34 | 0.29 | |
| B2O3** | | | | 0.0019 | |
| BeO** | | | | 0.0015 | |
| H2O+ | | | | | |
| H2O- | | | | | |
| F | | | | | |
| Sc2O3 | | | | | |
| SnO2 | | | | | |
| Nb2O5 | | | | | |
| Ta2O5 | | | | | |
| UO2 | | | | | |
| PbO | 0.01 | | | 0.01 | |
| WO3 | | | | | |
| ZnO | | | | | |
| ZrO2 | | | | | |
| HfO2 | | | | | |
| Tl2O | | | 0.011* | | |
| Ga2O3 | | 0.009 | 0.006* | | |
| Sb2O3 | | | | | |
| Totals (%) | 99.22 | 100.02 | 16.84 | 100.13 | 0.00 |

-all values in wt.%

*unpublished data from P. Cerny

** Left justified values collected by SIMS. Each value represents average of 2 data points.

**Appendix II: Average mineral compositions in zone 20**

| Mineral | Albite | Albite | K-feldspar | K-feldspar | K-feldspar |
|---|---|---|---|---|---|
| Analysis | EMPA** | | ICP/AA | EMPA** | |
| | Brown (2001) | Stilling (1998) | Brown (2001) | Brown (2001) | Stilling (1998) |
| Mode | | 40.7% | | | 15.0% |
| n | 26 | | 38 | 15 | |
| SiO2 | 68.38 | 67.6 | | 63.62 | 64.65 |
| Al2O3 | 19.74 | 20.06 | | 18.36 | 18.93 |
| TiO2 | | | | | |
| Fe2O3 | 0.01 | | | 0.01 | |
| FeO | | | | | |
| MnO | 0.01 | | | 0.00 | |
| MgO | 0.00 | | | 0.00 | |
| CaO | 0.08 | 0.43 | 0.095 | 0.00 | 0.20 |
| BaO | 0.02 | | 0.006 | 0.02 | |
| SrO | 0.03 | | 0.014 | 0.04 | |
| Li2O** | 0.00026 | | 0.032 | 0.019 | 0.03 |
| Na2O | 11.74 | 11.57 | 2.0 | 0.36 | 1.70 |
| K2O | 0.07 | | 12.1 | 15.59 | 13.00 |
| Rb2O | 0.05 | | 1.45 | 1.48 | 1.20 |
| Cs2O | 0.00 | | 0.105 | 0.05 | 0.03 |
| P2O5 | 0.16 | 0.35 | 0.40 | 0.34 | 0.35 |
| B2O3** | 0.0013 | | 0.0014 | | |
| BeO** | 0.00058 | | 0.0015 | | |
| H2O+ | | | | | |
| H2O- | | | | | |
| F | | | | | |
| Sc2O3 | | | | | |
| SnO2 | | | | | |
| Nb2O5 | | | | | |
| Ta2O5 | | | | | |
| UO2 | | | | | |
| PbO | 0.01 | | | 0.01 | |
| WO3 | | | | | |
| ZnO | | | | | |
| ZrO2 | | | | | |
| HfO2 | | | | | |
| Tl2O | | | 0.012* | | 0.01 |
| Ga2O3 | | 0.009 | 0.007* | | 0.01 |
| Sb2O3 | | | | | |
| Totals (%) | 100.28 | 100.02 | 16.22 | 99.90 | 100.11 |

-all values in wt.%

*unpublished data from P. Cerny

** Left justified values collected by SIMS. K-feldspar values represent average of 2 data points. Albite values represent average of 4 data points.

**Appendix II: Average mineral compositions in zone 30**

| Mineral | Albite | Albite | K-feldspar | K-feldspar | K-feldspar |
|---|---|---|---|---|---|
| Analysis | EMPA** | | ICP/AA | EMPA** | |
| | Brown (2001) | Stilling (1998) | Brown (2001) | Brown (2001) | Stilling (1998) |
| Mode | x | | | 0 | |
| n | 14 | | 0 | 0 | |
| SiO2 | 68.32 | 67.55 | | | |
| Al2O3 | 19.57 | 20.08 | | | |
| TiO2 | | | | | |
| Fe2O3 | 0.01 | | | | |
| FeO | | | | | |
| MnO | 0.01 | | | | |
| MgO | 0.00 | | | | |
| CaO | 0.06 | 0.43 | | | |
| BaO | 0.02 | | | | |
| SrO | 0.02 | | | | |
| Li2O** | 0.00006 | | | | |
| Na2O | 11.67 | 11.57 | | | |
| K2O | 0.07 | | | | |
| Rb2O | 0.05 | | | | |
| Cs2O | 0.00 | | | | |
| P2O5 | 0.13 | 0.38 | | | |
| B2O3** | 0.0024 | | | | |
| BeO** | 0.0011 | | | | |
| H2O+ | | | | | |
| H2O- | | | | | |
| F | | | | | |
| Sc2O3 | | | | | |
| SnO2 | | | | | |
| Nb2O5 | | | | | |
| Ta2O5 | | | | | |
| UO2 | | | | | |
| PbO | 0.01 | | | | |
| WO3 | | | | | |
| ZnO | | | | | |
| ZrO2 | | | | | |
| HfO2 | | | | | |
| Tl2O | | | | | |
| Ga2O3 | | 0.009 | | | |
| Sb2O3 | | | | | |
| Totals (%) | 99.93 | 100.02 | | | |

-all values in wt.%

*unpublished data from P. Cerny

** Left justified values collected by SIMS. Each value represents average of 2 data points.

**Appendix II: Average mineral compositions in zone 40**

| Mineral Analysis | Albite EMPA** Brown (2001) | Albite Stilling (1998) | K-feldspar ICP/AA Brown (2001) | K-feldspar EMPA** Brown (2001) | K-feldspar Stilling (1998) |
|---|---|---|---|---|---|
| Mode | | 25.0% | | | 24.0% |
| n | 34 | | 29 | 12 | |
| SiO2 | 68.29 | 67.78 | | 63.32 | 64.77 |
| Al2O3 | 19.74 | 19.91 | | 18.54 | 18.88 |
| TiO2 | | | | | |
| Fe2O3 | 0.01 | | | 0.01 | |
| FeO | | | | | |
| MnO | 0.01 | | | 0.00 | |
| MgO | 0.00 | | | 0.00 | |
| CaO | 0.06 | 0.21 | 0.082 | 0.00 | 0.02 |
| BaO | 0.01 | | 0.004 | 0.03 | |
| SrO | 0.02 | | 0.018 | 0.03 | |
| Li2O** | 0.00007 | | 0.048 | 0.019 | 0.08 |
| Na2O | 11.74 | 11.69 | 1.8 | 0.35 | 1.80 |
| K2O | 0.06 | | 12.4 | 15.18 | 13.20 |
| Rb2O | 0.05 | | 2.01 | 2.13 | 1.85 |
| Cs2O | 0.00 | | 0.151 | 0.10 | 0.12 |
| P2O5 | 0.19 | 0.4 | 0.47 | 0.45 | 0.44 |
| B2O3** | 0.0017 | | | 0.0023 | |
| BeO** | 0.0012 | | | 0.00093 | |
| H2O+ | | | | | |
| H2O- | | | | | |
| F | | | | | |
| Sc2O3 | | | | | |
| SnO2 | | | | | |
| Nb2O5 | | | | | |
| Ta2O5 | | | | | |
| UO2 | | | | | |
| PbO | 0.01 | | | 0.01 | |
| WO3 | | | | | |
| ZnO | | | | | |
| ZrO2 | | | | | |
| HfO2 | | | | | |
| Tl2O | | | 0.012* | | 0.012 |
| Ga2O3 | | 0.009 | 0.009* | | 0.009 |
| Sb2O3 | | | | | |
| Totals (%) | 100.20 | 100.00 | 16.93 | 100.17 | 101.18 |

-all values in wt.%

*unpublished data from P. Cerny

** Left justified values collected by SIMS. K-feldspar values represent average of 2 data points. Albite values represent average of 4 data points.

**Appendix II: Average mineral compositions in zone 50**

| Mineral | Albite | Albite | K-feldspar | K-feldspar | K-feldspar |
|---|---|---|---|---|---|
| Analysis | EMPA** | | ICP/AA | EMPA** | |
| | Brown (2001) | Stilling (1998) | Brown (2001) | Brown (2001) | Stilling (1998) |
| Mode | | 7.0% | | | 25.0% |
| n | 14 | | 20 | 12 | |
| SiO2 | 68.33 | 67.73 | | 63.29 | 63.95 |
| Al2O3 | 19.64 | 19.93 | | 18.55 | 18.60 |
| TiO2 | | | | | |
| Fe2O3 | 0.01 | | | 0.01 | |
| FeO | | | | | |
| MnO | 0.01 | | | 0.01 | |
| MgO | 0.00 | | | 0.00 | |
| CaO | 0.06 | 0.21 | 0.096 | 0.00 | 0.07 |
| BaO | 0.02 | | 0.003 | 0.02 | |
| SrO | 0.02 | | 0.028 | 0.04 | |
| Li2O** | 0.00006 | | 0.095 | 0.023 | 0.08 |
| Na2O | 11.71 | 11.69 | 1.6 | 0.31 | 1.40 |
| K2O | 0.06 | | 12.4 | 15.17 | 13.20 |
| Rb2O | 0.04 | | 2.06 | 2.22 | 2.30 |
| Cs2O | 0.00 | | 0.136 | 0.11 | 0.20 |
| P2O5 | 0.17 | 0.42 | 0.47 | 0.45 | 0.42 |
| B2O3** | 0.0013 | | 0.0016 | | |
| BeO** | 0.00063 | | 0.0010 | | |
| H2O+ | | | | | |
| H2O- | | | | | |
| F | | | | | |
| Sc2O3 | | | | | |
| SnO2 | | | | | |
| Nb2O5 | | | | | |
| Ta2O5 | | | | | |
| UO2 | | | | | |
| PbO | 0.01 | | | 0.01 | |
| WO3 | | | | | |
| ZnO | | | | | |
| ZrO2 | | | | | |
| HfO2 | | | | | |
| Tl2O | | | 0.025* | | 0.024 |
| Ga2O3 | | 0.009 | 0.008* | | 0.009 |
| Sb2O3 | | | | | |
| Totals (%) | 100.07 | 99.99 | 16.82 | 100.19 | 100.25 |

-all values in wt.%

*unpublished data from P. Cerny

** Left justified values collected by SIMS. K-feldspar values represent average of 2 data points. Albite values represent average of 4 data points.

**Appendix II: Average mineral compositions in zone 60**

| Mineral Analysis | Albite EMPA** Brown (2001) | Albite Stilling (1998) | K-feldspar ICP/AA Brown (2001) | K-feldspar EMPA** Brown (2001) | K-feldspar Stilling (1998) |
|---|---|---|---|---|---|
| Mode | | 20.0% | | | 50.0% |
| n | 14 | | 14 | 9 | |
| SiO2 | 68.31 | 67.64 | | 63.05 | 63.74 |
| Al2O3 | 19.69 | 19.97 | | 18.29 | 18.70 |
| TiO2 | | | | | |
| Fe2O3 | 0.01 | | | 0.01 | |
| FeO | | | | | |
| MnO | 0.01 | | | 0.01 | |
| MgO | 0.00 | | | 0.00 | |
| CaO | 0.06 | 0.21 | 0.094 | 0.00 | 0.10 |
| BaO | 0.02 | | 0.008 | 0.02 | |
| SrO | 0.02 | | 0.022 | 0.04 | |
| Li2O** | 0.00005 | | 0.050 | 0.026 | 0.06 |
| Na2O | 11.74 | 11.69 | 1.2 | 0.31 | 1.10 |
| K2O | 0.07 | | 13.1 | 14.97 | 13.80 |
| Rb2O | 0.05 | | 2.66 | 2.47 | 2.20 |
| Cs2O | 0.00 | | 0.267 | 0.30 | 0.24 |
| P2O5 | 0.14 | 0.48 | 0.36 | 0.31 | 0.52 |
| B2O3** | 0.0015 | | | 0.0024 | |
| BeO** | 0.00067 | | | 0.00058 | |
| H2O+ | | | | | |
| H2O- | | | | | |
| F | | | | | |
| Sc2O3 | | | | | |
| SnO2 | | | | | |
| Nb2O5 | | | | | |
| Ta2O5 | | | | | |
| UO2 | | | | | |
| PbO | 0.01 | | | 0.01 | |
| WO3 | | | | | |
| ZnO | | | | | |
| ZrO2 | | | | | |
| HfO2 | | | | | |
| Tl2O | | | 0.020* | | 0.02 |
| Ga2O3 | | 0.009 | 0.009* | | 0.011 |
| Sb2O3 | | | | | |
| Totals (%) | 100.12 | 100.00 | 17.73 | 99.82 | 100.49 |

-all values in wt.%

*unpublished data from P. Cerny

** Left justified values collected by SIMS. K-feldspar values represent average of 2 data points. Albite values represent average of 4 data points.

**Appendix II: Average mineral compositions in zone 70**

| Mineral | Albite | Albite | K-feldspar | K-feldspar | K-feldspar |
|---|---|---|---|---|---|
| Analysis | EMPA | | ICP/AA | EMPA | |
| | Brown (2001) | Stilling (1998) | Brown (2001) | Brown (2001) | Stilling (1998) |
| Mode | | 0.1% | | | 2.0% |
| n | 2 | | 0 | 0 | |
| SiO2 | 68.38 | 68.47 | | | 63.95 |
| Al2O3 | 19.51 | 19.62 | | | 18.60 |
| TiO2 | | | | | |
| Fe2O3 | 0.03 | | | | |
| FeO | | | | | |
| MnO | 0.01 | | | | |
| MgO | 0.00 | | | | |
| CaO | 0.06 | 0.21 | | | 0.07 |
| BaO | 0.02 | | | | |
| SrO | 0.02 | | | | |
| Li2O | | | | | 0.08 |
| Na2O | 11.73 | 11.69 | | | 1.40 |
| K2O | 0.06 | | | | 13.20 |
| Rb2O | 0.05 | | | | 2.30 |
| Cs2O | 0.01 | | | | 0.20 |
| P2O5 | 0.11 | | | | 0.42 |
| B2O3 | | | | | |
| BeO | | | | | |
| H2O+ | | | | | |
| H2O- | | | | | |
| F | | | | | |
| Sc2O3 | | | | | |
| SnO2 | | | | | |
| Nb2O5 | | | | | |
| Ta2O5 | | | | | |
| UO2 | | | | | |
| PbO | 0.00 | | | | |
| WO3 | | | | | |
| ZnO | | | | | |
| ZrO2 | | | | | |
| HfO2 | | | | | |
| Tl2O | | | | | 0.02 |
| Ga2O3 | | 0.009 | | | 0.01 |
| Sb2O3 | | | | | |
| Totals (%) | 99.99 | 100.00 | | | 100.25 |

-all values in wt.%

**Appendix II: Average mineral compositions in zone 80**

| Mineral | Albite | Albite | K-feldspar | K-feldspar | K-feldspar |
|---|---|---|---|---|---|
| Analysis | EMPA** | | ICP/AA | EMPA** | |
| | Brown (2001) | Stilling (1998) | Brown (2001) | Brown (2001) | Stilling (1998) |
| Mode | | 5.0% | | | 2.5% |
| n | 6 | | 3 | 3 | |
| SiO2 | 68.38 | 67.64 | | 62.54 | 63.95 |
| Al2O3 | 19.58 | 19.97 | | 18.27 | 18.60 |
| TiO2 | | | | | |
| Fe2O3 | 0.01 | | | 0.00 | |
| FeO | | | | | |
| MnO | 0.00 | | | 0.01 | |
| MgO | 0.00 | | | 0.00 | |
| CaO | 0.05 | 0.21 | 0.078 | 0.00 | 0.07 |
| BaO | 0.02 | | 0.017 | 0.02 | |
| SrO | 0.03 | | 0.026 | 0.04 | |
| Li2O** | 0.00027 | | 0.052 | 0.045 | 0.08 |
| Na2O | 11.64 | 11.69 | 1.1 | 0.22 | 1.40 |
| K2O | 0.07 | | 12.7 | 14.98 | 13.20 |
| Rb2O | 0.05 | | 3.09 | 2.59 | 2.30 |
| Cs2O | 0.00 | | 0.287 | 0.27 | 0.20 |
| P2O5 | 0.14 | 0.48 | 0.44 | 0.30 | 0.42 |
| B2O3** | 0.00048 | | | 0.0024 | |
| BeO** | 0.00023 | | | 0.00086 | |
| H2O+ | | | | | |
| H2O- | | | | | |
| F | | | | | |
| Sc2O3 | | | | | |
| SnO2 | | | | | |
| Nb2O5 | | | | | |
| Ta2O5 | | | | | |
| UO2 | | | | | |
| PbO | 0.01 | | | 0.00 | |
| WO3 | | | | | |
| ZnO | | | | | |
| ZrO2 | | | | | |
| HfO2 | | | | | |
| Tl2O | | | 0.012* | | 0.024 |
| Ga2O3 | | 0.009 | 0.001* | | 0.009 |
| Sb2O3 | | | | | |
| Totals (%) | 99.99 | 100.00 | 17.80 | 99.28 | 100.25 |

-all values in wt.%

*unpublished data from P. Cerny

** Left justified values collected by SIMS. Each value represents average of 2 data points.

**Appendix II: Average mineral compositions in zone 90**

| Mineral | Albite | Albite | K-feldspar | K-feldspar | K-feldspar |
|---|---|---|---|---|---|
| Analysis | EMPA** | | ICP/AA | EMPA** | |
| | Brown (2001) | Stilling (1998) | Brown (2001) | Brown (2001) | Stilling (1998) |
| Mode | | 8.0% | | | 10.0% |
| n | 2 | | 5 | 7 | |
| SiO2 | 68.57 | 67.64 | | 63.11 | 63.74 |
| Al2O3 | 19.40 | 19.97 | | 18.31 | 18.70 |
| TiO2 | | | | | |
| Fe2O3 | 0.01 | | | 0.01 | |
| FeO | | | | | |
| MnO | 0.01 | | | 0.00 | |
| MgO | 0.00 | | | 0.00 | |
| CaO | 0.05 | 0.21 | 0.130 | 0.00 | 0.10 |
| BaO | 0.00 | | 0.006 | 0.02 | |
| SrO | 0.02 | | 0.021 | 0.04 | |
| Li2O** | 0.00023 | | 0.059 | 0.0089 | 0.06 |
| Na2O | 11.82 | 11.69 | 1.4 | 0.27 | 1.10 |
| K2O | 0.06 | | 12.5 | 15.20 | 13.80 |
| Rb2O | 0.05 | | 2.64 | 2.42 | 2.20 |
| Cs2O | 0.00 | | 0.247 | 0.24 | 0.24 |
| P2O5 | 0.11 | 0.48 | 0.38 | 0.28 | 0.52 |
| B2O3** | 0.0026 | | | 0.00037 | |
| BeO** | 0.0014 | | | 0.00002 | |
| H2O+ | | | | | |
| H2O- | | | | | |
| F | | | | | |
| Sc2O3 | | | | | |
| SnO2 | | | | | |
| Nb2O5 | | | | | |
| Ta2O5 | | | | | |
| UO2 | | | | | |
| PbO | 0.00 | | | 0.01 | |
| WO3 | | | | | |
| ZnO | | | | | |
| ZrO2 | | | | | |
| HfO2 | | | | | |
| Tl2O | | | | | 0.02 |
| Ga2O3 | | 0.009 | 0.010 | | 0.011 |
| Sb2O3 | | | | | |
| Totals (%) | 100.11 | 100.00 | 17.44 | 99.90 | 100.49 |

-all values in wt.%

*unpublished data from P. Cerny

** Left justified values collected by SIMS. Each value represents average of 2 data points.

**Appendix III**: K-feldspar sample compostions (EMPA data)

| Sample | 94-10-R | TAN-3 | SLE-18 | SLE-19 | SLW-0A | SLW-0D | SLW-1B |
|---|---|---|---|---|---|---|---|
| Zone | 10 | 10 | 12 | 12 | 12 | 12 | 12 |
| Type | 1 | 1 | 1 | 1 | 1 | 1 | 1 |
| $P_2O_5$ | 0.31 | 0.19 | 0.22 | 0.20 | 0.42 | 0.34 | 0.18 |
| $SiO_2$ | 63.80 | 63.72 | 64.02 | 63.28 | 63.33 | 63.65 | 63.99 |
| $AL_2O_3$ | 18.44 | 18.17 | 18.37 | 18.43 | 18.39 | 18.49 | 18.31 |
| MGO | 0.00 | 0.00 | 0.00 | 0.00 | 0.00 | 0.00 | 0.00 |
| CAO | 0.00 | 0.00 | 0.00 | 0.00 | 0.00 | 0.00 | 0.00 |
| MNO | 0.00 | 0.01 | 0.00 | 0.00 | 0.00 | 0.00 | 0.00 |
| $FE_2O_3$ | 0.00 | 0.00 | 0.00 | 0.00 | 0.00 | 0.01 | 0.01 |
| SRO | 0.02 | 0.07 | 0.02 | 0.03 | 0.06 | 0.02 | 0.01 |
| BAO | 0.02 | 0.00 | 0.03 | 0.02 | 0.09 | 0.03 | 0.02 |
| PBO | 0.00 | 0.00 | 0.02 | 0.01 | 0.00 | 0.00 | 0.02 |
| $NA_2O$ | 0.27 | 0.16 | 0.19 | 0.18 | 0.35 | 0.38 | 0.28 |
| $K_2O$ | 15.91 | 15.19 | 15.87 | 15.58 | 15.37 | 15.81 | 15.74 |
| $RB_2O$ | 1.29 | 2.65 | 1.56 | 1.83 | 2.28 | 1.25 | 1.50 |
| $CS_2O$ | 0.05 | 0.18 | 0.06 | 0.11 | 0.33 | 0.02 | 0.07 |
| TOTAL | 100.13 | 100.35 | 100.37 | 99.68 | 100.62 | 100.01 | 100.12 |
| $P^{5+}$ | 0.012 | 0.008 | 0.009 | 0.008 | 0.016 | 0.013 | 0.007 |
| $SI^{4+}$ | 2.972 | 2.985 | 2.980 | 2.972 | 2.962 | 2.967 | 2.984 |
| $AL^{3+}$ | 1.013 | 1.003 | 1.008 | 1.020 | 1.014 | 1.016 | 1.006 |
| $MG^{2+}$ | 0.000 | 0.000 | 0.000 | 0.000 | 0.000 | 0.000 | 0.000 |
| $CA^{2+}$ | 0.000 | 0.000 | 0.000 | 0.000 | 0.000 | 0.000 | 0.000 |
| $MN^{2+}$ | 0.000 | 0.000 | 0.000 | 0.000 | 0.000 | 0.000 | 0.000 |
| $FE^{3+}$ | 0.000 | 0.000 | 0.000 | 0.000 | 0.000 | 0.000 | 0.001 |
| $SR^{2+}$ | 0.001 | 0.002 | 0.001 | 0.001 | 0.002 | 0.001 | 0.000 |
| $BA^{2+}$ | 0.000 | 0.000 | 0.000 | 0.000 | 0.002 | 0.000 | 0.001 |
| $PB^{2+}$ | 0.000 | 0.000 | 0.000 | 0.000 | 0.000 | 0.000 | 0.000 |
| $NA^{+}$ | 0.024 | 0.015 | 0.017 | 0.017 | 0.032 | 0.035 | 0.026 |
| $K^{+}$ | 0.946 | 0.908 | 0.943 | 0.934 | 0.917 | 0.940 | 0.937 |
| $RB^{+}$ | 0.039 | 0.080 | 0.047 | 0.055 | 0.068 | 0.037 | 0.045 |
| $CS^{+}$ | 0.001 | 0.004 | 0.001 | 0.002 | 0.006 | 0.000 | 0.001 |
| $\Sigma T$ | 3.997 | 3.996 | 3.997 | 4.000 | 3.992 | 3.996 | 3.997 |
| $TO^{2-}$ | 1.001 | 0.996 | 0.999 | 1.012 | 0.997 | 1.003 | 0.999 |
| Si+2P | 2.997 | 3.000 | 2.998 | 2.988 | 2.994 | 2.994 | 2.998 |
| Si+2P/Al-P | 2.995 | 3.013 | 3.001 | 2.953 | 3.002 | 2.986 | 2.999 |
| $\Sigma M$ | 1.010 | 1.007 | 1.008 | 1.008 | 1.023 | 1.012 | 1.008 |
| $M^{+}$ | 1.012 | 1.010 | 1.011 | 1.010 | 1.031 | 1.015 | 1.009 |
| $M^{*}$ | 0.011 | 0.014 | 0.012 | -0.002 | 0.033 | 0.012 | 0.010 |

Note: $\Sigma T$ = Si+Al+P; $TO^{2-}$ = Al-P
$\Sigma M$ = Na+K+Rb+Cs; $M^{+}$ = 2*(Ca+Sr+Ba)+Na+K+Rb+Cs
$M^{*} = M^{+} - TO^{2-}$

-all compositions are averages of 2-5 analyses

**Appendix III: K-feldspar sample compostions (EMPA data)**

| Sample | SLW-1C | SLW-2A2 | SLW-2B | 12-15-2A | 12-15-2B | 12-15-2C | 12-15-2E |
|---|---|---|---|---|---|---|---|
| Zone | 12 | 12 | 12 | 20 | 20 | 20 | 20 |
| Type | 1 | 1 | 1 | 1 | 1 | 1 | 1 |
| $P_2O_6$ | 0.29 | 0.32 | 0.47 | 0.37 | 0.39 | 0.08 | 0.54 |
| $SiO_2$ | 63.76 | 63.66 | 63.09 | 63.41 | 63.46 | 63.64 | 62.69 |
| $AL_2O_3$ | 18.38 | 18.43 | 18.46 | 18.44 | 18.41 | 18.20 | 18.40 |
| MGO | 0.00 | 0.00 | 0.00 | 0.00 | 0.00 | 0.00 | 0.00 |
| CAO | 0.00 | 0.00 | 0.00 | 0.00 | 0.00 | 0.00 | 0.00 |
| MNO | 0.01 | 0.00 | 0.00 | 0.00 | 0.00 | 0.00 | 0.01 |
| $FE_2O_3$ | 0.00 | 0.00 | 0.00 | 0.00 | 0.00 | 0.00 | 0.00 |
| SRO | 0.03 | 0.03 | 0.03 | 0.05 | 0.03 | 0.03 | 0.04 |
| BAO | 0.01 | 0.00 | 0.03 | 0.02 | 0.02 | 0.04 | 0.00 |
| PBO | 0.01 | 0.00 | 0.00 | 0.00 | 0.03 | 0.00 | 0.00 |
| $NA_2O$ | 0.34 | 0.32 | 0.29 | 0.32 | 0.32 | 0.24 | 0.29 |
| $K_2O$ | 15.86 | 15.84 | 15.49 | 15.58 | 15.48 | 15.38 | 15.17 |
| $RB_2O$ | 1.31 | 1.36 | 1.83 | 1.93 | 1.99 | 2.19 | 2.17 |
| $CS_2O$ | 0.03 | 0.04 | 0.15 | 0.04 | 0.11 | 0.05 | 0.05 |
| TOTAL | 100.03 | 100.01 | 99.85 | 100.17 | 100.23 | 99.85 | 99.35 |
| $P^{5+}$ | 0.011 | 0.013 | 0.019 | 0.014 | 0.015 | 0.003 | 0.021 |
| $Si^{4+}$ | 2.974 | 2.970 | 2.958 | 2.964 | 2.966 | 2.988 | 2.954 |
| $AL^{3+}$ | 1.010 | 1.013 | 1.020 | 1.016 | 1.014 | 1.007 | 1.022 |
| $MG^{2+}$ | 0.000 | 0.000 | 0.000 | 0.000 | 0.000 | 0.000 | 0.000 |
| $CA^{2+}$ | 0.000 | 0.000 | 0.000 | 0.000 | 0.000 | 0.000 | 0.000 |
| $MN^{2+}$ | 0.000 | 0.000 | 0.000 | 0.000 | 0.000 | 0.000 | 0.000 |
| $FE^{3+}$ | 0.000 | 0.000 | 0.000 | 0.000 | 0.000 | 0.000 | 0.000 |
| $SR^{2+}$ | 0.001 | 0.001 | 0.001 | 0.002 | 0.001 | 0.001 | 0.001 |
| $BA^{2+}$ | 0.000 | 0.000 | 0.001 | 0.000 | 0.000 | 0.001 | 0.000 |
| $PB^{2+}$ | 0.000 | 0.000 | 0.000 | 0.000 | 0.000 | 0.000 | 0.000 |
| $NA^{+}$ | 0.031 | 0.029 | 0.027 | 0.029 | 0.029 | 0.022 | 0.026 |
| $K^{+}$ | 0.944 | 0.943 | 0.927 | 0.929 | 0.923 | 0.921 | 0.912 |
| $RB^{+}$ | 0.040 | 0.041 | 0.055 | 0.058 | 0.060 | 0.066 | 0.065 |
| $CS^{+}$ | 0.001 | 0.001 | 0.003 | 0.001 | 0.002 | 0.001 | 0.001 |
| $\Sigma T$ | 3.995 | 3.996 | 3.997 | 3.995 | 3.995 | 3.998 | 3.998 |
| $TO^{2-}$ | 0.999 | 1.001 | 1.002 | 1.002 | 0.999 | 1.003 | 1.001 |
| Si+2P | 2.996 | 2.996 | 2.996 | 2.993 | 2.996 | 2.994 | 2.997 |
| Si+2P/Al-P | 2.999 | 2.994 | 2.991 | 2.988 | 2.999 | 2.984 | 2.995 |
| $\Sigma M$ | 1.015 | 1.014 | 1.012 | 1.017 | 1.014 | 1.011 | 1.005 |
| $M^{+}$ | 1.016 | 1.016 | 1.015 | 1.021 | 1.017 | 1.014 | 1.008 |
| $M^{*}$ | 0.017 | 0.015 | 0.013 | 0.019 | 0.018 | 0.011 | 0.007 |

**Note:**

**Appendix III**: K-feldspar sample compostions (EMPA data)

| Sample | 76-05-A | 76-23-N | 76-23-O | 78-21-G | 78-21-H | 94-10-B | C-045-V |
|---|---|---|---|---|---|---|---|
| Zone | 20 | 20 | 20 | 20 | 20 | 20 | 20 |
| Type | 1 | 1 | 1 | 1 | 1 | 1 | 1 |
| $P_2O_5$ | 0.32 | 0.33 | 0.30 | 0.34 | 0.34 | 0.36 | 0.41 |
| $SIO_2$ | 63.93 | 63.90 | 63.66 | 64.08 | 64.11 | 63.65 | 63.65 |
| $AL_2O_3$ | 18.29 | 18.43 | 18.36 | 18.29 | 18.46 | 18.44 | 18.45 |
| MGO | 0.00 | 0.00 | 0.00 | 0.00 | 0.00 | 0.00 | 0.00 |
| CAO | 0.00 | 0.00 | 0.00 | 0.00 | 0.00 | 0.00 | 0.00 |
| MNO | 0.00 | 0.00 | 0.00 | 0.00 | 0.01 | 0.00 | 0.00 |
| $FE_2O_3$ | 0.01 | 0.02 | 0.01 | 0.00 | 0.01 | 0.00 | 0.01 |
| SRO | 0.02 | 0.06 | 0.04 | 0.05 | 0.03 | 0.03 | 0.04 |
| BAO | 0.01 | 0.00 | 0.00 | 0.08 | 0.00 | 0.03 | 0.02 |
| PBO | 0.03 | 0.00 | 0.01 | 0.02 | 0.01 | 0.00 | 0.00 |
| $NA_2O$ | 0.37 | 0.40 | 0.30 | 0.32 | 0.56 | 0.37 | 0.71 |
| $K_2O$ | 15.74 | 15.89 | 15.95 | 16.04 | 15.72 | 15.57 | 15.24 |
| $RB_2O$ | 1.24 | 0.90 | 0.98 | 0.73 | 0.76 | 1.49 | 1.29 |
| $CS_2O$ | 0.02 | 0.00 | 0.04 | 0.01 | 0.00 | 0.04 | 0.06 |
| TOTAL | 99.97 | 99.93 | 99.65 | 99.94 | 100.01 | 99.99 | 99.89 |
| $P^{5+}$ | 0.012 | 0.013 | 0.012 | 0.013 | 0.014 | 0.014 | 0.016 |
| $SI^{4+}$ | 2.979 | 2.973 | 2.974 | 2.980 | 2.975 | 2.969 | 2.966 |
| $AL^{3+}$ | 1.004 | 1.011 | 1.011 | 1.003 | 1.009 | 1.014 | 1.013 |
| $MG^{2+}$ | 0.000 | 0.000 | 0.000 | 0.000 | 0.000 | 0.000 | 0.000 |
| $CA^{2+}$ | 0.000 | 0.000 | 0.000 | 0.000 | 0.000 | 0.000 | 0.000 |
| $MN^{2+}$ | 0.000 | 0.000 | 0.000 | 0.000 | 0.000 | 0.000 | 0.000 |
| $FE^{3+}$ | 0.000 | 0.000 | 0.000 | 0.000 | 0.000 | 0.000 | 0.000 |
| $SR^{2+}$ | 0.001 | 0.002 | 0.001 | 0.001 | 0.001 | 0.001 | 0.001 |
| $BA^{2+}$ | 0.000 | 0.000 | 0.000 | 0.002 | 0.000 | 0.000 | 0.000 |
| $PB^{2+}$ | 0.000 | 0.000 | 0.000 | 0.000 | 0.000 | 0.000 | 0.000 |
| $NA^{+}$ | 0.034 | 0.036 | 0.028 | 0.029 | 0.051 | 0.033 | 0.064 |
| $K^{+}$ | 0.935 | 0.943 | 0.951 | 0.952 | 0.931 | 0.927 | 0.906 |
| $RB^{+}$ | 0.037 | 0.027 | 0.030 | 0.022 | 0.023 | 0.045 | 0.039 |
| $CS^{+}$ | 0.001 | 0.000 | 0.001 | 0.000 | 0.000 | 0.001 | 0.001 |
| $\Sigma T$ | 3.995 | 3.996 | 3.996 | 3.995 | 3.997 | 3.997 | 3.996 |
| $TO^{2-}$ | 0.992 | 0.998 | 0.999 | 0.990 | 0.996 | 1.000 | 0.997 |
| Si+2P | 3.003 | 2.998 | 2.997 | 3.006 | 3.002 | 2.997 | 2.999 |
| Si+2P/Al-P | 3.028 | 3.003 | 2.999 | 3.037 | 3.014 | 2.997 | 3.008 |
| $\Sigma M$ | 1.007 | 1.006 | 1.009 | 1.002 | 1.004 | 1.005 | 1.011 |
| $M^{+}$ | 1.009 | 1.009 | 1.012 | 1.007 | 1.006 | 1.008 | 1.014 |
| $M^{*}$ | 0.017 | 0.011 | 0.013 | 0.017 | 0.010 | 0.008 | 0.017 |

**Note:**

**Appendix III:** K-feldspar sample compostions (EMPA data)

| Sample | C-090-B | C-096-A | L-12-E | L-12-F | 76-05-G | 76-23-B | 86-07-T |
|---|---|---|---|---|---|---|---|
| Zone | 20 | 20 | 20 | 20 | 40 | 40 | 40 |
| Type | 1 | 1 | 1 | 1 | 1 | 1 | 1 |
| $P_2O_5$ | 0.42 | 0.24 | 0.33 | 0.35 | 0.43 | 0.33 | 0.41 |
| $SiO_2$ | 62.85 | 63.42 | 63.83 | 64.07 | 63.70 | 64.10 | 63.19 |
| $AL_2O_3$ | 18.23 | 18.17 | 18.40 | 18.47 | 18.65 | 18.62 | 18.48 |
| MGO | 0.00 | 0.00 | 0.00 | 0.00 | 0.00 | 0.01 | 0.00 |
| CAO | 0.00 | 0.00 | 0.00 | 0.00 | 0.00 | 0.00 | 0.00 |
| MNO | 0.00 | 0.01 | 0.00 | 0.00 | 0.00 | 0.01 | 0.01 |
| $FE_2O_3$ | 0.01 | 0.00 | 0.01 | 0.00 | 0.02 | 0.00 | 0.01 |
| SRO | 0.08 | 0.03 | 0.03 | 0.04 | 0.03 | 0.02 | 0.05 |
| BAO | 0.00 | 0.03 | 0.03 | 0.01 | 0.02 | 0.02 | 0.05 |
| PBO | 0.00 | 0.00 | 0.00 | 0.00 | 0.00 | 0.01 | 0.01 |
| $NA_2O$ | 0.28 | 0.27 | 0.35 | 0.36 | 0.36 | 0.29 | 0.32 |
| $K_2O$ | 15.02 | 15.48 | 15.83 | 15.73 | 15.41 | 15.97 | 15.24 |
| $RB_2O$ | 2.54 | 1.84 | 0.91 | 1.25 | 1.81 | 1.04 | 1.95 |
| $CS_2O$ | 0.16 | 0.15 | 0.05 | 0.03 | 0.03 | 0.01 | 0.08 |
| TOTAL | 99.56 | 99.66 | 99.76 | 100.31 | 100.46 | 100.39 | 99.80 |
| $P^{5+}$ | 0.017 | 0.010 | 0.013 | 0.014 | 0.017 | 0.013 | 0.016 |
| $SI^{4+}$ | 2.966 | 2.979 | 2.975 | 2.974 | 2.961 | 2.971 | 2.962 |
| $AL^{3+}$ | 1.014 | 1.007 | 1.011 | 1.010 | 1.022 | 1.017 | 1.021 |
| $MG^{2+}$ | 0.000 | 0.000 | 0.000 | 0.000 | 0.000 | 0.001 | 0.000 |
| $CA^{2+}$ | 0.000 | 0.000 | 0.000 | 0.000 | 0.000 | 0.000 | 0.000 |
| $MN^{2+}$ | 0.000 | 0.001 | 0.000 | 0.000 | 0.000 | 0.000 | 0.000 |
| $FE^{3+}$ | 0.000 | 0.000 | 0.000 | 0.000 | 0.000 | 0.000 | 0.000 |
| $SR^{2+}$ | 0.002 | 0.001 | 0.001 | 0.001 | 0.001 | 0.001 | 0.001 |
| $BA^{2+}$ | 0.000 | 0.000 | 0.001 | 0.000 | 0.000 | 0.001 | 0.001 |
| $PB^{2+}$ | 0.000 | 0.000 | 0.000 | 0.000 | 0.000 | 0.000 | 0.000 |
| $NA^{+}$ | 0.026 | 0.025 | 0.031 | 0.033 | 0.033 | 0.026 | 0.029 |
| $K^{+}$ | 0.904 | 0.928 | 0.941 | 0.931 | 0.914 | 0.944 | 0.912 |
| $RB^{+}$ | 0.077 | 0.056 | 0.027 | 0.037 | 0.054 | 0.031 | 0.059 |
| $CS^{+}$ | 0.004 | 0.003 | 0.001 | 0.000 | 0.001 | 0.000 | 0.001 |
| $\Sigma T$ | 3.996 | 3.996 | 3.999 | 3.998 | 4.000 | 4.000 | 3.999 |
| $TO^{2-}$ | 0.997 | 0.997 | 0.998 | 0.997 | 1.005 | 1.004 | 1.004 |
| Si+2P | 2.999 | 2.999 | 3.001 | 3.001 | 2.995 | 2.997 | 2.995 |
| Si+2P/Al-P | 3.008 | 3.008 | 3.008 | 3.011 | 2.978 | 2.986 | 2.982 |
| $\Sigma M$ | 1.010 | 1.011 | 1.000 | 1.002 | 1.001 | 1.000 | 1.000 |
| $M^{+}$ | 1.014 | 1.014 | 1.004 | 1.005 | 1.004 | 1.003 | 1.005 |
| $M^{*}$ | 0.016 | 0.017 | 0.006 | 0.008 | -0.002 | 0.000 | 0.001 |

**Note:**

**Appendix III**: K-feldspar sample compostions (EMPA data)

| **Sample** | 92-11-L | 94-10-K | C-022-V | C-033-H | C-045-Q | C-107-E | **AD-88-J** |
|---|---|---|---|---|---|---|---|
| **Zone** | 40 | 40 | 40 | 40 | 40 | 40 | 40 |
| **Type** | 1 | 1 | 1 | 1 | 1 | 1 | 6 |
| $P_2O_5$ | 0.55 | 0.33 | 0.57 | 0.41 | 0.45 | 0.47 | 0.00 |
| $SiO_2$ | 62.61 | 64.03 | 63.34 | 63.41 | 63.66 | 62.79 | 65.24 |
| $AL_2O_3$ | 18.48 | 18.65 | 18.70 | 18.46 | 18.55 | 18.52 | 17.92 |
| MGO | 0.00 | 0.00 | 0.00 | 0.00 | 0.00 | 0.00 | 0.00 |
| CAO | 0.00 | 0.00 | 0.00 | 0.00 | 0.00 | 0.00 | 0.00 |
| MNO | 0.02 | 0.00 | 0.00 | 0.00 | 0.01 | 0.00 | 0.01 |
| $FE_2O_3$ | 0.01 | 0.00 | 0.01 | 0.00 | 0.02 | 0.02 | 0.00 |
| SRO | 0.02 | 0.05 | 0.04 | 0.04 | 0.03 | 0.03 | 0.03 |
| BAO | 0.04 | 0.00 | 0.03 | 0.03 | 0.01 | 0.01 | 0.10 |
| PBO | 0.00 | 0.01 | 0.00 | 0.02 | 0.01 | 0.00 | 0.00 |
| $NA_2O$ | 0.44 | 0.43 | 0.40 | 0.43 | 0.32 | 0.19 | 0.03 |
| $K_2O$ | 14.66 | 15.70 | 14.99 | 14.63 | 15.34 | 15.12 | 16.78 |
| $RB_2O$ | 2.78 | 1.11 | 2.40 | 2.61 | 2.24 | 2.51 | 0.00 |
| $CS_2O$ | 0.10 | 0.02 | 0.10 | 0.30 | 0.11 | 0.14 | 0.00 |
| **TOTAL** | 99.71 | 100.31 | 100.58 | 100.34 | 100.74 | 99.80 | 100.09 |
| $P^{5+}$ | 0.022 | 0.013 | 0.023 | 0.016 | 0.018 | 0.019 | 0.000 |
| $SI^{4+}$ | 2.950 | 2.969 | 2.950 | 2.966 | 2.962 | 2.954 | 3.018 |
| $AL^{3+}$ | 1.026 | 1.019 | 1.027 | 1.018 | 1.017 | 1.027 | 0.977 |
| $MG^{2+}$ | 0.000 | 0.000 | 0.000 | 0.000 | 0.000 | 0.000 | 0.000 |
| $CA^{2+}$ | 0.000 | 0.000 | 0.000 | 0.000 | 0.000 | 0.000 | 0.000 |
| $MN^{2+}$ | 0.001 | 0.000 | 0.000 | 0.000 | 0.000 | 0.000 | 0.000 |
| $FE^{3+}$ | 0.000 | 0.000 | 0.000 | 0.000 | 0.001 | 0.001 | 0.000 |
| $SR^{2+}$ | 0.001 | 0.001 | 0.001 | 0.001 | 0.001 | 0.001 | 0.001 |
| $BA^{2+}$ | 0.001 | 0.000 | 0.001 | 0.000 | 0.000 | 0.000 | 0.002 |
| $PB^{2+}$ | 0.000 | 0.000 | 0.000 | 0.000 | 0.000 | 0.000 | 0.000 |
| $NA^{+}$ | 0.040 | 0.038 | 0.036 | 0.039 | 0.029 | 0.017 | 0.003 |
| $K^{+}$ | 0.881 | 0.929 | 0.891 | 0.873 | 0.911 | 0.907 | 0.991 |
| $RB^{+}$ | 0.084 | 0.033 | 0.072 | 0.078 | 0.067 | 0.076 | 0.000 |
| $CS^{+}$ | 0.002 | 0.001 | 0.002 | 0.006 | 0.002 | 0.003 | 0.000 |
| $\Sigma T$ | 3.998 | 4.001 | 4.000 | 4.000 | 3.997 | 4.000 | 3.995 |
| $TO^{2-}$ | 1.005 | 1.006 | 1.004 | 1.001 | 1.000 | 1.008 | 0.977 |
| Si+2P | 2.993 | 2.995 | 2.996 | 2.999 | 2.997 | 2.992 | 3.018 |
| Si+2P/Al-P | 2.979 | 2.977 | 2.984 | 2.995 | 2.996 | 2.966 | 3.089 |
| $\Sigma M$ | 1.007 | 1.001 | 1.000 | 0.996 | 1.008 | 1.003 | 0.993 |
| $M^{+}$ | 1.010 | 1.003 | 1.004 | 1.000 | 1.010 | 1.005 | 0.997 |
| $M^{*}$ | 0.005 | -0.004 | 0.000 | -0.002 | 0.010 | -0.004 | 0.020 |

**Note:**

**Appendix III**: K-feldspar sample compostions (EMPA data)

| Sample | 95-08-K | C-045-Ha | 10-25-4 | 10-25-3a | 10-25-3b | 10-25-3c | 10-25-3d |
|---|---|---|---|---|---|---|---|
| Zone | 45 | 45 | 47 | 50 | 50 | 50 | 50 |
| Type | 1 | 1 | 1 | 1 | 1 | 1 | 1 |
| $P_2O_5$ | 0.57 | 0.38 | 0.52 | 0.46 | 0.52 | 0.53 | 0.53 |
| $SiO_2$ | 62.51 | 63.56 | 62.90 | 62.71 | 63.66 | 63.20 | 63.96 |
| $AL_2O_3$ | 18.47 | 18.47 | 18.47 | 18.81 | 18.62 | 18.55 | 18.48 |
| MGO | 0.00 | 0.00 | 0.00 | 0.00 | 0.00 | 0.00 | 0.00 |
| CAO | 0.00 | 0.00 | 0.00 | 0.00 | 0.00 | 0.00 | 0.00 |
| MNO | 0.01 | 0.00 | 0.00 | 0.00 | 0.01 | 0.02 | 0.01 |
| $FE_2O_3$ | 0.00 | 0.00 | 0.00 | 0.01 | 0.01 | 0.01 | 0.01 |
| SRO | 0.02 | 0.03 | 0.06 | 0.02 | 0.05 | 0.03 | 0.03 |
| BAO | 0.04 | 0.00 | 0.05 | 0.01 | 0.00 | 0.03 | 0.04 |
| PBO | 0.00 | 0.00 | 0.02 | 0.01 | 0.01 | 0.01 | 0.00 |
| $NA_2O$ | 0.33 | 0.42 | 0.30 | 0.25 | 0.30 | 0.46 | 0.26 |
| $K_2O$ | 15.02 | 15.41 | 14.72 | 15.27 | 15.02 | 14.90 | 15.16 |
| $RB_2O$ | 2.40 | 1.77 | 2.90 | 2.23 | 2.21 | 2.11 | 2.32 |
| $CS_2O$ | 0.07 | 0.05 | 0.15 | 0.09 | 0.17 | 0.08 | 0.09 |
| TOTAL | 99.44 | 100.09 | 100.09 | 99.87 | 100.58 | 99.92 | 100.86 |
| $P^{5+}$ | 0.023 | 0.015 | 0.020 | 0.018 | 0.021 | 0.021 | 0.021 |
| $SI^{4+}$ | 2.949 | 2.967 | 2.955 | 2.944 | 2.961 | 2.957 | 2.968 |
| $AL^{3+}$ | 1.027 | 1.016 | 1.023 | 1.041 | 1.020 | 1.023 | 1.010 |
| $MG^{2+}$ | 0.000 | 0.000 | 0.000 | 0.000 | 0.000 | 0.000 | 0.000 |
| $CA^{2+}$ | 0.000 | 0.000 | 0.000 | 0.000 | 0.000 | 0.000 | 0.000 |
| $MN^{2+}$ | 0.000 | 0.000 | 0.000 | 0.000 | 0.000 | 0.001 | 0.001 |
| $FE^{3+}$ | 0.000 | 0.000 | 0.000 | 0.000 | 0.000 | 0.000 | 0.000 |
| $SR^{2+}$ | 0.001 | 0.001 | 0.002 | 0.001 | 0.002 | 0.001 | 0.001 |
| $BA^{2+}$ | 0.001 | 0.000 | 0.001 | 0.000 | 0.000 | 0.001 | 0.001 |
| $PB^{2+}$ | 0.000 | 0.000 | 0.000 | 0.000 | 0.000 | 0.000 | 0.000 |
| $NA^{+}$ | 0.030 | 0.038 | 0.028 | 0.023 | 0.027 | 0.042 | 0.023 |
| $K^{+}$ | 0.904 | 0.917 | 0.882 | 0.915 | 0.891 | 0.889 | 0.897 |
| $RB^{+}$ | 0.073 | 0.053 | 0.088 | 0.067 | 0.066 | 0.063 | 0.069 |
| $CS^{+}$ | 0.001 | 0.001 | 0.003 | 0.002 | 0.003 | 0.002 | 0.002 |
| $\Sigma T$ | 3.999 | 3.998 | 3.999 | 4.003 | 4.002 | 4.000 | 3.998 |
| $TO^{2-}$ | 1.004 | 1.001 | 1.003 | 1.023 | 1.000 | 1.002 | 0.990 |
| Si+2P | 2.995 | 2.997 | 2.996 | 2.980 | 3.002 | 2.998 | 3.009 |
| Si+2P/Al-P | 2.983 | 2.993 | 2.988 | 2.913 | 3.002 | 2.990 | 3.040 |
| $\Sigma M$ | 1.008 | 1.009 | 1.000 | 1.007 | 0.987 | 0.995 | 0.991 |
| $M^{+}$ | 1.011 | 1.011 | 1.006 | 1.009 | 0.990 | 0.999 | 0.993 |
| $M^{*}$ | 0.007 | 0.009 | 0.003 | -0.014 | -0.010 | -0.003 | 0.003 |

**Note:**

**Appendix III:** K-feldspar sample compostions (EMPA data)

| Sample | 10-25-3e | 12-15-1A | 12-15-1AB | 12-15-1D | 86-07-C | 94-10-G | B-06-C |
|---|---|---|---|---|---|---|---|
| Zone | 50 | 50 | 50 | 50 | 50 | 50 | 50 |
| Type | 1 | 1 | 1 | 1 | 1 | 1 | 1 |
| $P_2O_5$ | 0.41 | 0.31 | 0.36 | 0.40 | 0.50 | 0.53 | 0.53 |
| $SiO_2$ | 62.98 | 64.34 | 62.86 | 63.42 | 62.50 | 63.27 | 63.17 |
| $AL_2O_3$ | 18.65 | 18.53 | 18.80 | 18.51 | 18.47 | 18.47 | 18.39 |
| MGO | 0.00 | 0.00 | 0.00 | 0.00 | 0.00 | 0.00 | 0.00 |
| CAO | 0.00 | 0.01 | 0.00 | 0.01 | 0.00 | 0.00 | 0.00 |
| MNO | 0.01 | 0.00 | 0.01 | 0.01 | 0.00 | 0.00 | 0.01 |
| $FE_2O_3$ | 0.01 | 0.01 | 0.00 | 0.01 | 0.01 | 0.01 | 0.01 |
| SRO | 0.04 | 0.04 | 0.05 | 0.03 | 0.03 | 0.02 | 0.04 |
| BAO | 0.03 | 0.01 | 0.03 | 0.02 | 0.00 | 0.01 | 0.01 |
| PBO | 0.01 | 0.01 | 0.00 | 0.00 | 0.00 | 0.00 | 0.01 |
| $NA_2O$ | 0.23 | 0.21 | 0.37 | 0.41 | 0.29 | 0.26 | 0.43 |
| $K_2O$ | 14.83 | 15.54 | 15.34 | 15.47 | 14.58 | 15.34 | 15.00 |
| $RB_2O$ | 2.98 | 1.77 | 1.74 | 1.64 | 3.19 | 2.29 | 2.32 |
| $CS_2O$ | 0.18 | 0.08 | 0.05 | 0.05 | 0.22 | 0.10 | 0.10 |
| TOTAL | 100.35 | 100.85 | 99.63 | 99.98 | 99.80 | 100.30 | 100.01 |
| $P^{5+}$ | 0.016 | 0.012 | 0.014 | 0.016 | 0.020 | 0.021 | 0.021 |
| $SI^{4+}$ | 2.954 | 2.978 | 2.950 | 2.963 | 2.952 | 2.958 | 2.959 |
| $AL^{3+}$ | 1.031 | 1.011 | 1.040 | 1.019 | 1.028 | 1.017 | 1.015 |
| $MG^{2+}$ | 0.000 | 0.000 | 0.000 | 0.000 | 0.000 | 0.000 | 0.000 |
| $CA^{2+}$ | 0.000 | 0.001 | 0.000 | 0.000 | 0.000 | 0.000 | 0.000 |
| $MN^{2+}$ | 0.000 | 0.000 | 0.000 | 0.000 | 0.000 | 0.000 | 0.000 |
| $FE^{3+}$ | 0.001 | 0.000 | 0.000 | 0.000 | 0.000 | 0.000 | 0.000 |
| $SR^{2+}$ | 0.001 | 0.002 | 0.001 | 0.001 | 0.001 | 0.001 | 0.001 |
| $BA^{2+}$ | 0.001 | 0.000 | 0.001 | 0.000 | 0.000 | 0.000 | 0.000 |
| $PB^{2+}$ | 0.000 | 0.000 | 0.000 | 0.000 | 0.000 | 0.000 | 0.000 |
| $NA^{+}$ | 0.021 | 0.019 | 0.034 | 0.038 | 0.027 | 0.024 | 0.039 |
| $K^{+}$ | 0.888 | 0.917 | 0.919 | 0.922 | 0.879 | 0.915 | 0.897 |
| $RB^{+}$ | 0.090 | 0.053 | 0.053 | 0.049 | 0.097 | 0.069 | 0.070 |
| $CS^{+}$ | 0.004 | 0.002 | 0.001 | 0.001 | 0.004 | 0.002 | 0.002 |
| $\Sigma T$ | 4.001 | 4.001 | 4.004 | 3.998 | 4.000 | 3.996 | 3.996 |
| $TO^{2-}$ | 1.015 | 0.999 | 1.026 | 1.004 | 1.008 | 0.997 | 0.994 |
| Si+2P | 2.986 | 3.002 | 2.978 | 2.994 | 2.992 | 2.999 | 3.001 |
| Si+2P/Al-P | 2.940 | 3.005 | 2.904 | 2.982 | 2.967 | 3.008 | 3.017 |
| $\Sigma M$ | 1.003 | 0.990 | 1.006 | 1.010 | 1.006 | 1.010 | 1.008 |
| $M^{+}$ | 1.006 | 0.994 | 1.010 | 1.013 | 1.009 | 1.011 | 1.010 |
| $M^{*}$ | -0.010 | -0.005 | -0.015 | 0.009 | 0.001 | 0.014 | 0.015 |

**Note:**

**Appendix III**: K-feldspar sample compostions (EMPA data)

| Sample | C-C | ADPV-1 | ADPV-2 | AD-86-S | 12-15-12 | 12-15-4 | 12-15-6 |
|---|---|---|---|---|---|---|---|
| Zone | 50 | 50 | 50 | 50 | 60 | 60 | 60 |
| Type | 1 | 6 | 6 | 6 | 1 | 1 | 1 |
| $P_2O_5$ | 0.29 | 0.01 | 0.01 | 0.00 | 0.38 | 0.27 | 0.23 |
| $SiO_2$ | 63.44 | 65.13 | 63.79 | 65.27 | 62.61 | 63.20 | 63.39 |
| $AL_2O_3$ | 18.30 | 17.97 | 17.95 | 18.01 | 18.46 | 18.42 | 18.25 |
| MGO | 0.00 | 0.00 | 0.00 | 0.00 | 0.00 | 0.00 | 0.00 |
| CAO | 0.00 | 0.00 | 0.00 | 0.00 | 0.00 | 0.00 | 0.00 |
| MNO | 0.01 | 0.00 | 0.01 | 0.00 | 0.02 | 0.01 | 0.00 |
| $FE_2O_3$ | 0.01 | 0.01 | 0.01 | 0.01 | 0.01 | 0.00 | 0.01 |
| SRO | 0.05 | 0.03 | 0.04 | 0.03 | 0.06 | 0.05 | 0.05 |
| BAO | 0.00 | 0.06 | 0.01 | 0.05 | 0.00 | 0.03 | 0.01 |
| PBO | 0.01 | 0.01 | 0.03 | 0.00 | 0.01 | 0.04 | 0.00 |
| $NA_2O$ | 0.27 | 0.03 | 0.01 | 0.03 | 0.34 | 0.78 | 0.23 |
| $K_2O$ | 15.62 | 16.79 | 15.14 | 16.67 | 15.05 | 14.50 | 15.24 |
| $RB_2O$ | 1.80 | 0.02 | 3.21 | 0.00 | 2.66 | 2.36 | 2.31 |
| $CS_2O$ | 0.07 | 0.00 | 0.05 | 0.01 | 0.37 | 0.33 | 0.24 |
| TOTAL | 99.86 | 100.05 | 100.24 | 100.07 | 99.98 | 99.96 | 99.98 |
| $P^{5+}$ | 0.011 | 0.000 | 0.000 | 0.000 | 0.015 | 0.011 | 0.009 |
| $SI^{4+}$ | 2.973 | 3.014 | 3.001 | 3.017 | 2.954 | 2.967 | 2.978 |
| $AL^{3+}$ | 1.010 | 0.980 | 0.995 | 0.981 | 1.027 | 1.019 | 1.010 |
| $MG^{2+}$ | 0.000 | 0.000 | 0.000 | 0.000 | 0.000 | 0.000 | 0.000 |
| $CA^{2+}$ | 0.000 | 0.000 | 0.000 | 0.000 | 0.000 | 0.000 | 0.000 |
| $MN^{2+}$ | 0.000 | 0.000 | 0.000 | 0.000 | 0.001 | 0.000 | 0.000 |
| $FE^{3+}$ | 0.000 | 0.000 | 0.000 | 0.000 | 0.000 | 0.000 | 0.000 |
| $SR^{2+}$ | 0.001 | 0.001 | 0.001 | 0.001 | 0.002 | 0.002 | 0.001 |
| $BA^{2+}$ | 0.000 | 0.001 | 0.000 | 0.001 | 0.000 | 0.001 | 0.000 |
| $PB^{2+}$ | 0.000 | 0.000 | 0.000 | 0.000 | 0.000 | 0.001 | 0.000 |
| $NA^{+}$ | 0.024 | 0.003 | 0.001 | 0.003 | 0.031 | 0.071 | 0.021 |
| $K^{+}$ | 0.934 | 0.991 | 0.908 | 0.983 | 0.906 | 0.869 | 0.914 |
| $RB^{+}$ | 0.054 | 0.000 | 0.098 | 0.000 | 0.081 | 0.072 | 0.070 |
| $CS^{+}$ | 0.001 | 0.000 | 0.001 | 0.000 | 0.007 | 0.007 | 0.005 |
| $\Sigma T$ | 3.995 | 3.995 | 3.996 | 3.998 | 3.995 | 3.997 | 3.997 |
| $TO^{2-}$ | 0.999 | 0.980 | 0.995 | 0.981 | 1.012 | 1.008 | 1.001 |
| Si+2P | 2.996 | 3.015 | 3.001 | 3.017 | 2.984 | 2.989 | 2.996 |
| Si+2P/Al-P | 2.998 | 3.075 | 3.015 | 3.075 | 2.949 | 2.965 | 2.991 |
| $\Sigma M$ | 1.014 | 0.994 | 1.007 | 0.986 | 1.026 | 1.018 | 1.009 |
| $M^{+}$ | 1.016 | 0.999 | 1.009 | 0.990 | 1.029 | 1.023 | 1.012 |
| $M^{*}$ | 0.017 | 0.018 | 0.014 | 0.008 | 0.017 | 0.014 | 0.011 |

**Note:**

**Appendix III**: K-feldspar sample compostions (EMPA data)

| Sample | C-022-J | C-022-K | C-090-J | C-096-I | C-S | TA-A-3 | BL-jar1 |
|---|---|---|---|---|---|---|---|
| Zone | 60 | 60 | 60 | 60 | 60 | 60 | 60 |
| Type | 1 | 1 | 1 | 1 | 1 | 4 | 2 |
| $P_2O_5$ | 0.34 | 0.32 | 0.29 | 0.43 | 0.34 | 0.00 | 0.25 |
| $SiO_2$ | 62.87 | 63.26 | 62.84 | 62.83 | 63.20 | 64.07 | 63.31 |
| $AL_2O_3$ | 18.15 | 18.25 | 18.28 | 18.38 | 18.38 | 18.15 | 18.33 |
| MGO | 0.00 | 0.00 | 0.00 | 0.00 | 0.00 | 0.00 | 0.00 |
| CAO | 0.01 | 0.00 | 0.00 | 0.00 | 0.00 | 0.00 | 0.00 |
| MNO | 0.00 | 0.01 | 0.01 | 0.01 | 0.01 | 0.00 | 0.02 |
| $FE_2O_3$ | 0.02 | 0.03 | 0.03 | 0.00 | 0.00 | 0.01 | 0.00 |
| SRO | 0.05 | 0.04 | 0.03 | 0.06 | 0.02 | 0.02 | 0.04 |
| BAO | 0.00 | 0.03 | 0.01 | 0.05 | 0.01 | 0.03 | 0.05 |
| PBO | 0.03 | 0.00 | 0.00 | 0.02 | 0.00 | 0.01 | 0.01 |
| $NA_2O$ | 0.24 | 0.21 | 0.17 | 0.28 | 0.28 | 0.05 | 0.33 |
| $K_2O$ | 14.79 | 15.19 | 15.14 | 14.88 | 14.96 | 15.60 | 14.96 |
| $RB_2O$ | 2.53 | 2.21 | 2.73 | 2.47 | 2.51 | 2.15 | 2.36 |
| $CS_2O$ | 0.32 | 0.27 | 0.25 | 0.31 | 0.33 | 0.04 | 0.28 |
| TOTAL | 99.33 | 99.82 | 99.78 | 99.72 | 100.05 | 100.14 | 99.95 |
| $P^{5+}$ | 0.014 | 0.013 | 0.012 | 0.017 | 0.014 | 0.000 | 0.010 |
| $SI^{4+}$ | 2.974 | 2.973 | 2.967 | 2.961 | 2.969 | 2.998 | 2.974 |
| $AL^{3+}$ | 1.012 | 1.011 | 1.017 | 1.021 | 1.017 | 1.001 | 1.015 |
| $MG^{2+}$ | 0.000 | 0.000 | 0.000 | 0.000 | 0.000 | 0.000 | 0.000 |
| $CA^{2+}$ | 0.001 | 0.000 | 0.000 | 0.000 | 0.000 | 0.000 | 0.000 |
| $MN^{2+}$ | 0.000 | 0.000 | 0.000 | 0.000 | 0.000 | 0.000 | 0.001 |
| $FE^{3+}$ | 0.001 | 0.001 | 0.001 | 0.000 | 0.000 | 0.000 | 0.000 |
| $SR^{2+}$ | 0.002 | 0.001 | 0.001 | 0.002 | 0.000 | 0.001 | 0.001 |
| $BA^{2+}$ | 0.000 | 0.000 | 0.000 | 0.001 | 0.000 | 0.001 | 0.001 |
| $PB^{2+}$ | 0.001 | 0.000 | 0.000 | 0.000 | 0.000 | 0.000 | 0.000 |
| $NA^{+}$ | 0.022 | 0.019 | 0.016 | 0.026 | 0.026 | 0.004 | 0.030 |
| $K^{+}$ | 0.893 | 0.911 | 0.912 | 0.894 | 0.897 | 0.931 | 0.897 |
| $RB^{+}$ | 0.077 | 0.067 | 0.083 | 0.075 | 0.076 | 0.065 | 0.071 |
| $CS^{+}$ | 0.007 | 0.005 | 0.005 | 0.006 | 0.007 | 0.001 | 0.006 |
| $\Sigma T$ | 3.999 | 3.997 | 3.996 | 3.999 | 3.999 | 3.999 | 3.999 |
| $TO^{2-}$ | 0.998 | 0.998 | 1.006 | 1.004 | 1.003 | 1.001 | 1.005 |
| Si+2P | 3.001 | 2.999 | 2.991 | 2.994 | 2.996 | 2.998 | 2.994 |
| Si+2P/Al-P | 3.006 | 3.000 | 2.971 | 2.981 | 2.986 | 2.995 | 2.980 |
| $\Sigma M$ | 0.998 | 1.002 | 1.016 | 1.001 | 1.005 | 1.001 | 1.004 |
| $M^{+}$ | 1.003 | 1.006 | 1.018 | 1.007 | 1.006 | 1.004 | 1.010 |
| $M^{*}$ | 0.004 | 0.006 | 0.011 | 0.003 | 0.003 | 0.003 | 0.005 |

**Note:**

**Appendix III**: K-feldspar sample compostions (EMPA data)

| Sample | BL-jar2 | BLM-506 | LM-1 | C-M | 10-25-1 | 10-25-2 | 12-15-19 |
|---|---|---|---|---|---|---|---|
| Zone | 60 | 60 | 60 | 63 | 80 | 80 | 80 |
| Type | 2 | 2 | 2 | 1 | 1 | 1 | 1 |
| $P_2O_5$ | 0.25 | 0.31 | 0.12 | 0.19 | 0.45 | 0.43 | 0.03 |
| $SiO_2$ | 63.93 | 63.75 | 63.91 | 63.29 | 62.29 | 62.40 | 62.94 |
| $AL_2O_3$ | 18.24 | 18.25 | 18.40 | 18.03 | 18.38 | 18.36 | 18.08 |
| MGO | 0.00 | 0.00 | 0.00 | 0.00 | 0.00 | 0.00 | 0.00 |
| CAO | 0.00 | 0.00 | 0.00 | 0.00 | 0.00 | 0.00 | 0.00 |
| MNO | 0.00 | 0.00 | 0.00 | 0.00 | 0.02 | 0.01 | 0.00 |
| $FE_2O_3$ | 0.00 | 0.01 | 0.01 | 0.01 | 0.01 | 0.00 | 0.00 |
| SRO | 0.06 | 0.03 | 0.02 | 0.02 | 0.06 | 0.04 | 0.01 |
| BAO | 0.00 | 0.03 | 0.02 | 0.01 | 0.04 | 0.03 | 0.00 |
| PBO | 0.00 | 0.00 | 0.01 | 0.00 | 0.00 | 0.00 | 0.01 |
| $NA_2O$ | 0.31 | 0.29 | 0.15 | 0.28 | 0.27 | 0.25 | 0.15 |
| $K_2O$ | 15.00 | 15.05 | 15.60 | 15.00 | 14.69 | 14.87 | 15.38 |
| $RB_2O$ | 2.36 | 2.26 | 2.20 | 2.42 | 2.92 | 2.50 | 2.36 |
| $CS_2O$ | 0.33 | 0.25 | 0.18 | 0.29 | 0.34 | 0.33 | 0.14 |
| TOTAL | 100.49 | 100.24 | 100.60 | 99.50 | 99.44 | 99.19 | 99.08 |
| $P^{5+}$ | 0.010 | 0.013 | 0.005 | 0.008 | 0.018 | 0.017 | 0.001 |
| $SI^{4+}$ | 2.985 | 2.980 | 2.982 | 2.987 | 2.954 | 2.958 | 2.986 |
| $AL^{3+}$ | 1.003 | 1.005 | 1.012 | 1.003 | 1.027 | 1.026 | 1.011 |
| $MG^{2+}$ | 0.000 | 0.000 | 0.000 | 0.000 | 0.000 | 0.000 | 0.000 |
| $CA^{2+}$ | 0.000 | 0.000 | 0.000 | 0.000 | 0.000 | 0.000 | 0.000 |
| $MN^{2+}$ | 0.000 | 0.000 | 0.000 | 0.000 | 0.001 | 0.000 | 0.000 |
| $FE^{3+}$ | 0.000 | 0.000 | 0.000 | 0.000 | 0.001 | 0.000 | 0.000 |
| $SR^{2+}$ | 0.002 | 0.001 | 0.001 | 0.001 | 0.002 | 0.001 | 0.001 |
| $BA^{2+}$ | 0.000 | 0.000 | 0.001 | 0.000 | 0.001 | 0.001 | 0.000 |
| $PB^{2+}$ | 0.000 | 0.000 | 0.000 | 0.000 | 0.000 | 0.000 | 0.000 |
| $NA^{+}$ | 0.028 | 0.027 | 0.013 | 0.026 | 0.025 | 0.023 | 0.014 |
| $K^{+}$ | 0.893 | 0.898 | 0.928 | 0.903 | 0.888 | 0.900 | 0.931 |
| $RB^{+}$ | 0.071 | 0.068 | 0.066 | 0.074 | 0.089 | 0.076 | 0.072 |
| $CS^{+}$ | 0.007 | 0.005 | 0.004 | 0.006 | 0.007 | 0.007 | 0.003 |
| $\Sigma T$ | 3.998 | 3.998 | 3.999 | 3.997 | 3.999 | 4.000 | 3.997 |
| $TO^{2-}$ | 0.994 | 0.993 | 1.007 | 0.995 | 1.010 | 1.009 | 1.010 |
| Si+2P | 3.004 | 3.005 | 2.992 | 3.002 | 2.989 | 2.992 | 2.988 |
| Si+2P/Al-P | 3.023 | 3.027 | 2.972 | 3.017 | 2.959 | 2.966 | 2.959 |
| $\Sigma M$ | 0.999 | 0.997 | 1.011 | 1.008 | 1.008 | 1.005 | 1.020 |
| $M^{+}$ | 1.002 | 0.999 | 1.014 | 1.009 | 1.013 | 1.008 | 1.021 |
| $M^{*}$ | 0.009 | 0.006 | 0.007 | 0.014 | 0.003 | -0.001 | 0.011 |

**Note:**

**Appendix III: K-feldspar sample compostions (EMPA data)**

| Sample | A-10 | Poll-6a | PM1-8a | PMx-d | PM1-3 | 10-25-6 | 12-15-10 |
|---|---|---|---|---|---|---|---|
| Zone | 80 | 80 | 80 | 80 | 82 | 90 | 90 |
| Type | 4 | 4 | 3 | 3 | 3 | 1 | 1 |
| $P_2O_5$ | 0.01 | 0.18 | 0.15 | 0.47 | 0.18 | 0.36 | 0.10 |
| $SIO_2$ | 62.59 | 63.36 | 62.50 | 62.39 | 63.26 | 62.60 | 63.29 |
| $AL_2O_3$ | 17.80 | 18.35 | 18.22 | 18.28 | 18.16 | 18.48 | 18.20 |
| MGO | 0.00 | 0.00 | 0.00 | 0.00 | 0.00 | 0.00 | 0.00 |
| CAO | 0.00 | 0.04 | 0.00 | 0.00 | 0.00 | 0.00 | 0.00 |
| MNO | 0.01 | 0.01 | 0.00 | 0.01 | 0.01 | 0.00 | 0.01 |
| $FE_2O_3$ | 0.00 | 0.01 | 0.02 | 0.01 | 0.01 | 0.01 | 0.00 |
| SRO | 0.06 | 0.02 | 0.05 | 0.06 | 0.01 | 0.05 | 0.05 |
| BAO | 0.01 | 0.10 | 0.00 | 0.00 | 0.02 | 0.01 | 0.02 |
| PBO | 0.01 | 0.00 | 0.01 | 0.01 | 0.00 | 0.00 | 0.00 |
| $NA_2O$ | 0.03 | 0.12 | 0.18 | 0.18 | 0.18 | 0.30 | 0.23 |
| $K_2O$ | 13.54 | 15.44 | 14.71 | 14.02 | 14.59 | 15.15 | 15.28 |
| $RB_2O$ | 5.76 | 2.28 | 3.68 | 4.80 | 3.55 | 2.59 | 2.34 |
| $CS_2O$ | 0.26 | 0.14 | 0.31 | 0.37 | 0.20 | 0.35 | 0.16 |
| TOTAL | 100.08 | 100.02 | 99.83 | 100.61 | 100.17 | 99.89 | 99.67 |
| $P^{5+}$ | 0.000 | 0.007 | 0.006 | 0.019 | 0.007 | 0.014 | 0.004 |
| $SI^{4+}$ | 2.993 | 2.976 | 2.969 | 2.955 | 2.982 | 2.954 | 2.983 |
| $AL^{3+}$ | 1.004 | 1.016 | 1.020 | 1.021 | 1.009 | 1.028 | 1.011 |
| $MG^{2+}$ | 0.000 | 0.000 | 0.000 | 0.000 | 0.000 | 0.000 | 0.000 |
| $CA^{2+}$ | 0.000 | 0.002 | 0.000 | 0.000 | 0.000 | 0.000 | 0.000 |
| $MN^{2+}$ | 0.000 | 0.000 | 0.000 | 0.000 | 0.000 | 0.000 | 0.000 |
| $FE^{3+}$ | 0.000 | 0.001 | 0.001 | 0.000 | 0.000 | 0.000 | 0.000 |
| $SR^{2+}$ | 0.002 | 0.001 | 0.001 | 0.002 | 0.000 | 0.002 | 0.001 |
| $BA^{2+}$ | 0.000 | 0.002 | 0.000 | 0.000 | 0.000 | 0.000 | 0.000 |
| $PB^{2+}$ | 0.000 | 0.000 | 0.000 | 0.000 | 0.000 | 0.000 | 0.000 |
| $NA^{+}$ | 0.003 | 0.011 | 0.017 | 0.017 | 0.017 | 0.027 | 0.021 |
| $K^{+}$ | 0.826 | 0.925 | 0.892 | 0.847 | 0.878 | 0.912 | 0.919 |
| $RB^{+}$ | 0.177 | 0.069 | 0.112 | 0.146 | 0.108 | 0.079 | 0.071 |
| $CS^{+}$ | 0.005 | 0.003 | 0.006 | 0.007 | 0.004 | 0.007 | 0.003 |
| $\Sigma T$ | 3.997 | 3.998 | 3.995 | 3.995 | 3.999 | 3.996 | 3.997 |
| $TO^{2-}$ | 1.003 | 1.009 | 1.014 | 1.002 | 1.002 | 1.014 | 1.007 |
| Si+2P | 2.994 | 2.990 | 2.981 | 2.993 | 2.997 | 2.983 | 2.990 |
| Si+2P/Al-P | 2.984 | 2.963 | 2.938 | 2.987 | 2.990 | 2.942 | 2.970 |
| $\Sigma M$ | 1.011 | 1.008 | 1.027 | 1.017 | 1.006 | 1.025 | 1.014 |
| $M^{+}$ | 1.015 | 1.017 | 1.030 | 1.021 | 1.007 | 1.029 | 1.017 |
| $M^{*}$ | 0.012 | 0.007 | 0.015 | 0.019 | 0.005 | 0.015 | 0.010 |

Note:

**Appendix III**: K-feldspar sample compostions (EMPA data)

| Sample | 12-15-17 | 12-15-21 | 12-15-23 | P-26 | 96-11-B |
|---|---|---|---|---|---|
| Zone | 90 | 90 | 90 | 96 | 99 |
| Type | 1 | 1 | 1 | 1 | 1 |
| $P_2O_5$ | 0.15 | 0.30 | 0.38 | 0.29 | 0.37 |
| $SiO_2$ | 63.02 | 62.95 | 63.83 | 62.83 | 63.22 |
| $AL_2O_3$ | 18.19 | 18.57 | 18.11 | 18.28 | 18.34 |
| MGO | 0.00 | 0.00 | 0.01 | 0.00 | 0.00 |
| CAO | 0.00 | 0.00 | 0.00 | 0.00 | 0.00 |
| MNO | 0.01 | 0.01 | 0.00 | 0.01 | 0.00 |
| $FE_2O_3$ | 0.02 | 0.02 | 0.01 | 0.01 | 0.01 |
| SRO | 0.02 | 0.04 | 0.05 | 0.02 | 0.02 |
| BAO | 0.02 | 0.01 | 0.00 | 0.04 | 0.03 |
| PBO | 0.00 | 0.00 | 0.02 | 0.02 | 0.00 |
| $NA_2O$ | 0.23 | 0.25 | 0.28 | 0.26 | 0.35 |
| $K_2O$ | 15.22 | 15.23 | 14.80 | 15.14 | 15.55 |
| $RB_2O$ | 2.83 | 2.51 | 2.68 | 2.49 | 1.46 |
| $CS_2O$ | 0.18 | 0.33 | 0.34 | 0.29 | 0.04 |
| TOTAL | 99.88 | 100.24 | 100.48 | 99.67 | 99.39 |
| $P^{5+}$ | 0.006 | 0.012 | 0.015 | 0.012 | 0.014 |
| $SI^{4+}$ | 2.975 | 2.958 | 2.984 | 2.967 | 2.968 |
| $AL^{3+}$ | 1.012 | 1.028 | 0.998 | 1.017 | 1.015 |
| $MG^{2+}$ | 0.000 | 0.000 | 0.001 | 0.000 | 0.000 |
| $CA^{2+}$ | 0.000 | 0.000 | 0.000 | 0.000 | 0.000 |
| $MN^{2+}$ | 0.000 | 0.000 | 0.000 | 0.000 | 0.000 |
| $FE^{3+}$ | 0.001 | 0.001 | 0.001 | 0.000 | 0.000 |
| $SR^{2+}$ | 0.001 | 0.001 | 0.002 | 0.001 | 0.001 |
| $BA^{2+}$ | 0.000 | 0.000 | 0.000 | 0.001 | 0.000 |
| $PB^{2+}$ | 0.000 | 0.000 | 0.000 | 0.000 | 0.000 |
| $NA^{+}$ | 0.021 | 0.023 | 0.025 | 0.024 | 0.031 |
| $K^{+}$ | 0.917 | 0.913 | 0.883 | 0.913 | 0.931 |
| $RB^{+}$ | 0.086 | 0.076 | 0.081 | 0.076 | 0.044 |
| $CS^{+}$ | 0.003 | 0.006 | 0.007 | 0.006 | 0.001 |
| $\Sigma T$ | 3.994 | 3.998 | 3.996 | 3.996 | 3.997 |
| $TO^{2-}$ | 1.006 | 1.016 | 0.983 | 1.006 | 1.000 |
| Si+2P | 2.987 | 2.982 | 3.014 | 2.990 | 2.997 |
| Si+2P/Al-P | 2.967 | 2.932 | 3.066 | 2.973 | 2.995 |
| $\Sigma M$ | 1.027 | 1.018 | 0.995 | 1.017 | 1.008 |
| $M^{+}$ | 1.029 | 1.021 | 0.998 | 1.020 | 1.010 |
| $M^{*}$ | 0.022 | 0.004 | 0.015 | 0.015 | 0.010 |

Note:

**Appendix IV**: Albite (Types A & B) sample compostions (EMPA data)

| Sample | SLW-4B | SLW-3C | SLE-20A | SLE-11 | SLE-27 | 78-21-C | C-096-Z |
|---|---|---|---|---|---|---|---|
| Zone | 12 | 12 | 12 | 12 | 12 | 20 | 20 |
| Type | A | A | A | A | A | A | A |
| $P_2O_5$ | 0.10 | 0.03 | 0.09 | 0.22 | 0.30 | 0.16 | 0.19 |
| $SiO_2$ | 67.66 | 67.77 | 67.43 | 67.43 | 67.34 | 68.18 | 67.86 |
| $AL_2O_3$ | 19.51 | 19.43 | 19.50 | 19.69 | 19.56 | 19.72 | 19.77 |
| MGO | 0.00 | 0.00 | 0.00 | 0.00 | 0.00 | 0.00 | 0.00 |
| CAO | 0.10 | 0.03 | 0.08 | 0.17 | 0.04 | 0.12 | 0.19 |
| MNO | 0.00 | 0.01 | 0.01 | 0.00 | 0.00 | 0.01 | 0.01 |
| $FE_2O_3$ | 0.00 | 0.02 | 0.00 | 0.00 | 0.01 | 0.00 | 0.02 |
| SRO | 0.04 | 0.02 | 0.03 | 0.01 | 0.03 | 0.02 | 0.04 |
| BAO | 0.02 | 0.00 | 0.01 | 0.03 | 0.04 | 0.03 | 0.01 |
| PBO | 0.01 | 0.01 | 0.01 | 0.00 | 0.00 | 0.00 | 0.02 |
| $NA_2O$ | 11.63 | 11.75 | 11.52 | 11.54 | 11.68 | 11.56 | 11.57 |
| $K_2O$ | 0.08 | 0.08 | 0.12 | 0.08 | 0.05 | 0.10 | 0.08 |
| $RB_2O$ | 0.05 | 0.04 | 0.05 | 0.05 | 0.04 | 0.06 | 0.06 |
| $CS_2O$ | 0.00 | 0.00 | 0.00 | 0.00 | 0.00 | 0.00 | 0.00 |
| TOTAL | 99.19 | 99.15 | 98.84 | 99.22 | 99.07 | 99.94 | 99.79 |
| $P^{5+}$ | 0.004 | 0.001 | 0.003 | 0.008 | 0.011 | 0.006 | 0.007 |
| $SI^{4+}$ | 2.983 | 2.988 | 2.982 | 2.971 | 2.971 | 2.980 | 2.973 |
| $AL^{3+}$ | 1.014 | 1.010 | 1.017 | 1.022 | 1.017 | 1.016 | 1.021 |
| $MG^{2+}$ | 0.000 | 0.000 | 0.000 | 0.000 | 0.000 | 0.000 | 0.000 |
| $CA^{2+}$ | 0.004 | 0.001 | 0.004 | 0.008 | 0.002 | 0.005 | 0.009 |
| $MN^{2+}$ | 0.000 | 0.000 | 0.000 | 0.000 | 0.000 | 0.000 | 0.000 |
| $FE^{3+}$ | 0.000 | 0.001 | 0.000 | 0.000 | 0.000 | 0.000 | 0.000 |
| $SR^{2+}$ | 0.001 | 0.001 | 0.001 | 0.000 | 0.001 | 0.001 | 0.001 |
| $BA^{2+}$ | 0.001 | 0.000 | 0.000 | 0.001 | 0.001 | 0.000 | 0.000 |
| $PB^{2+}$ | 0.000 | 0.000 | 0.000 | 0.000 | 0.000 | 0.000 | 0.000 |
| $NA^{+}$ | 0.994 | 1.005 | 0.988 | 0.986 | 0.999 | 0.980 | 0.983 |
| $K^{+}$ | 0.005 | 0.005 | 0.007 | 0.004 | 0.003 | 0.005 | 0.004 |
| $RB^{+}$ | 0.001 | 0.002 | 0.001 | 0.001 | 0.001 | 0.002 | 0.002 |
| $CS^{+}$ | 0.000 | 0.000 | 0.000 | 0.000 | 0.000 | 0.000 | 0.000 |
| $\Sigma T$ | 4.000 | 3.998 | 4.002 | 4.001 | 3.999 | 4.002 | 4.001 |
| $TO^{2-}$ | 1.010 | 1.009 | 1.013 | 1.014 | 1.006 | 1.010 | 1.014 |
| Si+2P | 2.990 | 2.989 | 2.989 | 2.987 | 2.993 | 2.992 | 2.987 |
| Si+2P/Al-P | 2.960 | 2.961 | 2.949 | 2.946 | 2.974 | 2.962 | 2.945 |
| $\Sigma M$ | 1.000 | 1.011 | 0.996 | 0.992 | 1.003 | 0.987 | 0.989 |
| $M^{+}$ | 1.011 | 1.014 | 1.005 | 1.010 | 1.010 | 0.999 | 1.009 |
| $M^{*}$ | 0.001 | 0.004 | -0.008 | -0.004 | 0.003 | -0.011 | -0.006 |

**Note:** $\Sigma T$ = Si+Al+P; $TO^{2-}$ = Al-P
$\Sigma M$ = Na+K+Rb+Cs; $M^{*}$ = 2*(Ca+Sr+Ba)+Na+K+Rb+Cs
$M^{*} = M^{+} - TO^{2-}$

-all compositions are averages of 3-8 analyses

**Appendix IV: Albite (Types A & B) sample compostions (EMPA data)**

| Sample | 76-05-R | 76-05-H | C-Z3 | C-045-W | L-12-A | L-12-M | 76-23-T |
|---|---|---|---|---|---|---|---|
| Zone | 20 | 20 | 20 | 20 | 20 | 20 | 20 |
| Type | A | A | A | A | A | A | A |
| $P_2O_5$ | 0.31 | 0.24 | 0.09 | 0.08 | 0.09 | 0.12 | 0.10 |
| $SiO_2$ | 67.41 | 68.10 | 68.56 | 68.56 | 68.60 | 68.63 | 68.31 |
| $AL_2O_3$ | 19.89 | 19.69 | 19.85 | 19.62 | 19.82 | 19.84 | 19.54 |
| MGO | 0.00 | 0.00 | 0.00 | 0.00 | 0.00 | 0.00 | 0.00 |
| CAO | 0.05 | 0.03 | 0.05 | 0.07 | 0.06 | 0.05 | 0.06 |
| MNO | 0.02 | 0.01 | 0.02 | 0.01 | 0.01 | 0.02 | 0.01 |
| $FE_2O_3$ | 0.01 | 0.00 | 0.00 | 0.01 | 0.04 | 0.01 | 0.01 |
| SRO | 0.03 | 0.03 | 0.01 | 0.01 | 0.02 | 0.03 | 0.03 |
| BAO | 0.01 | 0.02 | 0.02 | 0.03 | 0.00 | 0.02 | 0.03 |
| PBO | 0.00 | 0.01 | 0.01 | 0.01 | 0.00 | 0.01 | 0.01 |
| $NA_2O$ | 11.93 | 11.88 | 11.80 | 11.64 | 11.85 | 11.86 | 11.61 |
| $K_2O$ | 0.04 | 0.07 | 0.09 | 0.10 | 0.07 | 0.06 | 0.08 |
| $RB_2O$ | 0.04 | 0.05 | 0.06 | 0.06 | 0.04 | 0.05 | 0.05 |
| $CS_2O$ | 0.01 | 0.01 | 0.00 | 0.00 | 0.00 | 0.00 | 0.00 |
| TOTAL | 99.74 | 100.12 | 100.55 | 100.19 | 100.60 | 100.69 | 99.83 |
| $P^{5+}$ | 0.011 | 0.009 | 0.003 | 0.003 | 0.003 | 0.004 | 0.004 |
| $SI^{4+}$ | 2.957 | 2.975 | 2.981 | 2.990 | 2.981 | 2.980 | 2.989 |
| $AL^{3+}$ | 1.029 | 1.014 | 1.017 | 1.008 | 1.015 | 1.015 | 1.008 |
| $MG^{2+}$ | 0.000 | 0.000 | 0.000 | 0.000 | 0.000 | 0.000 | 0.000 |
| $CA^{2+}$ | 0.002 | 0.001 | 0.002 | 0.004 | 0.003 | 0.002 | 0.003 |
| $MN^{2+}$ | 0.001 | 0.000 | 0.001 | 0.000 | 0.000 | 0.001 | 0.000 |
| $FE^{3+}$ | 0.000 | 0.000 | 0.000 | 0.000 | 0.001 | 0.000 | 0.000 |
| $SR^{2+}$ | 0.001 | 0.001 | 0.000 | 0.001 | 0.001 | 0.001 | 0.001 |
| $BA^{2+}$ | 0.000 | 0.000 | 0.000 | 0.001 | 0.000 | 0.000 | 0.001 |
| $PB^{2+}$ | 0.000 | 0.000 | 0.000 | 0.000 | 0.000 | 0.000 | 0.000 |
| $NA^{+}$ | 1.014 | 1.006 | 0.995 | 0.984 | 0.999 | 0.998 | 0.986 |
| $K^{+}$ | 0.002 | 0.004 | 0.005 | 0.005 | 0.004 | 0.003 | 0.004 |
| $RB^{+}$ | 0.001 | 0.001 | 0.002 | 0.002 | 0.001 | 0.002 | 0.002 |
| $CS^{+}$ | 0.000 | 0.000 | 0.000 | 0.000 | 0.000 | 0.000 | 0.000 |
| $\Sigma T$ | 3.997 | 3.997 | 4.001 | 4.001 | 3.999 | 4.000 | 4.001 |
| $TO^{2-}$ | 1.017 | 1.005 | 1.014 | 1.005 | 1.012 | 1.011 | 1.004 |
| Si+2P | 2.980 | 2.992 | 2.987 | 2.996 | 2.988 | 2.989 | 2.997 |
| Si+2P/Al-P | 2.928 | 2.977 | 2.946 | 2.980 | 2.949 | 2.957 | 2.984 |
| $\Sigma M$ | 1.018 | 1.011 | 1.002 | 0.991 | 1.004 | 1.003 | 0.991 |
| $M^{+}$ | 1.024 | 1.016 | 1.008 | 1.000 | 1.010 | 1.009 | 0.999 |
| $M^{*}$ | 0.007 | 0.011 | -0.006 | -0.005 | -0.003 | -0.002 | -0.005 |

**Note:**

**Appendix IV**: Albite (Types A & B) sample compostions (EMPA data)

| Sample | 76-23-M | C-096-B | 76-23-G | C-096-S | C-096-T | C-096-U | ABMA |
|---|---|---|---|---|---|---|---|
| Zone | 20 | 20 | 30 | 30 | 30 | 30 | 30 |
| Type | A | A | A | A | A | A | A |
| $P_2O_5$ | 0.18 | 0.13 | 0.07 | 0.10 | 0.11 | 0.20 | 0.14 |
| $SiO_2$ | 67.97 | 68.74 | 68.46 | 68.65 | 68.51 | 68.69 | 67.81 |
| $AL_2O_3$ | 19.57 | 19.50 | 19.42 | 19.54 | 19.48 | 19.61 | 19.59 |
| MGO | 0.00 | 0.00 | 0.00 | 0.00 | 0.01 | 0.00 | 0.00 |
| CAO | 0.05 | 0.08 | 0.07 | 0.05 | 0.08 | 0.03 | 0.06 |
| MNO | 0.01 | 0.01 | 0.01 | 0.01 | 0.00 | 0.01 | 0.01 |
| $FE_2O_3$ | 0.00 | 0.01 | 0.01 | 0.02 | 0.01 | 0.01 | 0.00 |
| SRO | 0.02 | 0.03 | 0.03 | 0.03 | 0.02 | 0.03 | 0.02 |
| BAO | 0.02 | 0.02 | 0.02 | 0.02 | 0.01 | 0.00 | 0.06 |
| PBO | 0.01 | 0.00 | 0.00 | 0.00 | 0.00 | 0.01 | 0.00 |
| $NA_2O$ | 11.62 | 11.55 | 11.61 | 11.64 | 11.44 | 11.71 | 11.68 |
| $K_2O$ | 0.08 | 0.09 | 0.08 | 0.07 | 0.07 | 0.05 | 0.06 |
| $RB_2O$ | 0.06 | 0.06 | 0.05 | 0.05 | 0.07 | 0.04 | 0.05 |
| $CS_2O$ | 0.00 | 0.00 | 0.00 | 0.00 | 0.00 | 0.01 | 0.00 |
| TOTAL | 99.57 | 100.22 | 99.81 | 100.18 | 99.78 | 100.39 | 99.48 |
| $P^{5+}$ | 0.007 | 0.005 | 0.002 | 0.004 | 0.004 | 0.008 | 0.005 |
| $SI^{4+}$ | 2.983 | 2.995 | 2.996 | 2.993 | 2.996 | 2.987 | 2.980 |
| $AL^{3+}$ | 1.012 | 1.001 | 1.002 | 1.004 | 1.004 | 1.005 | 1.015 |
| $MG^{2+}$ | 0.000 | 0.000 | 0.000 | 0.000 | 0.000 | 0.000 | 0.000 |
| $CA^{2+}$ | 0.003 | 0.004 | 0.004 | 0.002 | 0.004 | 0.001 | 0.003 |
| $MN^{2+}$ | 0.000 | 0.000 | 0.001 | 0.000 | 0.000 | 0.000 | 0.000 |
| $FE^{3+}$ | 0.000 | 0.000 | 0.000 | 0.000 | 0.000 | 0.000 | 0.000 |
| $SR^{2+}$ | 0.000 | 0.001 | 0.001 | 0.001 | 0.000 | 0.001 | 0.000 |
| $BA^{2+}$ | 0.000 | 0.000 | 0.000 | 0.000 | 0.000 | 0.000 | 0.001 |
| $PB^{2+}$ | 0.000 | 0.000 | 0.000 | 0.000 | 0.000 | 0.000 | 0.000 |
| $NA^{+}$ | 0.988 | 0.976 | 0.985 | 0.984 | 0.970 | 0.987 | 0.995 |
| $K^{+}$ | 0.005 | 0.005 | 0.004 | 0.004 | 0.004 | 0.003 | 0.004 |
| $RB^{+}$ | 0.002 | 0.002 | 0.001 | 0.002 | 0.002 | 0.001 | 0.001 |
| $CS^{+}$ | 0.000 | 0.000 | 0.000 | 0.000 | 0.000 | 0.000 | 0.000 |
| $\Sigma T$ | 4.001 | 4.001 | 4.000 | 4.001 | 4.004 | 4.000 | 4.000 |
| $TO^{2-}$ | 1.006 | 0.997 | 0.999 | 1.000 | 1.000 | 0.998 | 1.010 |
| Si+2P | 2.996 | 3.004 | 3.000 | 3.000 | 3.003 | 3.003 | 2.991 |
| Si+2P/Al-P | 2.979 | 3.014 | 3.002 | 2.998 | 3.003 | 3.009 | 2.962 |
| $\Sigma M$ | 0.995 | 0.982 | 0.990 | 0.989 | 0.976 | 0.991 | 1.000 |
| $M^{+}$ | 1.001 | 0.992 | 0.999 | 0.995 | 0.984 | 0.995 | 1.007 |
| $M^{*}$ | -0.005 | -0.005 | 0.000 | -0.005 | -0.017 | -0.002 | -0.002 |

**Note:**

**Appendix IV**: Albite (Types A & B) sample compostions (EMPA data)

| Sample | P-30 | 22-F | 76-23-J | C-096-L | C-096-M | 12-15-11 | 12-15-14 |
|---|---|---|---|---|---|---|---|
| Zone | 30 | 30 | 30 | 30 | 30 | 30 | 30 |
| Type | A | A | A | A | A | A | A |
| $P_2O_6$ | 0.06 | 0.31 | 0.14 | 0.10 | 0.13 | 0.09 | 0.05 |
| $SIO_2$ | 67.97 | 67.56 | 69.07 | 68.68 | 68.37 | 68.13 | 68.04 |
| $AL_2O_3$ | 19.54 | 19.69 | 19.66 | 19.54 | 19.78 | 19.56 | 19.55 |
| MGO | 0.00 | 0.00 | 0.00 | 0.00 | 0.00 | 0.00 | 0.00 |
| CAO | 0.04 | 0.10 | 0.09 | 0.04 | 0.05 | 0.05 | 0.03 |
| MNO | 0.01 | 0.01 | 0.01 | 0.01 | 0.00 | 0.01 | 0.01 |
| $FE_2O_3$ | 0.00 | 0.01 | 0.01 | 0.02 | 0.00 | 0.00 | 0.02 |
| SRO | 0.02 | 0.01 | 0.03 | 0.04 | 0.03 | 0.01 | 0.03 |
| BAO | 0.03 | 0.02 | 0.02 | 0.02 | 0.04 | 0.02 | 0.02 |
| PBO | 0.01 | 0.02 | 0.01 | 0.00 | 0.01 | 0.01 | 0.00 |
| $NA_2O$ | 11.74 | 11.61 | 11.89 | 11.63 | 11.81 | 11.64 | 11.70 |
| $K_2O$ | 0.06 | 0.05 | 0.06 | 0.09 | 0.06 | 0.06 | 0.09 |
| $RB_2O$ | 0.04 | 0.05 | 0.04 | 0.05 | 0.06 | 0.04 | 0.03 |
| $CS_2O$ | 0.01 | 0.00 | 0.00 | 0.00 | 0.00 | 0.00 | 0.01 |
| TOTAL | 99.52 | 99.43 | 101.02 | 100.21 | 100.33 | 99.61 | 99.56 |
| $P^{5+}$ | 0.002 | 0.011 | 0.005 | 0.004 | 0.005 | 0.003 | 0.002 |
| $SI^{4+}$ | 2.986 | 2.969 | 2.989 | 2.993 | 2.980 | 2.988 | 2.987 |
| $AL^{3+}$ | 1.012 | 1.020 | 1.002 | 1.004 | 1.016 | 1.011 | 1.012 |
| $MG^{2+}$ | 0.000 | 0.000 | 0.000 | 0.000 | 0.000 | 0.000 | 0.000 |
| $CA^{2+}$ | 0.002 | 0.005 | 0.005 | 0.002 | 0.002 | 0.002 | 0.001 |
| $MN^{2+}$ | 0.000 | 0.000 | 0.000 | 0.000 | 0.000 | 0.001 | 0.000 |
| $FE^{3+}$ | 0.000 | 0.000 | 0.001 | 0.001 | 0.000 | 0.000 | 0.001 |
| $SR^{2+}$ | 0.001 | 0.000 | 0.001 | 0.001 | 0.001 | 0.000 | 0.001 |
| $BA^{2+}$ | 0.001 | 0.001 | 0.000 | 0.000 | 0.001 | 0.000 | 0.001 |
| $PB^{2+}$ | 0.000 | 0.000 | 0.000 | 0.000 | 0.000 | 0.000 | 0.000 |
| $NA^{+}$ | 1.000 | 0.990 | 0.997 | 0.983 | 0.998 | 0.990 | 0.996 |
| $K^{+}$ | 0.004 | 0.003 | 0.003 | 0.005 | 0.003 | 0.003 | 0.005 |
| $RB^{+}$ | 0.001 | 0.001 | 0.001 | 0.002 | 0.002 | 0.001 | 0.001 |
| $CS^{+}$ | 0.000 | 0.000 | 0.000 | 0.000 | 0.000 | 0.000 | 0.000 |
| $\Sigma T$ | 4.000 | 4.001 | 3.996 | 4.001 | 4.000 | 4.002 | 4.000 |
| $TO^{2-}$ | 1.010 | 1.009 | 0.997 | 1.000 | 1.011 | 1.008 | 1.010 |
| Si+2P | 2.991 | 2.992 | 2.999 | 3.001 | 2.989 | 2.994 | 2.990 |
| Si+2P/Al-P | 2.962 | 2.964 | 3.007 | 2.999 | 2.956 | 2.972 | 2.958 |
| $\Sigma M$ | 1.005 | 0.993 | 1.001 | 0.989 | 1.003 | 0.994 | 1.002 |
| $M^{+}$ | 1.010 | 1.004 | 1.012 | 0.995 | 1.010 | 1.000 | 1.007 |
| $M^{*}$ | 0.000 | -0.005 | 0.015 | -0.005 | -0.001 | -0.008 | -0.004 |

**Note:**

**Appendix IV**: Albite (Types A & B) sample compostions (EMPA data)

| Sample | 12-15-13 | BLM-508 | C-045-T | L-12-K | C-107-O | C-107-K | 76-05-D |
|---|---|---|---|---|---|---|---|
| Zone | 30 | 36 | 40 | 40 | 40 | 40 | 40 |
| Type | A | A | A | A | A | A | A |
| $P_2O_6$ | 0.14 | 0.25 | 0.32 | 0.27 | 0.33 | 0.12 | 0.13 |
| $SiO_2$ | 68.25 | 68.27 | 67.74 | 68.59 | 67.99 | 68.22 | 68.47 |
| $AL_2O_3$ | 19.51 | 19.55 | 19.78 | 20.00 | 19.96 | 19.66 | 19.77 |
| MGO | 0.00 | 0.00 | 0.00 | 0.00 | 0.00 | 0.00 | 0.00 |
| CAO | 0.04 | 0.09 | 0.07 | 0.04 | 0.10 | 0.04 | 0.06 |
| MNO | 0.01 | 0.01 | 0.00 | 0.01 | 0.02 | 0.01 | 0.01 |
| $FE_2O_3$ | 0.01 | 0.02 | 0.01 | 0.03 | 0.01 | 0.01 | 0.01 |
| SRO | 0.02 | 0.02 | 0.01 | 0.02 | 0.04 | 0.02 | 0.03 |
| BAO | 0.00 | 0.03 | 0.03 | 0.00 | 0.01 | 0.02 | 0.03 |
| PBO | 0.02 | 0.03 | 0.02 | 0.00 | 0.01 | 0.02 | 0.00 |
| $NA_2O$ | 11.62 | 11.62 | 11.73 | 11.93 | 11.77 | 11.65 | 11.72 |
| $K_2O$ | 0.04 | 0.11 | 0.05 | 0.04 | 0.07 | 0.06 | 0.07 |
| $RB_2O$ | 0.04 | 0.05 | 0.04 | 0.07 | 0.06 | 0.04 | 0.03 |
| $CS_2O$ | 0.01 | 0.00 | 0.00 | 0.00 | 0.00 | 0.00 | 0.00 |
| TOTAL | 99.69 | 100.03 | 99.79 | 101.01 | 100.34 | 99.87 | 100.33 |
| $P^{5+}$ | 0.005 | 0.009 | 0.012 | 0.010 | 0.012 | 0.004 | 0.005 |
| $SI^{4+}$ | 2.989 | 2.982 | 2.967 | 2.969 | 2.963 | 2.984 | 2.982 |
| $AL^{3+}$ | 1.007 | 1.007 | 1.021 | 1.021 | 1.025 | 1.014 | 1.015 |
| $MG^{2+}$ | 0.000 | 0.000 | 0.000 | 0.000 | 0.000 | 0.000 | 0.000 |
| $CA^{2+}$ | 0.002 | 0.004 | 0.003 | 0.002 | 0.005 | 0.002 | 0.003 |
| $MN^{2+}$ | 0.000 | 0.000 | 0.000 | 0.000 | 0.001 | 0.000 | 0.000 |
| $FE^{3+}$ | 0.000 | 0.001 | 0.000 | 0.001 | 0.000 | 0.001 | 0.000 |
| $SR^{2+}$ | 0.001 | 0.000 | 0.000 | 0.000 | 0.001 | 0.001 | 0.001 |
| $BA^{2+}$ | 0.000 | 0.001 | 0.001 | 0.000 | 0.000 | 0.000 | 0.000 |
| $PB^{2+}$ | 0.000 | 0.000 | 0.000 | 0.000 | 0.000 | 0.000 | 0.000 |
| $NA^{+}$ | 0.987 | 0.984 | 0.996 | 1.001 | 0.994 | 0.988 | 0.989 |
| $K^{+}$ | 0.003 | 0.006 | 0.003 | 0.002 | 0.004 | 0.003 | 0.004 |
| $RB^{+}$ | 0.001 | 0.001 | 0.001 | 0.002 | 0.002 | 0.001 | 0.001 |
| $CS^{+}$ | 0.000 | 0.000 | 0.000 | 0.000 | 0.000 | 0.000 | 0.000 |
| $\Sigma T$ | 4.002 | 3.998 | 4.000 | 4.000 | 4.000 | 4.003 | 4.001 |
| $TO^{2-}$ | 1.002 | 0.998 | 1.009 | 1.011 | 1.013 | 1.010 | 1.010 |
| Si+2P | 3.000 | 3.001 | 2.991 | 2.989 | 2.987 | 2.993 | 2.992 |
| Si+2P/Al-P | 2.993 | 3.006 | 2.963 | 2.954 | 2.948 | 2.963 | 2.961 |
| $\Sigma M$ | 0.991 | 0.992 | 1.000 | 1.005 | 1.000 | 0.992 | 0.994 |
| $M^{+}$ | 0.995 | 1.002 | 1.008 | 1.009 | 1.012 | 0.998 | 1.002 |
| $M^{*}$ | -0.007 | 0.004 | -0.001 | -0.003 | -0.002 | -0.012 | -0.008 |

Note:

**Appendix IV**: Albite (Types A & B) sample compostions (EMPA data)

| Sample | C-107-C | 86-07-Q | 86-07-I | C-V | C-090-P | C-045-P | C-096-V |
|---|---|---|---|---|---|---|---|
| Zone | 40 | 40 | 40 | 40 | 40 | 40 | 40 |
| Type | A | A | A | A | A | A | A |
| $P_2O_5$ | 0.35 | 0.38 | 0.04 | 0.20 | 0.13 | 0.22 | 0.07 |
| $SiO_2$ | 67.93 | 67.67 | 68.41 | 68.02 | 68.44 | 68.11 | 68.80 |
| $AL_2O_3$ | 20.04 | 19.80 | 19.66 | 19.77 | 19.59 | 19.71 | 19.70 |
| MGO | 0.00 | 0.00 | 0.00 | 0.00 | 0.00 | 0.00 | 0.00 |
| CAO | 0.08 | 0.09 | 0.03 | 0.08 | 0.03 | 0.09 | 0.03 |
| MNO | 0.01 | 0.00 | 0.02 | 0.01 | 0.01 | 0.00 | 0.01 |
| $FE_2O_3$ | 0.01 | 0.02 | 0.01 | 0.00 | 0.00 | 0.02 | 0.00 |
| SRO | 0.02 | 0.04 | 0.02 | 0.02 | 0.02 | 0.02 | 0.02 |
| BAO | 0.00 | 0.00 | 0.01 | 0.02 | 0.02 | 0.02 | 0.00 |
| PBO | 0.00 | 0.02 | 0.00 | 0.01 | 0.00 | 0.00 | 0.00 |
| $NA_2O$ | 11.82 | 11.60 | 11.58 | 11.76 | 11.71 | 11.64 | 11.87 |
| $K_2O$ | 0.06 | 0.06 | 0.13 | 0.04 | 0.07 | 0.07 | 0.07 |
| $RB_2O$ | 0.05 | 0.05 | 0.09 | 0.06 | 0.06 | 0.03 | 0.06 |
| $CS_2O$ | 0.00 | 0.01 | 0.00 | 0.01 | 0.00 | 0.00 | 0.00 |
| TOTAL | 100.37 | 99.76 | 100.00 | 99.98 | 100.07 | 99.92 | 100.64 |
| $P^{5+}$ | 0.013 | 0.014 | 0.002 | 0.008 | 0.005 | 0.008 | 0.003 |
| $SI^{4+}$ | 2.959 | 2.965 | 2.990 | 2.974 | 2.988 | 2.977 | 2.988 |
| $AL^{3+}$ | 1.029 | 1.022 | 1.012 | 1.019 | 1.008 | 1.016 | 1.008 |
| $MG^{2+}$ | 0.000 | 0.000 | 0.000 | 0.000 | 0.000 | 0.000 | 0.000 |
| $CA^{2+}$ | 0.004 | 0.004 | 0.001 | 0.004 | 0.001 | 0.004 | 0.002 |
| $MN^{2+}$ | 0.000 | 0.000 | 0.001 | 0.000 | 0.000 | 0.000 | 0.001 |
| $FE^{3+}$ | 0.000 | 0.001 | 0.000 | 0.000 | 0.000 | 0.001 | 0.000 |
| $SR^{2+}$ | 0.000 | 0.001 | 0.001 | 0.001 | 0.001 | 0.001 | 0.001 |
| $BA^{2+}$ | 0.000 | 0.000 | 0.000 | 0.000 | 0.000 | 0.000 | 0.000 |
| $PB^{2+}$ | 0.000 | 0.000 | 0.000 | 0.000 | 0.000 | 0.000 | 0.000 |
| $NA^{+}$ | 0.998 | 0.986 | 0.981 | 0.997 | 0.991 | 0.986 | 0.999 |
| $K^{+}$ | 0.003 | 0.003 | 0.008 | 0.002 | 0.004 | 0.004 | 0.004 |
| $RB^{+}$ | 0.001 | 0.001 | 0.003 | 0.002 | 0.002 | 0.001 | 0.002 |
| $CS^{+}$ | 0.000 | 0.000 | 0.000 | 0.000 | 0.000 | 0.000 | 0.000 |
| $\Sigma T$ | 4.000 | 4.001 | 4.004 | 4.001 | 4.000 | 4.001 | 3.999 |
| $TO^{2-}$ | 1.016 | 1.008 | 1.011 | 1.012 | 1.003 | 1.008 | 1.006 |
| Si+2P | 2.985 | 2.993 | 2.993 | 2.989 | 2.997 | 2.994 | 2.993 |
| Si+2P/Al-P | 2.937 | 2.968 | 2.960 | 2.955 | 2.987 | 2.969 | 2.977 |
| $\Sigma M$ | 1.003 | 0.990 | 0.991 | 1.001 | 0.997 | 0.991 | 1.005 |
| $M^{+}$ | 1.011 | 1.002 | 0.996 | 1.010 | 1.000 | 1.001 | 1.009 |
| $M^{*}$ | -0.005 | -0.007 | -0.015 | -0.002 | -0.003 | -0.008 | 0.004 |

**Note:**

**Appendix IV**: Albite (Types A & B) sample compostions (EMPA data)

| **Sample** | 10-25-5 | L-12-G | 86-07-P | 86-07-E | C-096-K | C-045-M | C-107-H |
|---|---|---|---|---|---|---|---|
| **Zone** | 47 | 50 | 50 | 50 | 57 | 60 | 60 |
| **Type** | A | A | A | A | A | A | A |
| **$P_2O_6$** | 0.09 | 0.25 | 0.11 | 0.10 | 0.10 | 0.20 | 0.04 |
| **$SIO_2$** | 68.03 | 68.50 | 68.62 | 68.36 | 68.08 | 67.91 | 68.36 |
| **$AL_2O_3$** | 19.46 | 19.80 | 19.61 | 19.63 | 19.51 | 19.84 | 19.63 |
| **MGO** | 0.00 | 0.00 | 0.00 | 0.00 | 0.00 | 0.00 | 0.00 |
| **CAO** | 0.02 | 0.04 | 0.03 | 0.03 | 0.03 | 0.08 | 0.03 |
| **MNO** | 0.01 | 0.01 | 0.01 | 0.00 | 0.00 | 0.01 | 0.01 |
| **$FE_2O_3$** | 0.00 | 0.02 | 0.00 | 0.01 | 0.01 | 0.01 | 0.00 |
| **SRO** | 0.01 | 0.03 | 0.03 | 0.01 | 0.03 | 0.03 | 0.03 |
| **BAO** | 0.01 | 0.02 | 0.01 | 0.01 | 0.01 | 0.02 | 0.01 |
| **PBO** | 0.01 | 0.01 | 0.01 | 0.00 | 0.01 | 0.01 | 0.00 |
| **$NA_2O$** | 11.69 | 11.88 | 11.67 | 11.62 | 11.74 | 11.90 | 11.70 |
| **$K_2O$** | 0.05 | 0.07 | 0.08 | 0.06 | 0.06 | 0.13 | 0.04 |
| **$RB_2O$** | 0.05 | 0.04 | 0.05 | 0.06 | 0.05 | 0.07 | 0.05 |
| **$CS_2O$** | 0.01 | 0.01 | 0.00 | 0.00 | 0.00 | 0.00 | 0.00 |
| **TOTAL** | 99.43 | 100.66 | 100.22 | 99.90 | 99.62 | 100.21 | 99.90 |
| **$P^{5+}$** | 0.003 | 0.009 | 0.004 | 0.004 | 0.004 | 0.007 | 0.001 |
| **$SI^{4+}$** | 2.989 | 2.975 | 2.990 | 2.988 | 2.987 | 2.967 | 2.990 |
| **$AL^{3+}$** | 1.008 | 1.013 | 1.008 | 1.012 | 1.009 | 1.022 | 1.012 |
| **$MG^{2+}$** | 0.000 | 0.000 | 0.000 | 0.000 | 0.000 | 0.000 | 0.000 |
| **$CA^{2+}$** | 0.001 | 0.002 | 0.001 | 0.001 | 0.002 | 0.004 | 0.001 |
| **$MN^{2+}$** | 0.000 | 0.000 | 0.000 | 0.000 | 0.000 | 0.000 | 0.000 |
| **$FE^{3+}$** | 0.000 | 0.000 | 0.000 | 0.000 | 0.000 | 0.000 | 0.000 |
| **$SR^{2+}$** | 0.000 | 0.001 | 0.001 | 0.000 | 0.001 | 0.001 | 0.001 |
| **$BA^{2+}$** | 0.000 | 0.000 | 0.000 | 0.000 | 0.000 | 0.000 | 0.000 |
| **$PB^{2+}$** | 0.000 | 0.000 | 0.000 | 0.000 | 0.000 | 0.000 | 0.000 |
| **$NA^{+}$** | 0.996 | 1.000 | 0.986 | 0.985 | 0.999 | 1.008 | 0.992 |
| **$K^{+}$** | 0.003 | 0.004 | 0.004 | 0.004 | 0.003 | 0.007 | 0.002 |
| **$RB^{+}$** | 0.001 | 0.001 | 0.001 | 0.002 | 0.001 | 0.002 | 0.001 |
| **$CS^{+}$** | 0.000 | 0.000 | 0.000 | 0.000 | 0.000 | 0.000 | 0.000 |
| **$\Sigma T$** | 4.000 | 3.997 | 4.002 | 4.003 | 3.999 | 3.996 | 4.002 |
| **$TO^{2-}$** | 1.004 | 1.004 | 1.003 | 1.008 | 1.005 | 1.015 | 1.010 |
| **Si+2P** | 2.996 | 2.993 | 2.999 | 2.995 | 2.994 | 2.982 | 2.992 |
| **Si+2P/Al-P** | 2.983 | 2.980 | 2.989 | 2.970 | 2.978 | 2.938 | 2.961 |
| **$\Sigma M$** | 1.000 | 1.006 | 0.992 | 0.990 | 1.003 | 1.017 | 0.996 |
| **$M^{+}$** | 1.003 | 1.012 | 0.995 | 0.994 | 1.008 | 1.027 | 1.000 |
| **$M^{*}$** | -0.002 | 0.007 | -0.008 | -0.015 | 0.003 | 0.013 | -0.010 |

**Note:**

**Appendix IV**: Albite (Types A & B) sample compostions (EMPA data)

| Sample | C-107-J | C-107-F | 76-23-Q | C-R | C-045-B | 76-23-R | C-N |
|---|---|---|---|---|---|---|---|
| Zone | 60 | 60 | 60 | 60 | 60 | 60 | 63 |
| Type | A | A | A | A | A | A | A |
| $P_2O_5$ | 0.16 | 0.31 | 0.19 | 0.10 | 0.07 | 0.15 | 0.15 |
| $SiO_2$ | 68.32 | 68.14 | 68.27 | 68.29 | 68.30 | 68.82 | 68.37 |
| $AL_2O_3$ | 19.74 | 20.05 | 19.63 | 19.87 | 19.61 | 19.72 | 19.81 |
| MGO | 0.00 | 0.00 | 0.00 | 0.00 | 0.00 | 0.00 | 0.00 |
| CAO | 0.09 | 0.11 | 0.04 | 0.07 | 0.03 | 0.08 | 0.06 |
| MNO | 0.01 | 0.01 | 0.00 | 0.00 | 0.01 | 0.02 | 0.01 |
| $FE_2O_3$ | 0.00 | 0.01 | 0.05 | 0.01 | 0.00 | 0.01 | 0.01 |
| SRO | 0.02 | 0.02 | 0.02 | 0.03 | 0.02 | 0.02 | 0.02 |
| BAO | 0.00 | 0.02 | 0.01 | 0.03 | 0.01 | 0.02 | 0.02 |
| PBO | 0.00 | 0.01 | 0.00 | 0.00 | 0.00 | 0.00 | 0.00 |
| $NA_2O$ | 11.73 | 11.86 | 11.74 | 11.65 | 11.81 | 11.88 | 11.66 |
| $K_2O$ | 0.03 | 0.05 | 0.07 | 0.11 | 0.10 | 0.06 | 0.07 |
| $RB_2O$ | 0.05 | 0.06 | 0.04 | 0.06 | 0.05 | 0.03 | 0.05 |
| $CS_2O$ | 0.00 | 0.01 | 0.00 | 0.00 | 0.00 | 0.00 | 0.01 |
| TOTAL | 100.17 | 100.65 | 100.05 | 100.24 | 100.01 | 100.81 | 100.23 |
| $P^{5+}$ | 0.006 | 0.012 | 0.007 | 0.004 | 0.003 | 0.005 | 0.006 |
| $SI^{4+}$ | 2.980 | 2.961 | 2.982 | 2.978 | 2.986 | 2.984 | 2.980 |
| $AL^{3+}$ | 1.015 | 1.027 | 1.010 | 1.022 | 1.011 | 1.008 | 1.018 |
| $MG^{2+}$ | 0.000 | 0.000 | 0.000 | 0.000 | 0.000 | 0.000 | 0.000 |
| $CA^{2+}$ | 0.004 | 0.005 | 0.002 | 0.003 | 0.002 | 0.004 | 0.003 |
| $MN^{2+}$ | 0.000 | 0.000 | 0.000 | 0.000 | 0.000 | 0.001 | 0.000 |
| $FE^{3+}$ | 0.000 | 0.000 | 0.002 | 0.000 | 0.000 | 0.000 | 0.000 |
| $SR^{2+}$ | 0.000 | 0.001 | 0.001 | 0.001 | 0.001 | 0.001 | 0.001 |
| $BA^{2+}$ | 0.000 | 0.000 | 0.000 | 0.001 | 0.000 | 0.000 | 0.000 |
| $PB^{2+}$ | 0.000 | 0.000 | 0.000 | 0.000 | 0.000 | 0.000 | 0.000 |
| $NA^{+}$ | 0.992 | 1.000 | 0.994 | 0.986 | 1.001 | 0.998 | 0.985 |
| $K^{+}$ | 0.002 | 0.003 | 0.004 | 0.006 | 0.005 | 0.003 | 0.004 |
| $RB^{+}$ | 0.001 | 0.002 | 0.001 | 0.002 | 0.001 | 0.001 | 0.002 |
| $CS^{+}$ | 0.000 | 0.000 | 0.000 | 0.000 | 0.000 | 0.000 | 0.000 |
| $\Sigma T$ | 4.001 | 4.000 | 3.999 | 4.003 | 3.999 | 3.997 | 4.003 |
| $TO^{2-}$ | 1.009 | 1.016 | 1.003 | 1.018 | 1.008 | 1.002 | 1.012 |
| Si+2P | 2.992 | 2.984 | 2.996 | 2.985 | 2.991 | 2.994 | 2.992 |
| Si+2P/Al-P | 2.965 | 2.938 | 2.981 | 2.931 | 2.967 | 2.987 | 2.956 |
| $\Sigma M$ | 0.995 | 1.004 | 0.998 | 0.993 | 1.008 | 1.002 | 0.991 |
| $M^{+}$ | 1.005 | 1.016 | 1.003 | 1.003 | 1.013 | 1.011 | 0.998 |
| $M^{*}$ | -0.005 | 0.000 | -0.002 | -0.015 | 0.004 | 0.008 | -0.014 |

**Note:**

**Appendix IV**: Albite (Types A & B) sample compostions (EMPA data)

| Sample | 86-07-H | C-045-J | Poll-2 | Poll-4 | Poll-5 | SLE-24 | L-12-C |
|---|---|---|---|---|---|---|---|
| Zone | 64 | 67 | 80 | 80 | 80 | 12 | 20 |
| Type | A | A | A | A | A | B | B |
| $P_2O_5$ | 0.11 | 0.15 | 0.19 | 0.29 | 0.15 | 0.30 | 0.26 |
| $SiO_2$ | 68.58 | 68.31 | 68.29 | 68.28 | 68.47 | 67.99 | 67.80 |
| $AL_2O_3$ | 19.50 | 19.64 | 19.61 | 19.77 | 19.58 | 19.70 | 19.82 |
| MGO | 0.00 | 0.00 | 0.00 | 0.00 | 0.00 | 0.00 | 0.00 |
| CAO | 0.05 | 0.07 | 0.07 | 0.08 | 0.08 | 0.09 | 0.17 |
| MNO | 0.02 | 0.01 | 0.01 | 0.00 | 0.00 | 0.00 | 0.01 |
| $FE_2O_3$ | 0.00 | 0.01 | 0.00 | 0.01 | 0.00 | 0.01 | 0.01 |
| SRO | 0.02 | 0.02 | 0.02 | 0.06 | 0.04 | 0.02 | 0.02 |
| BAO | 0.03 | 0.03 | 0.03 | 0.02 | 0.04 | 0.03 | 0.03 |
| PBO | 0.01 | 0.02 | 0.00 | 0.01 | 0.02 | 0.01 | 0.01 |
| $NA_2O$ | 11.64 | 11.65 | 11.54 | 11.55 | 11.54 | 11.53 | 11.67 |
| $K_2O$ | 0.07 | 0.08 | 0.13 | 0.05 | 0.08 | 0.03 | 0.05 |
| $RB_2O$ | 0.04 | 0.05 | 0.06 | 0.04 | 0.05 | 0.05 | 0.03 |
| $CS_2O$ | 0.00 | 0.02 | 0.01 | 0.00 | 0.01 | 0.00 | 0.00 |
| TOTAL | 100.06 | 100.04 | 99.95 | 100.16 | 100.04 | 99.78 | 99.88 |
| $P^{5+}$ | 0.004 | 0.006 | 0.007 | 0.010 | 0.005 | 0.011 | 0.010 |
| $SI^{4+}$ | 2.993 | 2.984 | 2.985 | 2.976 | 2.989 | 2.975 | 2.968 |
| $AL^{3+}$ | 1.003 | 1.011 | 1.010 | 1.016 | 1.007 | 1.016 | 1.023 |
| $MG^{2+}$ | 0.000 | 0.000 | 0.000 | 0.000 | 0.000 | 0.000 | 0.000 |
| $CA^{2+}$ | 0.002 | 0.003 | 0.003 | 0.004 | 0.004 | 0.004 | 0.008 |
| $MN^{2+}$ | 0.001 | 0.001 | 0.000 | 0.000 | 0.000 | 0.000 | 0.000 |
| $FE^{3+}$ | 0.000 | 0.000 | 0.000 | 0.001 | 0.000 | 0.001 | 0.000 |
| $SR^{2+}$ | 0.001 | 0.001 | 0.001 | 0.002 | 0.001 | 0.001 | 0.001 |
| $BA^{2+}$ | 0.001 | 0.000 | 0.001 | 0.000 | 0.001 | 0.000 | 0.001 |
| $PB^{2+}$ | 0.000 | 0.000 | 0.000 | 0.000 | 0.000 | 0.000 | 0.000 |
| $NA^{+}$ | 0.985 | 0.987 | 0.978 | 0.976 | 0.976 | 0.979 | 0.990 |
| $K^{+}$ | 0.004 | 0.004 | 0.007 | 0.003 | 0.005 | 0.002 | 0.003 |
| $RB^{+}$ | 0.001 | 0.001 | 0.001 | 0.001 | 0.001 | 0.002 | 0.001 |
| $CS^{+}$ | 0.000 | 0.000 | 0.000 | 0.000 | 0.000 | 0.000 | 0.000 |
| $\Sigma T$ | 4.000 | 4.001 | 4.001 | 4.002 | 4.002 | 4.003 | 4.000 |
| $TO^{2-}$ | 0.999 | 1.006 | 1.003 | 1.005 | 1.002 | 1.005 | 1.013 |
| Si+2P | 3.001 | 2.995 | 2.998 | 2.997 | 3.000 | 2.998 | 2.987 |
| Si+2P/Al-P | 3.003 | 2.978 | 2.988 | 2.979 | 2.994 | 2.981 | 2.949 |
| $\Sigma M$ | 0.990 | 0.992 | 0.987 | 0.980 | 0.982 | 0.982 | 0.994 |
| $M^{+}$ | 0.996 | 1.001 | 0.996 | 0.991 | 0.993 | 0.993 | 1.012 |
| $M^{*}$ | -0.003 | -0.005 | -0.007 | -0.015 | -0.009 | -0.013 | -0.001 |

**Note:**

**Appendix IV**: Albite (Types A & B) sample compostions (EMPA data)

| Sample | L-12-D | 94-10-Q | 95-08-C | 76-23-L | C-033-A | 96-08-JJ | C-022-A |
|---|---|---|---|---|---|---|---|
| Zone | 20 | 20 | 20 | 20 | 20 | 20 | 20 |
| Type | B | B | B | B | B | B | B |
| $P_2O_5$ | 0.32 | 0.08 | 0.27 | 0.12 | 0.27 | 0.19 | 0.10 |
| $SIO_2$ | 67.79 | 68.57 | 67.50 | 68.89 | 67.73 | 68.31 | 69.20 |
| $AL_2O_3$ | 19.90 | 19.84 | 19.63 | 19.81 | 19.87 | 19.68 | 19.67 |
| MGO | 0.00 | 0.00 | 0.00 | 0.00 | 0.00 | 0.00 | 0.00 |
| CAO | 0.20 | 0.04 | 0.13 | 0.08 | 0.14 | 0.06 | 0.02 |
| MNO | 0.01 | 0.00 | 0.00 | 0.01 | 0.01 | 0.01 | 0.01 |
| $FE_2O_3$ | 0.00 | 0.01 | 0.01 | 0.01 | 0.01 | 0.01 | 0.00 |
| SRO | 0.03 | 0.02 | 0.04 | 0.04 | 0.03 | 0.02 | 0.00 |
| BAO | 0.02 | 0.01 | 0.02 | 0.03 | 0.00 | 0.01 | 0.02 |
| PBO | 0.00 | 0.02 | 0.01 | 0.00 | 0.00 | 0.00 | 0.01 |
| $NA_2O$ | 11.62 | 11.81 | 11.61 | 11.79 | 11.63 | 11.82 | 11.87 |
| $K_2O$ | 0.06 | 0.07 | 0.05 | 0.08 | 0.05 | 0.06 | 0.05 |
| $RB_2O$ | 0.05 | 0.06 | 0.05 | 0.06 | 0.04 | 0.05 | 0.05 |
| $CS_2O$ | 0.00 | 0.00 | 0.00 | 0.00 | 0.00 | 0.00 | 0.00 |
| TOTAL | 100.00 | 100.52 | 99.32 | 100.90 | 99.77 | 100.20 | 100.99 |
| $P^{5+}$ | 0.012 | 0.003 | 0.010 | 0.005 | 0.010 | 0.007 | 0.004 |
| $SI^{4+}$ | 2.963 | 2.982 | 2.971 | 2.984 | 2.967 | 2.979 | 2.993 |
| $AL^{3+}$ | 1.026 | 1.017 | 1.019 | 1.012 | 1.026 | 1.012 | 1.003 |
| $MG^{2+}$ | 0.000 | 0.000 | 0.000 | 0.000 | 0.000 | 0.000 | 0.000 |
| $CA^{2+}$ | 0.010 | 0.001 | 0.006 | 0.004 | 0.007 | 0.003 | 0.001 |
| $MN^{2+}$ | 0.000 | 0.000 | 0.000 | 0.001 | 0.000 | 0.000 | 0.000 |
| $FE^{3+}$ | 0.000 | 0.000 | 0.000 | 0.000 | 0.000 | 0.000 | 0.000 |
| $SR^{2+}$ | 0.001 | 0.001 | 0.001 | 0.001 | 0.001 | 0.001 | 0.000 |
| $BA^{2+}$ | 0.000 | 0.000 | 0.000 | 0.001 | 0.000 | 0.000 | 0.000 |
| $PB^{2+}$ | 0.000 | 0.000 | 0.000 | 0.000 | 0.000 | 0.000 | 0.000 |
| $NA^{+}$ | 0.985 | 0.996 | 0.991 | 0.991 | 0.987 | 0.999 | 0.995 |
| $K^{+}$ | 0.003 | 0.004 | 0.003 | 0.004 | 0.003 | 0.004 | 0.003 |
| $RB^{+}$ | 0.001 | 0.002 | 0.001 | 0.002 | 0.001 | 0.001 | 0.001 |
| $CS^{+}$ | 0.000 | 0.000 | 0.000 | 0.000 | 0.000 | 0.000 | 0.000 |
| $\Sigma T$ | 4.001 | 4.001 | 4.000 | 4.000 | 4.002 | 3.998 | 3.999 |
| $TO^{2-}$ | 1.014 | 1.014 | 1.008 | 1.007 | 1.016 | 1.005 | 0.999 |
| Si+2P | 2.987 | 2.987 | 2.991 | 2.993 | 2.986 | 2.993 | 3.000 |
| Si+2P/Al-P | 2.947 | 2.944 | 2.965 | 2.972 | 2.938 | 2.978 | 3.003 |
| $\Sigma M$ | 0.990 | 1.001 | 0.995 | 0.997 | 0.991 | 1.004 | 0.999 |
| $M^{+}$ | 1.011 | 1.006 | 1.010 | 1.008 | 1.006 | 1.011 | 1.002 |
| $M^{*}$ | -0.003 | -0.009 | 0.001 | 0.000 | -0.010 | 0.006 | 0.003 |

**Note:**

**Appendix IV**: Albite (Types A & B) sample compostions (EMPA data)

| Sample | L-12-N | L-12-B | 86-07-Y | 78-21-D | 95-08-N | M-17-I | C-022-Z2 |
|---|---|---|---|---|---|---|---|
| Zone | 20 | 20 | 20 | 20 | 20 | 20 | 20 |
| Type | B | B | B | B | B | B | B |
| $P_2O_5$ | 0.22 | 0.09 | 0.20 | 0.12 | 0.08 | 0.17 | 0.02 |
| $SIO_2$ | 67.95 | 68.85 | 68.72 | 68.95 | 68.51 | 68.70 | 69.43 |
| $AL_2O_3$ | 19.77 | 19.61 | 19.98 | 19.77 | 19.49 | 19.93 | 19.72 |
| MGO | 0.00 | 0.00 | 0.00 | 0.00 | 0.00 | 0.00 | 0.00 |
| CAO | 0.04 | 0.04 | 0.11 | 0.02 | 0.05 | 0.06 | 0.01 |
| MNO | 0.01 | 0.00 | 0.01 | 0.00 | 0.01 | 0.01 | 0.00 |
| $FE_2O_3$ | 0.01 | 0.01 | 0.01 | 0.00 | 0.00 | 0.01 | 0.01 |
| SRO | 0.03 | 0.02 | 0.03 | 0.02 | 0.01 | 0.05 | 0.05 |
| BAO | 0.02 | 0.01 | 0.01 | 0.02 | 0.01 | 0.03 | 0.00 |
| PBO | 0.01 | 0.00 | 0.01 | 0.00 | 0.00 | 0.01 | 0.00 |
| $NA_2O$ | 11.90 | 11.81 | 11.79 | 11.80 | 11.67 | 11.84 | 11.84 |
| $K_2O$ | 0.04 | 0.05 | 0.07 | 0.12 | 0.07 | 0.05 | 0.05 |
| $RB_2O$ | 0.04 | 0.04 | 0.05 | 0.04 | 0.05 | 0.04 | 0.05 |
| $CS_2O$ | 0.00 | 0.00 | 0.01 | 0.00 | 0.01 | 0.00 | 0.00 |
| TOTAL | 100.03 | 100.54 | 100.99 | 100.85 | 99.97 | 100.88 | 101.15 |
| $P^{6+}$ | 0.008 | 0.003 | 0.008 | 0.004 | 0.003 | 0.006 | 0.001 |
| $SI^{4+}$ | 2.971 | 2.992 | 2.974 | 2.987 | 2.993 | 2.977 | 2.998 |
| $AL^{3+}$ | 1.019 | 1.004 | 1.019 | 1.010 | 1.004 | 1.018 | 1.003 |
| $MG^{2+}$ | 0.000 | 0.000 | 0.000 | 0.000 | 0.000 | 0.000 | 0.000 |
| $CA^{2+}$ | 0.002 | 0.002 | 0.005 | 0.001 | 0.002 | 0.003 | 0.001 |
| $MN^{2+}$ | 0.001 | 0.000 | 0.000 | 0.000 | 0.000 | 0.000 | 0.000 |
| $FE^{3+}$ | 0.000 | 0.000 | 0.000 | 0.000 | 0.000 | 0.000 | 0.000 |
| $SR^{2+}$ | 0.001 | 0.001 | 0.001 | 0.001 | 0.000 | 0.002 | 0.001 |
| $BA^{2+}$ | 0.000 | 0.000 | 0.000 | 0.000 | 0.000 | 0.001 | 0.000 |
| $PB^{2+}$ | 0.000 | 0.000 | 0.000 | 0.000 | 0.000 | 0.000 | 0.000 |
| $NA^{+}$ | 1.008 | 0.995 | 0.989 | 0.991 | 0.988 | 0.995 | 0.991 |
| $K^{+}$ | 0.003 | 0.003 | 0.004 | 0.007 | 0.004 | 0.003 | 0.003 |
| $RB^{+}$ | 0.001 | 0.001 | 0.001 | 0.001 | 0.002 | 0.001 | 0.002 |
| $CS^{+}$ | 0.000 | 0.000 | 0.000 | 0.000 | 0.000 | 0.000 | 0.000 |
| $\Sigma T$ | 3.998 | 3.999 | 4.001 | 4.001 | 4.000 | 4.001 | 4.002 |
| $TO^{2-}$ | 1.010 | 1.001 | 1.012 | 1.005 | 1.000 | 1.012 | 1.002 |
| Si+2P | 2.988 | 2.998 | 2.989 | 2.996 | 3.000 | 2.989 | 3.000 |
| Si+2P/Al-P | 2.956 | 2.994 | 2.954 | 2.980 | 2.999 | 2.955 | 2.994 |
| $\Sigma M$ | 1.012 | 0.999 | 0.994 | 0.998 | 0.994 | 0.999 | 0.995 |
| $M^{+}$ | 1.018 | 1.004 | 1.006 | 1.002 | 1.000 | 1.008 | 0.998 |
| $M^{*}$ | 0.007 | 0.002 | -0.006 | -0.003 | -0.001 | -0.004 | -0.005 |

Note:

**Appendix IV**: Albite (Types A & B) sample compostions (EMPA data)

| Sample | C-033-I | C-107-B | C-033-X | C-033-W | C-107-N | 92-11-N | C-107-A |
|---|---|---|---|---|---|---|---|
| Zone | 40 | 40 | 40 | 40 | 40 | 40 | 40 |
| Type | B | B | B | B | B | B | B |
| $P_2O_6$ | 0.13 | 0.22 | 0.35 | 0.16 | 0.11 | 0.31 | 0.32 |
| $SiO_2$ | 68.01 | 68.21 | 67.42 | 68.12 | 68.27 | 67.95 | 68.06 |
| $AL_2O_3$ | 19.60 | 19.76 | 19.91 | 19.64 | 19.75 | 19.70 | 19.88 |
| MGO | 0.00 | 0.00 | 0.00 | 0.00 | 0.00 | 0.00 | 0.00 |
| CAO | 0.02 | 0.07 | 0.17 | 0.12 | 0.10 | 0.11 | 0.10 |
| MNO | 0.02 | 0.00 | 0.02 | 0.00 | 0.00 | 0.01 | 0.01 |
| $FE_2O_3$ | 0.02 | 0.01 | 0.00 | 0.00 | 0.01 | 0.00 | 0.00 |
| SRO | 0.01 | 0.01 | 0.04 | 0.01 | 0.03 | 0.02 | 0.02 |
| BAO | 0.03 | 0.01 | 0.01 | 0.00 | 0.02 | 0.01 | 0.02 |
| PBO | 0.00 | 0.00 | 0.01 | 0.00 | 0.00 | 0.00 | 0.01 |
| $NA_2O$ | 11.71 | 11.73 | 11.53 | 11.69 | 11.80 | 11.67 | 11.82 |
| $K_2O$ | 0.07 | 0.11 | 0.05 | 0.06 | 0.05 | 0.05 | 0.04 |
| $RB_2O$ | 0.04 | 0.04 | 0.06 | 0.04 | 0.04 | 0.04 | 0.07 |
| $CS_2O$ | 0.00 | 0.00 | 0.00 | 0.00 | 0.01 | 0.00 | 0.00 |
| TOTAL | 99.67 | 100.18 | 99.57 | 99.86 | 100.17 | 99.86 | 100.34 |
| $P^{5+}$ | 0.005 | 0.008 | 0.013 | 0.006 | 0.004 | 0.012 | 0.012 |
| $SI^{4+}$ | 2.982 | 2.976 | 2.960 | 2.980 | 2.979 | 2.973 | 2.966 |
| $AL^{3+}$ | 1.013 | 1.016 | 1.030 | 1.013 | 1.016 | 1.016 | 1.021 |
| $MG^{2+}$ | 0.000 | 0.000 | 0.000 | 0.000 | 0.000 | 0.000 | 0.000 |
| $CA^{2+}$ | 0.001 | 0.003 | 0.008 | 0.005 | 0.005 | 0.005 | 0.005 |
| $MN^{2+}$ | 0.001 | 0.000 | 0.001 | 0.000 | 0.000 | 0.000 | 0.000 |
| $FE^{3+}$ | 0.001 | 0.000 | 0.000 | 0.000 | 0.000 | 0.000 | 0.000 |
| $SR^{2+}$ | 0.000 | 0.001 | 0.001 | 0.000 | 0.001 | 0.001 | 0.001 |
| $BA^{2+}$ | 0.000 | 0.000 | 0.000 | 0.000 | 0.000 | 0.000 | 0.000 |
| $PB^{2+}$ | 0.000 | 0.000 | 0.000 | 0.000 | 0.000 | 0.000 | 0.000 |
| $NA^{+}$ | 0.996 | 0.992 | 0.982 | 0.992 | 0.998 | 0.990 | 0.999 |
| $K^{+}$ | 0.004 | 0.006 | 0.003 | 0.004 | 0.003 | 0.003 | 0.002 |
| $RB^{+}$ | 0.001 | 0.001 | 0.002 | 0.001 | 0.001 | 0.001 | 0.002 |
| $CS^{+}$ | 0.000 | 0.000 | 0.000 | 0.000 | 0.000 | 0.000 | 0.000 |
| $\Sigma T$ | 4.000 | 4.000 | 4.003 | 4.000 | 4.000 | 4.000 | 3.999 |
| $TO^{2-}$ | 1.009 | 1.008 | 1.017 | 1.007 | 1.012 | 1.004 | 1.009 |
| Si+2P | 2.992 | 2.992 | 2.986 | 2.992 | 2.987 | 2.996 | 2.989 |
| Si+2P/Al-P | 2.964 | 2.969 | 2.936 | 2.971 | 2.950 | 2.983 | 2.962 |
| $\Sigma M$ | 1.001 | 0.999 | 0.986 | 0.997 | 1.002 | 0.994 | 1.003 |
| $M^{+}$ | 1.004 | 1.007 | 1.005 | 1.008 | 1.014 | 1.005 | 1.015 |
| $M^{*}$ | -0.005 | 0.000 | -0.012 | 0.001 | 0.001 | 0.001 | 0.005 |

**Note:**

**Appendix IV**: Albite (Types A & B) sample compostions (EMPA data)

| Sample | C-096-F | 92-11-A | 92-11-M | C-Y | C-U | C-022-O | 92-11-B |
|---|---|---|---|---|---|---|---|
| Zone | 40 | 40 | 40 | 40 | 40 | 40 | 40 |
| Type | B | B | B | B | B | B | B |
| $P_2O_5$ | 0.11 | 0.18 | 0.21 | 0.24 | 0.26 | 0.04 | 0.05 |
| $SiO_2$ | 69.28 | 68.16 | 67.68 | 68.81 | 68.32 | 68.67 | 68.74 |
| $AL_2O_3$ | 19.81 | 19.60 | 19.56 | 19.78 | 19.89 | 19.81 | 19.49 |
| MGO | 0.00 | 0.00 | 0.00 | 0.00 | 0.00 | 0.00 | 0.00 |
| CAO | 0.01 | 0.08 | 0.05 | 0.03 | 0.06 | 0.06 | 0.03 |
| MNO | 0.01 | 0.00 | 0.02 | 0.01 | 0.01 | 0.01 | 0.00 |
| $FE_2O_3$ | 0.00 | 0.00 | 0.01 | 0.01 | 0.01 | 0.01 | 0.00 |
| SRO | 0.02 | 0.03 | 0.02 | 0.02 | 0.04 | 0.01 | 0.02 |
| BAO | 0.03 | 0.02 | 0.02 | 0.01 | 0.02 | 0.00 | 0.00 |
| PBO | 0.00 | 0.00 | 0.00 | 0.01 | 0.00 | 0.03 | 0.00 |
| $NA_2O$ | 11.79 | 11.77 | 11.73 | 11.79 | 11.69 | 11.87 | 11.73 |
| $K_2O$ | 0.06 | 0.07 | 0.07 | 0.05 | 0.05 | 0.06 | 0.06 |
| $RB_2O$ | 0.02 | 0.04 | 0.05 | 0.07 | 0.05 | 0.05 | 0.06 |
| $CS_2O$ | 0.01 | 0.00 | 0.01 | 0.01 | 0.00 | 0.00 | 0.00 |
| TOTAL | 101.12 | 99.97 | 99.41 | 100.84 | 100.39 | 100.62 | 100.19 |
| $P^{5+}$ | 0.004 | 0.007 | 0.008 | 0.009 | 0.009 | 0.001 | 0.002 |
| $SI^{4+}$ | 2.991 | 2.980 | 2.976 | 2.981 | 2.973 | 2.984 | 2.997 |
| $AL^{3+}$ | 1.008 | 1.010 | 1.014 | 1.010 | 1.020 | 1.014 | 1.001 |
| $MG^{2+}$ | 0.000 | 0.000 | 0.000 | 0.000 | 0.000 | 0.000 | 0.000 |
| $CA^{2+}$ | 0.000 | 0.004 | 0.002 | 0.001 | 0.003 | 0.003 | 0.001 |
| $MN^{2+}$ | 0.001 | 0.000 | 0.001 | 0.000 | 0.000 | 0.000 | 0.000 |
| $FE^{3+}$ | 0.000 | 0.000 | 0.000 | 0.000 | 0.000 | 0.000 | 0.000 |
| $SR^{2+}$ | 0.001 | 0.001 | 0.001 | 0.001 | 0.001 | 0.000 | 0.001 |
| $BA^{2+}$ | 0.001 | 0.001 | 0.000 | 0.000 | 0.000 | 0.000 | 0.000 |
| $PB^{2+}$ | 0.000 | 0.000 | 0.000 | 0.000 | 0.000 | 0.000 | 0.000 |
| $NA^{+}$ | 0.987 | 0.998 | 1.000 | 0.991 | 0.986 | 1.000 | 0.991 |
| $K^{+}$ | 0.003 | 0.004 | 0.004 | 0.003 | 0.003 | 0.003 | 0.003 |
| $RB^{+}$ | 0.001 | 0.001 | 0.001 | 0.002 | 0.002 | 0.001 | 0.002 |
| $CS^{+}$ | 0.000 | 0.000 | 0.000 | 0.000 | 0.000 | 0.000 | 0.000 |
| $\Sigma T$ | 4.003 | 3.997 | 3.998 | 4.000 | 4.002 | 3.999 | 3.999 |
| $TO^{2-}$ | 1.004 | 1.004 | 1.006 | 1.002 | 1.011 | 1.013 | 0.999 |
| Si+2P | 2.999 | 2.994 | 2.992 | 2.999 | 2.992 | 2.987 | 3.000 |
| Si+2P/Al-P | 2.987 | 2.983 | 2.972 | 2.993 | 2.960 | 2.948 | 3.002 |
| $\Sigma M$ | 0.991 | 1.003 | 1.005 | 0.996 | 0.991 | 1.005 | 0.996 |
| $M^{+}$ | 0.993 | 1.013 | 1.011 | 1.000 | 0.998 | 1.012 | 1.000 |
| $M^{*}$ | -0.012 | 0.010 | 0.005 | -0.002 | -0.012 | -0.001 | 0.001 |

**Note:**

**Appendix IV**: Albite (Types A & B) sample compostions (EMPA data)

| Sample | C-045-S | C-022-N | C-033-O | M-17-F | 96-08-JI | 95-08-B | C-033-Q |
|---|---|---|---|---|---|---|---|
| Zone | 40 | 40 | 40 | 40 | 45 | 45 | 45 |
| Type | B | B | B | B | B | B | B |
| $P_2O_5$ | 0.07 | 0.19 | 0.20 | 0.01 | 0.04 | 0.31 | 0.24 |
| $SiO_2$ | 68.93 | 68.91 | 68.46 | 69.04 | 69.16 | 67.38 | 68.04 |
| $AL_2O_3$ | 19.75 | 19.87 | 19.71 | 19.78 | 19.77 | 19.64 | 19.57 |
| MGO | 0.00 | 0.00 | 0.00 | 0.00 | 0.00 | 0.00 | 0.00 |
| CAO | 0.01 | 0.10 | 0.09 | 0.06 | 0.04 | 0.07 | 0.08 |
| MNO | 0.02 | 0.01 | 0.01 | 0.00 | 0.01 | 0.01 | 0.00 |
| $FE_2O_3$ | 0.00 | 0.00 | 0.00 | 0.00 | 0.02 | 0.01 | 0.00 |
| SRO | 0.04 | 0.01 | 0.02 | 0.03 | 0.02 | 0.01 | 0.03 |
| BAO | 0.00 | 0.00 | 0.00 | 0.02 | 0.03 | 0.02 | 0.02 |
| PBO | 0.02 | 0.00 | 0.00 | 0.01 | 0.00 | 0.00 | 0.00 |
| $NA_2O$ | 11.89 | 11.71 | 11.61 | 11.94 | 11.98 | 11.75 | 11.59 |
| $K_2O$ | 0.04 | 0.13 | 0.06 | 0.03 | 0.08 | 0.04 | 0.05 |
| $RB_2O$ | 0.05 | 0.04 | 0.05 | 0.04 | 0.06 | 0.02 | 0.07 |
| $CS_2O$ | 0.01 | 0.02 | 0.01 | 0.00 | 0.00 | 0.00 | 0.00 |
| TOTAL | 100.80 | 100.97 | 100.22 | 100.95 | 101.18 | 99.25 | 99.71 |
| $P^{5+}$ | 0.003 | 0.007 | 0.007 | 0.000 | 0.002 | 0.011 | 0.009 |
| $Si^{4+}$ | 2.988 | 2.982 | 2.983 | 2.990 | 2.989 | 2.967 | 2.981 |
| $AL^{3+}$ | 1.009 | 1.013 | 1.012 | 1.009 | 1.007 | 1.019 | 1.011 |
| $MG^{2+}$ | 0.000 | 0.000 | 0.000 | 0.000 | 0.000 | 0.000 | 0.000 |
| $CA^{2+}$ | 0.000 | 0.005 | 0.004 | 0.003 | 0.002 | 0.003 | 0.003 |
| $MN^{2+}$ | 0.001 | 0.001 | 0.000 | 0.000 | 0.001 | 0.000 | 0.000 |
| $FE^{3+}$ | 0.000 | 0.000 | 0.000 | 0.000 | 0.001 | 0.000 | 0.000 |
| $SR^{2+}$ | 0.001 | 0.001 | 0.001 | 0.001 | 0.001 | 0.000 | 0.001 |
| $BA^{2+}$ | 0.000 | 0.000 | 0.000 | 0.000 | 0.001 | 0.001 | 0.001 |
| $PB^{2+}$ | 0.000 | 0.000 | 0.000 | 0.000 | 0.000 | 0.000 | 0.000 |
| $NA^{+}$ | 1.000 | 0.983 | 0.981 | 1.002 | 1.004 | 1.003 | 0.985 |
| $K^{+}$ | 0.003 | 0.007 | 0.003 | 0.002 | 0.005 | 0.002 | 0.003 |
| $RB^{+}$ | 0.002 | 0.001 | 0.001 | 0.001 | 0.002 | 0.001 | 0.002 |
| $CS^{+}$ | 0.000 | 0.001 | 0.000 | 0.000 | 0.000 | 0.000 | 0.000 |
| $\Sigma T$ | 4.000 | 4.002 | 4.003 | 3.999 | 3.997 | 3.998 | 4.000 |
| $TO^{2-}$ | 1.007 | 1.006 | 1.005 | 1.009 | 1.006 | 1.008 | 1.002 |
| Si+2P | 2.993 | 2.996 | 2.998 | 2.990 | 2.992 | 2.990 | 2.998 |
| Si+2P/Al-P | 2.974 | 2.978 | 2.983 | 2.963 | 2.974 | 2.967 | 2.992 |
| $\Sigma M$ | 1.004 | 0.991 | 0.986 | 1.005 | 1.010 | 1.007 | 0.989 |
| $M^{+}$ | 1.006 | 1.002 | 0.995 | 1.013 | 1.015 | 1.015 | 0.999 |
| $M^{*}$ | -0.001 | -0.004 | -0.010 | 0.003 | 0.008 | 0.008 | -0.003 |

**Note:**

**Appendix IV**: Albite (Types A & B) sample compostions (EMPA data)

| Sample | 96-08-JC | B-06-B | 92-11-O | B-06-E | 91-16-JD | C-D | 95-08-H |
|---|---|---|---|---|---|---|---|
| Zone | 50 | 50 | 50 | 50 | 50 | 50 | 50 |
| Type | B | B | B | B | B | B | B |
| $P_2O_5$ | 0.06 | 0.18 | 0.20 | 0.35 | 0.16 | 0.14 | 0.09 |
| $SiO_2$ | 68.34 | 67.89 | 68.29 | 67.98 | 68.73 | 68.38 | 68.13 |
| $AL_2O_3$ | 19.51 | 19.60 | 19.58 | 19.77 | 19.76 | 19.71 | 19.59 |
| MGO | 0.00 | 0.01 | 0.00 | 0.00 | 0.00 | 0.00 | 0.00 |
| CAO | 0.05 | 0.11 | 0.05 | 0.11 | 0.06 | 0.07 | 0.06 |
| MNO | 0.01 | 0.00 | 0.01 | 0.00 | 0.01 | 0.01 | 0.01 |
| $FE_2O_3$ | 0.00 | 0.00 | 0.00 | 0.00 | 0.00 | 0.01 | 0.00 |
| SRO | 0.02 | 0.02 | 0.04 | 0.03 | 0.02 | 0.03 | 0.02 |
| BAO | 0.03 | 0.03 | 0.04 | 0.02 | 0.03 | 0.03 | 0.01 |
| PBO | 0.01 | 0.02 | 0.01 | 0.00 | 0.01 | 0.01 | 0.03 |
| $NA_2O$ | 11.77 | 11.61 | 11.76 | 11.66 | 11.74 | 11.62 | 11.70 |
| $K_2O$ | 0.04 | 0.11 | 0.06 | 0.06 | 0.05 | 0.07 | 0.07 |
| $RB_2O$ | 0.06 | 0.06 | 0.04 | 0.03 | 0.04 | 0.05 | 0.05 |
| $CS_2O$ | 0.00 | 0.00 | 0.00 | 0.00 | 0.00 | 0.00 | 0.00 |
| TOTAL | 99.89 | 99.65 | 100.06 | 100.01 | 100.60 | 100.12 | 99.76 |
| $P^{5+}$ | 0.002 | 0.007 | 0.007 | 0.013 | 0.006 | 0.005 | 0.003 |
| $SI^{4+}$ | 2.991 | 2.979 | 2.983 | 2.969 | 2.984 | 2.984 | 2.985 |
| $AL^{3+}$ | 1.006 | 1.014 | 1.008 | 1.018 | 1.011 | 1.013 | 1.012 |
| $MG^{2+}$ | 0.000 | 0.001 | 0.000 | 0.000 | 0.000 | 0.000 | 0.000 |
| $CA^{2+}$ | 0.002 | 0.005 | 0.002 | 0.006 | 0.003 | 0.003 | 0.003 |
| $MN^{2+}$ | 0.000 | 0.000 | 0.000 | 0.000 | 0.000 | 0.000 | 0.000 |
| $FE^{3+}$ | 0.000 | 0.000 | 0.000 | 0.000 | 0.000 | 0.000 | 0.000 |
| $SR^{2+}$ | 0.001 | 0.001 | 0.001 | 0.001 | 0.000 | 0.001 | 0.001 |
| $BA^{2+}$ | 0.001 | 0.001 | 0.001 | 0.000 | 0.001 | 0.000 | 0.000 |
| $PB^{2+}$ | 0.000 | 0.000 | 0.000 | 0.000 | 0.000 | 0.000 | 0.000 |
| $NA^{+}$ | 0.998 | 0.988 | 0.996 | 0.988 | 0.988 | 0.983 | 0.994 |
| $K^{+}$ | 0.002 | 0.006 | 0.003 | 0.003 | 0.003 | 0.004 | 0.004 |
| $RB^{+}$ | 0.002 | 0.002 | 0.001 | 0.001 | 0.001 | 0.001 | 0.001 |
| $CS^{+}$ | 0.000 | 0.000 | 0.000 | 0.000 | 0.000 | 0.000 | 0.000 |
| $\Sigma T$ | 3.998 | 3.999 | 3.998 | 4.000 | 4.001 | 4.002 | 4.000 |
| $TO^{2-}$ | 1.004 | 1.007 | 1.001 | 1.005 | 1.005 | 1.008 | 1.009 |
| Si+2P | 2.995 | 2.992 | 2.997 | 2.995 | 2.996 | 2.994 | 2.992 |
| Si+2P/Al-P | 2.983 | 2.971 | 2.995 | 2.981 | 2.980 | 2.968 | 2.966 |
| $\Sigma M$ | 1.002 | 0.996 | 1.000 | 0.991 | 0.992 | 0.989 | 0.998 |
| $M^{+}$ | 1.008 | 1.010 | 1.008 | 1.005 | 0.999 | 0.998 | 1.006 |
| $M^{*}$ | 0.004 | 0.003 | 0.007 | 0.000 | -0.007 | -0.011 | -0.002 |

**Note:**

**Appendix IV**: Albite (Types A & B) sample compostions (EMPA data)

| Sample | C-G | C-E | 95-08-J | 92-11-H | C-033-U | C-K | 92-11-P |
|---|---|---|---|---|---|---|---|
| Zone | 50 | 50 | 50 | 60 | 60 | 63 | 70 |
| Type | B | B | B | B | B | B | B |
| $P_2O_6$ | 0.27 | 0.22 | 0.09 | 0.12 | 0.02 | 0.24 | 0.00 |
| $SIO_2$ | 68.48 | 68.54 | 68.26 | 68.11 | 68.16 | 68.37 | 67.85 |
| $AL_2O_3$ | 19.81 | 19.65 | 19.45 | 19.50 | 19.38 | 19.67 | 19.25 |
| MGO | 0.00 | 0.00 | 0.00 | 0.00 | 0.00 | 0.00 | 0.00 |
| CAO | 0.09 | 0.07 | 0.02 | 0.05 | 0.02 | 0.05 | 0.06 |
| MNO | 0.01 | 0.01 | 0.01 | 0.01 | 0.00 | 0.01 | 0.02 |
| $FE_2O_3$ | 0.01 | 0.01 | 0.01 | 0.00 | 0.01 | 0.02 | 0.04 |
| SRO | 0.03 | 0.02 | 0.00 | 0.01 | 0.01 | 0.03 | 0.02 |
| BAO | 0.01 | 0.02 | 0.02 | 0.03 | 0.00 | 0.01 | 0.02 |
| PBO | 0.00 | 0.01 | 0.02 | 0.00 | 0.01 | 0.01 | 0.00 |
| $NA_2O$ | 11.76 | 11.73 | 11.65 | 11.74 | 11.64 | 11.79 | 11.66 |
| $K_2O$ | 0.05 | 0.06 | 0.04 | 0.06 | 0.05 | 0.06 | 0.08 |
| $RB_2O$ | 0.01 | 0.05 | 0.05 | 0.05 | 0.05 | 0.06 | 0.06 |
| $CS_2O$ | 0.00 | 0.01 | 0.00 | 0.00 | 0.00 | 0.00 | 0.00 |
| TOTAL | 100.54 | 100.38 | 99.63 | 99.67 | 99.35 | 100.32 | 99.04 |
| $P^{5+}$ | 0.010 | 0.008 | 0.003 | 0.004 | 0.001 | 0.009 | 0.000 |
| $SI^{4+}$ | 2.975 | 2.983 | 2.992 | 2.986 | 2.997 | 2.979 | 2.995 |
| $AL^{3+}$ | 1.014 | 1.008 | 1.004 | 1.008 | 1.004 | 1.010 | 1.002 |
| $MG^{2+}$ | 0.000 | 0.000 | 0.000 | 0.000 | 0.000 | 0.000 | 0.000 |
| $CA^{2+}$ | 0.004 | 0.003 | 0.001 | 0.002 | 0.001 | 0.002 | 0.003 |
| $MN^{2+}$ | 0.000 | 0.000 | 0.000 | 0.000 | 0.000 | 0.000 | 0.001 |
| $FE^{3+}$ | 0.001 | 0.000 | 0.000 | 0.000 | 0.000 | 0.001 | 0.002 |
| $SR^{2+}$ | 0.001 | 0.001 | 0.000 | 0.000 | 0.000 | 0.001 | 0.001 |
| $BA^{2+}$ | 0.000 | 0.000 | 0.000 | 0.001 | 0.000 | 0.000 | 0.001 |
| $PB^{2+}$ | 0.000 | 0.000 | 0.000 | 0.000 | 0.000 | 0.000 | 0.000 |
| $NA^{+}$ | 0.991 | 0.990 | 0.990 | 0.998 | 0.992 | 0.996 | 0.998 |
| $K^{+}$ | 0.003 | 0.003 | 0.002 | 0.003 | 0.003 | 0.003 | 0.004 |
| $RB^{+}$ | 0.000 | 0.001 | 0.001 | 0.002 | 0.001 | 0.002 | 0.002 |
| $CS^{+}$ | 0.000 | 0.000 | 0.000 | 0.000 | 0.000 | 0.000 | 0.000 |
| $\Sigma T$ | 3.999 | 3.999 | 4.000 | 3.998 | 4.001 | 3.997 | 3.997 |
| $TO^{2-}$ | 1.004 | 1.000 | 1.001 | 1.003 | 1.003 | 1.001 | 1.002 |
| Si+2P | 2.995 | 2.999 | 2.999 | 2.995 | 2.998 | 2.996 | 2.995 |
| Si+2P/Al-P | 2.981 | 2.999 | 2.995 | 2.985 | 2.987 | 2.990 | 2.986 |
| $\Sigma M$ | 0.994 | 0.995 | 0.994 | 1.003 | 0.996 | 1.001 | 1.003 |
| $M^{+}$ | 1.005 | 1.002 | 0.997 | 1.008 | 0.998 | 1.009 | 1.011 |
| $M^{*}$ | 0.000 | 0.002 | -0.005 | 0.005 | -0.005 | 0.007 | 0.008 |

**Note:**

**Appendix IV**: Albite (Types A & B) sample compostions (EMPA data)

| Sample | C-F | Poll-6 | 12-15-15 | Poll-CsA-1 | 12-15-22 | 1C-10 |
|---|---|---|---|---|---|---|
| Zone | 70 | 80 | 80 | 80 | 90 | 90 |
| Type | B | B | B | B | B | B |
| $P_2O_6$ | 0.23 | 0.16 | 0.03 | 0.03 | 0.05 | 0.17 |
| $SiO_2$ | 68.92 | 67.84 | 68.90 | 68.54 | 68.77 | 68.37 |
| $AL_2O_3$ | 19.77 | 19.58 | 19.50 | 19.43 | 19.22 | 19.57 |
| MGO | 0.00 | 0.00 | 0.00 | 0.00 | 0.00 | 0.00 |
| CAO | 0.05 | 0.05 | 0.01 | 0.04 | 0.03 | 0.06 |
| MNO | 0.00 | 0.01 | 0.00 | 0.01 | 0.01 | 0.02 |
| $FE_2O_3$ | 0.01 | 0.01 | 0.01 | 0.00 | 0.00 | 0.01 |
| SRO | 0.02 | 0.02 | 0.01 | 0.05 | 0.03 | 0.01 |
| BAO | 0.02 | 0.05 | 0.00 | 0.01 | 0.01 | 0.00 |
| PBO | 0.01 | 0.01 | 0.03 | 0.00 | 0.00 | 0.01 |
| $NA_2O$ | 11.81 | 11.60 | 11.99 | 11.63 | 11.74 | 11.91 |
| $K_2O$ | 0.05 | 0.05 | 0.07 | 0.05 | 0.07 | 0.06 |
| $RB_2O$ | 0.03 | 0.05 | 0.05 | 0.05 | 0.06 | 0.05 |
| $CS_2O$ | 0.02 | 0.00 | 0.00 | 0.01 | 0.00 | 0.00 |
| TOTAL | 100.94 | 99.43 | 100.56 | 99.84 | 99.97 | 100.24 |
| $P^{6+}$ | 0.008 | 0.006 | 0.001 | 0.001 | 0.002 | 0.006 |
| $SI^{4+}$ | 2.983 | 2.981 | 2.996 | 2.998 | 3.004 | 2.982 |
| $AL^{3+}$ | 1.008 | 1.014 | 0.999 | 1.001 | 0.990 | 1.006 |
| $MG^{2+}$ | 0.000 | 0.000 | 0.000 | 0.000 | 0.000 | 0.000 |
| $CA^{2+}$ | 0.002 | 0.002 | 0.000 | 0.001 | 0.001 | 0.003 |
| $MN^{2+}$ | 0.000 | 0.000 | 0.000 | 0.000 | 0.000 | 0.001 |
| $FE^{3+}$ | 0.000 | 0.000 | 0.000 | 0.000 | 0.000 | 0.000 |
| $SR^{2+}$ | 0.000 | 0.001 | 0.001 | 0.001 | 0.001 | 0.001 |
| $BA^{2+}$ | 0.000 | 0.001 | 0.000 | 0.000 | 0.000 | 0.000 |
| $PB^{2+}$ | 0.000 | 0.000 | 0.001 | 0.000 | 0.000 | 0.000 |
| $NA^{+}$ | 0.991 | 0.989 | 1.010 | 0.986 | 0.994 | 1.007 |
| $K^{+}$ | 0.003 | 0.003 | 0.004 | 0.003 | 0.004 | 0.003 |
| $RB^{+}$ | 0.001 | 0.001 | 0.001 | 0.001 | 0.002 | 0.001 |
| $CS^{+}$ | 0.000 | 0.000 | 0.000 | 0.000 | 0.000 | 0.000 |
| $\Sigma T$ | 3.999 | 4.001 | 3.995 | 4.000 | 3.995 | 3.994 |
| $TO^{2-}$ | 1.000 | 1.008 | 0.999 | 1.000 | 0.988 | 1.000 |
| Si+2P | 2.999 | 2.993 | 2.997 | 3.000 | 3.007 | 2.995 |
| Si+2P/Al-P | 2.997 | 2.968 | 3.001 | 2.999 | 3.044 | 2.995 |
| $\Sigma M$ | 0.995 | 0.993 | 1.015 | 0.990 | 1.000 | 1.012 |
| $M^{+}$ | 1.001 | 1.000 | 1.017 | 0.995 | 1.003 | 1.019 |
| $M^{*}$ | 0.001 | -0.008 | 0.018 | -0.005 | 0.015 | 0.019 |

**Note:**

**Appendix V:** Wet chemistry sample compositions. Element values in ppm. *Ga contents systematically low - see text for details

| Sample | Zone | Type | Ba | Ca | Ga* | Li | P | Sr | Rb | Cs | K | Na | K/Rb | K/Cs | Rb/Cs | K/Na | K/Ba |
|---|---|---|---|---|---|---|---|---|---|---|---|---|---|---|---|---|---|
| 94-10-R | 10 | 1 | 290 | 430 | 48 | 70 | 1523 | 111 | 10220 | 829 | 111826 | 14701 | 10.9 | 135 | 12.3 | 7.6 | 386 |
| SLE-18 | 12 | 1 | 59 | 780 | 49 | 95 | 1123 | 119 | 14379 | 697 | 94546 | 21566 | 6.6 | 136 | 20.6 | 4.4 | 1614 |
| SLW-1A | 12 | 1 | 166 | 944 | 50 | 44 | 1519 | 148 | 15724 | 1420 | 93944 | 23221 | 6.0 | 66 | 11.1 | 4.0 | 565 |
| SLW-1B | 12 | 1 | 257 | 1002 | 51 | 54 | 1066 | 150 | 19319 | 1623 | 104843 | 14127 | 5.4 | 65 | 11.9 | 7.4 | 408 |
| SLW-1C | 12 | 1 | 130 | 1476 | 50 | 49 | 1693 | 135 | 11904 | 659 | 100151 | 19889 | 8.4 | 152 | 18.1 | 5.0 | 773 |
| SLW-2A2 | 12 | 1 | 174 | 1057 | 0 | 51 | 1711 | 138 | 14398 | 963 | 99161 | 17828 | 6.9 | 103 | 14.9 | 5.6 | 571 |
| SLW-2B | 12 | 1 | 73 | 1361 | 56 | 104 | 1717 | 164 | 17348 | 1178 | 104477 | 15411 | 6.0 | 89 | 14.7 | 6.8 | 1431 |
| SLW-0D | 12 | 1 | 56 | 348 | 41 | 52 | 1464 | 136 | 14003 | 765 | 98369 | 19346 | 7.0 | 129 | 18.3 | 5.1 | 1768 |
| L-12-E | 20 | 1 | 116 | 406 | 49 | 25 | 1432 | 82 | 6936 | 686 | 84981 | 23341 | 12.3 | 124 | 10.1 | 3.6 | 732 |
| 12-15-2A | 20 | 1 | 40 | 1306 | 59 | 189 | 2083 | 149 | 16995 | 1255 | 97758 | 12522 | 5.8 | 78 | 13.5 | 7.8 | 2466 |
| 12-15-2B | 20 | 1 | 70 | 853 | 49 | 130 | 1760 | 136 | 16727 | 1073 | 104688 | 10717 | 6.3 | 98 | 15.6 | 9.8 | 1498 |
| 12-15-2C | 20 | 1 | 18 | 1317 | 50 | 263 |  | 144 | 17363 | 868 | 94983 | 15701 | 5.5 | 109 | 20.0 | 6.0 | 5149 |
| 12-15-2E | 20 | 1 | 41 | 1142 | 66 | 179 | 2780 | 166 | 20067 | 1078 | 97095 | 13743 | 4.8 | 90 | 18.6 | 7.1 | 2346 |
| 12-15-3A | 20 | 1 | 102 | 767 | 66 | 113 | 1841 | 139 | 16077 | 1052 | 100087 | 11797 | 6.2 | 95 | 15.3 | 8.5 | 983 |
| 12-15-3B | 20 | 1 | 172 | 644 | 60 | 147 | 2057 | 149 | 17396 | 1025 | 99333 | 11811 | 5.7 | 97 | 17.0 | 8.4 | 577 |
| 12-15-3C | 20 | 1 | 17 | 1012 | 48 | 149 | 2238 | 150 | 16494 | 928 | 95108 | 16199 | 5.8 | 102 | 17.8 | 5.9 | 5560 |
| L-12-F | 20 | 1 | 10 | 443 | 51 | 102 | 628 | 91 | 10865 | 542 | 95063 | 16646 | 8.7 | 176 | 20.1 | 5.7 | 9671 |
| L-12-O | 20 | 1 | 25 | 429 | 45 | 111 | 1404 | 108 | 13550 | 997 | 99870 | 14974 | 7.4 | 100 | 13.6 | 6.7 | 3958 |
| C-A | 20 | 1 | 32 | 960 | 51 | 183 | 1805 | 94 | 10126 | 673 | 103462 | 15046 | 10.2 | 154 | 15.1 | 6.9 | 3212 |
| C-B | 20 | 1 | 15 | 781 | 68 | 188 | 2102 | 161 | 15142 | 1331 | 104609 | 12679 | 6.9 | 79 | 11.4 | 8.3 | 6802 |
| 76-05-A | 20 | 1 | 24 | 493 | 48 | 108 | 1643 | 100 | 10325 | 897 | 100459 | 17055 | 9.7 | 112 | 11.5 | 5.9 | 4222 |
| 76-05-I | 20 | 1 | 49 | 815 | 48 | 113 | 1725 | 85 | 9811 | 694 | 103161 | 18136 | 10.5 | 149 | 14.1 | 5.7 | 2106 |
| 76-05-K | 20 | 1 | 76 | 291 | 43 | 165 | 1547 | 124 | 16790 | 1314 | 117807 | 8060 | 7.0 | 90 | 12.8 | 14.6 | 1553 |
| C-090-A | 20 | 1 | 15 | 507 | 54 | 173 | 1838 | 124 | 18636 | 1773 | 110316 | 7893 | 5.9 | 62 | 10.5 | 14.0 | 7261 |
| C-090-B | 20 | 1 | 13 | 624 | 58 | 128 | 1891 | 128 | 19879 | 1924 | 103502 | 12152 | 5.2 | 54 | 10.3 | 8.5 | 7877 |
| C-090-Q | 20 | 1 | 5 | 479 | 52 | 242 | 1847 | 108 | 15055 | 1210 | 106433 | 10256 | 7.1 | 88 | 12.4 | 10.4 | 20025 |
| C-090-S | 20 | 1 | 15 | 992 | 54 | 239 | 1846 | 74 | 11649 | 1187 | 91822 | 18024 | 7.9 | 77 | 9.8 | 5.1 | 6078 |
| C-045-V | 20 | 1 | 58 | 848 | 46 | 91 | 1736 | 124 | 11974 | 1253 | 97707 | 19093 | 8.2 | 78 | 9.6 | 5.1 | 1674 |
| C-096-A | 20 | 1 | 223 | 641 | 57 | 96 | 1529 | 138 | 13884 | 1486 | 103805 | 14101 | 7.5 | 70 | 9.3 | 7.4 | 465 |
| C-096-C | 20 | 1 | 77 | 660 | 48 | 106 | 1528 | 75 | 10886 | 1070 | 91341 | 17136 | 8.4 | 85 | 10.2 | 5.3 | 1183 |
| 76-23-N | 20 | 1 | 57 | 357 | 46 | 115 | 1664 | 58 | 7214 | 371 | 97240 | 20754 | 13.5 | 262 | 19.4 | 4.7 | 1715 |
| 76-23-O | 20 | 1 | 92 | 373 | 46 | 79 | 1635 | 61 | 6842 | 384 | 97414 | 21437 | 14.2 | 254 | 17.8 | 4.5 | 1062 |

**Appendix V:** Wet chemistry sample compositions. Element values in ppm. *Ga contents systematically low - see text for details

| Sample | Zone | Type | Ba | Ca | Ga* | Li | P | Sr | Rb | Cs | K | Na | K/Rb | K/Cs | Rb/Cs | K/Na | K/Ba |
|---|---|---|---|---|---|---|---|---|---|---|---|---|---|---|---|---|---|
| 78-21-B | 20 | 1 | 12 | 499 | 46 | 144 | 1736 | 105 | 12980 | 1194 | 102880 | 11891 | 7.9 | 86 | 10.9 | 8.7 | 8408 |
| 78-21-G | 20 | 1 | 133 | 342 | 52 | 234 | 1606 | 93 | 8568 | 908 | 93358 | 18820 | 10.9 | 103 | 9.4 | 5.0 | 703 |
| 78-21-H | 20 | 1 | 114 | 560 | 45 | 123 | 1549 | 84 | 7675 | 542 | 96704 | 20132 | 12.6 | 179 | 14.2 | 4.8 | 852 |
| M-17-K | 20 | 1 | 8 | 492 | 55 | 121 | 1564 | 125 | 14418 | 930 | 101535 | 13138 | 7.0 | 109 | 15.5 | 7.7 | 12105 |
| 94-10-B | 20 | 1 | 9 | 349 | 50 | 311 | 1919 | 129 | 13870 | 1091 | 109301 | 13427 | 7.9 | 100 | 12.7 | 8.1 | 11876 |
| 94-10-P | 20 | 1 | 19 | 417 | 51 | 124 | 1566 | 123 | 9975 | 773 | 107143 | 17518 | 10.7 | 139 | 12.9 | 6.1 | 5545 |
| C-022-B | 20 | 1 | 42 | 584 | 49 | 120 | 1553 | 105 | 10686 | 691 | 99230 | 16408 | 9.3 | 144 | 15.5 | 6.0 | 2384 |
| C-022-C | 20 | 1 | 37 | 509 | 52 | 85 | 1688 | 120 | 13014 | 734 | 106463 | 17220 | 8.2 | 145 | 17.7 | 6.2 | 2854 |
| C-022-Y | 20 | 1 | 5 | 750 | 71 | 119 | 1950 | 163 | 18896 | 1159 | 103030 | 12414 | 5.5 | 89 | 16.3 | 8.3 | 19017 |
| C-022-Z3 | 20 | 1 | 180 | 1385 | 46 | 97 | 1649 | 117 | 8719 | 390 | 95423 | 19533 | 10.9 | 245 | 22.3 | 4.9 | 531 |
| 96-08-B | 20 | 1 | 29 | 599 | 48 | 120 | 1669 | 107 | 11145 | 596 | 95408 | 15084 | 8.6 | 160 | 18.7 | 6.3 | 3303 |
| 96-08-C | 20 | 1 | 19 | 1264 | 48 | 276 | 1424 | 117 | 15438 | 1026 | 104041 | 9997 | 6.7 | 101 | 15.0 | 10.4 | 5507 |
| 96-08-H | 20 | 1 | 33 | 520 | 62 | 192 | 2277 | 147 | 15910 | 1512 | 107054 | 8162 | 6.7 | 71 | 10.5 | 13.1 | 3214 |
| 96-08-J | 20 | 1 | 36 | 373 | 50 | 132 | 1440 | 111 | 12046 | 1093 | 100040 | 12992 | 8.3 | 92 | 11.0 | 7.7 | 2746 |
| C-107-B | 40 | 1 | 8 | 292 | 57 | 185 | 1898 | 75 | 15110 | 1148 | 109280 | 12211 | 7.2 | 95 | 13.2 | 8.9 | 13025 |
| 10-25-4 | 47 | 1 | 15 | 1133 | 80 | 234 | 2499 | 233 | 28326 | 1611 | 99877 | 8483 | 3.5 | 62 | 17.6 | 11.8 | 6577 |
| C-107-E | 40 | 1 | 12 | 364 | 68 | 397 | 2621 | 84 | 18556 | 1309 | 101703 | 12378 | 5.5 | 78 | 14.2 | 8.2 | 8183 |
| C-107-L | 40 | 1 | 10 | 447 | 54 | 170 | 2024 | 115 | 14368 | 968 | 101245 | 15986 | 7.0 | 105 | 14.8 | 6.3 | 10610 |
| 76-05-G | 40 | 1 | 112 | 564 | 57 | 468 | 2260 | 137 | 15491 | 1122 | 109321 | 11966 | 7.1 | 97 | 13.8 | 9.1 | 975 |
| C-090-F | 40 | 1 | 43 | 539 | 49 | 129 | 1666 | 79 | 11499 | 966 | 104942 | 15391 | 9.1 | 109 | 11.9 | 6.8 | 2438 |
| C-045-O | 40 | 1 | 4 | 748 | 69 | 286 | 2736 | 185 | 18966 | 1365 | 105798 | 13539 | 5.6 | 78 | 13.9 | 7.8 | 27505 |
| C-045-Q | 40 | 1 | 3 | 538 | 65 | 248 | 2076 | 171 | 16819 | 1487 | 100193 | 13171 | 6.0 | 67 | 11.3 | 7.6 | 31003 |
| C-096-E | 40 | 1 | 44 | 352 | 47 | 125 | 1635 | 71 | 8608 | 666 | 94957 | 18261 | 11.0 | 143 | 12.9 | 5.2 | 2165 |
| C-096-G | 40 | 1 | 13 | 404 | 54 | 138 | 1660 | 83 | 11401 | 719 | 99334 | 15987 | 8.7 | 138 | 15.9 | 6.2 | 7538 |
| 76-23-B | 40 | 1 | 47 | 700 | 50 | 194 | 1474 | 55 | 8882 | 535 | 95104 | 20277 | 10.7 | 178 | 16.6 | 4.7 | 2008 |
| 86-07-T | 40 | 1 | 17 | 432 | 57 | 437 | 2016 | 130 | 16498 | 1141 | 101719 | 11905 | 6.2 | 89 | 14.5 | 8.5 | 5845 |
| M-17-D | 40 | 1 | 9 | 774 | 68 | 259 | 2468 | 148 | 19657 | 1284 | 100672 | 12565 | 5.1 | 78 | 15.3 | 8.0 | 10622 |
| M-17-G | 40 | 1 | 4 | 667 | 64 | 170 | 2480 | 151 | 20522 | 1362 | 102202 | 12268 | 5.0 | 75 | 15.1 | 8.3 | 26276 |
| 94-10-K | 40 | 1 | 70 | 379 | 49 | 169 | 1692 | 109 | 10219 | 765 | 104375 | 15929 | 10.2 | 136 | 13.4 | 6.6 | 1501 |
| 94-10-N | 40 | 1 | 6 | 304 | 51 | 114 | 1547 | 127 | 12672 | 979 | 112463 | 13120 | 8.9 | 115 | 12.9 | 8.6 | 18401 |
| C-022-E | 40 | 1 | 7 | 904 | 85 | 197 | 1873 | 209 | 27354 | 2584 | 110001 | 6450 | 4.0 | 43 | 10.6 | 17.1 | 14699 |
| C-022-P | 40 | 1 | 51 | 1055 | 68 | 165 | 1428 | 131 | 14460 | 1276 | 83561 | 22559 | 5.8 | 65 | 11.3 | 3.7 | 1623 |

**Appendix V:** Wet chemistry sample compositions. Element values in ppm. *Ga contents systematically low - see text for details

| Sample | Zone | Type | Ba | Ca | Ga* | Li | P | Sr | Rb | Cs | K | Na | K/Rb | K/Cs | Rb/Cs | K/Na | K/Ba |
|---|---|---|---|---|---|---|---|---|---|---|---|---|---|---|---|---|---|
| C-022-R | 40 | 1 | 114 | 485 | 71 | 115 | 1688 | 183 | 21491 | 2373 | 101367 | 26810 | 4.7 | 43 | 9.1 | 3.8 | 888 |
| C-022-V | 40 | 1 | 34 | 1132 | 84 | 180 | 2444 | 217 | 22995 | 1307 | 100729 | 13082 | 4.4 | 77 | 17.6 | 7.7 | 2927 |
| C-022-W | 40 | 1 | 27 | 1118 | 75 | 196 | 2287 | 190 | 21141 | 1223 | 98669 | 11190 | 4.7 | 81 | 17.3 | 8.8 | 3642 |
| 92-11-L | 40 | 1 | 2 | 617 | 82 | 206 | 3316 | 220 | 27659 | 1599 | 103454 | 12457 | 3.7 | 65 | 17.3 | 8.3 | 52051 |
| C-033-G | 40 | 1 | 134 | 372 | 78 | 227 | 2167 | 209 | 25188 | 2775 | 103264 | 8600 | 4.1 | 37 | 9.1 | 12.0 | 772 |
| C-033-H | 40 | 1 | 141 | 440 | 70 | 162 | 2011 | 209 | 25234 | 2802 | 109956 | 6752 | 4.4 | 39 | 9.0 | 16.3 | 782 |
| C-033-S | 40 | 1 | 45 | 543 | 33 | 133 | 828 | 156 | 22473 | 2314 | 110517 | 6811 | 4.9 | 48 | 9.7 | 16.2 | 2457 |
| 96-08-E | 45 | 1 | 12 | 497 | 53 | 340 | 1703 | 142 | 15416 | 1262 | 105196 | 10138 | 6.8 | 83 | 12.2 | 10.4 | 8582 |
| 95-08-A | 45 | 1 | 6 | 433 | 74 | 236 | 2355 | 184 | 26833 | 1931 | 103665 | 7761 | 3.9 | 54 | 13.9 | 13.4 | 17625 |
| 95-08-K | 45 | 1 | 8 | 501 | 67 | 290 | 2705 | 137 | 21960 | 1405 | 99743 | 12982 | 4.5 | 71 | 15.6 | 7.7 | 12570 |
| C-045-Ha | 45 | 1 | 9 | 298 | 57 | 326 | 1856 | 147 | 14095 | 955 | 102886 | 15174 | 7.3 | 108 | 14.8 | 6.8 | 11496 |
| C-C | 50 | 1 | 69 | 249 | 45 | 218 | 775 | 140 | 16905 | 1295 | 102259 | 16772 | 6.0 | 79 | 13.1 | 6.1 | 1472 |
| 86-07-C | 50 | 1 | 4 | 1146 | 82 | 297 | 2562 | 217 | 27338 | 2235 | 110284 | 8564 | 4.0 | 49 | 12.2 | 12.9 | 30184 |
| 94-10-G | 50 | 1 | 4 | 683 | 74 | 723 | 2624 | 175 | 18331 | 1534 | 103680 | 11643 | 5.7 | 68 | 12.0 | 8.9 | 26531 |
| 94-10-I | 50 | 1 | 7 | 601 | 58 | 874 | 1969 | 129 | 15636 | 1375 | 98832 | 12068 | 6.3 | 72 | 11.4 | 8.2 | 14299 |
| 91-16-JA | 50 | 1 | 15 | 405 | 48 | 87 | 1546 | 95 | 11883 | 826 | 100846 | 16168 | 8.5 | 122 | 14.4 | 6.2 | 6871 |
| 91-16-JB | 50 | 1 | 7 | 561 | 69 | 350 | 2236 | 113 | 15618 | 1434 | 106882 | 11306 | 6.8 | 75 | 10.9 | 9.5 | 14481 |
| 96-08-D | 50 | 1 | 21 | 643 | 57 | 611 | 1571 | 149 | 17812 | 1473 | 105690 | 4840 | 5.9 | 72 | 12.1 | 21.8 | 5113 |
| 96-08-JB | 50 | 1 | 13 | 342 | 58 | 412 | 1849 | 134 | 16796 | 1267 | 101840 | 9892 | 6.1 | 80 | 13.3 | 10.3 | 8141 |
| B-06-C | 50 | 1 | 6 | 888 | 80 | 374 | 2582 | 203 | 23891 | 1395 | 103199 | 12505 | 4.3 | 74 | 17.1 | 8.3 | 18397 |
| B-06-D | 50 | 1 | 46 | 1071 | 48 | 157 | 1031 | 114 | 17113 | 1152 | 109671 | 7716 | 6.4 | 95 | 14.9 | 14.2 | 2377 |
| 10-25-3a | 50 | 1 | 71 | 588 | 69 | 265 | 2553 | 156 | 19032 | 1165 | 99721 | 13086 | 5.2 | 86 | 16.3 | 7.6 | 1400 |
| 10-25-3b | 50 | 1 | 4 | 533 | 50 | 428 | 2356 | 171 | 21814 | 1350 | 103236 | 12231 | 4.7 | 76 | 16.2 | 8.4 | 25755 |
| 10-25-3c | 50 | 1 | 40 | 827 | 69 | 390 | 2697 | 171 | 20266 | 1222 | 99419 | 11527 | 4.9 | 81 | 16.6 | 8.6 | 2475 |
| 10-25-3d | 50 | 1 | 86 | 895 | 47 | 284 | 2647 | 170 | 21137 | 1206 | 98788 | 14471 | 4.7 | 82 | 17.5 | 6.8 | 1154 |
| 10-25-3e | 50 | 1 | 22 | 626 | 67 | 168 | 2301 | 234 | 29987 | 1696 | 102937 | 11248 | 3.4 | 61 | 17.7 | 9.2 | 4698 |
| 12-15-1A | 50 | 1 | 80 | 788 | 44 | 885 | 1748 | 126 | 17503 | 1000 | 103984 | 11253 | 5.9 | 104 | 17.5 | 9.2 | 1304 |
| 12-15-1B | 50 | 1 | 36 | 650 | 46 | 869 | 1872 | 139 | 15492 | 878 | 94710 | 10993 | 6.1 | 108 | 17.7 | 8.6 | 2655 |
| 12-15-1C | 50 | 1 | 33 | 1027 | 57 | 425 | 2017 | 172 | 18652 | 1198 | 102766 | 12367 | 5.5 | 86 | 15.6 | 8.3 | 3110 |
| 12-15-1D | 50 | 1 | 9 | 785 | 39 | 221 | 1987 | 144 | 15927 | 1026 | 100585 | 12169 | 6.3 | 98 | 15.5 | 8.3 | 10702 |
| 12-15-1E | 50 | 1 | 16 | 383 | 61 | 807 | 1841 | 140 | 15701 | 882 | 103524 | 11470 | 6.6 | 117 | 17.8 | 9.0 | 6500 |
| C-S | 60 | 1 | 41 | 1041 | 74 | 232 | 1792 | 230 | 22846 | 3046 | 111490 | 6396 | 4.9 | 37 | 7.5 | 17.4 | 2706 |

**Appendix V:** Wet chemistry sample compositions. Element values in ppm. *Ga contents systematically low - see text for details

| Sample | Zone | Type | Ba | Ca | Ga* | Li | P | Sr | Rb | Cs | K | Na | K/Rb | K/Cs | Rb/Cs | K/Na | K/Ba |
|---|---|---|---|---|---|---|---|---|---|---|---|---|---|---|---|---|---|
| 12-15-20 | 60 | 1 | 39 | 437 | 69 | 105 | 1809 | 198 | 26276 | 2775 | 107826 | 7323 | 4.1 | 39 | 9.5 | 14.7 | 2745 |
| 12-15-4 | 60 | 1 | 87 | 431 | 46 | 108 | 1217 | 195 | 26242 | 2589 | 113875 | 17033 | 4.3 | 44 | 10.1 | 6.7 | 1316 |
| 12-15-5 | 60 | 1 | 11 | 574 | 69 | 176 | 1994 | 279 | 34658 | 2770 | 98548 | 12599 | 2.8 | 36 | 12.5 | 7.8 | 8994 |
| 12-15-6 | 60 | 1 | 44 | 437 | 59 | 355 | 371 | 144 | 24236 | 1615 | 114498 | 4872 | 4.7 | 71 | 15.0 | 23.5 | 2610 |
| 12-15-7 | 60 | 1 | 29 | 714 | 70 | 181 | 1882 | 236 | 28482 | 1637 | 105208 | 10301 | 3.7 | 64 | 17.4 | 10.2 | 3584 |
| 12-15-8 | 60 | 1 | 20 | 1717 | 63 | 213 | 1910 | 211 | 27920 | 2042 | 112391 | 5310 | 4.0 | 55 | 13.7 | 21.2 | 5572 |
| BL-jar1 | 60 | 2 | 344 | 558 | 55 | 94 | 1118 | 216 | 25490 | 2571 | 107022 | 17161 | 4.2 | 42 | 9.9 | 6.2 | 311 |
| BL-jar2 | 60 | 2 | 317 | 339 | 34 | 89 | 1165 | 199 | 25648 | 2720 | 112851 | 10281 | 4.4 | 41 | 9.4 | 11.0 | 356 |
| BLM-506 | 60 | 2 | 41 | 466 | 83 | 333 | 1504 | 207 | 25879 | 2557 | 109515 | 9094 | 4.2 | 43 | 10.1 | 12.0 | 2639 |
| LM-1 | 60 | 2 | 155 | 970 | 67 | 151 |  | 179 | 25121 | 2224 | 114308 | 7327 | 4.6 | 51 | 11.3 | 15.6 | 738 |
| C-090-J | 60 | 1 | 9 | 590 | 83 | 249 | 1813 | 115 | 23582 | 2712 | 109695 | 7079 | 4.7 | 40 | 8.7 | 15.5 | 12582 |
| C-045-L | 60 | 1 | 200 | 477 | 66 | 325 | 888 | 140 | 17272 | 1802 | 111367 | 8882 | 6.4 | 62 | 9.6 | 12.5 | 557 |
| C-022-J | 60 | 1 | 94 | 847 | 90 | 266 | 1444 | 188 | 22928 | 2615 | 110083 | 6445 | 4.8 | 42 | 8.8 | 17.1 | 1175 |
| C-022-K | 60 | 1 | 84 | 638 | 82 | 294 | 1319 | 159 | 22150 | 2555 | 116243 | 2322 | 5.2 | 45 | 8.7 | 50.1 | 1387 |
| C-096-I | 60 | 1 | 126 | 503 | 57 | 216 | 2180 | 159 | 22074 | 2903 | 105147 | 9289 | 4.8 | 36 | 7.6 | 11.3 | 837 |
| C-096-J | 60 | 1 | 159 | 322 | 71 | 262 | 2243 | 174 | 23375 | 3582 | 104635 | 8958 | 4.5 | 29 | 6.5 | 11.7 | 659 |
| C-M | 63 | 1 | 26 | 657 | 70 | 240 | 1229 | 210 | 18656 | 2577 | 99343 | 16419 | 5.3 | 39 | 7.2 | 6.1 | 3767 |
| 10-25-1 | 80 | 1 | 222 | 438 | 73 | 315 | 2127 | 246 | 31360 | 2792 | 104741 | 7820 | 3.3 | 38 | 11.2 | 13.4 | 472 |
| 10-25-2 | 80 | 1 | 206 | 636 | 76 | 132 | 2041 | 200 | 26218 | 2432 | 105842 | 9825 | 4.0 | 44 | 10.8 | 10.8 | 513 |
| 12-15-19 | 80 | 1 | 21 | 588 | 64 | 284 |  | 211 | 27078 | 2899 | 106153 | 6789 | 3.9 | 37 | 9.3 | 15.6 | 5175 |
| 10-25-7 | 90 | 1 | 55 | 241 | 72 | 142 | 1769 | 200 | 23874 | 4165 | 97930 | 9739 | 4.1 | 24 | 5.7 | 10.1 | 1796 |
| 12-15-10 | 90 | 1 | 37 | 1861 | 54 | 236 |  | 197 | 25595 | 2273 | 114201 | 2639 | 4.5 | 50 | 11.3 | 43.3 | 3067 |
| 12-15-17 | 90 | 1 | 54 | 1350 | 117 | 422 | 1285 | 196 | 30840 | 2159 | 106884 | 16266 | 3.5 | 50 | 14.3 | 6.6 | 1991 |
| 12-15-23 | 90 | 1 | 13 | 654 | 67 | 128 | 1720 | 197 | 26553 | 2440 | 105000 | 7547 | 4.0 | 43 | 10.9 | 13.9 | 8178 |
| 96-11-B | 99 | 1 | 94 | 536 | 44 | 436 | 1689 | 115 | 13777 | 619 | 96888 | 15835 | 7.0 | 157 | 22.3 | 6.1 | 1029 |

| | Ba | Ca | Ga* | Li | P | Sr | Rb | Cs | K | Na | K/Rb | K/Cs | Rb/Cs | K/Na | K/Ba |
|---|---|---|---|---|---|---|---|---|---|---|---|---|---|---|---|
| max | 344 | 1861 | 117 | 885 | 3316 | 279 | 34658 | 4165 | 117807 | 26810 | 14.2 | 262 | 22.3 | 50.1 | 52051 |
| min | 2 | 241 | 0 | 25 | 371 | 55 | 6842 | 371 | 83561 | 2322 | 2.8 | 24 | 5.7 | 3.6 | 311 |
| average | 61 | 677 | 59 | 227 | 1818 | 148 | 18018 | 1469 | 102956 | 12993 | 6.4 | 89 | 13.5 | 9.6 | 6214 |
| 1σ | 70 | 320 | 14 | 165 | 480 | 46 | 6171 | 753 | 6069 | 4608 | 2.3 | 44 | 3.5 | 6.2 | 8067 |